University of Udine
Polytechnic Department of Engineering and Architecture
Ph.D. in Industrial and Information Engineering - 34^{th} cycle

Ph.D. dissertation

A dynamic optimization setting for problems in structural mechanics

Candidate:
Hassan Mohamed Abdelalim Abdalla

Advisors:
Dr. Daniele Casagrande
Prof. Francesco De Bona

To Raìsa,
may God compensate her.

Abstract

This dissertation is focused on the utility of variational principles and the vast possibilities they offer as powerful tools for a suggestive use to solve optimization problems in structural mechanics. To this purpose, an introduction to the analytical approach to continuous dynamic optimization problems and the development of a dedicated computational method are addressed in the first part of the dissertation. For the sake of establishing a level of practical effectiveness and clarifying their vitality, a few concrete applications ranging from shape optimization problems for thin-walled axisymmetric pressure vessels and straight and curved beams to material optimization problems for functionally graded elastic bodies are addressed. The corresponding decision variables are the meridian shape, the cross sectional area distribution and the mechanical properties distributions along specific directions throughout the body, respectively. Potential performance criteria destined for optimization and possible structural constraints consist of reasonable combinations of lightweightness, storage capacity, compliance, resistance to buckling and load-bearing capacity. These problems are formulated in the second part of the dissertation, solved and thoroughly discussed and, when possible, compared to literature. In some cases, optimal solutions are derived analytically and are accompanied by prompt design charts, otherwise, in case of a cumbersome analytical tractability, they are obtained numerically by means of the computational method developed in the first part.

List of Figures

List of Tables

List of publications

1. Abdalla HMA, Casagrande D, De Bona F, Thin-walled pressure vessels of minimum mass or maximum volume, *Struct Multidisc Optim* **61(1)**, pp. 111-121, 2020.

2. Abdalla HMA, Casagrande D, Analytical thickness distribution for minimum compliance axisymmetric vessels, *Thin-Walled Struct* **149**, 106641, 2020.

3. Abdalla HMA, Casagrande D, De Bona F, A dynamic optimization setting for functionally graded thick-walled cylinders, *Materials*, **13**, 3988, 2020.

4. Abdalla HMA, Casagrande D, Strozzi A, A unified relaxed approach easing the practical application of a paradox in curved beams, *Proc IMechC: J Mechanical Engineering Science* **234(22)**, pp. 4535-4542, 2020.

5. Abdalla HMA, Casagrande D, On the longest reach problem in large deflection elastic rods, *Int J Non Linear Mech* **119**, 103310, 2020.

6. Abdalla HMA, Casagrande D, Moro L, Thermo-mechanical analysis and optimization of functionally graded rotating disks, *J Strain Anal Eng Des*, **55(5-6)**, pp. 159–171, 2020.

7. D'Agostino S, Abdalla HMA, Strozzi A, Practical repercussions of a paradox in curved beams, *AIP Conf Proc* **2309**, 020035, 2020.

8. Abdalla HMA, Srnec JN, Casagrande D, Lower bound estimate for buckling in axially graded cantilever rods, *Eng Res Express* **2**, 035033, 2020.

9. Abdalla HMA, Casagrande D, Optimal area variation for maximum stiffness isostatic beams under parametric linear distributed loads, *Mech Res Commun* **111**, 103659, 2021.

10. Abdalla HMA, Casagrande D, De Bona F, De Monte T, Sortino M, Totis G, An optimized pressure vessel obtained by metal additive manufacturing: Preliminary results, *Int J Pres Ves Pip* **192**, 104434, 2021.

11. Abdalla HMA, Casagrande D, An intrinsic material tailoring approach for functionally graded axisymmetric hollow bodies under plane elasticity, *J Elast*, **144**, pp. 15-32, 2021.

12. Marcu GG, Abdalla HMA, Casagrande D, Less is better: Coated spherical vessels over-perform their entirely graded counterparts, *Compos Struct*, **276**, 114529, 2021.

Acronyms

AM	Additive Manufacturing
BVP	Boundary Value Problem
FE	Finite Element
FGM	Functionally Graded Material
IIS	Imposed Intrados Stress
IVP	Initial Value Problem
LGR	Legendre-Gauss-Radau
NLP	Nonlinear programming
SEM	Scanning Electron Microscope
SLM	Selective Laser Melting
STL	Standard Triangulation Language
TO	Topology Optimization
UIS	Unaltered Intrados Stress

Contents

Chapter 1

Introduction

When designing any engineering system, engineers have to take prompt decisions at several stages, whose primary goal is to provide safety and endurance under given circumstances. In the practice, this design process has been always including a mysterious element, since the designer chooses dimensions and materials by means of intuition and experience. Whereas this technique has proved effective results even in ancient times before accurate mathematical or mechanical theories were developed, today conceptual design processes should also include further aspects to continuously withstand global competition. Optimization methods, coupled with modern tools of computer-aided design, have been offering potential techniques to respond to this creative process of conceptual design.

Optimization problems can be classified in several ways. As far as the nature of the involved design variables is concerned, two broad categories of problems may arise. In the first category, values of design parameters that make some prescribed function of these parameters minimum and subject to certain constraints are sought. Such problems are often called *static* optimization problems; their optimal solution is derived by the application of the well-known Karush-Kuhn-Tucker necessary conditions. In the second category, the objective is to find the expression of design parameters that in turn are all (continuous) functions of a variable, so that a prescribed functional attains its minimum value and certain constraints are satisfied. These problems are referred to as *dynamic* optimization problems. Here, necessary conditions for optimality are derived within a variational framework, namely by making use of well established tool from calculus of variations.

While the overwhelming studies concerning optimization problems in

structural engineering are formulated within the first category, the second category gains ground rather in other disciplines (e.g., aerospace, control and chemical engineering). On the one hand, this is partly due to the relatively rich and well-established literature on methods and solution techniques for problems pertaining to the first category. In fact, although attempts to factually establish the extent of practical use of mathematical programming and other discrete variable optimization methods in structural engineering date back to several decades ago, as pointed out in [1], this research activity is still carried out and remarkably characterized by an increasing interest to employ meta-heuristic methods, e.g., [2, 3, 4]. On the other hand, reasons range from an existing gap between mathematical approaches to variational principles and their practical use when formulating problems in structural mechanics to the computational burden associated with the computation of optimal solutions. Moreover, unlike dynamic optimization problems, static problems stated in the realm of structural mechanics are fairly straightforward to implement as the shape of the structure remains unchanged [5]. As a consequence, it is easy to implement a design sensitivity analysis and therefore no refinement or modification is required for the finite element geometry model.

The above mentioned reasons are further emphasized in the next three sections by briefly addressing the common encountered challenges when optimizing the shape or the material distribution of elastic bodies by dynamic optimization problems, referring the reader, for more details concerning each problem, in the dedicated chapters.

1.1 Shape optimization of axisymmetric vessels

It can be seen that for axisymmetric problems, the notion of "shape" can have different meanings. In two-dimensional plane problems, by far the most commonly found in literature on shape optimization, the shape usually refers to the boundary shape. In particular, for axisymmetric thin-walled structures, shape can mean the midwall meridian shape as well as the inside and outside boundary surface shapes, namely the thickness distribution. For thin-walled pressurized vessels, it is arguable whether the shape of the midwall or the thickness distribution plays the most important role. On the one hand, studies concerning only the first decision variable and addressed within well-stated static optimization problems are more common in literature [6]. However, they are generally limited to address simple geometries such as those constituted by a cylinder of constant thickness with

end caps, cones, ellipsoids or toroids. Optimal characteristic dimensions of the resulting vessel depend on the problem under consideration. For instance, some works offer simple algebraic relations derived from the application of membrane theory of shells, e.g., [7, 8], while others heavily rely on successive finite element analyses coupled with internal optimization routes, e.g., [9]. On the other hand, studies dealing with the optimization of the thickness distribution of prefixed meridian shapes are rarely encountered in the literature, e.g., [10, 11, 12, 13], mostly due to the serious technological issues associated with the realization of the distribution of the thickness with standard manufacturing processes.

Nowadays, however, this technological challenge can be surmounted by taking into account the availability of last generation metal additive techniques, suggesting one to reconsider formulations where both the midwall meridian shape and the thickness distribution are decision variables. Attempts by using the calculus of variations are proposed in [14, 15], where the optimization problem is aimed at minimizing the mass for given shell strength and cavity volume. Optimal solutions are analytically obtained and under the hypothesis that the shell is made of a brittle or quasi-brittle material. The elegance of this treatise motivates the problem reconsideration, extending the formulation to include ductile materials and dealing with other objectives and constraints. Furthermore, among optimal solutions, it is also desired to choose a particular case for which a technological demonstrator can be manufactured and suitably verified by performing a reverse engineering process through three-dimensional scanning and finite element-based validation.

1.2 Shape optimization of beams

Shape optimization for elastic beams is still a very common topic of research as these structural elements are widely used as efficient load-carrying members. More specifically, elastic beams with straight and curved axes have been gaining considerable attention in structural mechanics, whose shape optimization mostly relies on dedicated computational models developed by means of topology optimization concepts and formulated within the three-dimensional elasticity theory. In [16], it is emphasized how topology optimization has been receiving a boost as it leads to a significant improvement in the quality of structures. A review on this approach and its application for continuum structures can be found in [17]. However, some fundamental issues of this field have not yet been sufficiently researched and

therefore the correctness and accuracy of methods and applications in a large number of papers is somewhat questionable [18]. Perhaps, the first successful application of the topology optimization in the design of beam sections has been reported in [19], where the finite element approach has been adopted. Other attempts relying on boundary element method or B-splines methods can be found in [20, 21]. Nevertheless, the derived optimal solutions are geometrically complex as, in most of the cases, they lead to free forms. Despite additive manufacture can accommodate significantly these complex geometries, additional rules are still needed to ensure manufacturability without requiring additional support material [22].

These considerations suggest one to make use of theories simpler than the three-dimensional theory of elasticity, yet capable to correctly mimic the mechanical behavior of these elastic structures. To this purpose, one can exploit the one-dimensional nature of beams by referring to the well-known Euler-Bernoulli and Winkler theories for straight and curved beams, respectively [23], and suitably formulate a few dynamic optimization problems whose decision variable is the cross sectional distribution along the beam axis and so that practical structural criteria such as the overall compliance, the weight and the resistance to buckling load are optimized. Cases where solutions can be expressed analytically can be taken as benchmark solutions for topology optimization problem solvers.

1.3 Material optimization of functionally graded pressurized cylinders

Functionally graded materials are a kind of composite material whose physical and mechanical properties vary spatially along specific directions over the entire domain. They are present in many engineering applications such as, for example, space planes, nuclear fusion reactors, energy conversion systems, and thermo generators [24]. Various applications of these materials have attracted considerable attention in recent years and their increasing use needs comprehensive mechanical analyses [25]. The optimum response of material properties to an actual environment is the main requirement in the design of these materials; nevertheless, very few works deal with the problem of optimal material distribution because, often, the optimization process heavily relies on subsequent finite element simulations.

Limiting ourselves to functionally graded axisymmetric bodies whose mechanical properties are given by certain models described by some parameters, it can be shown that stresses can be expressed explicitly in

terms of these parameters, whose tuning values are sought so that a prefixed mechanical response is minimized. Admittedly, however, the resulting optimization problems are analyzed merely from the theoretical point of view, without taking into account the practical aspects associated with the construction of the optimal property variations. A more realistic (and, in some sense, intrinsic) optimization problem should a priori consist in the search for optimal property variations in a set of functions and not merely in the search for optimal parameters associated with prefixed property behaviors.

To the extent of the author's knowledge, previous works dealing with this problem are rare, where a property variation is referred to as optimal if it maximizes or minimizes a (pre-defined) mechanical performance. For instance, a designer may be interested in the search for properties variation for a spherical vessel of minimum compliance, a cylinder of minimum hoop stress at a specific radius or a disk of uniform strength or minimum mass, possibly complying with other constraints which can be economic or related to the manufacturing process. These problems can also be formulated in the context of dynamic optimization theory, where governing equations are the equilibrium, the compatibility and the constitutive equations for linear, elastic, isotropic and heterogeneous materials. In particular, necessary conditions for optimal solutions can be derived by means of variational principles and solved either analytically or numerically, depending on the complexity of the involved equations.

1.4 Objective and structure of the dissertation

The present dissertation aims to bridge existing gaps between the mathematical tools offered by variational principles and their practical use for problems in structural engineering, where applications concerning the shape of membrane shells of revolution, one-dimensional structural elements and the best material distribution in internally pressurized heterogeneous cylinders are shown and discussed. In particular, functions describing the shape or the material distribution are sought so that prefixed functionals linked to practical design criteria attain their minimum values and other structural integrity constraints are satisfied. Whenever necessary conditions for optimality are hardly tackled analytically, a numerical approach based on orthogonal collocation method is employed.

The rest of dissertation is organized as follows. The overall content is divided into two main parts. In the first part (Part I), a concise introduction

to the theoretical background and the development of the numerical tools are addressed, whereas applications to structural mechanics are reported in the second part (Part II).

In particular, based on the basic definitions, lemmas and theorems in calculus of variations (presented in Appendix A), Chapter 2 extends the formulation of calculus of variation problems to those complying with algebraic-differential and inequality path constraints. Introducing states, costates and input functions, necessary conditions for optimality yield a boundary value problem which, boundary conditions apart, consists of a Hamiltonian dynamical system whose primary variables are optimal states and costates, a set of algebraic conditions and a relation expressing optimal input functions (Pontryagin's Principle). It is emphasized that the resulting boundary value problem is hardly tractably from the analytical point of view unless in a very few cases.

The development of a dedicated numerical tool is thus illustrated in Chapter 3, where states are approximated by Lagrange interpolating polynomials and differential constrains are collocated at Legendre-Gauss-Radau points destined to avoid numerical oscillations at the edges of the interval where the problem is defined. The conversion of the dynamic optimization problem into a static one is presented in two different schemes and the computation of the first-order derivatives is performed to decrease the number of function evaluations during the iterative process.

Chapter 4 addresses three dynamic optimization problems in the realm of membrane axisymmetric pressure vessels subject to internal uniform pressure. The decision variables are the meridian shape and the thickness distribution, not necessarily constant. The first one aims at minimizing the mass of the membrane shell once its cavity volume is fixed. The second one interchanges the former objective functional with the latter constraint and the third one concerns with the minimization of the compliance for a given material mass. The solution of these problems provided prompt design charts of ample validity in closed form, yet optimal forms are hardly obtained by means of standard technologies due to the variation of the thickness distribution. A first and preliminary attempt to the manufacturability of the resulting forms by metal additive techniques is thoroughly discussed.

Chapter 5 still deals with shape optimization problems, but for one-dimensional structural beam elements under the theory of linear elasticity, where cost functionals and constraints range from material volume to buckling loads and structural compliance. Shape optimization problems for initially straight beams as well as a recently stated problem addressing a paradox in curved beams have been considered.

Chapter 6 addresses the best material distribution in internally pressurized heterogeneous cylinders. The material is assumed to have mechanical properties that vary throughout the radial direction. Based on the theory of linear elasticity, the description of occurring stresses, strains in plane stress and plane strain conditions has been recalled. Unlike the overwhelming studies in the literature, the distribution of elastic properties along the radial direction is considered as the input function to be determined, thus offering an intrinsic setting for their derivation based on optimality principles. By taking different measures of the maximum stress, it is found that the obtained optimal solutions perform better than those associated with several gradation strategies commonly employed in the literature.

Finally, Chapter 7 summarizes the presented studies as well as a few extensions that may be destined for future works.

Part I

Theoretical background and computational framework

Chapter 2

Continuous dynamic optimization and Pontryagin's Principle

2.1 Introduction

Continuous dynamic (or functional) optimization is a subject where it is desired to determine certain inputs to a system of differential equations which describes the evolution of the variables that model a problem under consideration, so that a specified functional achieves its minimum value, while satisfying some constraints on the variable of the system. Its principles, that can be considered as an extension of calculus of variations, date back to the Fifties largely due to the works by Pontryagin and Bellman. Input functions and variables employed to model the problem are commonly referred to as *goal* (or *objective*) *functions* and *state variables*, respectively, whereas the functional to be optimized is called the *goal functional* or the *performance index*. The system of differential equations, usually employing the above mentioned states, is usually denoted as the *plant equations* or, more simply, the *dynamics*. The requirement that plant equations are given by a system of differential equations justifies the adjective "continuous", differently from problems where the system evolution is described by recurrence formulas, i.e., discrete relationships.

In Appendix A, elements of calculus of variations have been recalled and necessary conditions for the existence of extremals have been derived for different problems, yet a few aspects on which most of the analysis relies on have been unaltered. For instance, only integral goal functionals have

been exclusively considered. They consist of a distributed term along the interval of interest. Hereinafter, these functionals are referred to as Lagrange goal functionals. However, another type of goal functional depending only on initial and/or final conditions may also be stated. An example of such goal functional has been given in Example A.1 in Appendix A. This kind of goal functionals is referred to as Mayer goal functionals. Furthermore, boundary conditions apart, extremals were not enforced to satisfy specified plant equations throughout the interval of interest. In fact, if such condition is required, the inclusion of this type of differential constraint is necessary so that the problem results unconstrained and the previous tools can be borrowed. Moreover, only problems allowing variations in the final boundary conditions have been addressed. Dynamic optimization principles can encompasses all these variants (and more) so that necessary conditions are derived in a nice and versatile fashion.

To this purpose, the following notation is employed. Let

$$y_1(x),\, y_2(x),\, \ldots,\, y_n(x)$$

and

$$u_1(x),\, u_2(x),\, \ldots,\, u_m(x)$$

denote the states and the objective functions, respectively, of the considered problem at coordinate x, and suppose that the plant equations are given by

$$\frac{d\mathbf{y}(x)}{dx} = \mathbf{a}(x, \mathbf{y}(x), \mathbf{u}(x)),$$

where $\mathbf{y}$ and $\mathbf{u}$ are vectors whose i-th components are y_i and u_i, respectively, and the function $\mathbf{a}$ is generally nonlinear. Hereinafter, $\mathbf{y}$ and $\mathbf{u}$ are taken as column vectors, whereas the gradient of a scalar function with respect to any vector quantity, say $\boldsymbol{\xi} \in \mathbb{R}^k$, is a row vector, namely

$$\mathbf{y} = \begin{bmatrix} y_1 \\ y_2 \\ \vdots \\ y_n \end{bmatrix}, \quad \mathbf{u} = \begin{bmatrix} u_1 \\ u_2 \\ \vdots \\ u_m \end{bmatrix}, \quad \frac{\partial(.)}{\partial \boldsymbol{\xi}} = \begin{bmatrix} \frac{\partial(.)}{\partial \xi_1} & \frac{\partial(.)}{\partial \xi_2} & \cdots & \frac{\partial(.)}{\partial \xi_k} \end{bmatrix}.$$

Besides, the Jacobian of a vector quantity, say $\mathbf{v} \in \mathbb{R}^j$, with respect to $\boldsymbol{\xi}$ is

the $k \times j$ matrix

$$\frac{\partial \mathbf{v}}{\partial \boldsymbol{\xi}} = \begin{bmatrix} \frac{\partial v_1}{\partial \xi_1} & \frac{\partial v_1}{\partial \xi_2} & \cdots & \frac{\partial v_1}{\partial \xi_k} \\ \frac{\partial v_2}{\partial \xi_1} & \frac{\partial v_2}{\partial \xi_2} & \cdots & \frac{\partial v_2}{\partial \xi_k} \\ \vdots & \vdots & \cdots & \vdots \\ \frac{\partial v_j}{\partial \xi_1} & \frac{\partial v_j}{\partial \xi_2} & \cdots & \frac{\partial v_j}{\partial \xi_k} \end{bmatrix}. \tag{2.1}$$

As previously mentioned, unlike problems stated in Appendix A, in what follows it will be assumed that the performance index is evaluated by a measure of the form

$$J = \mathcal{M}(x_0, \mathbf{y}(x_0), x_f, \mathbf{y}(x_f)) + \int_{x_0}^{x_f} \mathcal{L}(x, \mathbf{y}(x), \mathbf{u}(x))\, dx,$$

where x_0, x_f, $\mathbf{y}(x_0)$ and $\mathbf{y}(x_f)$ may be specified or free, depending on the statement of the problem, while the first and second members at the right hand-side refer to Mayer and Lagrange costs, respectively. Besides, let $\boldsymbol{\phi}$ be the set of boundary conditions, abstractly recast as

$$\boldsymbol{\phi}(x_0, \mathbf{y}(x_0), x_f, \mathbf{y}(x_f)) = \mathbf{0},$$

letting functions $\mathbf{a}$, $\mathcal{M}$, $\mathcal{L}$ and $\boldsymbol{\phi}$ be defined by the following mappings: $\mathbf{a} : [x_0, x_f] \times \mathbb{R}^n \times \mathbb{R}^m \to \mathbb{R}^n$, $\mathcal{M} : \mathbb{R} \times \mathbb{R}^n \times \mathbb{R} \times \mathbb{R}^n \to \mathbb{R}$ and $\mathcal{L} : [x_0, x_f] \times \mathbb{R}^n \times \mathbb{R}^m \to \mathbb{R}$ and $\boldsymbol{\phi} : \mathbb{R} \times \mathbb{R}^n \times \mathbb{R} \times \mathbb{R}^n \to \mathbb{R}^b$ and denoting by a prime the first derivative with respect to x, a continuous dynamic optimization problem may be generally formulated as follows:

Problem 2.1. *Find the input functions $\mathbf{u}(x) \in \mathbb{R}^m$ which extremize the functional*

$$J = \mathcal{M}(x_0, \mathbf{y}(x_0), x_f, \mathbf{y}(x_f)) + \int_{x_0}^{x_f} \mathcal{L}(x, \mathbf{y}(x), \mathbf{u}(x))\, dx \tag{2.2}$$

and subject to the algebraic-differential constraints

$$\begin{cases} \mathbf{y}'(x) = \mathbf{a}(x, \mathbf{y}(x), \mathbf{u}(x)), \\ \boldsymbol{\phi}(x_0, \mathbf{y}(x_0), x_f, \mathbf{y}(x_f)) = \mathbf{0}, \end{cases} \tag{2.3}$$

where x_0, x_f, $\mathbf{y}(x_0)$ and $\mathbf{y}(x_f)$ are free (see Figure 2.1).

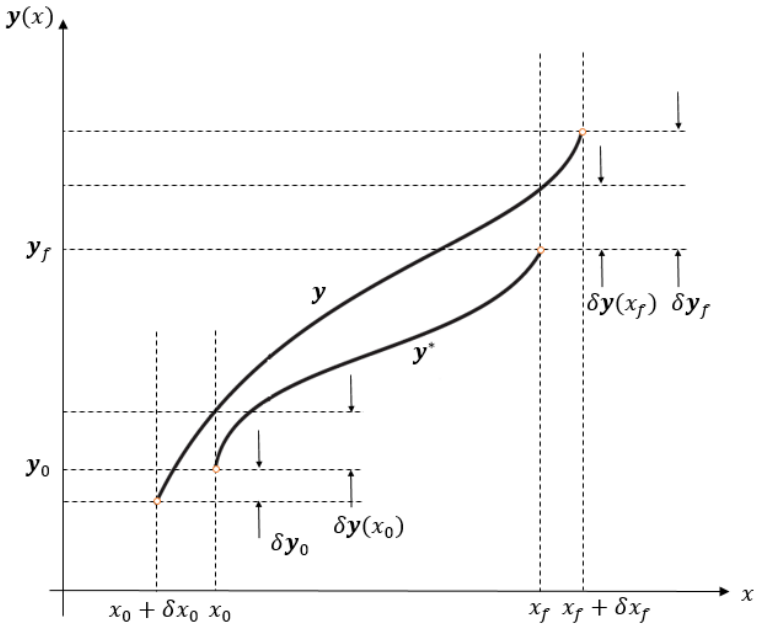

Figure 2.1: An extremal n-dimensional state and a comparison neighbor.

2.2 Necessary conditions for extremals

It is known that finding an extremal for the functional (2.2) alone may not satisfy constraints (2.3). Thus, one is hindered to incorporate these constraints into the problem formulation. One way is to consider the augmentation of the functional, just like what illustrated for Problem A.5 in Appendix A. Unlike for Problem A.5, however, multipliers should be multidimensional, i.e., vectors of numbers or functions of x, depending on the involved constraints. Yet once introduced in the problem formulation, the augmented problem yields extremals also for the original problem. In particular, letting $\boldsymbol{\nu} \in \mathbb{R}^b$ be the column vector containing multipliers accounting for boundary conditions, namely

$$\boldsymbol{\nu}^\top \boldsymbol{\phi}(x_0, \mathbf{y}(x_0), x_f, \mathbf{y}(x_f)), \tag{2.4}$$

where $(.)^\top$ denotes the transpose of $(.)$, and letting $\mathbf{p}(x) \in \mathbb{R}^n$ be the vector of multiplier functions (adjoint variables or costates) accounting for the dynamics, i.e.,

$$\int_{x_0}^{x_f} \mathbf{p}(x)^\top \left[\mathbf{a}(x, \mathbf{y}(x), \mathbf{u}(x)) - \mathbf{y}'(x)\right] \, dx, \tag{2.5}$$

from (2.2), (2.4) and (2.5), the augmented cost functional J^a may be recast as

$$\begin{aligned} J^a = &\mathcal{M}(x_0, \mathbf{y}(x_0), x_f, \mathbf{y}(x_f)) - \boldsymbol{\nu}^\top \boldsymbol{\phi}(x_0, \mathbf{y}(x_0), x_f, \mathbf{y}(x_f)) \\ &+ \int_{x_0}^{x_f} \left\{ \mathcal{L}(x, \mathbf{y}(x), \mathbf{u}(x)) + \mathbf{p}(x)^\top \left[\mathbf{a}(x, \mathbf{y}(x), \mathbf{u}(x)) - \mathbf{y}'(x) \right] \right\} dx, \end{aligned} \tag{2.6}$$

where the minus sign before the inner product $\boldsymbol{\nu}^\top \boldsymbol{\phi}$ is a convention. Note that an extremal for the functional (2.6) is also an extremal for the functional (2.2), since it should also satisfy the constraints given by (2.3). Equation (2.6) consists in two main parts, one is evaluated at initial and end points and the other is distributed along the interval $[x_0, x_f]$. To find necessary conditions for the existence of extremals, the variation of the augmented functional is needed. Setting the first variation equal to zero, one obtains

$$\begin{aligned} \delta J^a = &\delta \mathcal{M}(x_0, \mathbf{y}(x_0), x_f, \mathbf{y}(x_f)) - \delta \left(\boldsymbol{\nu}^\top \boldsymbol{\phi}(x_0, \mathbf{y}(x_0), x_f, \mathbf{y}(x_f)) \right) \\ &+ \delta \int_{x_0}^{x_f} \left\{ \mathcal{L}(x, \mathbf{y}(x), \mathbf{u}(x)) + \mathbf{p}(x)^\top \left[\mathbf{a}(x, \mathbf{y}(x), \mathbf{u}(x)) - \mathbf{y}'(x) \right] \right\} dx \\ = &0. \end{aligned} \tag{2.7}$$

It is worth to highlight that the quantities that can vary are the states $\mathbf{y}(.)$, the inputs $\mathbf{u}(.)$, the costates $\mathbf{p}(.)$, multipliers associated with boundary conditions $\boldsymbol{\nu}$, initial and end points x_0 and x_f, $\mathbf{y}_0$ and $\mathbf{y}_f$.

Firstly, the variation of $\mathcal{M}$ is computed with respect to its arguments. In particular, it is worth noting that the variation in x_0 does contribute to the variation of $\mathcal{M}$ as well as of $\mathbf{y}(x_0)$. Same considerations hold for the variation in x_f. Hence,

$$\begin{aligned} \delta \mathcal{M}(x_0, \mathbf{y}(x_0), x_f, \mathbf{y}(x_f)) = &\frac{\partial \mathcal{M}}{\partial x_0} \delta x_0 + \frac{\partial \mathcal{M}}{\partial \mathbf{y}(x_0)} \mathbf{y}'(x_0) \delta x_0 \\ &+ \frac{\partial \mathcal{M}}{\partial \mathbf{y}(x_0)} \delta \mathbf{y}(x_0) + \frac{\partial \mathcal{M}}{\partial x_f} \delta x_f \\ &+ \frac{\partial \mathcal{M}}{\partial \mathbf{y}(x_f)} \mathbf{y}'(x_f) \delta x_f + \frac{\partial \mathcal{M}}{\partial \mathbf{y}(x_f)} \delta \mathbf{y}(x_f) \end{aligned} \tag{2.8}$$

and extending Equation (A.26) and its counterpart for x_0 to the case of several states, i.e.,

$$\begin{cases} \delta \mathbf{y}_0 = \delta \mathbf{y}(x_0) + \mathbf{y}'(x_0) \delta x_0, \\ \delta \mathbf{y}_f = \delta \mathbf{y}(x_f) + \mathbf{y}'(x_f) \delta x_f, \end{cases} \tag{2.9}$$

the variation of $\mathcal{M}$ becomes

$$\begin{aligned}\delta\mathcal{M}(x_0, \mathbf{y}(x_0), x_f, \mathbf{y}(x_f)) = &\frac{\partial \mathcal{M}}{\partial x_0}\delta x_0 + \frac{\partial \mathcal{M}}{\partial \mathbf{y}(x_0)}\delta \mathbf{y}_0 \\ &+ \frac{\partial \mathcal{M}}{\partial x_f}\delta x_f + \frac{\partial \mathcal{M}}{\partial \mathbf{y}(x_f)}\delta \mathbf{y}_f.\end{aligned} \tag{2.10}$$

On the other hand, since $\boldsymbol{\phi}$ has the same arguments as $\mathcal{M}$, it is not difficult to conclude that

$$\begin{aligned}\delta\boldsymbol{\phi}(x_0, \mathbf{y}(x_0), x_f, \mathbf{y}(x_f)) = &\frac{\partial \boldsymbol{\phi}}{\partial x_0}\delta x_0 + \frac{\partial \boldsymbol{\phi}}{\partial \mathbf{y}(x_0)}\delta \mathbf{y}_0 \\ &+ \frac{\partial \boldsymbol{\phi}}{\partial x_f}\delta x_f + \frac{\partial \boldsymbol{\phi}}{\partial \mathbf{y}(x_f)}\delta \mathbf{y}_f\end{aligned} \tag{2.11}$$

and recalling therefore variations of the fixed term in (2.7), one obtains

$$\begin{aligned}\delta\mathcal{M} - \delta(\boldsymbol{\nu}^\top \boldsymbol{\phi}) = &-\delta\boldsymbol{\nu}^\top \boldsymbol{\phi} \\ &+ \left[\frac{\partial \mathcal{M}}{\partial x_0} - \boldsymbol{\nu}^\top \frac{\partial \boldsymbol{\phi}}{\partial x_0}\right]\delta x_0 \\ &+ \left[\frac{\partial \mathcal{M}}{\partial \mathbf{y}(x_0)} - \boldsymbol{\nu}^\top \frac{\partial \boldsymbol{\phi}}{\partial \mathbf{y}(x_0)}\right]\delta \mathbf{y}_0 \\ &+ \left[\frac{\partial \mathcal{M}}{\partial x_f} - \boldsymbol{\nu}^\top \frac{\partial \boldsymbol{\phi}}{\partial x_f}\right]\delta x_f \\ &+ \left[\frac{\partial \mathcal{M}}{\partial \mathbf{y}(x_f)} - \boldsymbol{\nu}^\top \frac{\partial \boldsymbol{\phi}}{\partial \mathbf{y}(x_f)}\right]\delta \mathbf{y}_f.\end{aligned} \tag{2.12}$$

The variation of the integral term in (2.7) is now computed. Defining the Hamiltonian function $\mathcal{H}$ as

$$\mathcal{H}(x, \mathbf{y}, \mathbf{u}, \mathbf{p}) = \mathcal{L}(x, \mathbf{y}, \mathbf{u}) + \mathbf{p}(x)^\top \mathbf{a}(x, \mathbf{y}, \mathbf{u}) \tag{2.13}$$

and considering Leibniz integral rule for differentiation, the variation of the

integral in Equation (2.7) is given by

$$\begin{aligned}
\delta \int_{x_0}^{x_f} \left(\mathcal{H} - \mathbf{p}^\top \mathbf{y}'\right) dx &= \int_{x_0}^{x_f} \delta \left(\mathcal{H} - \mathbf{p}^\top \mathbf{y}'\right) dx \\
&+ \left[\mathcal{H}(x_f) - \mathbf{p}(x_f)^\top \mathbf{y}'(x_f)\right] \delta x_f \\
&- \left[\mathcal{H}(x_0) - \mathbf{p}(x_0)^\top \mathbf{y}'(x_0)\right] \delta x_0 \\
&= \int_{x_0}^{x_f} \delta\mathcal{H}\, dx - \int_{x_0}^{x_f} \delta\mathbf{p}^\top \mathbf{y}'\, dx - \int_{x_0}^{x_f} \mathbf{p}^\top \delta\mathbf{y}'\, dx \\
&+ \left[\mathcal{H}(x_f) - \mathbf{p}(x_f)^\top \mathbf{y}'(x_f)\right] \delta x_f \\
&- \left[\mathcal{H}(x_0) - \mathbf{p}(x_0)^\top \mathbf{y}'(x_0)\right] \delta x_0 \\
&= \int_{x_0}^{x_f} \left(\frac{\partial \mathcal{H}}{\partial \mathbf{y}}\delta\mathbf{y} + \frac{\partial \mathcal{H}}{\partial \mathbf{u}}\delta\mathbf{u} + \frac{\partial \mathcal{H}}{\partial \mathbf{p}}\delta\mathbf{p}\right) dx \\
&- \int_{x_0}^{x_f} \delta\mathbf{p}^\top \mathbf{y}'\, dx - \mathbf{p}^\top(x_f)\left[\delta\mathbf{y}(x_f) + \mathbf{y}'(x_f)\delta x_f\right] \\
&+ \mathbf{p}^\top(x_0)\left[\delta\mathbf{y}(x_0) + \mathbf{y}'(x_0)\delta x_0\right] \\
&+ \mathcal{H}(x_f)\delta x_f - \mathcal{H}(x_0)\delta x_0 + \int_{x_0}^{x_f} \mathbf{p}'^\top \delta\mathbf{y}\, dx.
\end{aligned} \tag{2.14}$$

Making use of Equation (2.9) and realizing that $\delta\mathbf{p}^\top\mathbf{y}' = \mathbf{y}'^\top\delta\mathbf{p}$, the variation of the integral term reads

$$\begin{aligned}
\delta \int_{x_0}^{x_f} \left(\mathcal{H} - \mathbf{p}^\top \mathbf{y}'\right) dx &= \int_{x_0}^{x_f} \left(\frac{\partial \mathcal{H}}{\partial \mathbf{y}} + \mathbf{p}'^\top\right) \delta\mathbf{y}\, dx \\
&+ \int_{x_0}^{x_f} \frac{\partial \mathcal{H}}{\partial \mathbf{u}}\delta\mathbf{u}\, dx \\
&+ \int_{x_0}^{x_f} \left(\frac{\partial \mathcal{H}}{\partial \mathbf{p}} - \mathbf{y}'^\top\right) \delta\mathbf{p}\, dx \\
&+ \mathcal{H}(x_f)\delta x_f - \mathcal{H}(x_0)\delta x_0 \\
&+ \mathbf{p}^\top(x_0)\delta\mathbf{y}_0 - \mathbf{p}^\top(x_f)\delta\mathbf{y}_f
\end{aligned} \tag{2.15}$$

and therefore, considering (2.12), the overall variation (2.7) is given by

$$\begin{aligned}\delta J^a = &\int_{x_0}^{x_f} \left(\frac{\partial \mathcal{H}}{\partial \mathbf{y}} + \mathbf{p}'^{\top}\right) \delta\mathbf{y}\, dx + \int_{x_0}^{x_f} \frac{\partial \mathcal{H}}{\partial \mathbf{u}} \delta\mathbf{u}\, dx + \int_{x_0}^{x_f} \left(\frac{\partial \mathcal{H}}{\partial \mathbf{p}} - \mathbf{y}'^{\top}\right) \delta\mathbf{p}\, dx \\ &+ \left[\frac{\partial \mathcal{M}}{\partial x_0} - \boldsymbol{\nu}^{\top} \frac{\partial \boldsymbol{\phi}}{\partial x_0} - \mathcal{H}(x_0)\right] \delta x_0 \\ &+ \left[\frac{\partial \mathcal{M}}{\partial \mathbf{y}(x_0)} - \boldsymbol{\nu}^{\top} \frac{\partial \boldsymbol{\phi}}{\partial \mathbf{y}(x_0)} + \mathbf{p}^{\top}(x_0)\right] \delta\mathbf{y}_0 \\ &+ \left[\frac{\partial \mathcal{M}}{\partial x_f} - \boldsymbol{\nu}^{\top} \frac{\partial \boldsymbol{\phi}}{\partial x_f} + \mathcal{H}(x_f)\right] \delta x_f \\ &+ \left[\frac{\partial \mathcal{M}}{\partial \mathbf{y}(x_f)} - \boldsymbol{\nu}^{\top} \frac{\partial \boldsymbol{\phi}}{\partial \mathbf{y}(x_f)} - \mathbf{p}^{\top}(x_f)\right] \delta\mathbf{y}_f \\ &- \boldsymbol{\phi}^{\top} \delta\boldsymbol{\nu}.\end{aligned} \tag{2.16}$$

Necessary conditions for the existence of extremals are obtained provided that Equation (2.16) identically vanishes for independent variations of $\mathbf{y}$, $\mathbf{u}$, $\mathbf{p}$, x_0, x_f, $\mathbf{y}_0$, $\mathbf{y}_f$ and $\boldsymbol{\nu}$, namely

$$\mathbf{y}'(x) = \left[\frac{\partial}{\partial \mathbf{p}} \mathcal{H}(x, \mathbf{y}, \mathbf{u}, \mathbf{p})\right]^{\top} = \mathbf{a}(x, \mathbf{y}, \mathbf{u}), \tag{2.17}$$

$$\mathbf{p}'(x) = -\left[\frac{\partial}{\partial \mathbf{y}} \mathcal{H}(x, \mathbf{y}, \mathbf{u}, \mathbf{p})\right]^{\top}, \tag{2.18}$$

$$\frac{\partial}{\partial \mathbf{u}} \mathcal{H}(x, \mathbf{y}, \mathbf{u}, \mathbf{p}) = \mathbf{0}, \tag{2.19}$$

$$\mathcal{H}(x_0, \mathbf{y}(x_0), \mathbf{u}(x_0), \mathbf{p}(x_0)) = \frac{\partial \mathcal{M}}{\partial x_0} - \boldsymbol{\nu}^{\top} \frac{\partial \boldsymbol{\phi}}{\partial x_0}, \tag{2.20}$$

$$\mathcal{H}(x_f, \mathbf{y}(x_f), \mathbf{u}(x_f), \mathbf{p}(x_f)) = -\frac{\partial \mathcal{M}}{\partial x_f} + \boldsymbol{\nu}^{\top} \frac{\partial \boldsymbol{\phi}}{\partial x_f}, \tag{2.21}$$

$$\mathbf{p}^{\top}(x_0) = -\frac{\partial \mathcal{M}}{\partial \mathbf{y}(x_0)} + \boldsymbol{\nu}^{\top} \frac{\partial \boldsymbol{\phi}}{\partial \mathbf{y}(x_0)}, \tag{2.22}$$

$$\mathbf{p}^{\top}(x_f) = \frac{\partial \mathcal{M}}{\partial \mathbf{y}(x_f)} - \boldsymbol{\nu}^{\top} \frac{\partial \boldsymbol{\phi}}{\partial \mathbf{y}(x_f)}, \tag{2.23}$$

and

$$\boldsymbol{\phi}(x_0, \mathbf{y}(x_0), x_f, \mathbf{y}(x_f)) = \mathbf{0}. \tag{2.24}$$

Since Equations (2.17) and (2.18) arise from differentiation of a Hamiltonian function, they constitute a Hamiltonian system. Furthermore,

Equation (2.19) is used to obtain input functions so that the cost functional achieves its extremum. It is referred to as the *strong form* of the so-called *Pontryagin's Principle*, which is emphasized at the end of this chapter. Finally, the conditions on the initial and final costate and Hamiltonian functions given in Equations (2.20)-(2.23) are referred to as *transversality* conditions. Therefore, the Hamiltonian system (2.17)-(2.18), together with the boundary conditions (2.24) and transversality conditions (2.20)-(2.23) form the so-called Hamiltonian boundary value problem [26]. Any solution $\{\mathbf{y}^*(x), \mathbf{u}^*(x), \mathbf{p}^*(x), \boldsymbol{\nu}^*\}$ is called an extremal and consists of the state, costate and any multipliers that satisfy the boundary conditions. This extremal solution can be a maximum, minimum or saddle. The second-order sufficiency conditions must be inspected to determine which of the extremal solutions is a global minimum. The derivation of the second-order sufficiency conditions, however, is beyond the scope of this dissertation. For a local minimum, the particular extremal with the lowest cost is chosen.

It is worth noting that, in most of the cases, the solution of the aforementioned system of equations (2.17)-(2.24) is by no means an easy task. In fact, closed form solutions exist only for a few problems in the literature and for limited number of cases. An overview of such cases in engineering can be found in [26, 27, 28]. The reason being states and costates are coupled one another and may nonlinearly appear in the costate equations (2.18), hindering the analytical tractability of the resulting Hamiltonian boundary value problem.

2.3 Problems with inequality path constraints

In addition to the general formulation of the dynamic optimization problem (Problem 2.1), let some inequality *path constraints* having the form

$$\mathbf{c}(x, \mathbf{y}(x), \mathbf{u}(x)) \leq \mathbf{0} \tag{2.25}$$

be also present. These constraints apply over the whole interval of interest and as such they comprise of a set of infinite-dimensional constraints. The formultion of the problem is given next.

Problem 2.2. *Find the input functions* $\mathbf{u}(x) \in \mathbb{R}^m$ *which extremize the functional*

$$J = \mathcal{M}(x_0, \mathbf{y}(x_0), x_f, \mathbf{y}(x_f)) + \int_{x_0}^{x_f} \mathcal{L}(x, \mathbf{y}(x), \mathbf{u}(x))\, dx \tag{2.26}$$

and subject to the algebraic-differential constraints

$$\begin{cases} \mathbf{y}'(x) = \mathbf{a}(x, \mathbf{y}(x), \mathbf{u}(x)), \\ \boldsymbol{\phi}(x_0, \mathbf{y}(x_0), x_f, \mathbf{y}(x_f)) = \mathbf{0}, \\ \mathbf{c}(x, \mathbf{y}(x), \mathbf{u}(x)) \leq \mathbf{0}, \end{cases} \tag{2.27}$$

where x_0, x_f, $\mathbf{y}(x_0)$ *and* $\mathbf{y}(x_f)$ *are free (see Figure 2.1).*

Letting p be the number of path constraints and $\mathbf{m}(x) \in \mathbb{R}^p$ be the vector of the multiplier functions accounting for them, the augmented functional will have the form

$$J^a = \mathcal{M} - \boldsymbol{\nu}^\top \boldsymbol{\phi} + \int_{x_0}^{x_f} \left[\mathcal{L} + \mathbf{p}^\top \left(\mathbf{a} - \mathbf{y}' \right) - \mathbf{m}^\top \mathbf{c} \right] dx. \tag{2.28}$$

Also here, the minus sign before the inner product $\mathbf{m}^\top \mathbf{c}$ is a convention.

Following the above considerations, the Hamiltonian function will be given by

$$\mathcal{H}(x, \mathbf{y}, \mathbf{u}, \mathbf{p}, \mathbf{m}) = \mathcal{L} + \mathbf{p}^\top \mathbf{a} - \mathbf{m}^\top \mathbf{c} \tag{2.29}$$

and, setting the variation of the augmented functional (2.28) equal to zero, the so-called *complementary slackness* conditions [29, 30]

$$\begin{aligned} m_j(x) = 0\,, &\quad \text{when } c_j(x, \mathbf{y}, \mathbf{u}) < 0, \quad j = 1, 2, \ldots, p \\ m_j(x) < 0\,, &\quad \text{when } c_j(x, \mathbf{y}, \mathbf{u}) = 0, \quad j = 1, 2, \ldots, p \end{aligned} \tag{2.30}$$

hold in addition to necessary conditions (2.17)-(2.24). On the one hand, when $c_j < 0$, the path constraint in (2.25) is inactive. Therefore, by making $m_j(x) = 0$, the constraint is simply ignored in augmented functional (2.28). On the other hand, the negativity of m_j when $c_j = 0$ is interpreted such that improving the cost may only come from violating the constraint.

2.4 Pontryagin's Principle

The Pontryagin's Principle is used to determine the conditions for obtaining the objective functions $\mathbf{u}$ so that the cost functional is extremized. Equation (2.19) is referred to as the strong form of this principle. However, in some cases the strong form of the Pontryagin's Principle does not provide any information about extremal objective functions, e.g., when the Hamiltonian function is linear with respect to $\mathbf{u}$. To overcome these secnarios, suppose

$\mathbf{u}^*$ gives a local minimum of the cost functional J. Compatibly with the notation employed in Appendix A, one has

$$J(\mathbf{u}) - J(\mathbf{u}^*) = \Delta J(\mathbf{u}, \mathbf{u}^*) \geq 0 \tag{2.31}$$

for all admissible $\mathbf{u} \in \mathcal{U}$ sufficiently close to $\mathbf{u}^*$. If $\mathbf{u}$ is taken to be $\mathbf{u}^* + \delta\mathbf{u}$, then the change in the cost functional can be expressed as

$$\Delta J(\mathbf{u}, \mathbf{u}^*) = \delta J(\mathbf{u}^*, \delta\mathbf{u}) + \varepsilon||\delta\mathbf{u}|| \tag{2.32}$$

where $\varepsilon \to 0$ as $||\delta\mathbf{u}|| \to 0$. If $\delta\mathbf{u}$ is sufficiently small, then the cost has a local minimum if

$$\delta J(\mathbf{u}^*, \delta\mathbf{u}) \geq 0. \tag{2.33}$$

Since at the optimal solution $\{\mathbf{y}^*(x), \mathbf{u}^*(x), \mathbf{p}^*(x), \mathbf{m}^*(x), \boldsymbol{\nu}^*\}$, the differential equations, along with the boundary conditions, should be satisfied, therefore all coefficients of the variation terms in Equation (2.16) can be set equal to zero, except the term associate with $\delta\mathbf{u}$. This leaves the variation of the augmented cost as

$$\delta J^a(\mathbf{u}^*, \delta\mathbf{u}) = \int_{x_0}^{x_f} \left(\frac{\partial \mathcal{H}}{\partial \mathbf{u}}\right)_{\mathbf{y}^*, \mathbf{u}^*, \mathbf{p}^*, \mathbf{m}^*} \delta\mathbf{u}\, dx \tag{2.34}$$

Since the first-order approximation of the change in the Hamiltonian is given by

$$\left(\frac{\partial \mathcal{H}}{\partial \mathbf{u}}\right)_{\mathbf{y}^*, \mathbf{u}^*, \mathbf{p}^*, \mathbf{m}^*} \delta\mathbf{u} = \mathcal{H}(x, \mathbf{y}^*, \mathbf{u}^* + \delta\mathbf{u}, \mathbf{p}^*, \mathbf{m}^*) - \mathcal{H}(x, \mathbf{y}^*, \mathbf{u}^*, \mathbf{p}^*, \mathbf{m}^*), \tag{2.35}$$

the variation of the cost for all admissible and sufficiently small $\delta\mathbf{u}$ reads

$$\delta J^a(\mathbf{u}^*, \delta\mathbf{u}) = \int_{x_0}^{x_f} \left[\mathcal{H}(x, \mathbf{y}^*, \mathbf{u}^* + \delta\mathbf{u}, \mathbf{p}^*, \mathbf{m}^*) - \mathcal{H}(x, \mathbf{y}^*, \mathbf{u}^*, \mathbf{p}^*, \mathbf{m}^*)\right] dx. \tag{2.36}$$

In order for $\delta J(\mathbf{u}^*, \delta\mathbf{u})$ to be non-negative for any admissible variation $\delta\mathbf{u}$, the Hamiltonian must be greater than the optimal Hamiltonian for all x, namely

$$\mathcal{H}(x, \mathbf{y}^*, \mathbf{u}^* + \delta\mathbf{u}, \mathbf{p}^*, \mathbf{m}^*) \geq \mathcal{H}(x, \mathbf{y}^*, \mathbf{u}^*, \mathbf{p}^*, \mathbf{m}^*). \tag{2.37}$$

In other words, optimal objective functions $\mathbf{u}^*$ are the admissible controls that minimize $\mathcal{H}$, i.e.,

$$\mathbf{u}^*(x) = \arg\min_{\mathbf{u} \in \mathcal{U}} \mathcal{H}(x, \mathbf{y}^*(x), \mathbf{u}(x), \mathbf{p}^*(x), \mathbf{m}^*), \tag{2.38}$$

which is referred to as the *weak form* of Pontryagin's Principle. This relation is important in the particular case when the Hamiltonian function is linear with respect to $\mathbf{u}$. For instance, suppose that one input function $u : [x_0, x_f] \to \mathcal{U} = [\underline{u}, \overline{u}]$ is involved. Thus, the Hamiltonian function is formally given by

$$\mathcal{H}(x, \mathbf{y}, u, \mathbf{p}, \mathbf{m}) = \mathcal{A}(x, \mathbf{y}, \mathbf{p}, \mathbf{m}) + \mathcal{B}(x, \mathbf{y}, \mathbf{p}, \mathbf{m})\, u. \tag{2.39}$$

It is easy to show that the strong form of Pontryagin's Principle (2.19) does not supply any useful information, whereas the weak form (2.38) yields

$$u^*(x) = \arg\min_u \mathcal{H}(x, \mathbf{y}, u, \mathbf{p}, \mathbf{m}) = \begin{cases} \underline{u}\,, & \text{if } \mathcal{B}(x, \mathbf{y}, \mathbf{p}, \mathbf{m}) > 0\,, \\ \overline{u}\,, & \text{if } \mathcal{B}(x, \mathbf{y}, \mathbf{p}, \mathbf{m}) < 0\,, \\ ?\,, & \text{if } \mathcal{B}(x, \mathbf{y}, \mathbf{p}, \mathbf{m}) = 0\,, \end{cases} \tag{2.40}$$

namely the optimal input function either lies on the boundary of the feasible inputs set (depending on the sign of $\mathcal{B}$ along x) or can be found from other considerations (whenever $\mathcal{B}$ is identically zero on a finite subinterval $x_1 \leq x \leq x_2$). In the parlance of continuous dynamic optimization, such kinds of input functions are commonly referred to as *bang-bang* and *singular*, respectively.

2.5 Summary

In this chapter, variational principles to continuous dynamic optimization problems subject to algebraic-differential constraints have been applied to derive first-order necessary conditions for optimality. Moreover, Pontryagin's Principle in both its strong and weak forms has been introduced as a generalization of the fundamental theorem of calculus of variations, and problems with inequality path constraints have been discussed. In particular, it has been shown that necessary conditions can be written in the form of a boundary value problem, yet the primary variables are strongly coupled one another and therefore analytically tractable only for a few cases. For this purpose, the development of dedicated numerical tools becomes necessary for the determination of the input functions and states as well as the assessment of the performance index at optimal solutions.

Chapter 3

Development of computational tools

3.1 Introduction

Numerical methods for solving continuous dynamic optimization problems date back nearly five decades to the 1950s with the work of Bellman. From that time to the present, the variety of methods and corresponding complexity have increased tremendously. Generally, these numerical methods are classified into two major classes: *indirect* and *direct* methods. In indirect methods, the calculus of variations is used to determine the first-order optimality conditions of the original problem. Multiple-point boundary-value problems (BVPs) are therefore derived and their solutions determine candidate extremals. Each of the computed extremals is then examined to assess whether it is a local minimum, a local maximum or a saddle point. Of the locally optimizing solutions, the particular extremal with the lowest performance index in chosen. On the other hand, direct methods deal with the states and input functions directly, by discretizing them in some manner and transcribing the original problem into a nonlinear programming problem (NLP), which in turn are solved by means of well known optimization techniques.

The two philosophies of indirect and direct methods have led to a dichotomy in the numerical methods community. Researchers who focus on indirect methods are generally interested in differential equation theory, whereas researchers who focus on direct methods are interested more in optimization techniques. Excellent historical overviews of the two methods may be found in [31, 32, 33, 34]. While seemingly unrelated, in recent years

many researchers have delved quite deeply into the connections between the two methods. In fact, in [35] it is uncovered that the optimality conditions from many direct methods have a well-defined meaningful relationship, demonstrating how they merge as time progresses.

In indirect methods, principles of calculus of variations lead to a BVP, i.e., optimal solution is found by solving a system of first-order differential equations that satisfy endpoint conditions. The most well-know strategy pertaining to this method is the so-called *shooting* method, i.e., to start from one endpoint and guess the solutions at the other endpoint, then forward integrate the BVP as an initial value problem (IVP), where a check is made whether the corresponding boundary values are satisfied. If so, a solution is found, if not the initial guesses are adjusted [36]. However, despite of its simplicity, the shooting method presents significant shortcomings since errors in the unknown boundary conditions may considerably amplify as the dynamics are forwardly integrated. A solution to this numerical issue is offered by the so-called *multiple-shooting* methods, where the interval in which integration takes place is divided into many subintervals with initial values of the interior points need to be determined being unknown. Nevertheless, even this latter can not be much helpful if initial guesses are not well prescribed [37].

On the other hand, direct methods have been gaining much interest and their theoretical development is more and more refined which, together with the increasing improvement of computers generation, led researchers to efficient algorithms to numerically solve dynamic optimization problems [38]. Among these methods the so-called *orthogonal direct collocation* method (or *pseudospectral* method) has been increasing in popularity. This method permits the parameterization of the state and the control using specified functional forms and collocation is performed at chosen points. In particular, the state (and sometimes the control) of the original problem is approximate using global polynomials. The differential equations are then collocated using nodes obtained from quadrature points such that the dynamic optimization problem is transcribed to a standard NLP problem.

Pseudospectral methods have been employed in literature considering many types of collocation point sets and polynomial approximation basis functions. As far as collocation points are concerned, a considerable amount of work has been developed by using Legendre-Gauss, Legendre-Gauss-Lobatto, Legendre-Gauss-Radau, flipped Legendre-Gauss-Radau and Chebyshev points, e.g., [38, 39, 40, 41, 42]. A numerical framework for the numerical solution of continuous dynamic optimization problems using most of the aforementioned points is revisited

in [43] with particular attention devoted to the costate evaluation using Legendre-Gauss-Radau points. On the other hand, as far as the approximation of the state and/or the control is concerned, many attempts have been made available employing Chebyshev [44], Bernstein [45] and, more frequently, Lagrange polynomials [46, 47, 48], as these latter satisfy the isolation property.

The present chapter attempts to draw a concise introduction to the Legendre-Gauss-Radau (LGR) pseudospectral method in its *global* and *multistage* forms. The transcription of the dynamic optimization problem into a finite-dimensional NLP problem is mainly emphasized. Hints on the numerical implementation are also given and the resulting NLP problems are solved by dedicated NLP solvers. Solving the NLP as efficiently as possible requires that sparsity at first-derivative levels be exploited. Expressions for the objective functional gradient and constraint Jacobian are therefore borrowed from [49].

3.2 Mathematical preliminaries

In this section, the theoretical tools needed to develop the numerical framework are recalled. As a preliminary remark, note that all the optimization problems considered in this chapter are defined in a finite interval. Without loss of generality, the numerical framework is developed with respect to $[-1, 1]$ to which any finite interval can be mapped by a linear transformation.

3.2.1 Legendre polynomials

Legendre polynomials are a system of polynomial functions with several applications in physics and engineering. More precisely, they are a countable set of polynomials, herein denoted by $P_0, P_1, P_2, \dots$ which are the solutions to Legendre's differential equation [50]

$$\frac{d}{d\xi}\left[(1-\xi^2)\frac{d}{d\xi}P_k(\xi)\right] + k(k+1)P_k(\xi) = 0 \tag{3.1}$$

over the interval $\xi \in [-1, 1]$ (with $k = 0, 1, 2, \dots$). Their explicit expression can be obtained by setting [50]

$$\begin{cases} P_0 = 0\,, \\ P_1 = \xi \end{cases} \tag{3.2}$$

and by the recurrence relation

$$(k+1)P_{k+1}(\xi) = (2k+1)\xi P_k(\xi) - kP_{k-1}(\xi)\,, \qquad k = 1, 2, \ldots \tag{3.3}$$

An important property of Legendre polynomials is that they are orthogonal to one another, namely they have the following property

$$\int_{-1}^{1} P_i(\xi)P_j(\xi)\,d\xi = \frac{2\delta_{ij}}{2j+1}\,, \tag{3.4}$$

where δ_{ij} is Kronecker's delta.

3.2.2 Lagrange interpolating polynomials

Lagrange interpolating polynomials are used to approximate a function $f : \mathbb{R} \to \mathbb{R}$ whose values in a finite set of distinct points $\xi_1, \xi_2, \ldots, \xi_J$ are known. They are defined by [50]

$$\ell_i(\xi) = \prod_{j=1, j\neq i}^{J} \frac{\xi - \xi_j}{\xi_i - \xi_j}\,, \qquad i = 1, 2, ..., J, \tag{3.5}$$

and the approximation to which they lead can be written as

$$f(x) \approx \widetilde{f}(x) \triangleq \sum_{i=1}^{J} f(\xi_i)\ell_i(x)\,.$$

Note that since each ℓ_i is a polynomial of degree J, so is $\widetilde{f}$. As a consequence, $\widetilde{f} \equiv f$ whenever f is a polynomial of degree less than or equal to J. Moreover, if f is a polynomial of degree less than or equal to J then

$$\frac{d}{dx}f(x) = \sum_{i=1}^{J} f(\xi_i)\frac{d}{dx}\ell_i(x)\,. \tag{3.6}$$

From definition (3.5) it is easy to see that each polynomial satisfies the so-called isolation property, i.e.,

$$\ell_i(\xi_j) = \delta_{ij}\,. \tag{3.7}$$

As mentioned above, the pseudospectral methods described in the following sections are developed for the interval $[-1, 1]$. Hence the restriction of the polynomials to this interval will be of interest. Moreover, all the interpolation points will belong to this interval with $\xi_1 = -1$ and $\xi_J = 1$.

3.2.3 LGR points and quadrature weights

For a fixed $N \in \mathbb{N}$, the N Legendre-Gauss-Radau collocation points (all belonging to $[-1, 1]$) are the roots of the polynomial $P_{N-1}(\xi) + P_N(\xi)$ [51], where P_{N-1} and P_N are the Legendre polynomial (of degree $N-1$ and N, respectively). An important property of the LGR points is that for any polynomial ϕ of degree $2(N-1)$ or less [51], the identity

$$\int_{-1}^{1} \phi(\xi)\, d\xi = \sum_{i=1}^{N} \omega_i\, \phi(\xi_i)\,, \tag{3.8}$$

where ω_i $(i = 1, 2, \ldots, N)$ are the LGR quadrature weights, given by [51]

$$\begin{cases} \omega_1 = 2/N^2\,, \\ \omega_i = \dfrac{1}{(1-\xi_i)\left[\frac{dP_{N-1}}{d\xi}(\xi_i)\right]^2}\,, \qquad (i = 2, 3, \ldots, N) \end{cases} \tag{3.9}$$

holds true.

3.3 Continuous-to-discrete conversion

The aim of the transcription procedure is that mapping it into a constrained NLP that can be solved by using dedicated tools. According to [38], the minimum fundamental steps of a transcription consist of the domain discretization and the continuous-to-discrete conversion of states and/or controls. This transcription can be made on a single mesh interval (global pseudospectral method) or multiple mesh intervals (multistage pseudospectral method). Next, a systematic mathematical framework is devoted to each of the above mentioned two steps for both versions. The reader is also addressed to other variants of this formulation where f-LGR points (roots of $P_N(\xi) - P_{N-1}(\xi)$, namely the negative counterparts of the standard LGR points) are considered (see, e.g., [38, 52, 53]).

3.3.1 Global LGR pseudospectral method

Firstly, the noncollocated point $\xi_{N+1} = 1$ is introduced. Unlike the notation in the previous chapter, let all vector functions be row vectors. For instance, the state and the input vectors at ξ are written as

$$\mathbf{y}(\xi) = [y_1(\xi) \quad y_2(\xi) \quad \ldots \quad y_n(\xi)] \in \mathbb{R}^n$$

and

$$\mathbf{u}(\xi) = [u_1(\xi) \;\; u_2(\xi) \;\; \dots \;\; u_m(\xi)] \in \mathbb{R}^m \,,$$

respectively, where n and m are the number of states and inputs, respectively. The approximations of the states and the input functions at $\xi = \xi_i$ are denoted by $\mathbf{Y}_i$ and $\mathbf{U}_i$, respectively. Moreover, the matrix $\mathbf{Y} \in \mathbb{R}^{(N+1)\times n}$ refers to the state approximation, where the first N rows contain the approximations at the collocated points $\mathbf{Y}_1, \mathbf{Y}_2, \dots \mathbf{Y}_N$ and the last row contains the approximation at the noncollocated point, namely $\mathbf{Y}_{N+1}$. Analogously, the matrix $\mathbf{U} \in \mathbb{R}^{N\times m}$ refers to the input approximation, whose rows are $\mathbf{U}_i$ $(i = 1, 2, ..., N)$. Besides, the notation $\mathbf{Y}_{i:j}$ will be used to denote rows i through j of $\mathbf{Y}$, while the $\mathbf{D}_{i:j}$ denotes columns i through j of the differentiation matrix $\mathbf{D}$, defined below. Lastly, a dot refers to a first derivative with respect to ξ.

For the sake of a preliminary exposition of the transcription process, the unconstrained version of the most general dynamic optimization problem in the pseudospectral domain $\xi \in [-1, 1)$ is firstly addressed, namely

Problem 3.1.

$$\begin{aligned} \min_{\mathbf{u}\in\widetilde{C}([-1,1],\mathbb{R}^m)} \quad & J = \mathcal{M}\left(\mathbf{y}(1)\right) + \frac{x_f - x_0}{2}\int_{-1}^{1} \mathcal{L}\left(\xi, \mathbf{y}(\xi), \mathbf{u}(\xi)\right) d\xi \,, \\ s.t. \quad & \dot{\mathbf{y}}(\xi) = \frac{x_f - x_0}{2}\mathbf{a}(\xi, \mathbf{y}(\xi), \mathbf{u}(\xi)) \,, \\ & \mathbf{y}(-1) = \mathbf{y}_0 \,. \end{aligned} \tag{3.10}$$

Here, $\widetilde{C}([-1, 1], \mathbb{R}^m)$ denotes the set of piece-wise continuous functions from $[-1, 1]$ to $\mathbb{R}^m$ and $\mathbf{y}_0$, x_0 and x_f are assumed to be specified. Being free from path constraints apart, it is emphasized that the transcription process for Problem 2.1 is not much different from that of Problem 3.1, although this latter is defined on the pseudospectral domain. In fact, solutions for Problem 3.1 can be transformed into solutions for Problem 2.1 by taking into account the affine transformations from and to the original and the pseudospectral intervals, namely

$$\begin{cases} x = \dfrac{x_f - x_0}{2}\xi + \dfrac{x_f + x_0}{2} \,, \\ \xi = \dfrac{2x}{x_f - x_0} - \dfrac{x_f + x_0}{x_f - x_0} \,. \end{cases} \tag{3.11}$$

The transcription begins with considering collocation at the N LGR points $(\xi_1, \xi_2, ..., \xi_N)$ with $\xi_1 = -1$ and letting $\xi_{N+1} = 1$ be the noncollocated

point. The evolution of each coordinate of the state is approximated by a polynomial of degree N through Lagrange interpolation polynomials, i.e.,

$$\mathbf{y}(\xi) \approx \mathbf{Y}(\xi) = \sum_{i=1}^{N+1} \mathbf{Y}_i \ell_i(\xi)\,, \tag{3.12}$$

where, according to Equation (3.5),

$$\ell_i(\xi) = \prod_{j=1, j\neq i}^{N+1} \frac{\xi - \xi_j}{\xi_i - \xi_j}\,, \qquad i = 1, 2, \ldots, N+1\,. \tag{3.13}$$

It is worth noting that the state approximation (3.12) includes the Lagrange polynomial $\ell_{N+1}(\xi)$ (of degree N) associated with the noncollocated point $\xi_{N+1} = 1$. Differentiating Equation (3.12), one obtains

$$\dot{\mathbf{y}}(\xi) \approx \dot{\mathbf{Y}}(\xi) = \sum_{i=1}^{N+1} \mathbf{Y}_i \dot{\ell}_i(\xi)\,, \tag{3.14}$$

which is a polynomial of degree $N-1$. Evaluating Equation (3.14) at the generic collocation point ξ_j ($j = 1, 2, ..., N$), one obtains

$$\dot{\mathbf{Y}}(\xi_j) = \sum_{i=1}^{N+1} D_{ji} \mathbf{Y}_i\,, \tag{3.15}$$

where $D_{ji} = \dot{\ell}_i(\xi_j)$. Moreover, taking into account the right-hand side of the plant equations in Problem 3.1 at the collocation points, the approximations $\mathbf{Y}_i$ are found by imposing

$$\sum_{i=1}^{N+1} D_{ji} \mathbf{Y}_i = \frac{x_f - x_0}{2} \mathbf{a}(\xi_j, \mathbf{Y}_j, \mathbf{U}_j)\,, \qquad j = 1, 2, \ldots, N. \tag{3.16}$$

According to the notation previously specified, letting

$$\mathbf{Y}_{1:N} = \begin{bmatrix} \mathbf{Y}_1 \\ \mathbf{Y}_2 \\ \vdots \\ \mathbf{Y}_N \end{bmatrix}, \quad \mathbf{Y} = \begin{bmatrix} \mathbf{Y}_{1:N} \\ \mathbf{Y}_{N+1} \end{bmatrix}, \quad \mathbf{A}_{1:N} = \begin{bmatrix} \mathbf{a}_1 \\ \mathbf{a}_2 \\ \vdots \\ \mathbf{a}_N \end{bmatrix},$$

where $\mathbf{a}_i = \frac{x_f - x_0}{2}\mathbf{a}(\xi_i, \mathbf{Y}_i, \mathbf{U}_i)$, Equation (3.16) may be written in a more compact form as

$$\mathbf{D}\mathbf{Y} = \mathbf{A}_{1:N}, \tag{3.17}$$

where $\mathbf{D} \in \mathbb{R}^{N\times(N+1)}$ is the non-square differentiation matrix whose entries are the coefficients D_{ji}. The extra column of $\mathbf{D}$ is due to the Lagrange polynomial at the noncollocated point $\xi_{N+1} = 1$. Hence, recalling Equation (3.8), Problem 3.1 may be transcribed into the following discrete NLP problem:

Problem 3.2.

$$\begin{aligned} \min_{\mathbf{Y}_1,\dots,\mathbf{Y}_{N+1},\mathbf{U}_1,\dots,\mathbf{U}_N} \quad & J = \mathcal{M}(\mathbf{Y}_{N+1}) + \frac{x_f - x_0}{2}\sum_{i=1}^{N}\omega_i\mathcal{L}_i \\ s.t. \quad & \mathbf{\Delta} := \mathbf{D}\mathbf{Y} - \mathbf{A}_{1:N} = \mathbf{0}\,, \\ & \mathbf{Y}_1 - \mathbf{y}_0 = \mathbf{0}\,, \end{aligned} \tag{3.18}$$

where $\mathcal{L}_i = \mathcal{L}(\xi_i, \mathbf{Y}_i, \mathbf{U}_i)$ and $\mathbf{\Delta} \in \mathbb{R}^{N\times n}$ is referred to as the defect matrix. Problem 3.2 is a finite-dimensional NLP constrained problem, whose decision variables are the approximation of the state at the LGR points plus the final point and the control only at the LGR points. Moreover, it is appreciated that the summation term in Problem 3.2 gives an exact value of the integral term in Problem 3.1 whenever $\mathcal{L}$ is of degree at most $2(N-1)$ [51].

Eventually, the correspondence between Problem 3.2 and standard NLP problems is briefly addressed. Let $\mathbf{V}_i \in \mathbb{R}^{N+1}$ $(i = 1, 2, \dots, n)$ and $\mathbf{W}_j \in \mathbb{R}^N$ $(j = 1, 2, \dots, m)$ denote the generic columns of the state and input approximation matrices $\mathbf{Y}$ and $\mathbf{U}$, respectively. Let also

$$\mathbf{V} = \begin{bmatrix} \mathbf{V}_1 \\ \mathbf{V}_2 \\ \vdots \\ \mathbf{V}_n \end{bmatrix} \in \mathbb{R}^{n(N+1)}\,, \quad \mathbf{W} = \begin{bmatrix} \mathbf{W}_1 \\ \mathbf{W}_2 \\ \vdots \\ \mathbf{W}_m \end{bmatrix} \in \mathbb{R}^{mN}\,,$$

be the generalized state and control approximation vectors. The decision

variables of Problem 3.2 may therefore be collected in the following vector

$$\mathbf{Z} = \begin{bmatrix} \mathbf{V} \\ \mathbf{W} \\ x_0 \\ x_f \end{bmatrix} \in \mathbb{R}^{n(N+1)+mN+2},$$

serving as the vector of decision variables for the NLP problem. Hence, the reshape of the goal function and equality constraints in Problem 3.2 in terms of $\mathbf{Z}$ is straightforward.

3.3.2 Multistage LGR pseudospectral method

Unlike the previous section, the most general form of representing a dynamic optimization problem is rather considered, namely Problem 2.1, but with the addition of path constraints $\mathbf{c}(x, \mathbf{y}(x), \mathbf{u}(x)) \leq \mathbf{0}$. In this section, however, the dynamic optimization problem is slightly modified as follows. Let $s \in [-1, 1]$ be a new independent variable and be linked with $x \in [x_0, x_f]$ by the relation

$$x = \frac{x_f - x_0}{2} s + \frac{x_f + x_0}{2}. \tag{3.19}$$

The dynamic optimization problem is then defined in terms of the variable s as follows:

Problem 3.3. *Determine the vector* $\mathbf{u}(s) \in \mathbb{R}^m$ *which minimizes the functional*

$$J = \mathcal{M}(x_0, \mathbf{y}(-1), x_f, \mathbf{y}(1)) + \frac{x_f - x_0}{2} \int_{-1}^{1} \mathcal{L}(s, \mathbf{y}(s), \mathbf{u}(s))\, ds \tag{3.20}$$

and subject to the differential constraint

$$\frac{d\mathbf{y}(s)}{ds} = \frac{x_f - x_0}{2} \mathbf{a}(s, \mathbf{y}(s), \mathbf{u}(s)), \tag{3.21}$$

the inequality path constraints

$$\mathbf{c}(s, \mathbf{y}(s), \mathbf{u}(s)) \leq \mathbf{0}, \tag{3.22}$$

and the boundary conditions

$$\boldsymbol{\phi}(x_0, \mathbf{y}(-1), x_f, \mathbf{y}(1)) = \mathbf{0}. \tag{3.23}$$

Suppose now that the interval $s \in [-1,1]$ is divided into a mesh consisting of K mesh intervals $[s_{k-1}, s_k]$, $k = 1, 2, \ldots, K$, where $(x_0, s_1, \ldots, s_K)$ are the mesh points, which have the property $-1 = s_0 < s_1 < \cdots < s_K = 1$. Next, let $\mathbf{y}^{(k)}(s)$ and $\mathbf{u}^{(k)}(s)$ be the state and input functions in the mesh interval k. Thus, the objective functional (3.20) can be recast as

$$\begin{aligned} J =& \mathcal{M}\left(x_0, \mathbf{y}^{(1)}(-1), x_f, \mathbf{y}^{(K)}(1)\right) \\ &+ \frac{x_f - x_0}{2} \sum_{k=1}^{K} \int_{s_{k-1}}^{s_k} \mathcal{L}\left(s, \mathbf{y}^{(k)}(s), \mathbf{u}^{(k)}(s)\right) ds \,. \end{aligned} \tag{3.24}$$

Moreover, the differential constraint (3.21), the path constraints (3.22) in mesh interval k can be written as

$$\frac{d\mathbf{y}^{(k)}(s)}{ds} = \frac{x_f - x_0}{2} \mathbf{a}\left(s, \mathbf{y}^{(k)}(s), \mathbf{u}^{(k)}(s)\right) \tag{3.25}$$

and

$$\mathbf{c}\left(s, \mathbf{y}^{(k)}(s), \mathbf{u}^{(k)}(s)\right) \leq \mathbf{0} \,, \tag{3.26}$$

respectively, whereas the boundary conditions (3.23) may be recast as

$$\boldsymbol{\phi}\left(x_0, \mathbf{y}^{(1)}(-1), x_f, \mathbf{y}^{(K)}(1)\right) = \mathbf{0} \,. \tag{3.27}$$

Because the state must be continuous at each interior mesh point, it is required that the condition $\mathbf{y}(s_k^-) = \mathbf{y}(s_k^+)$ be satisfied at $(s_1, s_2, \ldots, s_{K-1})$. Using the LGR pseudospectral scheme, this continuity condition across mesh points is easy to implement. In particular, the state in each mesh interval $k = 1, 2, \ldots, K$ is approximated as

$$\mathbf{y}^{(k)}(s) \approx \mathbf{Y}^{(k)}(s) = \sum_{j=1}^{N_k+1} \mathbf{Y}_j^{(k)} \ell_j^{(k)}(s) = \sum_{j=1}^{N_k+1} \mathbf{Y}_j^{(k)} \prod_{l=1, l\neq j}^{N_k+1} \frac{s - s_l^{(k)}}{s_j^{(k)} - s_l^{(k)}} \,, \tag{3.28}$$

where $\mathbf{Y}_j^{(k)}$ $(j = 1, 2, \ldots, N_k)$ are the approximations of the state functions at the N_k LGR points in mesh interval k and $(s_1^{(k)}, s_2^{(k)}, \ldots, s_{N_k}^{(k)})$ are the LGR collocation points in mesh interval k defined on the subinterval $s \in [s_{k-1}, s_k]$. Moreover, it is worth noting that the point $s_{N_k+1}^{(k)}$ is a noncollocated point. Differentiating (3.28) with respect to s, one obtains

$$\frac{d\mathbf{Y}^{(k)}(s)}{ds} = \sum_{j=1}^{N_k+1} \mathbf{Y}_j^{(k)} \frac{\ell_j^{(k)}(s)}{ds} \,. \tag{3.29}$$

Besides, the cost functional of Equation (3.24) is then approximated using a multiple interval LGR quadrature as

$$J = \mathcal{M}\left(x_0, \mathbf{Y}_1^{(1)}, x_f, \mathbf{Y}_{N_K+1}^{(K)}\right) + \frac{x_f - x_0}{2} \sum_{k=1}^{K} \sum_{j=1}^{N_k} \omega_j^{(k)} \mathcal{L}\left(s_j^{(k)}, \mathbf{Y}_j^{(k)}, \mathbf{U}_j^{(k)}\right), \tag{3.30}$$

where $\omega_j^{(k)}$ $(j = 1, 2, \ldots, N_k)$ are the LGR quadrature weights in mesh interval k, $\mathbf{U}_j^{(k)}$ $(j = 1, 2, \ldots, N_k)$ are the approximations of the input functions at the N_k LGR points in mesh interval k, whereas $\mathbf{Y}_1^{(1)}$ and $\mathbf{Y}_{N_K+1}^{(K)}$ are the approximations of $\mathbf{y}(s_0 = -1)$ and $\mathbf{y}(s_K = 1)$, respectively. Collocating the differential constraints of Equation (3.25) at the N_k LGR points by means of (3.29), one obtains

$$\sum_{j=1}^{N_k+1} D_{ij}^{(k)} \mathbf{Y}_j^{(k)} - \frac{x_f - x_0}{2} \mathbf{a}\left(s_i^{(k)}, \mathbf{Y}_i^{(k)}, \mathbf{U}_i^{(k)}\right) = \mathbf{0}, \qquad i = 1, 2, \ldots, N_k, \tag{3.31}$$

where

$$D_{ij}^{(k)} = \left[\frac{d\ell_j^{(k)}(s)}{ds}\right]_{s_i^{(k)}}, \quad i = 1, \ldots, N_k, \quad j = 1, \ldots, N_k + 1, \quad k = 1, \ldots, K, \tag{3.32}$$

is the $N_k \times (N_k + 1)$ differentiation matrix in mesh interval k.

Next, the path constraint of Equation (3.26) in the mesh interval k are enforced at the N_k LGR points as

$$\mathbf{c}\left(s_i^{(k)}, \mathbf{Y}_i^{(k)}, \mathbf{U}_i^{(k)}\right) \leq \mathbf{0}, \qquad i = 1, 2, \ldots, N_k. \tag{3.33}$$

Furthermore, the boundary conditions of Equation (3.27) are approximated as

$$\boldsymbol{\phi}\left(x_0, \mathbf{Y}_1^{(1)}, x_f, \mathbf{Y}_{N_K+1}^{(K)}\right) = \mathbf{0}. \tag{3.34}$$

It is noted that the continuity in the state at the interior mesh points is enforced via the condition

$$\mathbf{Y}_{N_k+1}^{(k)} = \mathbf{Y}_1^{(k+1)}, \qquad k = 1, 2, \ldots, K - 1. \tag{3.35}$$

However, it is worth noting that this constraint is taken into account explicitly and therefore the NLP that arises from the LGR pseudospectral

approximation is then to minimize the cost function of Equation (3.30) subject to the algebraic constraints (3.31)-(3.34).

For the sake of a compact notation for the multi-stage version of the LGR pseudospectral method, consider the following notation and conventions. As before, all vector functions will be treated a row vectors, whereas any scalar vector that is denoted as a column vector. Moreover, if $\mathbf{f}(\mathbf{p})$ with $\mathbf{f} : \mathbb{R}^n \to \mathbb{R}^m$ is a function that maps row vectors $\mathbf{p} \in \mathbb{R}^n$ to row vectors $\mathbf{f}(\mathbf{p}) \in \mathbb{R}^m$, then the result of evaluating $\mathbf{f}(\mathbf{p})$ at points $(\mathbf{p}_1, \mathbf{p}_2, \ldots, \mathbf{p}_N)$ is the matrix $\mathbf{F}_N^1 = [\mathbf{f}(\mathbf{p}_k)]_1^N$, namely

$$\mathbf{F}_N^1 = [\mathbf{f}(\mathbf{p}_k)]_N^1 = \begin{bmatrix} \mathbf{f}(\mathbf{p}_1) \\ \mathbf{f}(\mathbf{p}_2) \\ \vdots \\ \mathbf{f}(\mathbf{p}_N) \end{bmatrix} \in \mathbb{R}^{N \times n}.$$

A single subscript i attached to a matrix $\mathbf{P} \in \mathbb{R}^{n \times m}$, i.e., $\mathbf{P}_i$, denotes the i-th row of the matrix $\mathbf{P}$, whereas $\mathbf{P}_{i,j}$ denotes the (i,j)-th element of the matrix $\mathbf{P}$. Moreover, the notation $\mathbf{P}_{:,j}$ will be used to denote all the rows and column j of a matrix $\mathbf{P}$ and the notation $\mathbf{P}^\top$ will be used to denote the transpose of $\mathbf{P}$.

Next, let $\mathbf{P}$ and $\mathbf{Q}$ be $n \times m$ matrices. Then, the element-by-element multiplication of $\mathbf{P}$ and $\mathbf{Q}$ is defined as

$$\mathbf{P} \circ \mathbf{Q} = \begin{bmatrix} p_{11}q_{11} & p_{12}q_{12} & \cdots & p_{1m}q_{1m} \\ p_{21}q_{21} & p_{22}q_{22} & \cdots & p_{2m}q_{2m} \\ \vdots & \vdots & \ddots & \vdots \\ p_{n1}q_{n1} & p_{n2}q_{n2} & \cdots & p_{nm}q_{nm} \end{bmatrix}.$$

It is noted that $\mathbf{P} \circ \mathbf{Q}$ is not standard matrix multiplication. Furthermore, if $\mathbf{p} \in \mathbb{R}^n$, then the operation $\text{diag}(\mathbf{p})$ denotes the $n \times n$ diagonal matrix

formed by the element of $\mathbf{p}$, namely

$$\operatorname{diag}(\mathbf{p}) = \begin{bmatrix} p_1 & 0 & \cdots & 0 \\ 0 & p_2 & \cdots & 0 \\ \vdots & \vdots & \ddots & \vdots \\ 0 & 0 & \cdots & p_n \end{bmatrix}.$$

The notation for derivatives of functions of vectors is defined next. First, let $f(\mathbf{p})$ with $f : \mathbb{R}^n \to \mathbb{R}$. Then, the gradient of f with respect to $\mathbf{p}$ is a row vector of length n and defined as

$$\nabla_{\mathbf{p}} f(\mathbf{p}) = \begin{bmatrix} \frac{\partial f}{\partial p_1} & \frac{\partial f}{\partial p_2} & \cdots & \frac{\partial f}{\partial p_n} \end{bmatrix} \in \mathbb{R}^n .$$

Finally, let $\mathbf{f}(\mathbf{p})$ with $\mathbf{f} : \mathbb{R}^n \to \mathbb{R}^m$, where $\mathbf{p}$ may be either a row or column vector and $\mathbf{f}(\mathbf{p})$ has the same orientation (i.e., either row or column vector) as $\mathbf{p}$. Then, the Jacobian of $\mathbf{f}$ with respect to $\mathbf{p}$ is the $m \times n$ matrix whose i-th row is $\nabla_{\mathbf{p}} f_i$, namely

$$\nabla_{\mathbf{p}} \mathbf{f} = \begin{bmatrix} \nabla_{\mathbf{p}} f_1 \\ \nabla_{\mathbf{p}} f_2 \\ \vdots \\ \nabla_{\mathbf{p}} f_m \end{bmatrix} = \begin{bmatrix} \frac{\partial f_1}{\partial p_1} & \frac{\partial f_1}{\partial p_2} & \cdots & \frac{\partial f_1}{\partial p_n} \\ \frac{\partial f_2}{\partial p_1} & \frac{\partial f_2}{\partial p_2} & \cdots & \frac{\partial f_2}{\partial p_n} \\ \vdots & \vdots & \ddots & \vdots \\ \frac{\partial f_m}{\partial p_1} & \frac{\partial f_m}{\partial p_2} & \cdots & \frac{\partial f_m}{\partial p_n} \end{bmatrix} \in \mathbb{R}^{m \times n} .$$

Coming back to the equivalent NLP problem, suppose now the following quantities in mesh intervals $k \in [1, 2, \ldots, K-1]$ and the final mesh interval K:

$$\mathbf{s}^{(k)} = \left[s_i^{(k)} \right]_{N_k}^1 , \quad k = 1, 2, \ldots, K-1, \quad \mathbf{s}^{(K)} = \left[s_i^{(K)} \right]_{N_K+1}^1$$

$$\mathbf{Y}^{(k)} = \left[\mathbf{Y}_i^{(k)} \right]_{N_k}^1 , \quad k = 1, 2, \ldots, K-1, \quad \mathbf{Y}^{(K)} = \left[\mathbf{Y}_i^{(K)} \right]_{N_K+1}^1$$

$$\mathbf{U}^{(k)} = \left[\mathbf{U}_i^{(k)} \right]_{N_k}^1 , \quad k = 1, 2, \ldots, K$$

$$\mathbf{L}^{(k)} = \left[\mathcal{L}\left(s_i^{(k)}, \mathbf{Y}_i^{(k)}, \mathbf{U}_i^{(k)} \right) \right]_{N_k}^1 , \quad k = 1, 2, \ldots, K$$

$$\mathbf{A}^{(k)} = \left[\mathbf{a}\left(s_i^{(k)}, \mathbf{Y}_i^{(k)}, \mathbf{U}_i^{(k)}\right)\right]_{N_k}^{1}, \quad k = 1, 2, \ldots, K$$

$$\mathbf{C}^{(k)} = \left[\mathbf{c}\left(s_i^{(k)}, \mathbf{Y}_i^{(k)}, \mathbf{U}_i^{(k)}\right)\right]_{N_k}^{1}, \quad k = 1, 2, \ldots, K$$

$$\mathbf{w}^{(k)} = \left[\omega_i^{(k)}\right]_{N_k}^{1}, \quad k = 1, 2, \ldots, K$$

and the following vectors:

$$\mathbf{s} = \begin{bmatrix} \mathbf{s}^{(1)} \\ \mathbf{s}^{(2)} \\ \vdots \\ \mathbf{s}^{(K)} \end{bmatrix} \in \mathbb{R}^{N+1}, \quad \mathbf{w} = \begin{bmatrix} \mathbf{w}^{(1)} \\ \mathbf{w}^{(2)} \\ \vdots \\ \mathbf{w}^{(K)} \end{bmatrix} \in \mathbb{R}^{N}, \quad \mathbf{Y} = \begin{bmatrix} \mathbf{Y}^{(1)} \\ \mathbf{Y}^{(2)} \\ \vdots \\ \mathbf{Y}^{(K)} \end{bmatrix} \in \mathbb{R}^{(N+1)\times n},$$

$$\mathbf{U} = \begin{bmatrix} \mathbf{U}^{(1)} \\ \mathbf{U}^{(2)} \\ \vdots \\ \mathbf{U}^{(K)} \end{bmatrix} \in \mathbb{R}^{N\times m}, \quad \mathbf{L} = \begin{bmatrix} \mathbf{L}^{(1)} \\ \mathbf{L}^{(2)} \\ \vdots \\ \mathbf{L}^{(K)} \end{bmatrix} \in \mathbb{R}^{N}, \quad \mathbf{A} = \begin{bmatrix} \mathbf{A}^{(1)} \\ \mathbf{A}^{(2)} \\ \vdots \\ \mathbf{A}^{(K)} \end{bmatrix} \in \mathbb{R}^{N\times n},$$

$$\mathbf{C} = \begin{bmatrix} \mathbf{C}^{(1)} \\ \mathbf{C}^{(2)} \\ \vdots \\ \mathbf{C}^{(K)} \end{bmatrix} \in \mathbb{R}^{N\times p},$$

where $N = \sum_{k=1}^{K} N_k$, whereas n, m and p are the number of states, inputs and path constraints. Therefore, the cost functional and discretized differential constraints given in Equations (3.30) and (3.31) can be written compactly as

$$J = \mathcal{M}\left(x_0, \mathbf{Y}_1, x_f, \mathbf{Y}_{N+1}\right) + \frac{x_f - x_0}{2} + \mathbf{w}^\top \mathbf{L} \tag{3.36}$$

and

$$\boldsymbol{\Delta} = \mathbf{D}\mathbf{Y} - \frac{x_f - x_0}{2}\mathbf{A} = \mathbf{0}, \tag{3.37}$$

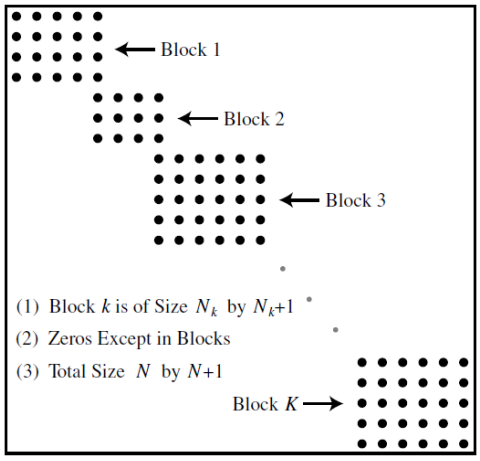

Figure 3.1: Structure of composite LGR differentiation matrix with K mesh intervals.

where $\mathbf{\Delta} \in \mathbb{R}^{N\times n}$ is the composite defect matrix and $\mathbf{D} \in \mathbb{R}^{N\times(N+1)}$ is the composite LGR differentiation matrix, which has a block structure with nonzero elements defined by the matrix given in Equation (3.32). Figure 3.1 shows the structure of the composite LGR differentiation matrix where the mesh consists of K mesh intervals.

Finally, the discretized path constraints of Equation (3.33) and boundary conditions of Equation (3.34) are expressed as

$$\mathbf{C} \leq \mathbf{0} \tag{3.38}$$

and

$$\boldsymbol{\phi}\left(x_0, \mathbf{Y}_1, x_f, \mathbf{Y}_{N+1}\right) = \mathbf{0}\,, \tag{3.39}$$

respectively.

3.4 Computation of the first-order derivatives

The NLP problem arising from the LGR pseudospectral method has the vector of decision variables $\mathbf{z} \in \mathbb{R}^{N(n+m)+2}$ and aims at minimizing

$$f(\mathbf{z}) = \mathcal{M}(\mathbf{z}) + \Gamma(\mathbf{z})\,, \tag{3.40}$$

where $\Gamma = \frac{x_f - x_0}{2}\mathbf{w}^\top \mathbf{L}$ and subject to the constraint

$$\mathbf{h}(\mathbf{z}) \leq \mathbf{0}\,,$$

where

$$\mathbf{z} = \begin{bmatrix} \mathbf{Y}_{:,1} \\ \mathbf{Y}_{:,2} \\ \vdots \\ \mathbf{Y}_{:,n} \\ \mathbf{U}_{:,1} \\ \mathbf{U}_{:,2} \\ \vdots \\ \mathbf{U}_{:,m} \\ x_0 \\ x_f \end{bmatrix}, \quad \mathbf{h} = \begin{bmatrix} \boldsymbol{\Delta}_{:,1} \\ \boldsymbol{\Delta}_{:,2} \\ \vdots \\ \boldsymbol{\Delta}_{:,n} \\ \mathbf{C}_{:,1} \\ \mathbf{C}_{:,2} \\ \vdots \\ \mathbf{C}_{:,p} \\ \boldsymbol{\phi}_{1:b} \end{bmatrix}.$$

In this section, expressions for the gradient of the NLP objective function and the Jacobian of the NLP constraints are determined. These NLP derivatives are obtained by differentiating the functions of the original continuous dynamic optimization problem [49].

3.4.1 Gradient of the objective function

The gradient of the objective function (3.40) with respect to the LGR pseudospectral NLP decision vector $\mathbf{z}$ is given as

$$\nabla_{\mathbf{z}} f = \nabla_{\mathbf{z}} \mathcal{M} + \nabla_{\mathbf{z}} \Gamma. \tag{3.41}$$

The derivative $\nabla_{\mathbf{z}} \mathcal{M}$ is obtained as

$$\nabla_{\mathbf{z}} \mathcal{M} = \begin{bmatrix} \nabla_{\mathbf{Y}} \mathcal{M} & \nabla_{\mathbf{U}} \mathcal{M} & \nabla_{x_0} \mathcal{M} & \nabla_{x_f} \mathcal{M} \end{bmatrix}, \tag{3.42}$$

where

$$\nabla_{\mathbf{Y}} \mathcal{M} = \begin{bmatrix} \nabla_{\mathbf{Y}_{:,1}} \mathcal{M} & \nabla_{\mathbf{Y}_{:,2}} \mathcal{M} & \dots & \nabla_{\mathbf{Y}_{:,n}} \mathcal{M} \end{bmatrix}, \quad \nabla_{\mathbf{U}} \mathcal{M} = \begin{bmatrix} \mathbf{0}_{1 \times Nm} \end{bmatrix}. \tag{3.43}$$

The derivatives $\nabla_{\mathbf{Y}_{:,i}} \mathcal{M}$, $\nabla_{x_0} \mathcal{M}$ and $\nabla_{x_f} \mathcal{M}$ are obtained as

$$\nabla_{\mathbf{Y}_{:,i}} \mathcal{M} = \begin{bmatrix} \frac{\partial \mathcal{M}}{\partial y_i(x_0)} & \mathbf{0}_{1 \times (N-1)} & \frac{\partial \mathcal{M}}{\partial y_i(x_f)} \end{bmatrix}, \quad i = 1, 2, \dots, n, \tag{3.44}$$

and

$$\nabla_{x_0}\mathcal{M} = \frac{\partial \mathcal{M}}{\partial x_0}\,, \quad \nabla_{x_f}\mathcal{M} = \frac{\partial \mathcal{M}}{\partial x_f}\,. \tag{3.45}$$

Next, $\nabla_{\mathbf{z}}\Gamma$ is given as

$$\nabla_{\mathbf{z}}\Gamma = \begin{bmatrix} \nabla_{\mathbf{Y}}\Gamma & \nabla_{\mathbf{U}}\Gamma & \nabla_{x_0}\Gamma & \nabla_{x_f}\Gamma \end{bmatrix}, \tag{3.46}$$

where

$$\nabla_{\mathbf{Y}}\Gamma = \begin{bmatrix} \nabla_{\mathbf{Y}_{:,1}}\Gamma & \nabla_{\mathbf{Y}_{:,2}}\Gamma & \dots & \nabla_{\mathbf{Y}_{:,n}}\Gamma \end{bmatrix}, \tag{3.47}$$

and

$$\nabla_{\mathbf{U}}\Gamma = \begin{bmatrix} \nabla_{\mathbf{U}_{:,1}}\Gamma & \nabla_{\mathbf{U}_{:,2}}\Gamma & \dots & \nabla_{\mathbf{U}_{:,m}}\Gamma \end{bmatrix}. \tag{3.48}$$

The derivatives $\nabla_{\mathbf{Y}_{:,i}}\Gamma$, $\nabla_{\mathbf{U}_{:,j}}\Gamma$, $\nabla_{x_0}\Gamma$ and $\nabla_{x_f}\Gamma$ are obtained as

$$\nabla_{\mathbf{Y}_{:,i}}\Gamma = \begin{bmatrix} \frac{x_f - x_0}{2} \left\{ \mathbf{w} \circ \left[\frac{\partial \mathcal{L}}{\partial y_i} \right]_N^1 \right\}^\top & 0 \end{bmatrix}, \quad i = 1, 2, \dots, n, \tag{3.49}$$

$$\nabla_{\mathbf{U}_{:,j}}\Gamma = \frac{x_f - x_0}{2} \left\{ \mathbf{w} \circ \left[\frac{\partial \mathcal{L}}{\partial u_j} \right]_N^1 \right\}^\top, \quad j = 1, 2, \dots, m, \tag{3.50}$$

$$\nabla_{x_0}\Gamma = -\frac{1}{2}\mathbf{w}^\top \mathbf{L}\,, \quad \nabla_{x_f}\Gamma = \frac{1}{2}\mathbf{w}^\top \mathbf{L}\,. \tag{3.51}$$

It is seen from Equations (3.41)-(3.51) that computing the objective function gradient requires that the first derivatives of $\mathcal{L}$ be determined with respect to the continuous states $\mathbf{y}$ and inputs $\mathbf{u}$, whereas the first derivatives of $\mathcal{M}$ be determined with respect to $\mathbf{y}(x_0)$, $\mathbf{y}(x_f)$, x_0 and x_f. Furthermore, these derivatives are computed at either the N collocation points or at the endpoints.

3.4.2 Constraints Jacobian

The Jacobian of the constraints is defined as

$$\nabla_{\mathbf{z}}\mathbf{h} = \begin{bmatrix} \nabla_{\mathbf{z}}\boldsymbol{\Delta}_{:,1} \\ \vdots \\ \nabla_{\mathbf{z}}\boldsymbol{\Delta}_{:,n} \\ \nabla_{\mathbf{z}}\mathbf{C}_{:,1} \\ \vdots \\ \nabla_{\mathbf{z}}\mathbf{C}_{:,p} \\ \nabla_{\mathbf{z}}\boldsymbol{\phi}_1 \\ \vdots \\ \nabla_{\mathbf{z}}\boldsymbol{\phi}_b \end{bmatrix}. \tag{3.52}$$

The first derivatives of the defect constraints are obtained by

$$\nabla_{\mathbf{z}}\boldsymbol{\Delta}_{:,l} = \begin{bmatrix} \nabla_{\mathbf{Y}}\boldsymbol{\Delta}_{:,l} & \nabla_{\mathbf{U}}\boldsymbol{\Delta}_{:,l} & \nabla_{x_0}\boldsymbol{\Delta}_{:,l} & \nabla_{x_f}\boldsymbol{\Delta}_{:,l} \end{bmatrix}, \quad l = 1, 2, \ldots, n, \tag{3.53}$$

where

$$\nabla_{\mathbf{Y}}\boldsymbol{\Delta}_{:,l} = \begin{bmatrix} \nabla_{\mathbf{Y}_{:,1}}\boldsymbol{\Delta}_{:,l} & \nabla_{\mathbf{Y}_{:,2}}\boldsymbol{\Delta}_{:,l} & \ldots & \nabla_{\mathbf{Y}_{:,n}}\boldsymbol{\Delta}_{:,l} \end{bmatrix}, \tag{3.54}$$

and

$$\nabla_{\mathbf{U}}\boldsymbol{\Delta}_{:,l} = \begin{bmatrix} \nabla_{\mathbf{U}_{:,1}}\boldsymbol{\Delta}_{:,l} & \nabla_{\mathbf{U}_{:,2}}\boldsymbol{\Delta}_{:,l} & \ldots & \nabla_{\mathbf{U}_{:,m}}\boldsymbol{\Delta}_{:,l} \end{bmatrix}. \tag{3.55}$$

The derivatives $\nabla_{\mathbf{Y}_{:,i}}\boldsymbol{\Delta}_{:,l}$, $\nabla_{\mathbf{U}_{:,j}}\boldsymbol{\Delta}_{:,l}$, $\nabla_{x_0}\boldsymbol{\Delta}_{:,l}$ and $\nabla_{x_f}\boldsymbol{\Delta}_{:,l}$ (with $l = 1, 2, \ldots, n$) are obtained as

$$\nabla_{\mathbf{Y}_{:,i}}\boldsymbol{\Delta}_{:,l} = \begin{bmatrix} \delta_{il}\mathbf{D}_{:,1:N} - \frac{x_f - x_0}{2}\mathrm{diag}\left(\left[\frac{\partial a_l}{\partial y_i}\right]_N^1\right) & \delta_{il}\mathbf{D}_{:,N+1} \end{bmatrix}, \quad i = 1, 2, \ldots, n, \tag{3.56}$$

where δ_{il} is the Kronecker delta function, and

$$\nabla_{\mathbf{U}_{:,j}}\boldsymbol{\Delta}_{:,l} = -\frac{x_f - x_0}{2}\mathrm{diag}\left(\left[\frac{\partial a_l}{\partial u_j}\right]_N^1\right), \quad j = 1, 2, \ldots, m, \tag{3.57}$$

$$\nabla_{x_0}\mathbf{\Delta}_{:,l} = \frac{1}{2}[a_l]_N^1\,, \quad \nabla_{x_f}\mathbf{\Delta}_{:,l} = -\frac{1}{2}[a_l]_N^1\,. \tag{3.58}$$

As far as the derivatives of the path constraints are concerned, one may write

$$\nabla_{\mathbf{z}}\mathbf{C}_{:,q} = \begin{bmatrix}\nabla_{\mathbf{Y}}\mathbf{C}_{:,q} & \nabla_{\mathbf{U}}\mathbf{C}_{:,q} & \mathbf{0}_{N\times 1} & \mathbf{0}_{N\times 1}\end{bmatrix}, \quad q = 1,2,\ldots,p, \tag{3.59}$$

where

$$\nabla_{\mathbf{Y}}\mathbf{C}_{:,q} = \begin{bmatrix}\nabla_{\mathbf{Y}_{:,1}}\mathbf{C}_{:,q} & \nabla_{\mathbf{Y}_{:,2}}\mathbf{C}_{:,q} & \ldots & \nabla_{\mathbf{Y}_{:,n}}\mathbf{C}_{:,q}\end{bmatrix}, \tag{3.60}$$

and

$$\nabla_{\mathbf{U}}\mathbf{C}_{:,q} = \begin{bmatrix}\nabla_{\mathbf{U}_{:,1}}\mathbf{C}_{:,q} & \nabla_{\mathbf{U}_{:,2}}\mathbf{C}_{:,q} & \ldots & \nabla_{\mathbf{U}_{:,m}}\mathbf{C}_{:,q}\end{bmatrix}, \tag{3.61}$$

where the derivatives $\nabla_{\mathbf{Y}_{:,i}}\mathbf{C}_{:,q}$ and $\nabla_{\mathbf{U}_{:,j}}\mathbf{C}_{:,q}$ (with $q = 1,2,\ldots,p$) are given by

$$\nabla_{\mathbf{Y}_{:,i}}\mathbf{C}_{:,q} = \begin{bmatrix}\operatorname{diag}\left(\left[\frac{\partial c_q}{\partial y_i}\right]\right) & \mathbf{0}_{N\times 1}\end{bmatrix} \quad i = 1,2,\ldots,n, \tag{3.62}$$

and

$$\nabla_{\mathbf{U}_{:,j}}\mathbf{C}_{:,q} = \operatorname{diag}\left(\left[\frac{\partial c_q}{\partial u_j}\right]\right), \quad j = 1,2,\ldots,m. \tag{3.63}$$

Finally, the first derivative of the boundary conditions are given as

$$\nabla_{\mathbf{z}}\phi_d = \begin{bmatrix}\nabla_{\mathbf{Y}}\phi_d & \nabla_{\mathbf{U}}\phi_d & \nabla_{x_0}\phi_d & \nabla_{x_f}\phi_d\end{bmatrix}, \quad d = 1,2,\ldots,b, \tag{3.64}$$

where

$$\nabla_{\mathbf{Y}}\phi_d = \begin{bmatrix}\nabla_{\mathbf{Y}_{:,1}}\phi_d & \nabla_{\mathbf{Y}_{:,2}}\phi_d & \ldots & \nabla_{\mathbf{Y}_{:,n}}\phi_d\end{bmatrix} \tag{3.65}$$

and

$$\nabla_{\mathbf{U}}\phi_d = \begin{bmatrix}\mathbf{0}_{1\times Nm}\end{bmatrix}. \tag{3.66}$$

The derivatives $\nabla_{\mathbf{Y}_{:,i}}\phi_d$, $\nabla_{x_0}\phi_d$ and $\nabla_{x_f}\phi_d$ (with $d = 1,2,\ldots,b$) are given by

$$\nabla_{\mathbf{Y}_{:,i}}\phi_d = \begin{bmatrix}\frac{\partial\phi_d}{\partial y_i(x_0)} & \mathbf{0}_{1\times(N-1)} & \frac{\partial\phi_d}{\partial y_i(x_f)}\end{bmatrix}, \quad i = 1,2,\ldots,n, \tag{3.67}$$

and

$$\nabla_{x_0}\phi_d = \frac{\partial\phi_d}{\partial x_0}\,, \quad \nabla_{x_f}\phi_d = \frac{\partial\phi_d}{\partial x_f}\,. \tag{3.68}$$

It is seen from Equations (3.52)-(3.68) that the NLP constraint Jacobian requires that the first derivatives of $\mathbf{c}$ and $\mathbf{a}$ with respect to the continuous states and inputs, whereas the derivatives of $\boldsymbol{\phi}$ are determined with respect to x_0, x_f, $\mathbf{y}(x_0)$ and $\mathbf{y}(x_f)$. Moreover, these derivatives are computed at either the N collocation points or at the endpoints.

3.5 Summary

In this chapter, a direct approach based on orthogonal collocation method is presented, where a dynamic optimization problem is transcribed into a finite-dimensional nonlinear programming problem. Both its global and multi-stage versions have been developed by taking Lagrange interpolation polynomials as basis functions and Legendre-Gauss-Radau points as points where the collocation of differential constraints is performed. Eventually, for the sake of efficient computation, explicit expressions for the first derivatives of the resulting nonlinear programming problem arising from the pseudospectral discretization of the continuous dynamic optimization problem have been computed.

Part II

Application to problems in structural mechanics

Chapter 4

Membrane axisymmetric pressure vessels

4.1 Introduction

The manufacturing process required to obtain a pressure vessel strongly constraints the choice of its shape. It follows that metal pressure vessels are generally constituted by a cylinder of constant thickness with end caps. Other shapes are also possible, but they are limited to simple geometries such as cones or toroids. In short, simple shapes are compatible with production requirements but at the same time they do not allow to optimize important characteristics such as the mechanical resistance, the weight or the volume of the vessel by assuming that other properties are fixed. For these reasons, as pointed out in [6], research works concerning with pressure vessel optimization are rare in the last decades.

Generally, literature deals with the optimization of nozzle regions and heads of cylindrical vessels. Limiting the review to the most recent works, the majority of studies considers numerical Finite Element (FE) integrated approaches. For instance, in [54], the shape optimization of the head and of the nozzle of axisymmetric pressure vessels was performed considering an integrated approach that makes use of a multi-objective procedure aiming to minimize the von Mises mechanical stresses in nozzle and head regions. Optimal solutions were obtained following a numerical procedure based on the FE method, leading to shapes different from the usual ones, which, however, are not profitable considering standard manufacturing processes. In [55], a numerical approach to the minimum weight design for toroidal shells subject to internal pressure is presented and optimal shapes were

obtained by means of particle swarm optimization and differential evolution algorithms. In [56], the problem of shape optimization of thin-walled pressure vessel heads was investigated. Also in this case a numerical procedure was followed, where the shape is described with Bezier functions and the optimal solution is obtained by using the simulated annealing algorithm. In [57], the shape optimization was carried out to find the optimal shape among shallow domes for mass minimization subject to external pressure and buckling constraints. The dome was described with cubic Bezier polynomials and results were validated with high fidelity FE analyses. In [58], the edge effect in three unconventional dished heads of a cylindrical pressure vessel subject to internal pressure was analytically studied and numerically predicted by means of FE analyses.

By using the calculus of variations, the optimization of axisymmetric membrane shells subjected to an internal pressure was proposed in [14, 15], where both the shape and the distribution of the thickness along the meridian were considered as design variables. The optimization problem was aimed at minimizing the mass for given shell strength and cavity volume. Optimal solutions were analytically obtained under the hypothesis that the shell is made of a brittle or quasi-brittle material. The elegance of this treatise motivated the problem reconsideration under different load conditions and dealing with other objectives. For instance, the formulation was extended to deal with membranes subject to cyclic loading with initial cracks [59], under geometric constraints [60] and made of anisotropic materials [61]. Moreover, in [13] the thickness distribution for minimum compliance vessels of fixed material mass and meridian profiles was analytically determined.

In this chapter, problems concerning the optimization of the meridian shape and thickness distribution of axisymmetric membrane shells of revolution under the actions of internal pressure are revisited and extended taking into account constraints accounting for the strength of the shell. Three formulations of the problem are given and the optimal design is analytically determined. Whereas the first one aims at minimizing the mass (objective functional) of the membrane shell once its cavity volume (constraint) is fixed and the second one interchanges the objective functional with the constraint, the third one concerns with the minimization of the compliance for a given material volume. The solution of these problems may provide prompt design charts of ample validity in closed form, yet the proposed shapes seems unfeasible with the usual manufacturing process. Nevertheless, this challenge has been surmounted due to availability of last generation metal additive techniques. For this purpose, an optimized

shape will be chosen, the geometrical parameters of a printed technological demonstrator, constructed on the basis of that shape, will be measured and the geometry of the manufactured vessel will be recast by an FE model which will be used to assess the compatibility with the initial strength constraints.

4.2 Mechanics of thin-walled axisymmetric shells

Every part of a structure, of a machine or of any other object is a three-dimensional body, no matter how small its dimensions may be. Nevertheless, the three-dimensional theory of elasticity is not often applied when stresses in such a body are computed. Take for instance, cables, shafts and columns. They are typical examples of structural elements which receive a force or a couple at one end and transmit it to the other. Yet, one does not consider these elements as three-dimensional objects, but rather as lines having some thickness, namely a kind of "physical lines" as opposed to the mathematical meaning of the word. Another example consists of all those objects which are made to bound or enclose some space, e.g., the wall of tank, the metal hull of an airplane, or the hull of a balloon. All these objects cannot be described by a line, but can be described by a curved surface, and consequently their stress analysis must be built on the concept of a "physical surface", a surface made of some more or less solid material, capable of transmitting loads form one part to another and undergoing consequent deformations.

In the development of the mathematical theory of such structural elements, it has become necessary to distinguish between plane walls (also called *plates*) and all walls shaped to curved surfaces (or *shells*). Therefore, one may define a shell as an object which, for the purpose of a simple stress analysis, may be considered as the materialization of a curved surface. This definition implies that the thickness of a shell is small compared with its other dimensions, but it does not require that the smallness be extreme. Mechanically, the middle surface and the thickness represent the shell in the same way as a bar is represented by its axis and the cross section. In most cases, a shell is bounded by two curved surfaces, commonly called as *interior* and *exterior* faces. The middle (or *neutral*) surface of such a shell is defined as the surface which passes midway between these two faces. The thickness of the shell may be the same everywhere or vary from point to point. If one knows the shape of the middle surface and the thickness of the shell for every one of its points, then the shell is fully described geometrically.

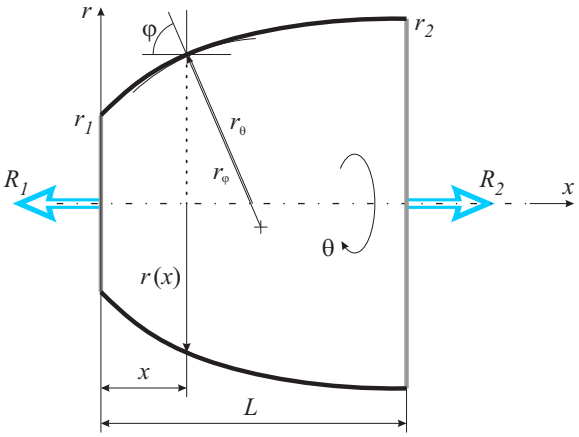

Figure 4.1: Meridian profile of an axisymmetric shell.

4.2.1 Governing equations

Consider a shell having the shape of a surface of revolution (see Figure 4.1) and let the x-axis denote the axis of the shell. The position of the meridian plane is specified by the angle θ, which is measured from a certain fixed meridian plane, and the alignment of the parallel circle is defined by the angle φ between the normal to the surface and the axis of rotation. Let L denote the length of the shell and let $r : [0, L] \to \mathbb{R}_+$ be the function describing the radius of the parallel circle, i.e., the distance from a point on the neutral surface of the shell to its axisymmetric axis. Let $h : [0, L] \to \mathbb{R}_+$ be the function representing the thickness of the shell (not necessarily constant) and measured along the normal to the neutral surface.

The thickness is assumed to satisfy the condition of *thin-walled* shells, namely [62, 63]

$$h_m := \max_{0\le x\le L} h(x) \ll \min\left\{\min_{0\le x\le L} r_\varphi(x), \min_{0\le x\le L} r_\theta(x)\right\}, \tag{4.1}$$

where $r_\varphi(x)$ and $r_\theta(x)$ are the *principal* radii of curvature denoting the radius of the osculating circle and the distance, along the normal to the surface, from the surface to the axis of the shell, respectively, at point of coordinate x. Denoting by prime and double prime the first and second derivatives with respect to x, respectively, principal radii of curvature can be expressed

in terms of the meridian profile by [62, 63]

$$r_\varphi(x) = \frac{-\left(1 + r'(x)^2\right)^{3/2}}{r''(x)}, \quad r_\theta(x) = r(x)\sqrt{1 + r'(x)^2}. \tag{4.2}$$

The shell is loaded with a constant internal pressure q and distributed shear forces on its ends. The resultants of which are R_1 at $x = 0$ and R_2 at $x = L$ and are directed along the axis of the shell. If the ends of the shell are fitted with circular end plates, then $R_1 = \pi q r_1^2$ and $R_2 = \pi q r_2^2$, where $r_1 = r(0)$ and $r_2 = r(L)$. A shell with $r_1 = r_2 = 0$ is said to be *naturally closed* and it is characterized by null shear forces, i.e., $R_1 = R_2 = 0$.

Consider, now, an element of a membrane shell. The equation for the equilibrium of the forces acting on the element, written for the direction normal to the neutral surface of the shell, is [62, 63]

$$\frac{\sigma_\varphi(x)}{r_\varphi(x)} + \frac{\sigma_\theta(x)}{r_\theta(x)} = \frac{q}{h(x)}, \tag{4.3}$$

where σ_φ and σ_θ are the meridian and hoop membrane stresses, respectively.

The equilibrium equation for the cut-off part of the shell $x < L$ in the axial direction is now considered. Firstly, let s be the curvilinear coordinate taken on the meridian profile. Hence,

$$ds(x) = \sqrt{dr^2(x) + dx^2} = \sqrt{1 + r'(x)^2}\, dx. \tag{4.4}$$

The force due to pressure on the infinitesimal element from 0 to x is given by

$$\int_{r_1}^{r(x)} 2\pi r(x) q\, dr(x) = \pi q \left(r(x)^2 - r_1^2\right). \tag{4.5}$$

Moreover, the meridian force due to the membrane stress σ_φ is given by

$$\begin{aligned} 2\pi r(x) h(x) \sigma_\varphi(x) \cos\left(\frac{\pi}{2} - \varphi(x)\right) &= 2\pi r(x) h(x) \sigma_\varphi(x) \frac{dx}{ds(x)} \\ &= \frac{2\pi r(x) h(x) \sigma_\varphi(x)}{\sqrt{1 + r'(x)^2}} \end{aligned} \tag{4.6}$$

Summing up these forces together with the resultant of forces on the plate at $x = 0$, namely $R_1 = \pi q r_1^2$, and setting them equal to zero one obtains

$$\frac{2\pi r(x) h(x) \sigma_\varphi(x)}{\sqrt{1 + r'(x)^2}} = \pi q r(x)^2 \tag{4.7}$$

and consequently

$$\sigma_\varphi(x) = \frac{qr(x)}{2h(x)}\sqrt{1+r'(x)^2}. \tag{4.8}$$

From Equation (4.3), the hoop stress can be written as

$$\sigma_\theta(x) = 2\sigma_\varphi(x) + \frac{qr(x)^2}{2h(x)}\frac{r''(x)}{\sqrt{1+r'(x)^2}}. \tag{4.9}$$

Example 4.1. *Consider a pressurized cylindrical shell has a meridian profile described by*

$$r(x) = R,$$

where R is the radius of the middle surface. Since R is a constant, the first and second derivative with respect to x are both zero and, from (4.2), the two radii of curvature are consequently $r_\theta = R$ and $r_\varphi \to -\infty$. If H denotes the (constant) thickness of the shell, membrane stresses (4.8) and (4.9) read $\sigma_\varphi = \frac{1}{2}qR/H$ and $\sigma_\theta = qR/H$, respectively.

Example 4.2. *Consider a pressurized spherical shell has a meridian profile described by*

$$r(x) = \sqrt{R^2 - (x-R)^2},$$

where R is the radius of the middle surface. Here, the two principal radii are equal to each other, namely $r_\varphi = r_\theta = R$. If H denotes the (constant) thickness of the shell, it is easy to show that the shell is uniformly stressed, i.e., $\sigma_\varphi = \sigma_\theta = \frac{1}{2}qR/H$.

4.2.2 Selected functionals and integrity constraints

In a membrane shell, two main design variables could be the meridian profile and the distribution of the thickness along the meridian axis. Generally speaking, one may be interested in their shape optimization by minimizing or maximizing a given cost functional, such as the mass, the stiffness, the total cost or even mixed performances with different weights. Nowadays, these requirements are fervently requested in different domains, e.g., in aeronautical and pharmaceutical applications. In fact, while the minimization of the mass of the shell implies reduction of material weight and consequently the reduction of its cost, the maximization of the shell volume implies, to some extent, the maximum exploitation of the material mass the shell is made of. These two functionals can be expressed as

$$M = 2\pi \int_0^L r(x)h(x)\sqrt{1+r'(x)^2}\,dx \tag{4.10}$$

and

$$V = \pi \int_0^L r(x)^2 \, dx \tag{4.11}$$

respectively.

Parallel to the aforementioned objectives, the maximization of the stiffness is concerned whenever shells are desired to exhibit the minimum deformation during operational life. The stiffness is related to the strain energy of deformation of the shell, namely the inner product between the strain and stress tensors. However, since the shell is geometrically assumed to be a thin object, only strains in the middle surface are considered. Assuming thus a stress plane condition for the shell, the energy of deformation can be expressed as [13]

$$\Phi = 2\pi \int_0^L [\varepsilon_\varphi(x)\sigma_\varphi(x) + \varepsilon_\theta(x)\sigma_\theta(x)] r(x) h(x) \sqrt{1 + r'(x)^2} \, dx, \tag{4.12}$$

where $\varepsilon_\varphi(x)$ and $\varepsilon_\theta(x)$ denote the meridian and hoop strains, respectively. In case of a linearly elastic, isotropic and homogeneous material, strains are related to the membrane stresses by Hooke's law, namely

$$E\varepsilon_\varphi(x) = \sigma_\varphi(x) - \nu\sigma_\theta(x), \quad E\varepsilon_\theta(x) = \sigma_\theta(x) - \nu\sigma_\varphi(x), \tag{4.13}$$

where E is Young's modulus and ν is Poisson's ratio. From Equations (4.12)-(4.13), the functional of deformation energy becomes

$$\Phi = \frac{2\pi}{E} \int_0^L \left[\sigma_\varphi^2(x) + \sigma_\theta^2(x) - 2\nu\sigma_\varphi(x)\sigma_\theta(x)\right] r(x) h(x) \sqrt{1 + r'(x)^2} \, dx \tag{4.14}$$

Eventually, as far as the structural integrity is concerned, it can be expressed by inequality

$$\sigma_{eq}(x) \leq \sigma_*,$$

where σ_{eq} and σ_* are the equivalent and allowable stresses, respectively. Based on the nature of the employed material, different expressions for σ_{eq} may be adopted. In particular, if the shell is made of brittle or quasi-brittle materials, one can consider the Galileo-Rankine-Navier failure criterion as strength condition, which simply asserts that the equivalent stress is the maximum value between the two principal stresses σ_φ and σ_θ. Namely

$$\sigma_{eq}(x) = \max\{\sigma_\varphi(x), \sigma_\theta(x)\} \leq \sigma_*, \tag{4.15}$$

otherwise, in case of a ductile material, Tresca's failure criterion can be used, namely

$$\sigma_{eq}(x) = \max\{|\sigma_\varphi(x) - \sigma_\theta(x)|, |\sigma_\theta(x) - \sigma_\nu(x)|, |\sigma_\varphi(x) - \sigma_\nu(x)|\} \leq \sigma_* \tag{4.16}$$

where $\sigma_\nu(x)$ is the normal stress to the meridian profile of the shell.

4.3 Minimum mass vessels

Consider the following problem.

Problem 4.1. *Given the length L and the isoperimetric constraint*

$$\pi \int_0^L r(x)^2 \, dx = \widehat{V} \tag{4.17}$$

accounting for the cavity volume of the shell, find the meridian shape $r^*(x)$ and the thickness distribution $h^*(x)$ which minimize the mass

$$M = 2\pi \int_0^L r(x) h(x) \sqrt{1 + r'(x)^2} \, dx \,, \tag{4.18}$$

subject to the constraint

$$\sigma_{eq}(x) \leq \sigma_* , \tag{4.19}$$

and to the boundary conditions

$$r(0) = r_1 \,, \quad r(L) = r_2 \,, \tag{4.20}$$

being σ_*, $\widehat{V}$, r_1 and r_2 specified positive constants.

In [14], Problem 4.1 has been solved for naturally closed vessels made of brittle materials. In the construction of the optimal solution, it is assumed that, throughout the whole interval $[0, L]$, inequality (4.15) turns into an equality, i.e., either

$$\sigma_\varphi(x) = \sigma_* \,, \quad \sigma_\theta(x) \leq \sigma_* \tag{4.21}$$

for all x (which, in what follows, is called case 1), or

$$\sigma_\theta(x) = \sigma_* \,, \quad \sigma_\varphi(x) \leq \sigma_* \tag{4.22}$$

for all x (case 2). This statement can be justified as follows. Suppose, by contradiction, that, on a certain segment $x \in [x_1, x_2]$ with $x_1 > 0$ and $x_2 < L$, the optimal solution $\{r^*(x), h^*(x)\}$ satisfies

$$h^*(x) > \frac{N_\varphi(x)}{\sigma_*} , \quad h^*(x) > \frac{N_\theta(x)}{\sigma_*} , \tag{4.23}$$

where N_φ and N_θ are the membrane forces corresponding to the meridian and hoop directions. On the other segments $[0, x_1)$ and $(x_2, L]$ of the closed interval $[0, L]$, it is assumed that the considered optimal solution $\{r^*(x), h^*(x)\}$ satisfies either (4.21) or (4.22), i.e., it is assumed that

inequality (4.15) turns into an equality. In this case, we construct an admissible design solution $\{\hat{r}(x), \hat{h}(x)\}$ in the following way:

$$\hat{r}(x) = r^*(x), \quad \hat{h}(x) = h^*(x)$$

for $x \in [0, x_1) \cup (x_2, L]$, and

$$\hat{r}(x) = r^*(x), \quad \hat{h}(x) = \frac{N_\varphi(x)}{\sigma_*} < h^*(x) \quad \text{or} \quad \hat{h}(x) = \frac{N_\theta(x)}{\sigma_*} < h^*(x)$$

for $x \in [x_1, x_2]$. The design $\{\hat{r}(x), \hat{h}(x)\}$ is admissible because they satisfy the strength condition (4.15) and the isoperimetric constraint imposed on the shell volume. Note that the admissible design satisfies the equality in (4.15) throughout the entire closed interval $[0, L]$. Thus, the constructed admissible solution is a full-strength design and, for this solution, one has

$$\begin{aligned} M[\hat{r}(x), \hat{h}(x)] = {} & 2\pi \int_0^{x_1} r^*(x) h^*(x) \sqrt{1 + r'^*(x)^2}\, dx \\ & + 2\pi \int_{x_1}^{x_2} r^*(x) \hat{h}(x) \sqrt{1 + r'^*(x)^2}\, dx \\ & + 2\pi \int_{x_2}^{L} r^*(x) h^*(x) \sqrt{1 + r'^*(x)^2}\, dx \\ < {} & 2\pi \int_0^{L} r^*(x) h^*(x) \sqrt{1 + r'^*(x)^2}\, dx = M[r^*(x), h^*(x)]. \end{aligned}$$

Thus, the contradictory inequality $M[\hat{r}, \hat{h}] < M[r^*, h^*]$ proves the assertion that, for the optimal solution, the strict equality in (4.15) is realized throughout the entire closed interval $[0, L]$.

4.3.1 Optimal solutions

Analytical solutions of the optimal design of a closed axisymmetric shell with rigid end plates can be derived by means of calculus of variations (see, e.g., [15]) and are reported in Table 4.1 for cases 1 and 2, where

$$\alpha = \frac{6\widehat{V}}{\pi L^3} - 3\Delta_+\,, \quad \alpha_0 = -\frac{(r_1 + r_2)^2}{L^2}\,, \quad c = L(\Delta_- + \alpha)\,,$$

$$\Delta_\pm = \frac{r_2^2 \pm r_1^2}{L^2}\,, \quad \chi(x) = \sqrt{\alpha(\alpha - 1)x^2 + c(1 - \alpha)x + c^2/4 + r_1^2}\,,$$

and subscripts φ or θ denote that the constraints on the meridian (case 1) or hoop (case 2) stress are active, respectively. Results are also depicted for

some values of α in Figures 4.2a and 4.2b, where the normalized meridian shape $\tilde{r} = \frac{r}{L}$ and the normalized thickness distribution $\tilde{h} = \frac{\sigma_* h}{qL}$ are shown for both cases, for $r_1 = L/2$ and $r_2 = L$. As a particular case, when $r_1 = r_2 = 0$ the analytical expressions of the meridian shape reported in Table 4.1 lead to oblate ellipsoids when $\alpha > 1$ (case 1, see solid lines in Figure 4.3a) and to prolate ellipsoids when $\alpha < 1$ (case 2, dashed lines in Figure 4.3a). The corresponding thicknesses are plotted in Figure 4.3b.

4.3.2 Practical indications

From the above considerations, it is evident that the parameter α is crucial both for discriminating between case 1 (in which $\alpha \geq 1$) and case 2 (in which $\alpha \leq 1$) and for determining the optimal shape and thickness. Therefore it is convenient to consider it as a function of the constraints and of the geometric data, namely

$$\alpha = \alpha(r_1, r_2, L, V)\,.$$

For practical references, contour levels of the parameter α as a function of r_1 and r_2 for different values of $v = \frac{V}{L^3}$ can be computed, allowing the designer to select the desired uniform-strength condition (i.e., either $\sigma_\varphi = \sigma_*$ or $\sigma_\theta = \sigma_*$ along the x-axis) of the membrane shell. As an example, in Figures 4.4a and 4.4b the iso-α lines for two values of v are reported. It is easy to see that optimal shells with $\sigma_\varphi = \sigma_*$ ($\alpha > 1$) are possible only when the point $(r_1/L, r_2/L)$ lies in the yellow region.

	Case 1 ($\sigma_\varphi = \sigma_*$ and $\sigma_\theta \leq \sigma_*$)	Case 2 ($\sigma_\theta = \sigma_*$ and $\sigma_\varphi \leq \sigma_*$)
$r^*(x)$	$\sqrt{-\alpha x^2 + cx + r_1^2}$	$\sqrt{-\alpha x^2 + cx + r_1^2}$
$h^*_{\varphi,\theta}(x)$	$\dfrac{q\sqrt{\alpha(\alpha-1)x^2 + c(1-\alpha)x + c^2/4 + r_1^2}}{2\sigma_*}$	$\dfrac{q\left[\chi(x) + (1-\alpha)\frac{-\alpha x^2 + cx + r_1^2}{\chi(x)}\right]}{2\sigma_*}$
Condition	$\alpha \geq 1$	$\alpha \leq 1$ and $\alpha \geq \alpha_0$

Table 4.1: Closed form optimal solutions for Problem 4.1.

4.3.3 Extension to ductile materials

In many applications such as aircraft systems, pharmaceutical technology and petrochemical transportation, vessels are mainly made of ductile materials. It is better therefore that the Galileo-Rankine-Navier yield criterion be replaced by those for ductile materials such as Tresca's or von Mises's ones. Generally, experiments suggest that the von Mises yield criterion is the one which provides better agreement with observed behavior than the Tresca yield criterion. However, this latter is here considered because of its mathematical simplicity. It can be shown, under some mild hypotheses, that the Tresca criterion can be formulated in a form equivalent to the Galileo-Rankine-Navier criterion as follows. First of all, since membrane shells are subjected to an internal pressure q, the stress behavior can be thought to be always positive, at least in the (open) interval $(0, L)$. This reasonable assumption leads to $\sigma_\varphi > 0$, $\sigma_\theta > 0$ and $\sigma_n \lesssim 0$. Moreover, $|\sigma_n|$ is almost equal to the pressure value q, since no other force is acting in this direction. According to the hypothesis of thin elastic shell (4.1)

$$|\sigma_n| < \sigma_\theta \,, \qquad |\sigma_n| < \sigma_\varphi \,.$$

As a consequence,

$$\sigma_\theta - \sigma_n > \sigma_\theta - \sigma_\varphi \,, \qquad \sigma_\theta - \sigma_n > 0 > \sigma_n - \sigma_\theta$$

and

$$\sigma_\varphi - \sigma_n > \sigma_\varphi - \sigma_\theta \,, \qquad \sigma_\varphi - \sigma_n > 0 > \sigma_n - \sigma_\varphi$$

yielding

$$\begin{aligned} \max\{|\sigma_\varphi - \sigma_\theta|, |\sigma_\theta - \sigma_n|, |\sigma_\varphi - \sigma_n|\} &\leq \max\{\sigma_\theta - \sigma_n, \sigma_\varphi - \sigma_n\} \\ &\leq \max\{\sigma_\theta + q, \sigma_\varphi + q\} \,, \end{aligned} \tag{4.24}$$

where in the last inequality the identity $\sigma_n = -q$ has been used. Since q is constant, the constraint $\max\{\sigma_\theta + q, \sigma_\varphi + q\} \leq \widetilde{\sigma}$ can be written as

$$\max\{\sigma_\theta, \sigma_\varphi\} \leq \sigma_* - q \,, \tag{4.25}$$

namely as a Galileo-Rankine-Navier criterion (4.15), provided that the (new) allowable stress is given by $\sigma_* - q$. Therefore the results obtained in the case of brittle materials can be easily extended to ductile materials providing that the constraint on the maximum admissible stress is transformed into the equivalent maximum admissible stress defined by (4.25).

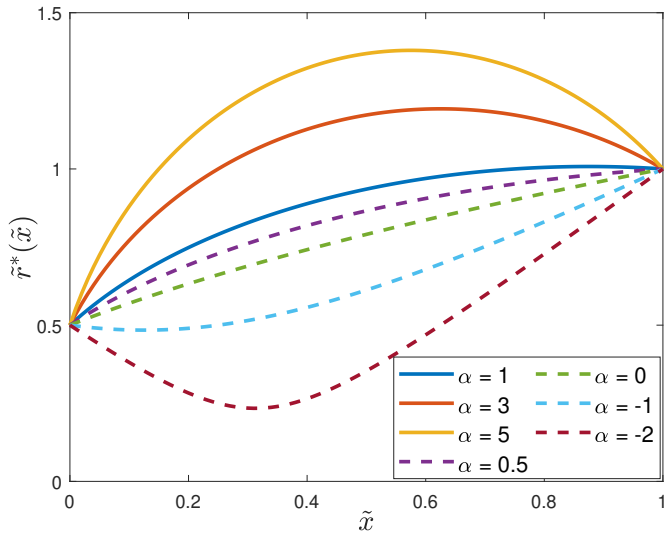

(a)

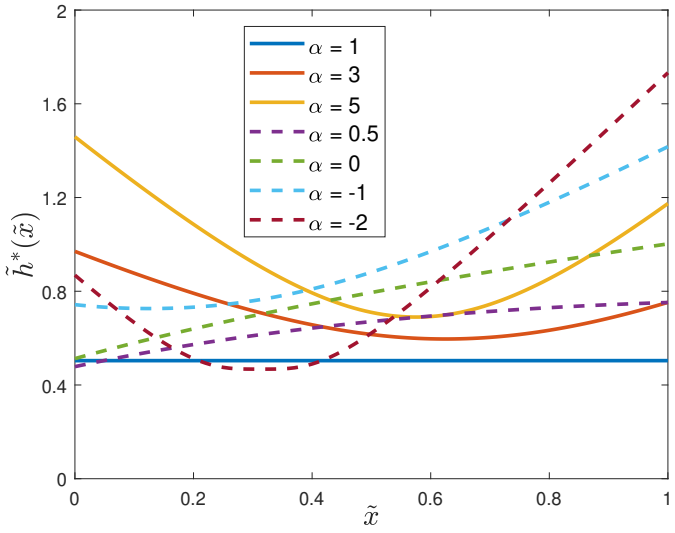

(b)

Figure 4.2: Normalized optimal meridian profile (a) and thickness distribution (b) for different values for α and for $r_1 = L/2$ and $r_2 = L$. Solid and dashed lines refer to cases 1 and 2, respectively.

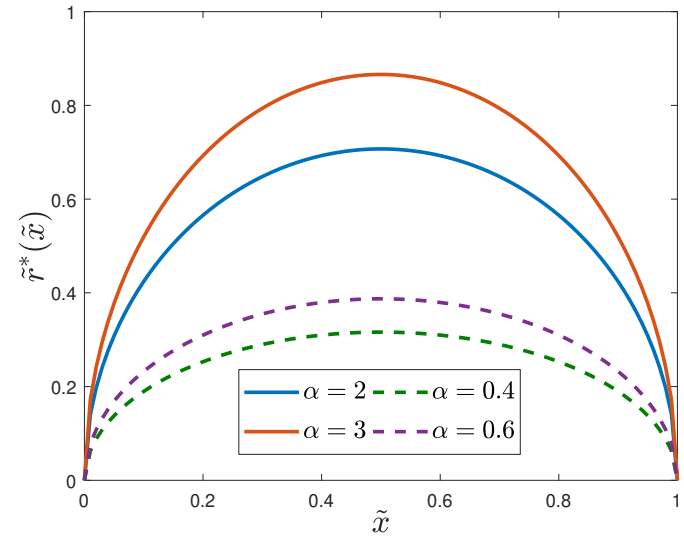

(a)

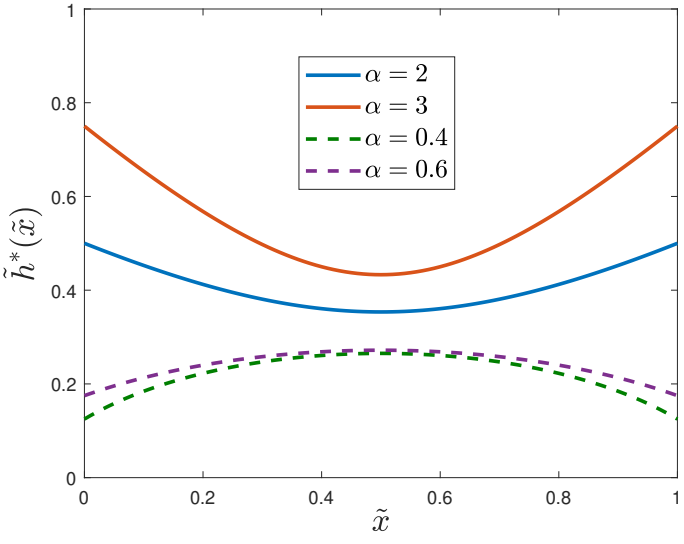

(b)

Figure 4.3: Optimal normalized meridian shapes (a) and optimal normalized thicknesses (b) for some values of α. Solid and dashed lines represent vessels of uniform meridian (oblate ellipsoids) and hoop (prolate ellipsoids) stress, respectively.

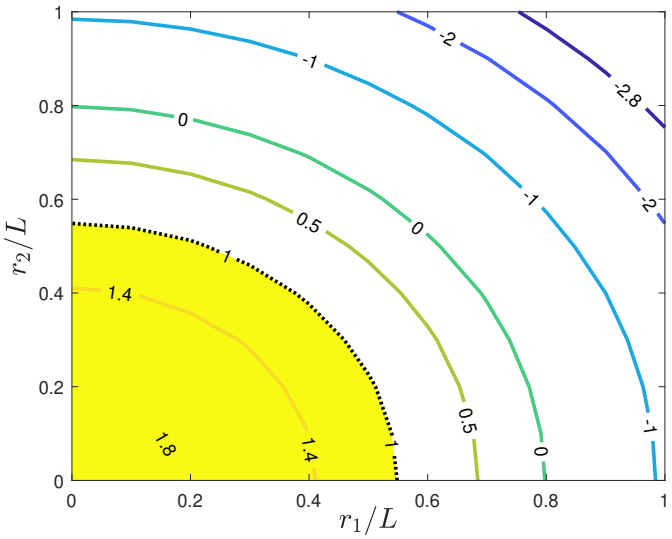

(a)

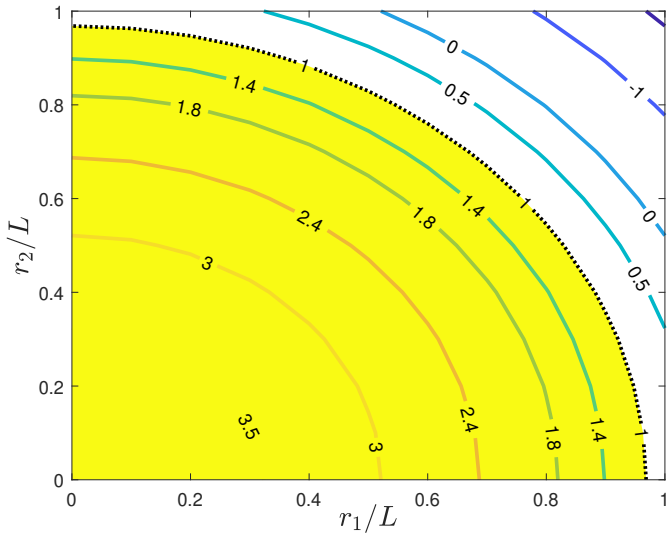

(b)

Figure 4.4: Iso-α lines for $v = 1$ (a) and $v = 2$ (b). Yellow zones indicate admissible regions where case 1 is achieved.

4.4 Maximum volume vessels

The problem concerning the cavity volume maximization once fixed the material mass is considered in this section. It is formulated as follows:

Problem 4.2. *Given the length L and the isoperimetric constraint*

$$2\pi \int_0^L r(x)h(x)\sqrt{1+r'(x)^2}\,dx = \widehat{M} \tag{4.26}$$

accounting for the material mass of the shell, find the meridian shape $r^*(x)$ and the thickness distribution $h^*(x)$ which maximizes the cavity volume

$$V = \pi \int_0^L r(x)^2\,dx\,, \tag{4.27}$$

subject to the constraint

$$\sigma_{eq}(x) \leq \sigma_*, \tag{4.28}$$

and to the boundary conditions

$$r(0) = r_1\,, \quad r(L) = r_2\,, \tag{4.29}$$

being σ_*, $\widehat{M}$, r_1 and r_2 specified positive constants.

Hereinafter, the maximization of (4.27) is conveniently replaced by the minimization of its negative counterpart, i.e.,

$$\bar{V} = -\pi \int_0^L r(x)^2\,dx\,. \tag{4.30}$$

The properties of optimal solutions considered in [14] are still valid, since the cost functional and the constraint are just inverted. Nevertheless, the reasoning that yields the practical suggestions previously exposed for Problem 4.1 leads to rather different conclusions for Problem 4.2. For this reason it is convenient to derive optimal solutions in order to better understand the differences between the two problems. However, unlike [14, 15] where the calculus of variations has been employed, necessary conditions for optimality (2.17)-(2.24) can be alternatively used, yet provided that a plant equation is suitably proposed. To this purpose, the state $y(x)$ and the input function $u(x)$ are selected to be the meridian profile $r(x)$ and its first derivative with respect to x, respectively, i.e.,

$$\frac{dr(x)}{dx} = u(x), \tag{4.31}$$

for case 1, while for case 2 the input function is the second derivative of the meridian profile with respect to x, namely

$$\begin{cases} \frac{dr(x)}{dx} = v(x), \\ \frac{dv(x)}{dx} = u(x). \end{cases} \tag{4.32}$$

In terms of the notations used in Chapter 2, vectors $\mathbf{y}(x)$ and $\mathbf{u}(x)$ are given by $r(x)$ and $u(x)$, respectively, for the case 1 ($n = m = 1$, i.e., both state and input vectors belong to $\mathbb{R}^1$), whereas $\mathbf{y}(x) = [r(x) \;\; v(x)] \in \mathbb{R}^2$ and $u(x)$ is the input function representing the second derivative of the meridian profile with respect to x for case 2 ($n = 2$ and $m = 1$). Moreover, $x_0 = 0$, $x_f = L$, $y(x_0) = r_1$ and $y(x_f) = r_2$, which are all specified quantities. Next, cases 1 and 2 are separately addressed.

Case 1: $\sigma_\varphi = \sigma_*$ and $\sigma_\theta \leq \sigma_*$

In this case, from (4.8), the thickness distribution is given by the relation

$$h_\varphi(x) = \frac{qr(x)}{2\sigma_*}\sqrt{1 + r'(x)^2}\,, \tag{4.33}$$

where the subscript φ denotes that the constraint on the meridian stress is active. Substituting (4.33) in the cost functional (4.30) and considering the isoperimetric constraint on the volume of the shell (4.26), the augmented cost functional takes the form

$$V^a = \bar{V} - \lambda\widehat{M} = \frac{\pi q}{\sigma_*}\int_0^L \left[-\frac{\sigma_*}{q}r(x)^2 - \lambda r(x)^2\left(1 + u(x)^2\right)\right] dx\,, \tag{4.34}$$

where λ is the Lagrangian multiplier corresponding to the isoperimetric constraint (4.26). From (4.34) and (4.31), the Hamiltonian function is given by

$$\mathcal{H}(x, r, u, p) = -\frac{\sigma_*}{q}r(x)^2 - \lambda r(x)^2\left(1 + u(x)^2\right) + p(x)u(x) \tag{4.35}$$

where p is the costate function. On the one hand, differentiating (4.35) with respect to u yields

$$\frac{\partial \mathcal{H}}{\partial u} = -2\lambda r(x)^2 u(x) + p(x) \tag{4.36}$$

and applying (2.19), one obtains

$$p(x) = 2\lambda r(x)^2 u(x). \tag{4.37}$$

On the other hand, differentiating the Hamiltonian with respect to r

$$\frac{\partial \mathcal{H}}{\partial r} = -\frac{2\sigma_*}{q} r(x) - 2\lambda r(x) - 2\lambda r(x) u(x)^2 \tag{4.38}$$

and applying (2.18), one obtains

$$\frac{dp(x)}{dx} = 2\left[\left(\frac{\sigma_*}{q} - \lambda\right) + \lambda u(x)^2\right] r(x). \tag{4.39}$$

Besides, differentiating (4.37) with respect to x

$$\frac{dp(x)}{dx} = 2\lambda \left[2u(x)^2 + r(x)u'(x)\right] r(x) \tag{4.40}$$

and equating (4.39) with (4.40), the following necessary condition

$$r'(x)^2 + r(x)r''(x) = 1 + \frac{\sigma_*}{\lambda q} \tag{4.41}$$

is derived, and optimal meridian profiles are obtained by solving the boundary value problem

$$(r(x)^2)'' = 2\mu, \quad r(0) = r_1, \quad r(L) = r_2\,, \tag{4.42}$$

where $\mu = 1 + \frac{\sigma_*}{\lambda q}$. The solution of problem (4.42) can be written in the form

$$r(x) = \sqrt{\mu x^2 + ax + r_1^2}\,, \tag{4.43}$$

where $a = L(\Delta_- - \mu)$. From Equation (4.33) the corresponding thickness distribution is given by

$$h_\varphi(x) = \frac{q}{2\sigma_*}\sqrt{\mu(\mu+1)x^2 + a(\mu+1)x + a^2/4 + r_1^2}\,. \tag{4.44}$$

Note that the optimal solutions have the same form of those reported in Table 4.1, but with different coefficients. The parameter μ is found using the information on the constraint (4.26), leading to the following second order algebraic equation

$$\mu^2 - 2\mu - 12\left(\frac{\widehat{M}\sigma_*}{\pi q L^3} - \frac{r_1^2}{L^2}\right) + 3\Delta_-(\Delta_- + 2) = 0\,, \tag{4.45}$$

whose discriminant Δ_μ is

$$\Delta_\mu = 4 + 48\left(\frac{\widehat{M}\sigma_*}{\pi q L^3} - \frac{r_1^2}{L^2}\right) - 12\Delta_-(\Delta_- + 2) \tag{4.46}$$

and whose solutions are

$$\mu_{1,2} = 1 \pm \frac{1}{2}\sqrt{\Delta_\mu}. \tag{4.47}$$

Admissible values for μ are obtained by solving the inequality $\sigma_\theta \leq \sigma_*$. From (4.8) and (4.9), this condition can be shown to be $\mu \leq -1$. If both $\mu_{1,2}$ satisfies this latter requirement, solution corresponding to the lowest maximum volume, given by

$$V_\varphi = \pi \left[\frac{\mu L^3}{3} + \frac{aL^2}{2} + r_1^2 L \right], \tag{4.48}$$

is discarded.

Case 2: $\sigma_\varphi \leq \sigma_*$ and $\sigma_\theta = \sigma_*$

In this case, from (4.9), the thickness distribution is given by the relation

$$h_\theta = \frac{qr(x)}{\sigma_*} \left(\frac{1}{2} r(x) u'(x) + u(x)^2 + 1 \right) (1 + u(x)^2)^{-1/2}, \tag{4.49}$$

where the subscript θ denotes that the constraint on the meridian stress is active. Substituting (4.49) in the cost functional (4.30) and considering the isoperimetric constraint on the volume of the shell (4.26), the augmented cost functional takes the form

$$V^a = \bar{V} - \lambda \widehat{M} = \frac{\pi q}{\sigma_*} \int_0^L \left\{ -\frac{\sigma_*}{q} - \lambda \left[2 + 2v(x)^2 + r(x)u(x) \right] \right\} r(x)^2 \, dx, \tag{4.50}$$

where λ is the Lagrangian multiplier corresponding to the isoperimetric constraint (4.26). From (4.50) and (4.32), the Hamiltonian function is given by

$$\begin{aligned} \mathcal{H}(x, r, u, v, p_1, p_2) = &\left\{ -\frac{\sigma_*}{q} - \lambda \left[2 + 2v(x)^2 + r(x)u(x) \right] \right\} r(x)^2 \\ &+ p_1(x)v(x) + p_2(x)u(x), \end{aligned} \tag{4.51}$$

where p_1 and p_2 are the costate functions. On the one hand, differentiating (4.51) with respect to u yields

$$\frac{\partial \mathcal{H}}{\partial u} = -\lambda r(x)^3 + p_2(x) \tag{4.52}$$

and applying (2.19), one obtains

$$p_2(x) = \lambda r(x)^3. \tag{4.53}$$

On the other hand, differentiating the Hamiltonian with respect to r and v one obtains

$$\begin{cases} \frac{\partial \mathcal{H}}{\partial r} = -2\frac{\sigma_*}{q} r(x) - 4\lambda r(x)\left(1 + v(x)^2\right) - 3\lambda r(x)^2 u(x) \\ \frac{\partial \mathcal{H}}{\partial v} = -4\lambda r(x)^2 v(x) + p_1(x). \end{cases} \tag{4.54}$$

Moreover, differentiating (4.53) with respect to x yields

$$\frac{dp_2(x)}{dx} = 3\lambda r(x)^2 \frac{dr(x)}{dx} = 3\lambda r(x)^2 v(x). \tag{4.55}$$

Applying Equation (2.18), one obtains

$$4\lambda r(x)^2 v(x) + p_1(x) = 3\lambda r(x)^2 v(x),$$

or

$$p_1(x) = -\lambda r(x)^2 v(x). \tag{4.56}$$

Furthermore, differentiating (4.56) with respect to x yields

$$\frac{dp_1(x)}{dx} = -2\lambda r(x)\frac{dr(x)}{dx} v(x) - \lambda r(x)^2 \frac{dv(x)}{dx} \tag{4.57}$$

or, from (4.32),

$$\frac{dp_1(x)}{dx} = -\lambda\left(2r(x)v(x)^2 + r(x)^2 u(x)\right). \tag{4.58}$$

Now, from (4.54) and applying Equation (2.18) again, one obtains

$$2\frac{\lambda\sigma_*}{q} r(x) + 4r(x)\left(1 + v(x)^2\right) + 3r(x)^2 u(x) = -\left(2r(x)v(x)^2 + r(x)^2 u(x)\right),$$

which, after some manipulations, leads to the following differential boundary value problem

$$(r(x)^2)'' = 2\eta, \quad r(0) = r_1, \quad r(L) = r_2\,, \tag{4.59}$$

where $\eta = -2 - \frac{\sigma_*}{\lambda q}$. The solution of problem (4.59) can be written in the form

$$r(x) = \sqrt{\eta x^2 + bx + r_1^2}\,, \tag{4.60}$$

where $b = L(\Delta_- - \eta)$. From Equation (4.49) the corresponding thickness distribution is given by

$$h_\theta(x) = \frac{q}{2\sigma_*}[\xi + (1+\eta)(\eta x^2 + bx + r_1^2)\xi^{-1}]\,, \tag{4.61}$$

where

$$\xi(x) = \sqrt{\eta(\eta+1)x^2 + b(\eta+1)x + b^2/4 + r_1^2}\,. \tag{4.62}$$

Also here, as before in case 1, optimal solutions have the same form of those reported in Table 4.1, but with different coefficients. The parameter η is found using the information on the constraint (4.26), leading to the following second order algebraic equation

$$\eta^2 + \eta(4 - 6\Delta_+) + 12\left(\frac{\widehat{M}\sigma_*}{\pi q L^3} - 2\frac{r_1^2}{L^2}\right) - 3\Delta_-^2 - 12\Delta_- = 0\,. \tag{4.63}$$

whose discriminant Δ_η is

$$\Delta_\eta = (4 - 6\Delta_+)^2 - 48\left(\frac{\widehat{M}\sigma_*}{\pi q L^3} - 2\frac{r_1^2}{L^2}\right) + 12\Delta_-(\Delta_- + 4) \tag{4.64}$$

and whose solutions are

$$\eta_{1,2} = -(2 - 3\Delta_+) \pm \frac{1}{2}\sqrt{\Delta_\eta}. \tag{4.65}$$

Admissible values for μ are obtained by solving the inequality $\sigma_\varphi \leq \sigma_*$. From (4.8) and (4.9), this condition can be shown to be $\mu \geq 1$. If both $\eta_{1,2}$ satisfies this latter requirement, the solution corresponding to the lowest maximum volume, which is still given by (4.48), is discarded.

4.4.1 Practical indications

By comparing the previous equations with those reported in Table 4.1, it can be observed that normalized meridian profiles and thicknesses reported in Figure 4.2a and 4.2b for Problem 4.1 are exactly the same as for Problem 4.2 by posing $\alpha = -\mu$ for case 1 and $\alpha = -\eta$ for case 2. Besides, from (4.45) and (4.63), one can note that μ and η not only depend on geometrical data r_1, r_2, L and on the isoperimetric constraint $\widehat{M}$, as in the mass minimization problem, but also on the values of q and σ_*, i.e.,

$$\mu = \mu(r_1, r_2, L, \widehat{M}, q, \sigma_*), \quad \eta = \eta(r_1, r_2, L, \widehat{M}, q, \sigma_*)\,.$$

Moreover, if $\Delta_\mu < 0$ no optimal solution exists, while if $\Delta_\mu \geq 0$ two values of μ are computed. An analogous result holds for η. If the two values are both admissible, then only the solution corresponding to the global maximum should be considered.

4.4.2 Comments on the spaces of optimal solutions

The analysis carried out above shows that the problem of the vessel of maximum internal volume, once fixed its mass, is not exactly the dual problem to the vessel of minimal mass, once fixed the volume of the cavity. In fact, given r_1, r_2, L, q and σ_*, there is always a curve $r(x)$ that minimizes the mass, once fixed the internal volume, provided that some constraints on the parameter α are fulfilled (see Table 4.1); on the contrary, the volume maximization problem presents additional algebraic constraints which, in turn, impose some restrictions to the set of admissible values for the parameters μ and η. In particular, both in the case of critical meridian stress and in the case of critical hoop stress, the designer has first to select geometrical data such that the second order algebraic equation on the parameter (being it μ or η) admits solutions. Then the solutions have to be consistent with the constraint representing the critical stress, namely $\mu \leq -1$ for the meridian stress and $\eta \geq 1$ for the hoop stress.

To ease the design process one may plot, for given values of the dimensionless parameters

$$m = \frac{\widehat{M}}{L^3}, \quad \tau = \frac{\sigma_*}{q}$$

the level lines of Δ_μ, μ, Δ_η and η in the plane $(r_1/L, r_2/L)$, representing the (dimensionless) magnitude of the end plates. Consider, as an example, the case $m = 0.05$ and $\tau = 100$. Level lines for Δ_μ (see Figure 4.5a) and μ (Figure 4.5b) show that for every r_1 and r_2 an optimal solution, such that $\sigma_\varphi = \sigma_*$, exists.

Instead, if $m = 0.01$ and $\tau = 100$, not all the values for r_1 and r_2 admit solution (see Figure 4.6a). Large positive values of Δ_μ are approximately in the region $(r_1/L, r_2/L) \in [0, 0.35] \times [0, 0.35]$, hence admissible values of μ are expectedly obtained in this particular region (see Figure 4.6b, where a suitable enlargement of the square $[0, 0.35] \times [0, 0.35]$ is shown).

Of course the same considerations can be done for the Δ_η and η. Figures 4.7a and 4.7b show level lines of Δ_η and η for the case $m = 0.02$ and $\tau = 100$. Note that high values of r_1 and r_2 admit solution (see Figure 4.7b, where a suitable enlargement of the square $[0.6, 1] \times [0.6, 1]$ is shown).

It is important to highlight that, while in Problem 4.1 optimal solutions are characterized by either uniform meridian or circumferential stress, in Problem 4.2 it is possible to have an intersection between the spaces for optimal solutions for both strength cases. This is illustrated in the following example.

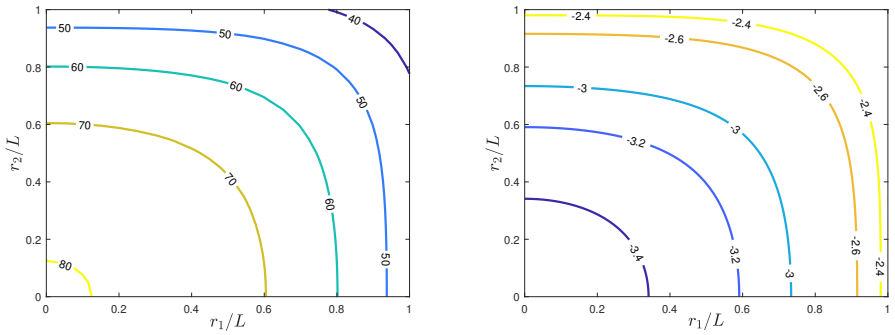

(a) (b)

Figure 4.5: Level lines of Δ_μ (a) and μ (b) for $m = 0.05$ and $\tau = 100$.

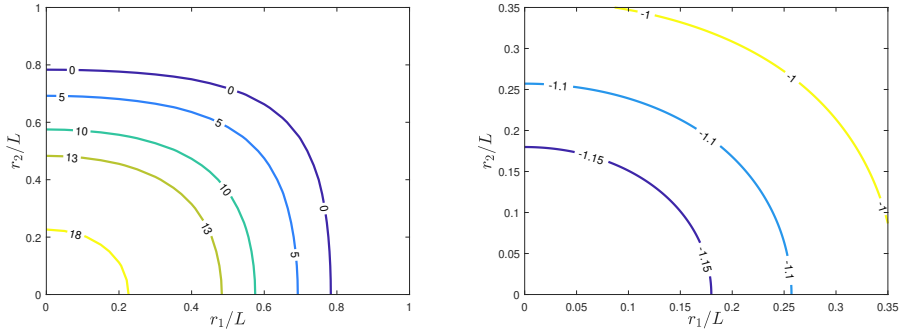

(a) (b)

Figure 4.6: Level lines of Δ_μ (a) and μ (b) for $m = 0.01$ and $\tau = 100$.

Example 4.3. *Consider the vessel with* $r_1 = 0.7$ *m,* $r_2 = 0.9$ *m,* $L = 1$ *m,* $m = 0.05$ *and* $\tau = 100$. *In order to have a vessel of maximum volume with uniform meridian stress, the algebraic constraint (4.45) leads to* $\mu_1 = -2.5107$ *and* $\mu_2 = 4.5107$. *Only* μ_1 *is admissible and leads to* $V_\varphi = 3.3566\ m^3$. *On the other hand, in order to have a vessel of maximum volume with uniform hoop stress, the algebraic constraint (4.63) leads to* $\eta_1 = 2.1918$ *and* $\eta_2 = 1.6082$. *Both of them are admissible and lead to* $V_{1\theta} = 1.2\ m^3$ *and* $V_{2\theta} = 0.8944\ m^3$, *respectively. Therefore, it is easy to conclude that* η_2 *corresponds to a local maximum and should be discarded. Figure 4.8 show the meridian section of the three vessels.*

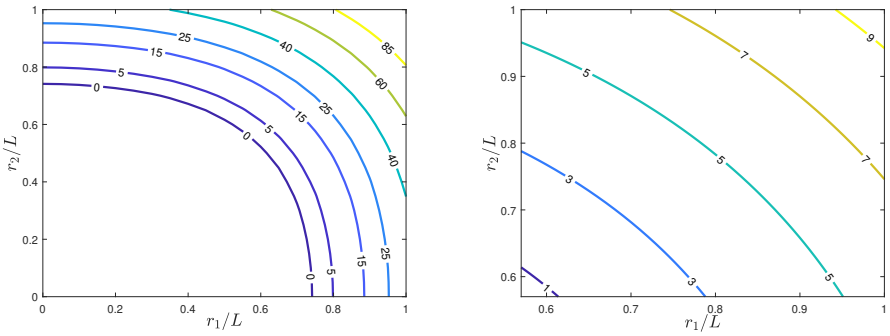

(a) (b)

Figure 4.7: Level lines of Δ_η (a) and η (b) for $m = 0.02$ and $\tau = 100$.

4.5 Minimum compliance vessels

The minimum compliance problem for membrane shells of revolution are considered in this section. Unlike Problems 4.1 and 4.2, the following problem is formulated for fixed standard and special meridian shapes, whereas the objective function is only the thickness distribution.

Problem 4.3. *Given the isoperimetric constraint*

$$2\pi\rho \int_0^L r(x)h(x)\sqrt{1+r'(x)^2}\,dx = \tilde{M}\,, \tag{4.66}$$

accounting for the weight of the shell, and the meridian shape $r(x)$, find the thickness distribution $h^*(x)$ which minimizes the compliance

$$\Phi = \frac{2\pi}{E}\int_0^L \left[\sigma_\varphi(x)^2 + \sigma_\theta(x)^2 - 2\nu\sigma_\varphi(x)\sigma_\theta(x)\right] r(x)h(x)\sqrt{1+r'(x)^2}\,dx\,, \tag{4.67}$$

being L, ν, E and ρ specified positive constants.

In order to avoid trivial solutions, the assumption that meridian profiles prescribed by

$$r_\theta(x) \neq k\,, \tag{4.68}$$

with k a constant, is made. This implies that cylindrical and spherical shells are not considered, where no optimization problem can be treated since the thickness is determined directly and uniquely from (4.66), once fixed $\tilde{M}$, ρ, L and the radius of the cylinder or the sphere.

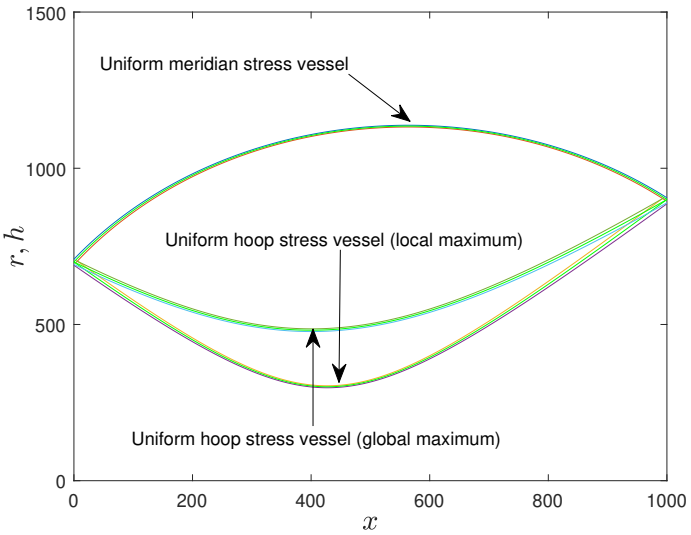

Figure 4.8: Meridian section of the three vessels considered in Example 4.3.

4.5.1 Optimal thickness distributions

Necessary conditions for minimizing (4.67) under geometrical constraints (4.66) are considered and optimal the thickness distribution is derived analytically. The augmented functional for fixed meridian shapes reads

$$\Phi^a = \Phi + \lambda \tilde{M} = \int_0^L G(h(x), x)\, dx\,, \tag{4.69}$$

where λ is the Lagrangian multiplier and

$$G(h(x), x) = \frac{2\pi}{E}[(\sigma_\varphi(x)^2 + \sigma_\theta(x)^2 - 2\nu\sigma_\varphi(x)\sigma_\theta(x)) + \lambda E\rho]r(x)h(x)\sqrt{1 + r'(x)^2}. \tag{4.70}$$

From (4.2), (4.8) and (4.9) it follows

$$\sigma_\varphi(x)^2 + \sigma_\theta(x)^2 - 2\nu\sigma_\varphi(x)\sigma_\theta(x) = \left(\frac{qr_\theta(x)\psi(x)}{2h(x)}\right)^2,$$

where

$$\psi(x) = \sqrt{\left(\frac{r_\theta(x)}{r_\varphi(x)} - 1\right)^2 + 2\tilde{\nu}\left(2 - \frac{r_\theta(x)}{r_\varphi(x)}\right)}$$

and $\tilde{\nu} = 1 - \nu > 0$. Note that for meridian profiles for which the ratio $\frac{r_\theta(x)}{r_\varphi(x)}$ tends to zero for all values of x, $\psi = \sqrt{1 + 4\tilde{\nu}} := \Psi$. Consequently, Equation

(4.70) may be recast as

$$G(h(x), x) = \frac{\pi q^2 r_\theta(x)^3}{2Eh(x)} \left(\psi(x)^2 + \frac{4\lambda E \rho h(x)^2}{q^2 r_\theta(x)^2} \right). \tag{4.71}$$

In order to find the solution to the optimization problem more easily, it is convenient to introduce the curvilinear coordinate t along the profile and express r and h as function of it. Hence, meridian profiles are given in parametric form, i.e., each of them is defined as the curve

$$x = x(t), \quad r = r(t)\,, \tag{4.72}$$

for given functions x and r and for $t \in [t_1, t_2]$.
By using (4.72), the augmented functional (4.69) can therefore be written as

$$\Phi^a = \int_{t_1}^{t_2} F\left(x(t), h(t)\right)\, dt\,, \tag{4.73}$$

with $F(h, x, \dot{x}) = G(h, x)\dot{x}$. The necessary condition for minimizing (4.73) is obtained considering the particular case where the integrand of the objective functional depends on the independent variable and the objective function and not on the derivative of this latter. The corresponding Euler-Lagrange equation will be (A.17), namely

$$\frac{\partial F}{\partial h} = 0\,, \tag{4.74}$$

which yields

$$-\frac{r_\theta(x)^2 \psi(x)^2}{h(x)^2} + \frac{4\lambda E \rho}{q^2} = 0 \tag{4.75}$$

or

$$h(x)^* = \pm \frac{1}{2} \frac{q r_\theta(x) \psi(x)}{\sqrt{\lambda^* \rho E}}\,, \tag{4.76}$$

where λ^* is obtained from (4.66). The sign of the right hand side term has to be chosen apposite to the sign of r_θ, that can be positive or negative, so that the optimal solution is always positive.

In the following, three different kinds of meridian profiles are considered: the conical shell, the elliptic shell and the Bezier end closure (see Figure 4.9, where a sample for each kind is depicted).

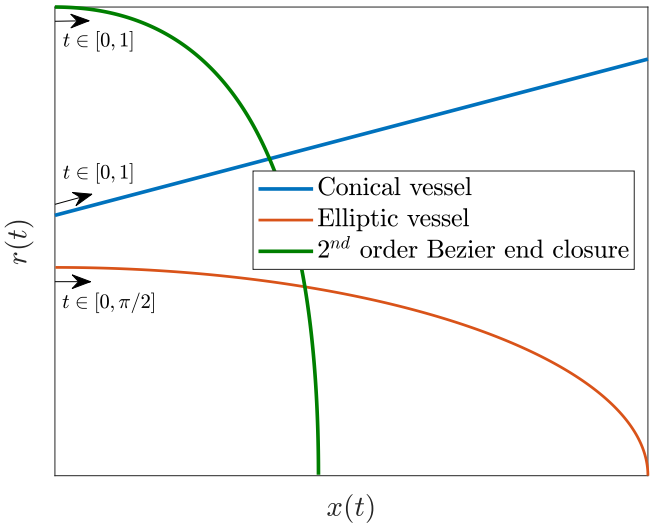

Figure 4.9: Graphical representation of the considered meridian shapes for Problem 4.3.

4.5.2 Three special cases

Conical shell

The meridian profile of a (truncated) conical shell of length L whose minimum and maximum radii are r_1 and r_2, respectively, is given by the parametric equations

$$x(t) = Lt\,, \quad r(t) = a + bt\,, \tag{4.77}$$

where $a = r_1$ and $b = r_2 - r_1$ and $t \in [0, 1]$.
Since $\frac{dr}{dx} = \frac{dr}{dt}\frac{dt}{dx}$, from (4.2) and (4.77) one obtains

$$r_\varphi \to \infty, \quad r_\theta(t) = \sqrt{1 + m^2}(a + bt)\,, \tag{4.78}$$

where $m = b/L$. Substituting into Equation (4.76), the optimal thickness distribution reads

$$h^*_{conical}(t) = -\frac{q\Psi}{2\sqrt{\lambda^* \rho E}}\sqrt{(1 + m^2)}(a + bt)\,. \tag{4.79}$$

Note that the optimal solution is linear with respect to t. Substituting (4.79) in (4.66), one obtains

$$\sqrt{\lambda^* \rho E} = \frac{\pi \rho q}{3\tilde{M}m}\Psi(1 + m^2)\left[a^3 - (a + b)^3\right]\,, \tag{4.80}$$

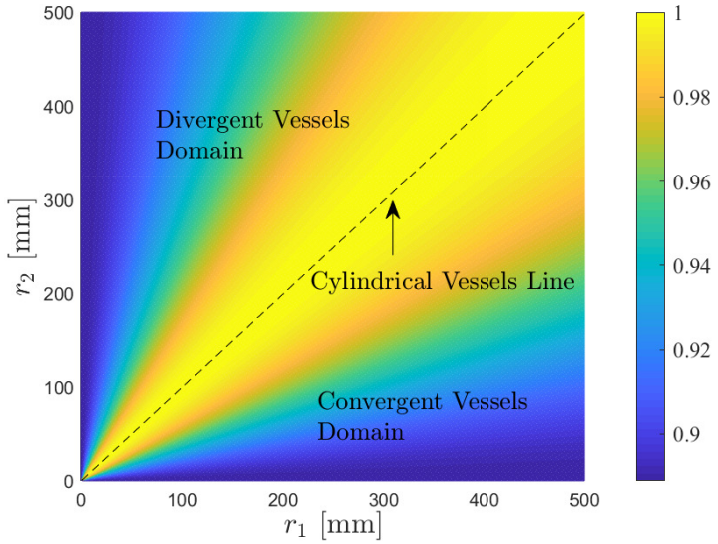

Figure 4.10: Contour levels of g for the conical shell.

and therefore

$$h^*_{conical}(t) = \frac{3\tilde{M}}{2\pi\rho}\frac{m}{\sqrt{1+m^2}}\frac{a+bt}{r_2^3 - r_1^3}\,. \tag{4.81}$$

Substituting (4.81) in (4.67) one obtains the associated optimal compliance

$$\Phi^*_{conical} = \frac{\pi^2\Psi q^2\rho}{9E\tilde{M}m^2}(1+m^2)^2(r_2^3 - r_1^3)^2, \tag{4.82}$$

and the compliance gain g, defined as the ratio between the optimal compliance Φ^* and the compliance of the constant-thickness vessel of the same mass Φ^c, will given by

$$g = \frac{8}{9}\frac{(r_1^2 + r_1r_2 + r_2^2)^2}{(r_1+r_2)^2(r_2^2+r_1^2)}\,, \tag{4.83}$$

whose minimum tends to $8/9(\approx 0.88)$ for either $r_1 \to 0$ or $r_2 \to 0$, as shown in Figure 4.10 for suitable ranges of $r_1 \times r_2$. The dashed line represents the cylindrical vessels domain, where $g = 1$ identically (see Equation 4.68). Note that *convergent* ($r_1 > r_2$) and *divergent* ($r_1 < r_2$) vessels have symmetric behavior, with respect to the dashed line, in terms of g.

Example 4.4. *Consider the divergent conical vessel with* $r_1 = 100$ *mm,* $r_2 = 200$ *mm,* $L = 500$ *mm,* $\tilde{M} = 3$ *kg,* $\nu = 0.3$ *and* $\rho = 7800$ *kg/m*^{3}*. The*

optimal thickness is an increasing linear function with $h^*|_{t=0} = 0.5145$ *mm and* $h^*|_{t=1} = 1.029$ *mm and the compliance gain is* $g = 0.9679$.

Elliptic shell

In this case the meridian profile is expressed in parametric form as

$$x(t) = A\sin t, \quad r(t) = B\cos t\,, \tag{4.84}$$

where A and B are the semi-axes and $t \in [0, \frac{\pi}{2}]$, due to symmetry considerations, while the principal radii are given by

$$r_\varphi(t) = \frac{1}{AB}\mu^3(t), \quad r_\theta(t) = \frac{B}{A}\mu(t). \tag{4.85}$$

where

$$\mu(t) = \sqrt{A^2\cos^2 t + B^2\sin^2 t}\,.$$

From (4.85), Equation (4.76) gives

$$h^*_{ellipse}(t) = \frac{Bq}{2A\sqrt{\lambda^*\rho E}}\sqrt{\eta(t)}, \tag{4.86}$$

where

$$\eta(t) = \frac{(B^2 - A^2)^2\cos^4 t}{\mu^2(t)} + 4\tilde{\nu}(A^2 - B^2)\cos^2 t + 2\tilde{\nu}B^2\,.$$

The Lagrangian multiplier λ^* can be obtained substituting (4.86) in (4.66), leading to

$$\sqrt{\lambda^*\rho E} = \frac{\pi\rho q B^2}{A\tilde{M}}I_1, \tag{4.87}$$

where $I_1 = \int_0^{\pi/2}\mu(t)\sqrt{\eta(t)}\cos t\,dt$ and therefore

$$h^*_{ellipse}(t) = \frac{\tilde{M}}{2\pi\rho B I_1}\sqrt{\eta(t)}\,. \tag{4.88}$$

Substituting (4.88) in (4.67) one obtains the associated optimal compliance

$$\Phi^*_{ellipse} = \frac{\pi^2 q^2\rho B^4 I_1^2}{E\tilde{M}A^2} \tag{4.89}$$

and the compliance gain in comparison with that of the constant-thickness vessel of the same mass is given by

$$g = \frac{I_1^2}{I_2 I_3}\,, \tag{4.90}$$

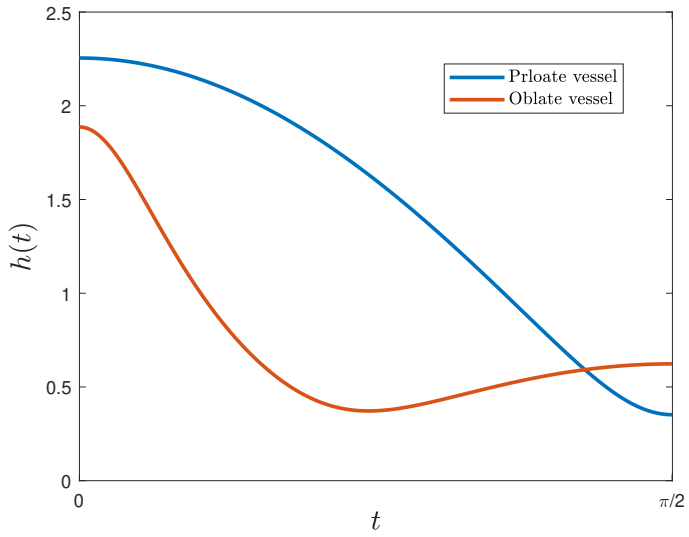

Figure 4.11: Optimal thickness distribution for the prolate (solid line) and oblate (dashed line) vessels considered in Example 4.5.

where $I_2 = \int_0^{\pi/2} \mu(t) \cos t \, dt$ and $I_3 = \int_0^{\pi/2} \mu(t)\eta(t) \cos t \, dt$.

Contour levels of g are depicted in Figure 4.12. The dashed line indicates the spherical vessel, where no optimization of the thickness distribution has been performed according to (4.68), namely $g = 1$. It is worth to draw a special attention to the absence of symmetry in terms of compliance reduction of *prolate* ($A > B$) and *oblate* ($A < B$) vessels with respect to the dashed line. Optimal oblate vessels show more significant compliance reduction than prolate vessels, both with respect to constant-thickness counterparts of the same mass. The following example is performed in order to highlight this result.

Example 4.5. *Consider the prolate and oblate vessels with semi-axes* 400 *mm and* 100 *mm,* $\tilde{M} = 3$ *kg,* $\nu = 0.3$ *and* $\rho = 7800$ *kg/m*^{3}*. The distribution of optimal thicknesses given by Equation (4.88) is shown in Figure 4.11. While* $g = 0.9573$ *in the prolate vessel (*$A = 400$ *mm and* $B = 100$ *mm), g reaches* 0.7416 *in the oblate one (*$A = 100$ *mm and* $B = 400$ *mm), demonstrating that oblate vessels with variable thickness presents a significant compliance reduction with respect to its constant-thickness counterpart (see Figure 4.12).*

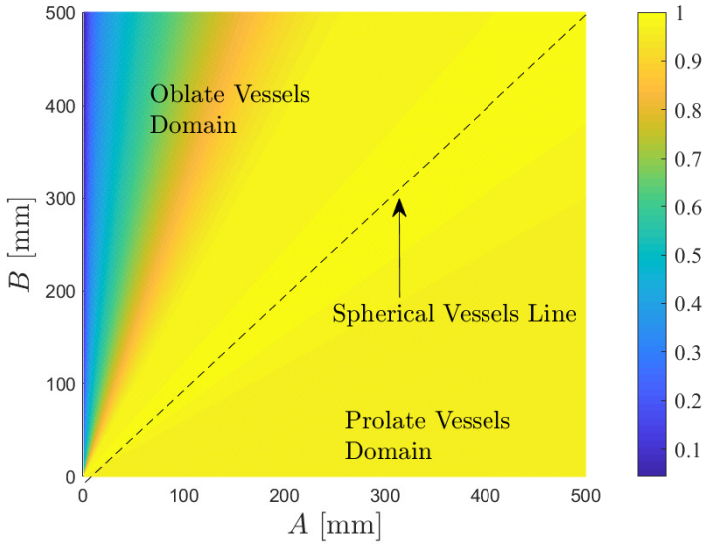

Figure 4.12: Contour levels of g for the elliptic shell.

Bezier curve end closure

Cylindrical pressure vessels can be closed at the ends by different types of closures. Traditional end closures, for instance the convex torispherical, ellipsoidal or hemispherical heads, present a discontinuity of meridian curvatures at the junction, disturbing the membrane stress state and influencing the strength of such structures. To avoid these latter disturbances, nonstandard designs for end closures have been recently gaining much attention. In particular, end closures described by generalized ellipses, Bezier curves, Cassini curves and Booth curves are employed.

For brevity, only Bezier curve end closure are considered. The parametric description of this latter in $\mathbb{R}^2$ is defined by

$$\mathbf{B}(t) = \sum_{i=0}^{n} \frac{n!}{i!(n-i)!} t^i (1-t)^{n-i} \mathbf{P}_i \,, \tag{4.91}$$

where $t \in [0,1]$, $\mathbf{P}_0$,..., $\mathbf{P}_n$ are called the *control points* and n is the *order* of the curve. The first and last control points are always the end points of the curve; however, the intermediate control points (if any) generally do not lie

on the curve. In the following, a Bezier curve defined by a polynomial form

$$\mathbf{B}(t) = \sum_{j=0}^{n} \mathbf{C}_j t^j \,, \tag{4.92}$$

where

$$\mathbf{C}_j = \frac{n!}{(n-j)!} \sum_{i=0}^{j} \frac{(-1)^{i+j} \mathbf{P}_i}{i!(j-i)!}$$

is considered. Letting $\mathbf{C}_j = (\xi_j, \rho_j)$ for $j = 0, 1, ..., n$, the projection of the curve $\mathbf{B}(t)$ on the x- and r- axes leads to the two parametric polynomials

$$x(t) = \sum_{j=0}^{n} \xi_j t^j, \quad r(t) = \sum_{j=0}^{n} \rho_j t^j \,, \tag{4.93}$$

with $t \in [0, 1]$. Denoting by $\dot{x}(t) = \frac{dx(t)}{dt}$ and $\dot{r}(t) = \frac{dr(t)}{dt}$ and omitting the dependence of t, the principal radii are given by

$$r_\theta = \frac{r}{\dot{x}} \sqrt{\dot{x}^2 + \dot{r}^2} \,, \quad r_\varphi = -\frac{\left(\dot{x}^2 + \dot{r}^2\right)^{3/2}}{\dot{x}\ddot{r} - \dot{r}\ddot{x}} \,, \tag{4.94}$$

and substituting in (4.76) one obtains

$$h^*_{Bezier} = \frac{qr}{2\dot{x}\sqrt{\lambda^* \rho E}} \sqrt{\dot{x}^2 + \dot{r}^2} \sqrt{\beta^2 + 2\tilde{\nu}(\beta + 1)} \,, \tag{4.95}$$

where

$$\beta = \frac{r(\dot{x}\ddot{r} - \dot{r}\ddot{x})}{\dot{x}(\dot{x}^2 + \dot{r}^2)} \,.$$

Substituting in (4.66) and after basic arrangements one obtains

$$h^*_{Bezier} = \frac{\tilde{M}}{2\pi\rho J_1} \frac{r}{\dot{x}} \sqrt{\dot{x}^2 + \dot{r}^2} \sqrt{\beta^2 + 2\tilde{\nu}(\beta + 1)} \,, \tag{4.96}$$

where

$$J_1 = \int_0^1 \frac{r(t)^2}{\dot{x}(t)} \left(\dot{x}(t)^2 + \dot{r}(t)^2\right) \sqrt{\beta(t)^2 + 2\tilde{\nu}(\beta(t) + 1)} \, dt \,.$$

Substituting (4.96) in (4.67) one obtains the associated optimal compliance

$$\Phi^*_{Bezier} = \frac{\pi^2 q^2 \rho J_1 J_2}{E\tilde{M}} \,, \tag{4.97}$$

where

$$J_2 = \int_0^1 \frac{r(t)^2[\beta(t)^2 + 2\beta(t)(1 + \tilde{\nu}) + 1 + 4\tilde{\nu}]}{\dot{x}(t)\sqrt{\beta(t)^2 + 2\tilde{\nu}(\beta(t) + 1)}} \, dt \,.$$

Example 4.6. *Consider the end closure of* $\tilde{M} = 2\ kg$, $\nu = 0.3$ *and* $\rho = 7800\ kg/m^3$, *whose meridian profile is described by a quadratic Bezier curve given by (see Figure 4.13a where the curve is depicted together with the standard elliptic end closure with* $A = 80\ mm$ *and* $B = 180\ mm$*)*

$$x(t) = -80t^2 + 160t\,, \quad r(t) = -180t^2 + 180\,. \tag{4.98}$$

Optimal thickness distribution is shown in Figure 4.13b (solid line) and compared to the optimal thickness distribution in case of an elliptic end closure (dashed line) of the same mass.

Despite of the practical similitude of the meridian profiles in Example 4.6 (Figure 4.13a), note their optimal thicknesses are totally different (Figure 4.13b).

4.6 Towards printed prototypes: Preliminary results

It is worth noting that optimal thicknesses associated with the previous problems continuously vary, in contrast with that usually obtained by means of optimization numerical algorithms, where the thickness varies in step-wise fashion. This may represent an engineering challenge from the realization viewpoint, since the proposed shapes seems unfeasible with the usual manufacturing process. Nevertheless, the availability of last generation metal additive manufacturing techniques shed a new light on this approach. These novel manufacturing techniques indeed have led to many opportunities in fabricating complex and novel products. In addition, the increase of printable materials and the emergence of novel fabrication processes continuously expand the possibility to create complex geometries with acceptable dimensional precision and with reduced defects.

In [64], the state-of-the-art developments in the design for additive manufacturing (AM) and structural optimization was presented. Moreover, topology optimization by means of density-based approaches, cellular structures and graded lattices were thoroughly reviewed. It was finally observed that the main challenge for the future is the development of optimized solutions for common engineering problems characterized by low computational costs. In the more specific field of pressure vessels design and optimization, additive technology has been rarely used. In [65], AM was used to construct test capsule made of a mixture of glass and nylon particles successively coated. Nevertheless, an optimized design

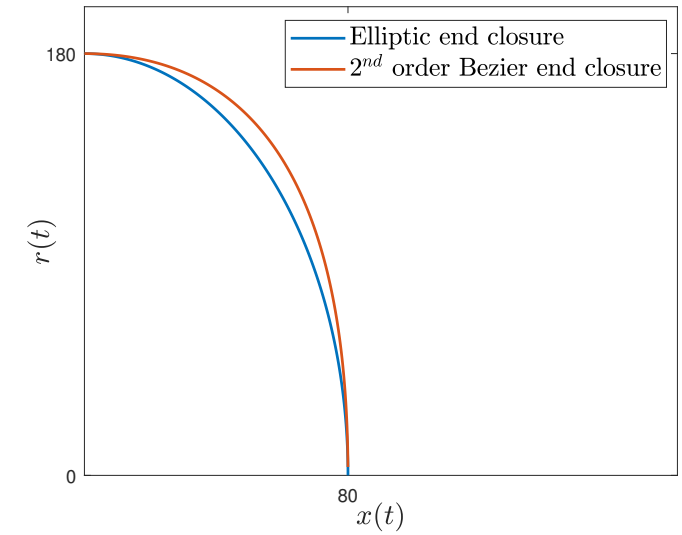

(a)

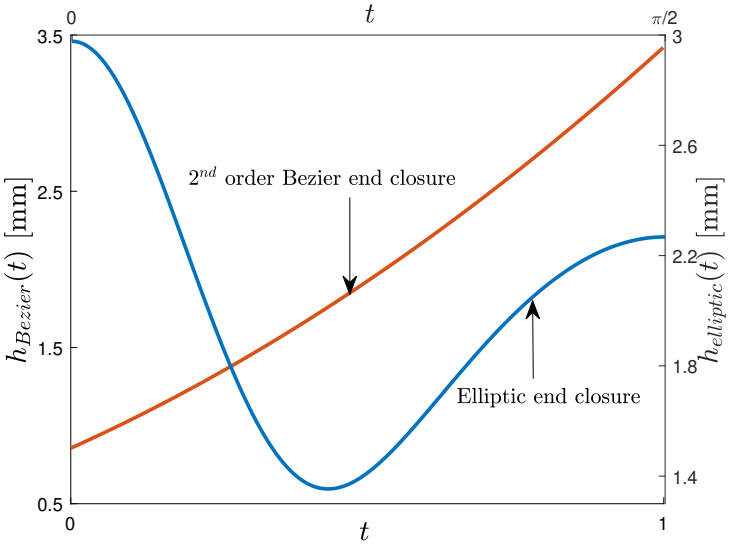

(b)

Figure 4.13: Meridian shapes (a) and optimal thickness distributions (b) of the second-order Bezier cure (solid) and elliptic (dashed) end closures considered in Example 4.6.

was not performed and the capsule exhibited the usual cylindrical shape with hemispherical ends. The use of AM to obtain pressure vessel of unconventional shape with reduced weight was proposed in [66]. In that case, a manual trial and error procedure was adopted by using a commercial FE code in which material in the lower and higher stressed regions was removed and added, respectively. This method showed promising results in terms of weight reduction. However, the proposed method is not an optimization procedure and moreover the feasibility of the proposed vessel geometries was not verified by manufacturing a demonstrator. Recently, the use of AM to re-design a pressure reducer valve integrated into an end-cap as a subcomponent of composite pressure vessel was proposed in [67]. Prototypes were constructed and relationship between manufacturing process and required geometrical tolerances were analyzed.

In agreement with the aim of performing only a preliminary feasibility study, a technological demonstrator consisting of a halved minimum mass vessel without nozzles is chosen and printed by metal additive manufacturing. In particular, among the possible geometries, a prolate ellipsoid with $\alpha = 0.4$, $L = 150$ mm, $(\sigma_* - q)/q = 9$ and a thickness distribution fulfilling case 2 and condition (4.1) is chosen. This solution was chosen in order to characterize the geometry of the printed halved ellipsoid and to verify whether the manufacturing process is adequate to obtain the desired thickness distribution. Although no functional testing of a complete vessel has been planned at this preliminary stage, the geometry of the real manufactured vessel will be recast by a finite element (FE) model which will be used to assess whether its geometry respects integrity constraints.

4.6.1 3D printing of the technological demonstrator

The production of the conceptual prototype was performed with the selective laser melting (SLM) technology. Combining high accuracy with high mechanical performance, this technique is one of the most used AM technologies for metals. The material used to produce the prototype was 316 L stainless steel, which might be suitable for this application due to its high corrosion-resistance, excellent strength and high ductility. The characteristics of the 316 L powder are given in Table 4.2 and Figure 4.14a The powders were characterized by scanning electron microscope (SEM) (see Figure 4.14b). The grains had a spherical shape, which is typical of gas-atomized powder. The particle size distribution had a slight positive skewness with a median diameter value of 28.64 μm, while the 10th and 90th percentile were 18.27 μm and 44.93 μm, respectively. It is worth noting

Element	Fe	Cr	Ni	Mo	Mn	Si	P	C	S
% weight	Bal.	17.7	12.6	2.35	1.14	0.61	<0.045	0.025	0.004

Table 4.2: Chemical composition of the 316 L stainless steel used for the prototype production.

that according to [68], 316 L stainless steel samples obtained by SLM show an isotropic behavior up to yielding. Such result confirms the linearity and isotropy assumptions made on the material in the formulation of the optimization problem.

Concerning build job preparation, the CAD file was converted to Standard Triangulation Language (STL) format and then imported in Magics RP software for STL model correction, part positioning and orientation, support structures generation and slicing operation. A view of the build job can be seen in Figure 4.15a. It is worth noting that the part was oriented with an angle of 45° with respect to the build platform (see Figure 4.15b). This choice was suggested by experience in order to achieve a good compromise between the required production time and the expected surface quality. The total height of the part is indeed reduced with respect to the vertical orientation. As a consequence, the total number of powder layers required to complete the job are considerably reduced as well. Furthermore, with the selected orientation, no supports were needed in the inner surface of the component. However, in case of 3D-printing of the complete vessel, some internal support structures should be added.

In a preliminary phase a bulk sacrificial sample was 3D printed by adopting the same process parameters used for the production of the semi vessel. Archimedes' tests were then carried out on this sample, proving its high relative density (about 99.9%). The absence of large pores or voids was also assessed by analyzing its microstructure through a cross section view that was aligned with the vertical direction and that was orthogonal to the laser beam trajectories, which is reported in Figure 4.16a. The obtained final prototype is shown in Figure 4.16b.

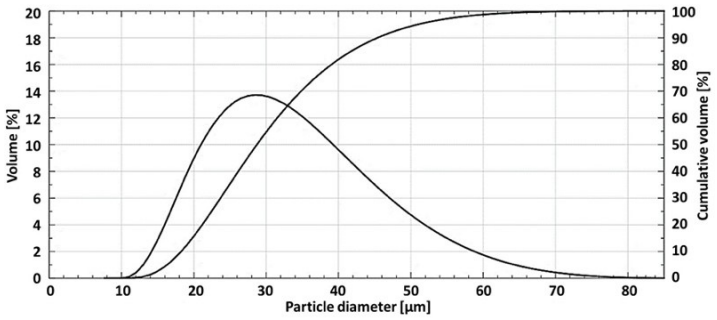

(a)

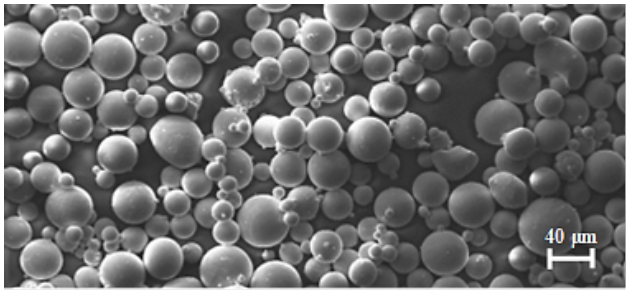

(b)

Figure 4.14: Progressive and cumulative distribution (a) and SEM view of the 316 L stainless steel powder (b).

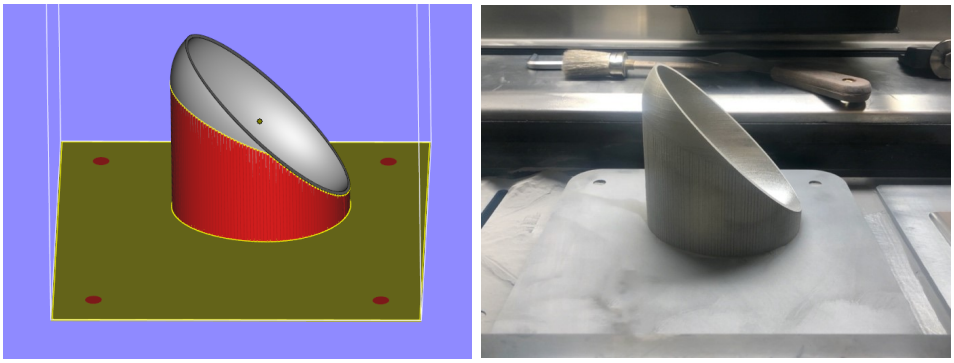

(a) (b)

Figure 4.15: View of the build job created with Magics RP (a) and view of the component after production (b).

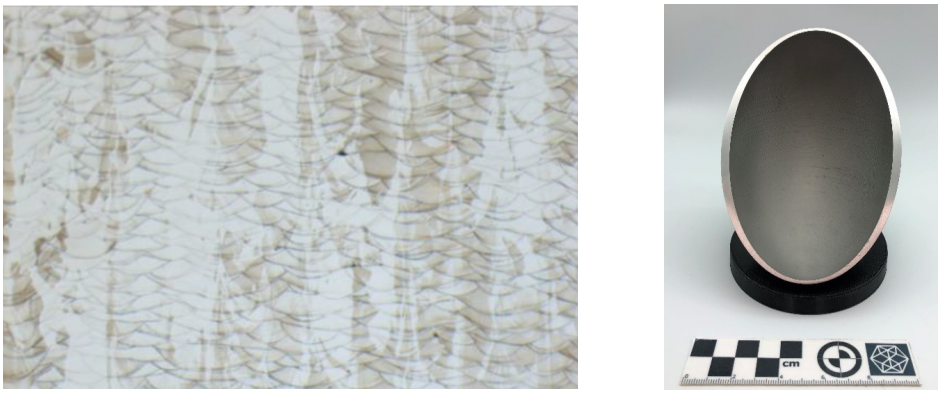

(a) (b)

Figure 4.16: Metallographic analysis of a sacrificial AISI 316 L sample (a) and final prototype of the optimized semi vessel (b).

4.6.2 Scanner measurement and reverse engineering

A 3D laser scanner measuring system (Hexagon RS5 Laser Scanner) was then used to perform a quantitative analysis of the error induced by the manufacturing process on the geometry of the prototype (see Figure 4.17a). The work piece topography was captured with the 3D scanner to describe the vessel geometry by a cloud of points (see Figure 4.17b, where about 18 million points were captured and successively elaborated by means of the ad-hoc codes to assess the accuracy of the manufacturing process).

In order to be coherent with the notation proposed in the previous sections, in the following measurement results are presented by considering different sections of the vessel, identified by the azimuth angle $\theta \in [0, \pi]$ describing a plane passing through the x-axis of the shell (see Figure 4.18). For each section the position of a generic point of the profile is defined by means of the x coordinate or considering the angle $\gamma \in [0, \pi]$ defined between the x-axis and the line passing through O' lying on the plane defined by θ.

Figure 4.19a shows the measured points superimposed to the theoretical profiles (internal and external) for $\theta = 0$ and $\theta = \pi$, while Figure 4.19b reports the corresponding normalized error $e_{r,m} = e_m/L$ measured at the internal and external surfaces, where e_m is the difference between theoretical and real profiles. Results are quite satisfactory: Only close to the ends an error of 0.4% of the axial length L is observed, whereas the remaining portion presents an error less than 0.2%. Similar results are obtained in the case $\theta = \pi/2$ (see Figures 4.20a and 4.20b).

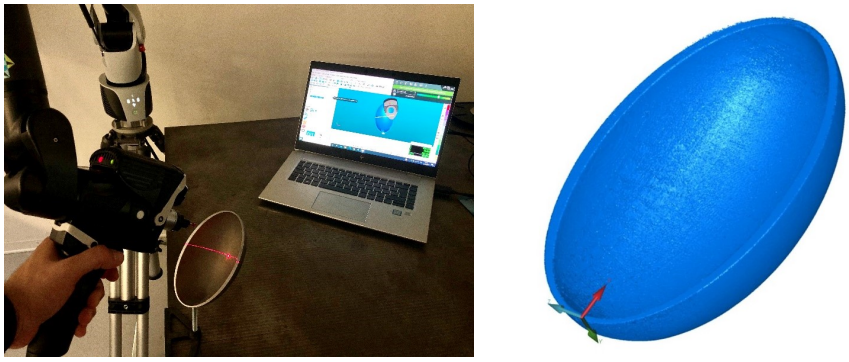

(a) (b)

Figure 4.17: Scanner measurement system (a) and its output consisting in the cloud of points describing the vessel geometry (b).

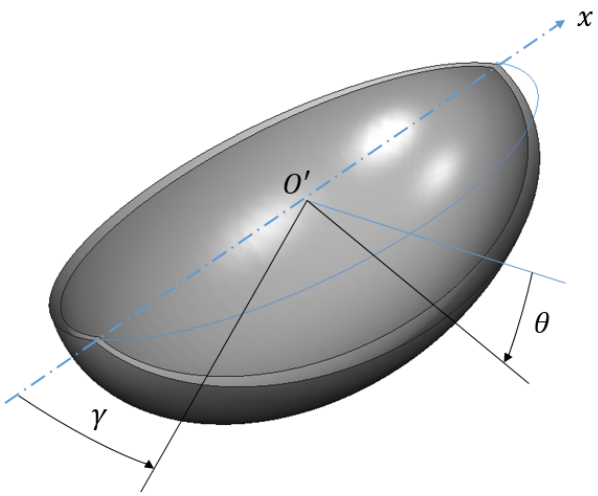

Figure 4.18: System of reference adopted to represent the scanner measurements.

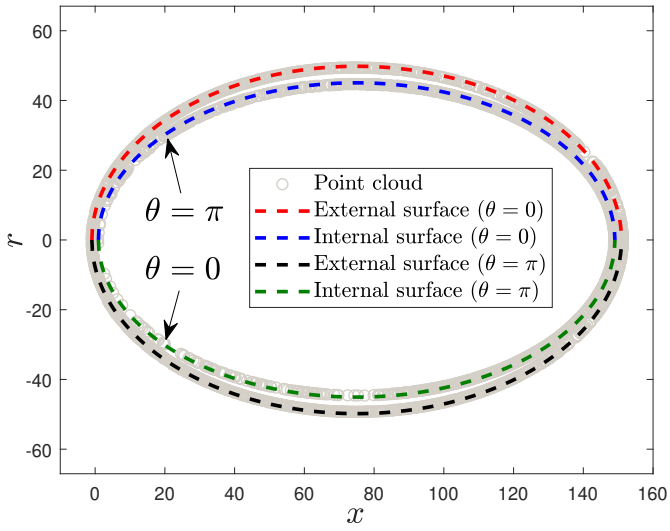

(a)

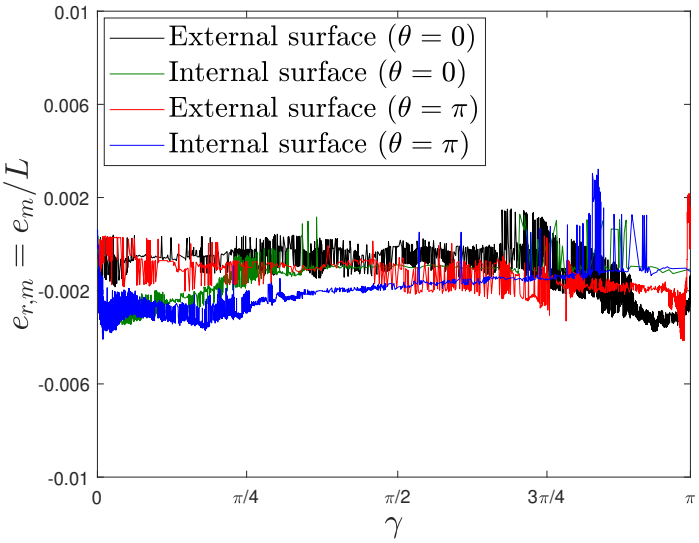

(b)

Figure 4.19: Measured points for internal and external theoretical profiles (a) and associated normalized errors $e_{r,m}$ (b) corresponding to $\theta = 0, \pi$.

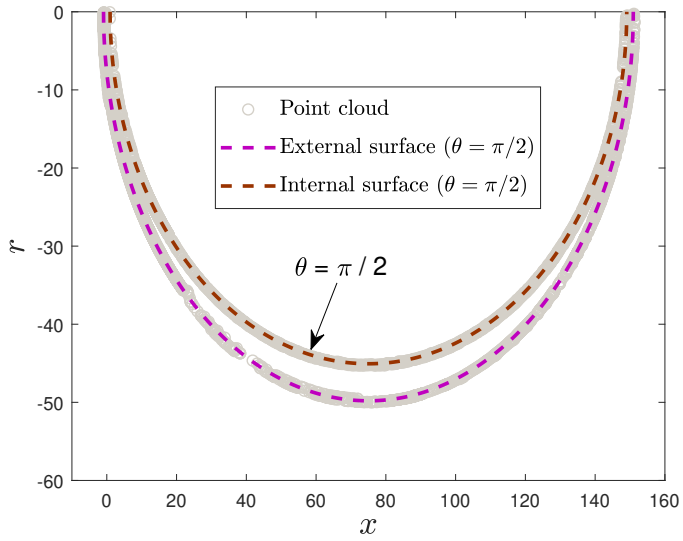

(a)

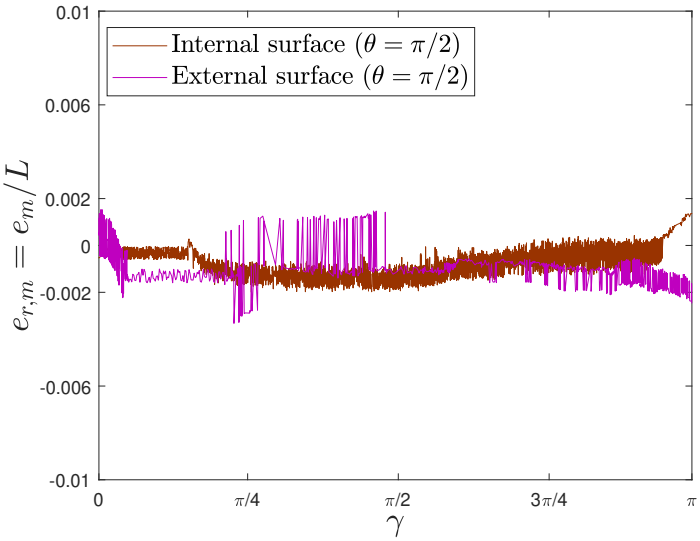

(b)

Figure 4.20: Measured points for internal and external theoretical profiles (a) and associated normalized errors $e_{r,m}$ (b) corresponding to $\theta = \pi/2$.

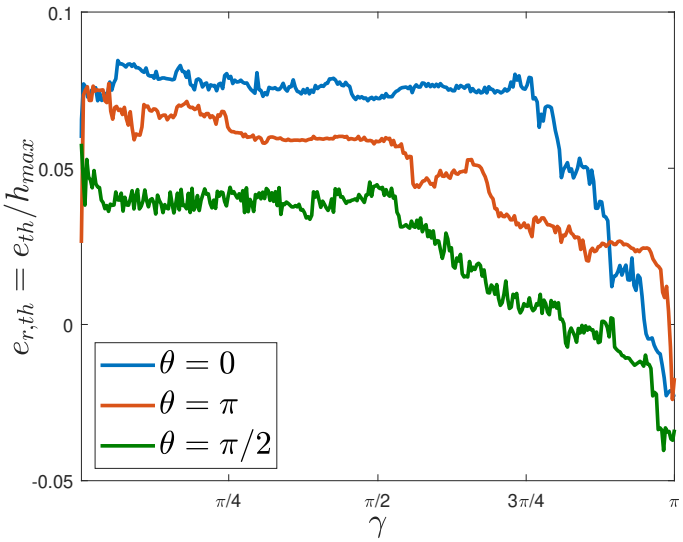

Figure 4.21: Thickness normalized error $e_{r,th}$ for the three considered sections ($\theta = 0, \pi/2, \pi$).

Finally, in Figure 4.21 the thickness normalized error $e_{r,th}$ is reported, which is defined as

$$e_{r,th} = \frac{(e_{r,me} - e_{r,mi})}{h_{max}} L \tag{4.99}$$

where $e_{r,me}$ and $e_{r,mi}$ are the meridian profile normalized errors associated with the external and internal surfaces, respectively, and h_m is the maximum value of the theoretical thickness, given by Equation (4.1). It can be observed that in this case the normalized error is obviously higher, nevertheless it is always lower than 8%. Comparing the three sections, a similar behavior is observed, with maximum positive errors close to the left end, that remain quite constant up to the middle point and subsequently decrease up to a negative error around 3%.

In the light of the above results, the theoretical optimization procedure described in the previous sections can be successfully implemented by using an additive manufacturing process. Nevertheless, for a final check, a linear elastic FE analysis by considering the real geometry of the obtained vessel prototype was also carried out. As Figure 4.21 clearly shows, the errors pattern is almost uniform with respect to the angle θ. It can be concluded that the final shape of the actual vessel is almost axisymmetric with respect to the x-axis and thus a plane axisymmetric FE model can

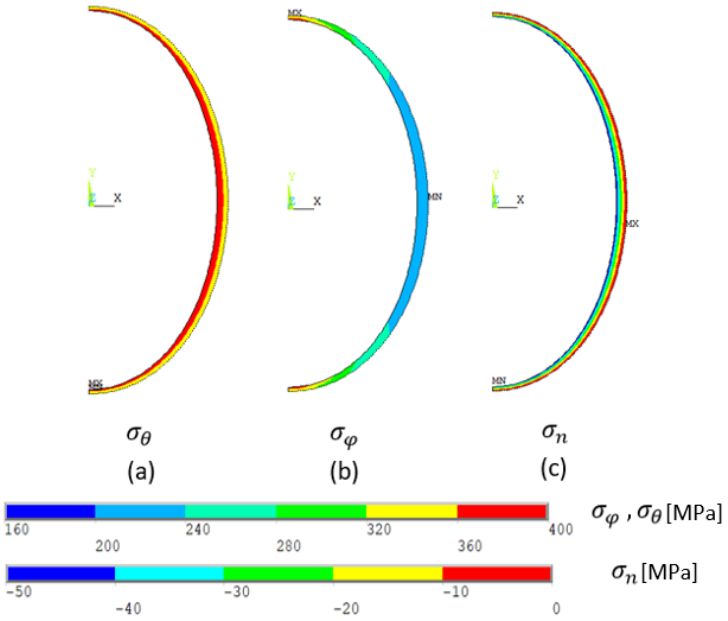

Figure 4.22: FE results for hoop (a), meridian (b) and normal (c) stresses in the vessel prototype.

be adopted. In particular, the internal and external actual profiles were interpolated with a series of high order spline functions and a mapped mesh made with axisymmetric quadrilateral element with 8 nodes was generated. Convergence is fully achieved by using 4 elements along the thickness with an aspect ratio always lower than 1.2. A model with 2806 nodes and 800 elements was finally obtained. Figure 4.22 shows the hoop, meridian and normal stresses in absolute values when the applied pressure is 50 MPa, while Fig. 4.23 reports the results of a comparison between the results obtained with the theoretical profile and the real one in terms of the normalized stress deviation defined as

$$\Delta\sigma_k = \frac{\sigma_{theo,k} - \sigma_{real,k}}{\sigma_{theo,k}}, \quad k = \theta, \varphi \tag{4.100}$$

where $\sigma_{theo,k}$ and $\sigma_{real,k}$ denote stresses obtained at the neutral surface with the theoretical and real profiles, respectively.

Figure 4.23 shows the comparison between theoretical and FE results in terms of hoop and meridian stresses which were assessed considering the nodes corresponding to the neutral surface. Such stress values are slightly

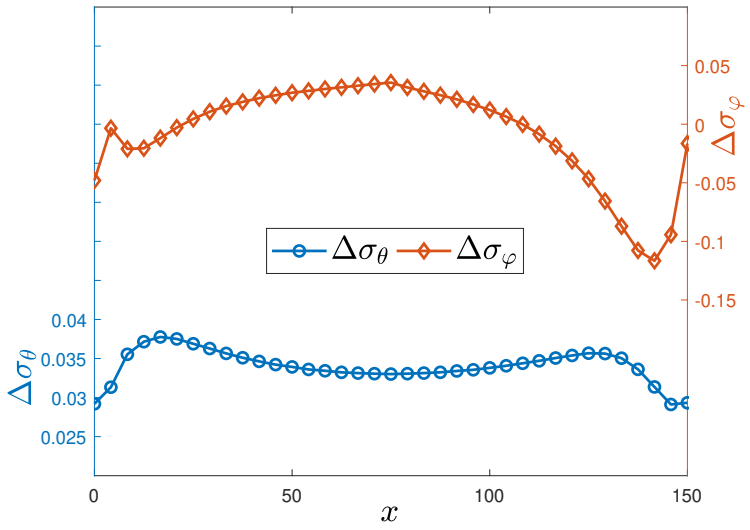

Figure 4.23: Normalized stress deviation between FE and theoretical results.

lower (less than 2%) with respect to those occurring at the inner surface and thus this approach was adopted, even if less conservative from a design point of view, to be coherent with the optimization stress constraints. In the actual structure also the meridian stress σ_φ shows a quite moderate deviation from the theoretical values, with a normalized error always lower than 1.5% (Figure 4.23, plot with rhombi). Nevertheless, the most significant results concern the hoop stress σ_θ. As already pointed out, the optimization criterion was in this case implemented according to case 2 condition, which should guarantee the uniformity of the hoop stress along the whole domain. As Figure 4.23 clearly shows (see the plot with circles), this condition is very well fulfilled, with a maximum normalized error (with respect to the theoretical value) of about 3.5%, but with a deviation from the mean value along the profile of less than 0.5%.

The achieved results are promising, albeit many problems are still open and require further investigation. First of all, in order to pursue the final objective of obtaining the complete vessel, the obvious solution of joining together two halves has to be compared with the more challenging approach of making use only of AM technologies. In the latter case, however, an internal support structure should be added and its influence, both in the mechanical behavior and in the inevitable weight augmentation and cavity

volume reduction, has to be taken into account.

Another important aspect to be considered is the need of integrating the optimized vessel with nozzles. This aspect could be solved by a local numerical optimization procedure, as illustrated in [69]. Besides, an accurate characterization of the mechanical properties of the AM material under cyclic loading conditions would be also required, e.g., by studying the microstructure and porosity induced by the technological process. Some data have been recently made available in literature, e.g., [70]. Moreover, the development of suitable surface post-treatment is also in progress (e.g., see [71]) to improve the irregular surface morphology.

Finally, many technological constraints still limit the applicability of the proposed procedure from an industrial viewpoint. Main reasons are the limitation of component dimensions due to the actual size of the powder bed, the need of additional supporting structures for external or internal part surfaces having an inclination below 45° with respect to the building platform, the long production times and the high production costs associated with modern metal AM techniques.

4.7 Summary

In this chapter, three optimization problems concerning membrane shells of revolutions have been formulated and solved. The main decision variables were the meridian profile and/or the thickness distribution, whereas the material mass, cavity volume and compliance play interchangeably the roles of cost functionals and constraints. The application of calculus of variations theorems and Pontryagin's Principle luckily led to closed form solutions and prompt design charts of ample validity. Necessary conditions for optimality revealed that optimal solutions depend on geometrical and load considerations. These aspects have been thoroughly discussed for all the encountered problems. Although original formulations take into account vessels made of brittle or quasi-brittle materials, it has been also shown that the extension to cases where ductile materials are used can be equivalently handled. Furthermore, an optimized solution has been chosen and preliminary results towards the manufacturability of the resulting nonstandard forms by means of metal additive technology have been discussed. Eventually, the technological demonstrator has been subject of scanning measurement, finite element based validation and rugosity evaluation, showing promising results.

Chapter 5

Straight and curved elastic beams

5.1 Introduction

Beams are among the most important classical structural components and are, therefore, subject of many well established analytical results, as well as design methods, available in the literature. In engineering, models of beams are of several types, depending on the nature of boundary conditions and applied loads. Although many classical textbooks treat the statically determinate (or *isostatic*) case, many researchers still investigate their static and dynamic behaviors, straight and initially curved [72, 73, 74, 75, 76, 77]. As far as straight beams are concerned, the search for the optimal shapes of beams under various loading conditions has a relatively long history dating back at least to the Sixties [78, 79]. Candidates for objective functionals and constraints vary from the weight, stiffness, to buckling loads and maximum induced stresses.

For instance, solutions to weight-constrained stiffness maximization are commonly referred to as *Michell structures* [80]. The stiffness maximization may possibly be attained either by taking the maximum deflection or the mean compliance as goal functionals to be minimized. Notwithstanding an idea on the stiffness is more likely given by the former approach, many good results in the literature have been attained by considering the latter (see, e.g., [81, 82, 83, 84, 85]). In [86], in fact, the former objective functional has been considered for cantilever beams and it has been shown that the free end deflection decreases by an extra 10% in comparison with the one obtained by minimizing the mean compliance. Yet, optimal solutions associated

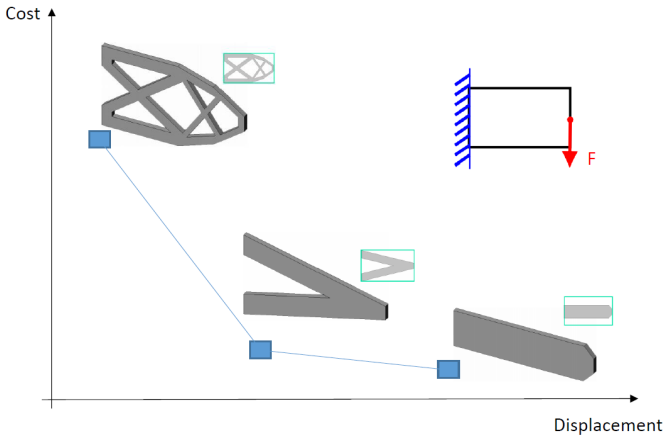

Figure 5.1: An illustrative cost-displacement diagram for three possible solutions for a cantilever beam loaded with a force at the free end.

with the mean compliance minimization problems are uniform along the beam axis as reported in [87] for weight-constrained cantilevers subject to distributed loads. Moreover, it has been shown that optimal cross sectional area distributions are equivalent to those obtained by (weight-constrained) maximum stress minimization.

Currently, the above mentioned structural optimization problems are solved mostly by using topology optimization (TO), which relies on FE simulations to evaluate the design performance. The design is optimized using either deterministic mathematical programming techniques or non-deterministic algorithms (such as neural networks or genetic algorithms) [88]. The computational burden associated with TO is often also accompanied with serious manufacturing issues due to the free forms that naturally occur [22]. Actually, in some cases the results can be implemented using only additive manufacturing. These considerations are highlighted in Figure 5.1 (inspired from [89]) where a cost-performance diagram for three possible solutions of a simple cantilever beam subjected to a force at the free end is shown: The three candidates have the same mass but the candidate with the best performance has the highest realization cost. To bypass these issues, different solutions may be adopted. One of the classical approaches is to consider *nonuniform* beams, namely beams with variable bending rigidity along the beam axis which may provide a better or more suitable distribution of mass and strength and therefore can meet special functional requirements. Herein lies the idea of variable cross sectional area

leads to a structure that represents a trade-off between performances and realization costs. Exploiting the one-dimensional nature of the beam, the resulting optimization problem can be addressed and may be analytically solved. Similar research can be found in the literature even though they impose different objectives and constraints [90, 91] or using multi-objective optimization [92, 93]. In the first part of this Chapter, Euler-Bernoulli isostatic beams subject to linearly distributed loads are considered, where the objective is to maximize the structural stiffness by reducing the mean compliance, which is computed as a distributed cost associated with the elastic energy along the beam axis. Optimal solutions are obtained by means of calculus of variations, constituting a peculiar advantage of the analytical approach for problems in mechanics as well as benchmark examples when employing TO for beam-like structures.

Another cost functional may be the first mode buckling load for elastic beams. The problem of determining the shape of compressed beam which has the largest Euler buckling load was formulated by Lagrange in 1773. In [94], a solution for a simply supported beam of circular cross section has been proposed, yet it did have points where the cross section vanishes, inducing infinite stresses in these points. Apparently, it seems that the first work which went beyond this theoretical solution is in [95], proposing a more practical one, where a constraint on the minimal value of the cross sectional area so that given limiting stresses are not exceeded is added. Since then, many results of structural optimization in the realm of beam theory have been addressed considering different load and boundary conditions [96, 97, 98, 99, 100, 101, 102, 103, 104, 105]. Besides, other works abandoned elastic constitutive laws in favor of simpler expressions for resultant forces and moments in terms of extension, curvatures and torsion. According to this line, many attempts posed Lagrange's problem (and other variants) within a generalized plane theory, namely including shear and compressibility effects [106] and when Eringen's nonlocal elasticity hypothesis is taken into account [107, 108]. As far as necessary conditions for optimal solutions are concerned, Pontryagin's Principle and calculus of variations have been considerably exploited. However, the cumbersomeness of the resulting systems of equations hinders one to derive analytical solutions, so that the use of numerical integration methods results mandatory. Hence, the orthogonal collocation method previously described in Chapter 3 is used for the determination of the solution numerically.

The third part concerns with the weight minimization of curved beams through a paradox recently stated and formulated in [109] for curved beams subjected to bending moment and normal force. The paradox consists in

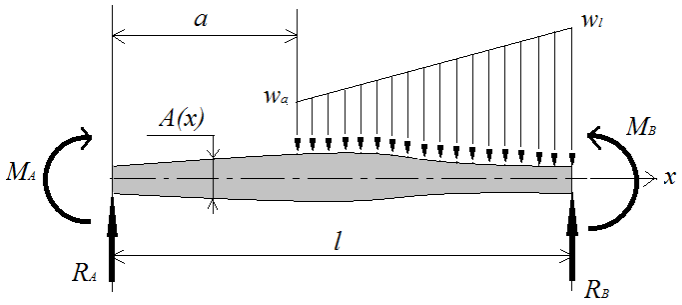

Figure 5.2: Generic nonuniform beam with partial linear distributed load. Definition of parameters a, w_a and w_l.

the fact that by laterally removing material from section zones close to the neutral axis, not only an obvious reduction of the beam mass can be obtained, but also an unexpected, though technically negligible, reduction of the stress. Such zones constitute a strip, whose delimiting radii can been evaluated analytically. This approach gave rise to an appreciable mass diminution (about 10%) and, at the same time, to a stress reduction as well, although technically less evident (about 1%). In a subsequent work [110], the demanding achievement of a concurrent stress and mass reduction is relaxed in favor of two weaker requests and applied to the optimization of a crane hook, showing a mass reduction up to 25%, without altering significantly the stress. Here, the assumption of a lightening pocket around the neutral axis is made. To further broaden the horizon of the theory, the simultaneous presence of bending moment and normal force is considered. Based on the linearized version of the objective functional, solutions for the radii delimiting the lateral groove are derived in closed form, whose results are compared to those obtained in [110] for the same crane hook and compared to FE solutions.

5.2 Minimum compliance straight beams

Consider a straight beam of length l (see Figure 5.2) made of elastic, linear, homogeneous and isotropic material and subject to a linearly distributed load along its axis. Suppose that the cross sectional area is not fixed and constant but, on the contrary, is allowed to vary along the beam axis. Indeed, it is the design variable and has to be determined in order to minimize, for

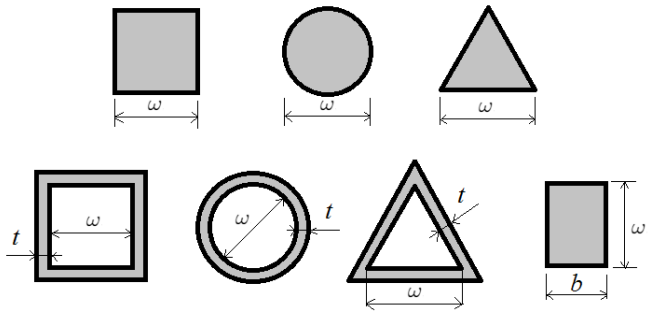

Figure 5.3: Considered cross sectional areas. Top: Solid sections; bottom: Hollow and rectangular sections.

a given load distribution, the compliance of the beam.

The compliance cost functional represents the elastic energy of the beam, which can be expressed as the work of external dead loads. In linear elasticity, under the assumption of zero normal forces, zero shear forces and zero torsional moments, the overall compliance Φ of a beam is given by the sum of the stress and strain elastic energies, namely [82]

$$\Phi = \int_0^l \frac{M(x)^2}{EI(x)}\, dx\,, \tag{5.1}$$

where E is Young's modulus and $M(x)$ and $I(x)$ are the bending moment and the moment of inertia, respectively, at a distance x from one of the extremes of the beam. While $M(x)$ depends on the load condition and, for a given load distribution, is known, $I(x)$ depends on the sectional area $A(x)$. To simplify the reasoning, the seven sections depicted in Figure 5.3 are considered. The shapes on the top are naturally associated with a one-dimensional problem, since the decision variable is the value of the edge denoted by ω (for the square and the equilateral triangle) or the diameter (for the circle). To keep the problem one-dimensional also for the shapes on the bottom, we suppose that one of the characteristic quantities, ω, is fixed while the other one, i.e., the width b of the rectangle and the thickness t of the hollow shapes, is the decision variable. For these sections, the relation between the moment of inertia and the area can be written as [82]

$$I(x) = \gamma\, c\, A(x)^n\,, \tag{5.2}$$

where γ, c and n are constants whose values are reported, for the seven sections, in Table 5.1.

Section type	γ	c	n
Square	$1/12$	1	2
Circular	$1/4\pi$	1	2
Triangular	$\sqrt{3}/18$	1	2
Rectangular	$1/12$	ω^2	1
Hollow square	$1/6$	ω^2	1
Hollow circle	$1/8$	ω^2	1
Hollow triangular	$1/12$	ω^2	1

Table 5.1: Values of γ and n for the cross sections in Figure 5.3.

Substituting (5.2) in (5.1) and rearranging one obtains

$$\Phi = \frac{1}{\gamma\, c\, E} \int_0^l \frac{M(x)^2}{A(x)^n}\, dx\,.$$

In addition, the (fixed) material volume is given by

$$V = \int_0^l A(x)\, dx\,.$$

As previously mentioned, the beam is subject to a linearly distributed load along its axis. More precisely (see Figure 5.2), the unit load (force per length), denoted by w, is considered to be zero in an interval $[0, a]$, with $a \in [0, l]$, and to vary linearly from $w(a) = w_a$ to $w(l) = w_l$. Moreover, R_A and R_B are the vertical end reactions at the left and right ends, respectively, and are positive upward; M_A and M_B are the reaction end moments. All moments are positive when producing compression on the upper portion of the beam cross section. All applied loads are positive as shown in Figure 5.2.

As far as the boundary conditions are concerned, the following analysis is limited to the following three cases:

$\mathcal{C}$: Cantilever beam (left-end free, right-end fixed, see Figure 5.4, left);

$\mathcal{SS}$: Simply supported beam (see Figure 5.4, middle);

$\mathcal{GS}$: Left-end guided and right-end simply supported beam (see Figure 5.4, right);

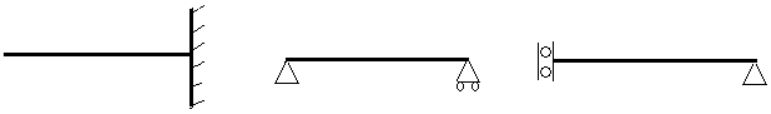

Figure 5.4: Boundary conditions: Cantilever $\mathcal{C}$ (left), simply supported $\mathcal{SS}$ (middle) and left-end guided and right-end simply supported $\mathcal{GS}$ (right).

Considering Clebsch's approach, the bending moment, expressed in terms of the reaction and of the moment at the left end, is given by [111]

$$M(x) = M_A + R_A x - \frac{w_a}{2}\langle x-a\rangle^2 - \frac{w_l - w_a}{6(l-a)}\langle x-a\rangle^3\,, \tag{5.3}$$

where $\langle x-a\rangle$ is the Macaulay bracket defined by

$$\langle x-a\rangle = \begin{cases} x-a\,, & \text{if } x \geq a\,, \\ 0\,, & \text{otherwise.} \end{cases} \tag{5.4}$$

The value of the left-end reaction R_A and left-end moment M_A depend on the boundary conditions. In particular [111]

- for the $\mathcal{C}$ beams $R_A = M_A = 0$;
- for the $\mathcal{SS}$ beams, $M_A = 0$ and

$$R_A = w_a(l-a)^2/(2l) + w_l(l-a)^2/(6l)\,; \tag{5.5}$$

- for the $\mathcal{GS}$ beams $R_A = 0$ and

$$M_A = w_a(l-a)^2/2 + w_l(l-a)^2/6\,. \tag{5.6}$$

For convenience, hereinafter the load configuration is represented by the pair (α, ξ), where $\alpha = a/l$ and $\xi = w_a/w_l$. As an example, $(0,0)$ and $(0,1)$ refer to triangularly and uniformly distributed loads, respectively. Once defined the pair load configuration (α, ξ), the kind of beam ($\mathcal{C}$, $\mathcal{SS}$ or $\mathcal{GS}$) and the type of the cross section (γ, c and n), the mean compliance minimization problem can be formulated as follows:

Problem 5.1. *Given the length l and the isoperimetric constraint*

$$\int_0^l A(x)\,dx = \widetilde{V}\,, \tag{5.7}$$

accounting for the volume of the beam, find the optimal cross sectional area distribution $A^*(x)$ which minimizes the compliance functional

$$\Phi = \frac{1}{\gamma\, c\, E}\int_0^l \frac{M(x)^2}{A(x)^n}\,dx\,, \tag{5.8}$$

for specified load configuration parameters (α, ξ) and for the aforementioned different boundary conditions ($\mathcal{C}$, $\mathcal{SS}$ and $\mathcal{GS}$).

Problem 5.1 is solved analytically by considering the calculus of variations. It is worth noting that the nature of the applied loads as well as the boundary conditions ensures that the bending moment is a continuous function along the beam axis, avoiding abrupt changes to the cross section.

5.2.1 Optimal area distributions

Using Equations (5.8) and (5.7), the augmented functional may be written as

$$\Phi^a = \Phi - \lambda\widetilde{V} = \int_0^l F(x, A(x))\,dx\,, \tag{5.9}$$

where λ is the Lagrangian multiplier associated with the isoperimetric constraint on the volume (5.7) and

$$F(x, A(x)) = \frac{M(x)^2}{\gamma\, E\, c\, A(x)^n} - \lambda A(x)\,. \tag{5.10}$$

The necessary condition for minimizing (5.10) is obtained considering the particular case where the integrand of the objective functional depends on the independent variable and the objective function and not on the derivative of this latter. The corresponding Euler-Lagrange equation will be (A.17), namely

$$\frac{\partial F}{\partial A} = 0\,, \tag{5.11}$$

leading to the following algebraic equation

$$\lambda\,\gamma\, E\, c\, A(x)^{n+1} + n\, M(x)^2 = 0\,, \tag{5.12}$$

or

$$A^*(x) = \left[-\frac{n\, M(x)^2}{\lambda^* \gamma\, E\, c} \right]^{\frac{1}{n+1}} . \tag{5.13}$$

The value λ^* appearing in (5.13) is the only value of λ that, when using (5.12) (or (5.13)) in (5.7) allows to fulfill the identity. More precisely, λ^* is such that

$$\frac{1}{(\lambda^*)^{\frac{1}{n+1}}} \int_0^l \left[-\frac{n\, M(x)^2}{\gamma\, E\, c} \right]^{\frac{1}{n+1}} dx = V\,, \tag{5.14}$$

which, solved for λ^*, yields

$$\lambda^* = \left(\frac{1}{\widetilde{V}} \int_0^l \left[-\frac{n\, M(x)^2}{\gamma\, E\, c} \right]^{\frac{1}{n+1}} dx \right)^{n+1} . \tag{5.15}$$

Substituting (5.15) into (5.13) one obtains the final expression for the optimal cross-sectional area:

$$A^*(x) = \widetilde{V}\, M(x)^{\frac{2}{n+1}} \left(\int_0^l M(x)^{\frac{2}{n+1}} dx \right)^{-1} , \tag{5.16}$$

or, introducing the normalized coordinate $\tilde{x} = x/l$ and the normalized area $\widetilde{A}^* = A^*\, l/\widetilde{V}$,

$$\widetilde{A}^*(\tilde{x}) = \tilde{x}^{\frac{2}{n+1}} \left(\int_0^1 M(\tilde{x})^{\frac{2}{n+1}} d\tilde{x} \right)^{-1} . \tag{5.17}$$

Equation (5.17) yields the explicit value of the optimal cross-sectional area provided that the integral appearing in the denominator at the right-hand side term can be solved in closed-form. Since, as shown in the following, the bending moment for $\mathcal{C}$, $\mathcal{SS}$ and $\mathcal{GS}$ beams is a polynomial function of $\tilde{x}$, a closed-form solution can easily be obtained, in all the three cases, when $n = 1$. When $n = 2$, however, the integral can be solved numerically thus providing an explicit practical value of the optimal area.

Analytical and closed-form solutions for $\mathcal{C}$ beams

In $\mathcal{C}$ beams both R_A and M_A are identically zero. In addition, it is easily shown that reasonable solutions are associated with a value of a equal to zero, otherwise the cost functional vanishes for all $x \in [0, a]$, and consequently $A(x)$ is zero in this interval, which is an infeasible, although theoretically

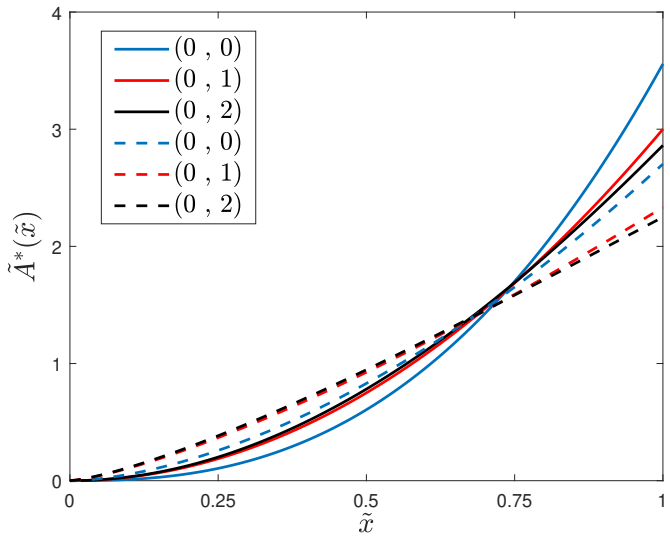

Figure 5.5: Optimal area distributions for $\mathcal{C}$ beams with $n = 1$ (solid lines) and $n = 2$ (dashed lines), considering $\xi = 0, 1, 2$.

admissible, solution. The corresponding bending moment is therefore given by

$$M(\tilde{x}) = -\frac{w_l l^2}{2}\left(\xi\tilde{x}^2 + \frac{1-\xi}{3}\tilde{x}^3\right), \tag{5.18}$$

which, substituted into (5.17), provides the optimal solution. When $n = 1$ the integral in (5.17), after the natural simplification between numerator and denominator, reduces to

$$\xi\int_0^1 \tilde{x}^2 d\tilde{x} + \frac{1-\xi}{3}\int_0^1 \tilde{x}^3 d\tilde{x} = \frac{\xi}{3} + \frac{1-\xi}{12} = \frac{1+3\xi}{12}. \tag{5.19}$$

Finally, the optimal cross-sectional area is

$$\widetilde{A}^*_{\mathcal{C},n=1}(x) = \frac{12}{1+3\xi}\left(\xi\tilde{x}^2 + \frac{1-\xi}{3}\tilde{x}^3\right), \tag{5.20}$$

which is represented in Figure 5.5 for $\xi = 0, 1, 2$ with solid lines. For cross sections with $n = 2$, normalized optimal solutions are given substituting (5.18) in (5.17). The integral term has been computed numerically and optimal solutions are represented in Figure 5.5 with dashed lines. It is worthwhile to note that optimal solutions vanish at the free end, evincing

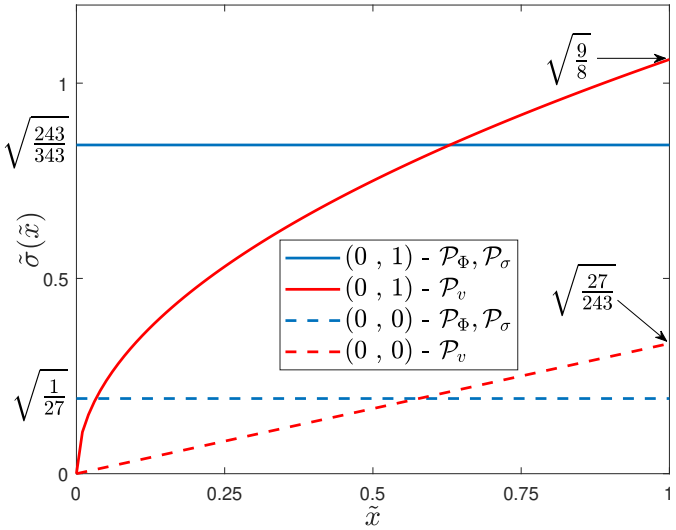

Figure 5.6: Normalized stresses resulting form $\mathcal{P}_\Phi$, $\mathcal{P}_v$ and $\mathcal{P}_\sigma$ optimization problems in $\mathcal{C}$ with a square cross section and with uniformly (solid lines) and triangularly (dashed lines) distributed loads.

an exploitation of the total material volume where the bending moment is not zero.

Equation (5.20) provides optimal solutions more general than those obtained in [87], in which the compliance, free end deflection and maximum stress minimization problems are solved only for beams with triangularly and uniformly distributed loads and only for a square cross section cantilever beam. In particular, it is shown that the solution for the minimum compliance problem (herein referred to as $\mathcal{P}_\Phi$) is identical to the maximum stress minimization problem ($\mathcal{P}_\sigma$), as previously stated in [78, 79]. Optimal solutions corresponding to these two problems lead to an iso-stress behavior along the beam axis (see Figure 5.6). For instance, a square cross section cantilever exhibits normalized constant bending stress $\tilde{\sigma} := \sqrt{\sigma^2 \widetilde{V}^3/(w_l^2 l^7)}$ equal to $\sqrt{243/343}$ or $\sqrt{1/27}$ when subjected to uniformly or triangularly distributed loads, respectively. On the other hand, the free end deflection minimization problem ($\mathcal{P}_v$) leads to variable bending stress along the beam axis. Precisely, the bending stress reads $\sqrt{9\tilde{x}/8}$ or $\sqrt{27/243}\,\tilde{x}$ for uniformly or triangularly distributed loads, respectively.

Closed-form solutions for $\mathcal{SS}$ and $\mathcal{GS}$ beams

On a hand, for $\mathcal{SS}$ beams $M_A = 0$, while R_A is given by (5.5). Substituting in (5.3), one obtains

$$M(\tilde{x}) = w_l(l-a)^2\left[\frac{1+2\xi}{6}\tilde{x} - \frac{\xi}{2}r(\tilde{x},\alpha)^2 - \frac{1-\xi}{6}r(\tilde{x},\alpha)^3\right], \tag{5.21}$$

where

$$r(\tilde{x},\alpha) = \frac{\langle \tilde{x}-\alpha\rangle}{(1-\alpha)}.$$

On the other hand, for $\mathcal{GS}$ beams $R_A = 0$ and M_A is given by (5.6). Substituting in (5.3) one obtains

$$M(\tilde{x}) = w_l(l-a)\left[\frac{1+2\xi}{6} - \frac{\xi}{2}r(\tilde{x},\alpha)^2 - \frac{1-\xi}{6}r(\tilde{x},\alpha)^3\right]. \tag{5.22}$$

Therefore, for $n = 1$ one obtains

$$\widetilde{A}^*_{\mathcal{SS},n=1}(\tilde{x}) = \frac{4\tilde{x}(1+2\xi) - 12\,\xi\, r(\tilde{x},\alpha)^2 - 4(1-\xi)r(\tilde{x},\alpha)^3}{(1+\xi)+(1+3\xi)\alpha}, \tag{5.23}$$

for $\mathcal{SS}$ beams (which is more general than that obtained for Euler-Bernoulli $\mathcal{SS}$ beams in [82], where only load conditions $(0,0)$ and $(0,1)$ are discussed) and

$$\widetilde{A}^*_{\mathcal{GS},n=1}(\tilde{x}) = \frac{4(1+2\xi) - 12\,\xi\, r(\tilde{x},\alpha)^2 - 4(1-\xi)r(\tilde{x},\alpha)^3}{(3+5\xi)+(1+3\xi)\alpha}. \tag{5.24}$$

for $\mathcal{GS}$ beams. The following simple sensitivity analysis shows how optimal solutions depend on the load parameters α and ξ. Solutions corresponding to triangularly and uniformly distributed loads, for three values of α, are shown in Figures 5.7a and 5.7b. It is worth noting that optimal solutions vanish at the extremities of the beam and only at $\tilde{x} = 1$ for $\mathcal{SS}$ and $\mathcal{GS}$ beams, respectively. Moreover, as far as $\mathcal{SS}$ beams are concerned, the optimal solution for the load configuration $(0,1)$ is perfectly symmetric, assuming the largest value where the bending moment is maximum, namely for $\tilde{x} = 0.5$, in agreement with [82]. Besides, as α increases, optimal solutions associated with $\mathcal{SS}$ beams lose symmetry. Finally, optimal solutions behave linearly in $\mathcal{SS}$ beams and tend to be constant in $\mathcal{GS}$ beams (slightly higher than their cylindrical uniform counterparts of the same volume) for $\tilde{x} < \alpha$ and do not vary sensibly as ξ increases (see Figures 5.8a and 5.8b).

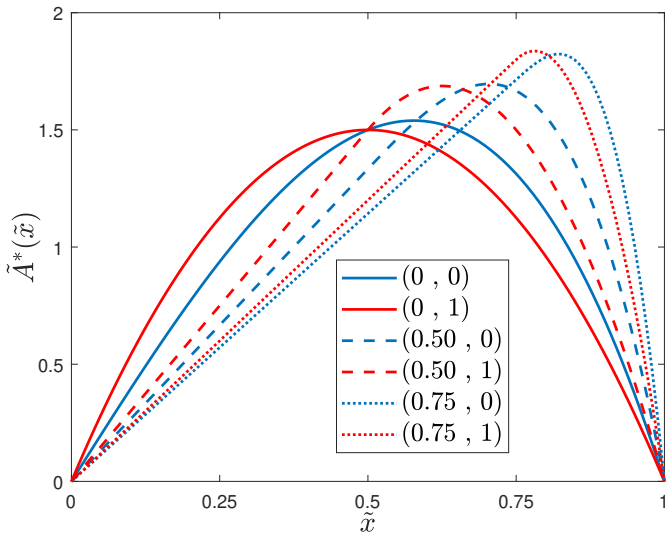

(a)

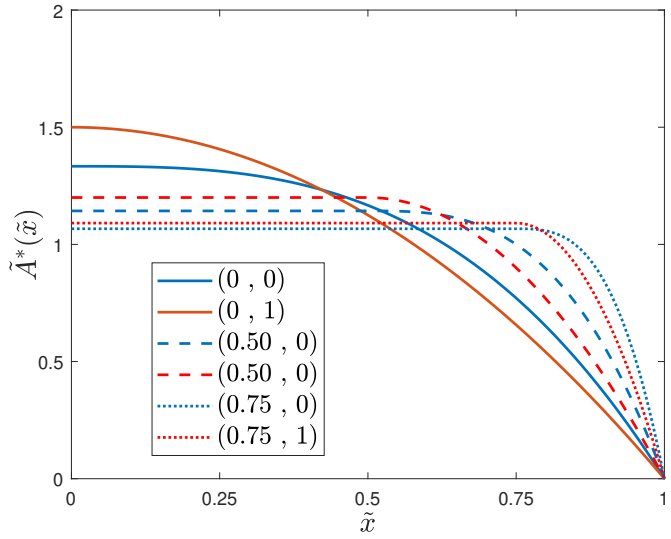

(b)

Figure 5.7: Optimal $\mathcal{SS}$ (a) and $\mathcal{GS}$ (b) area distributions for triangular and uniform loads with $\alpha = 0$ (solid lines), $\alpha = 0.5$ (dashed lines) and $\alpha = 0.75$ (dotted lines).

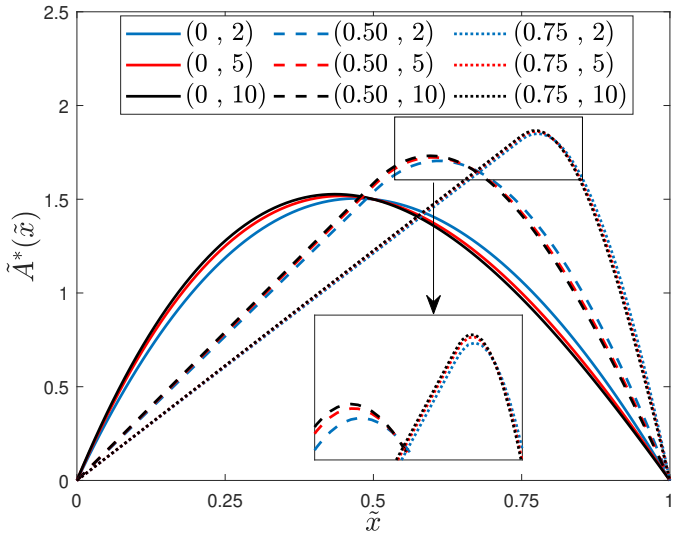

(a)

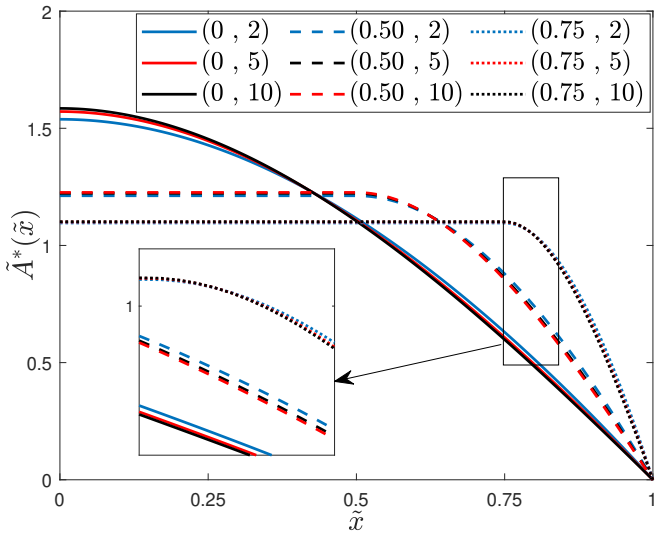

(b)

Figure 5.8: Optimal $\mathcal{SS}$ (a) and $\mathcal{GS}$ (b) area distributions for $\xi = 2, 5, 10$ and when $\alpha = 0$ (solid lines), $\alpha = 0.5$ (dashed lines) and $\alpha = 0.75$ (dotted lines).

Φ^*/Φ_{cyl} in the $\mathcal{C}$ configuration for solid shapes		
	$\xi = 0$	$\xi = 1$
Solid square	0.248	0.376
Solid circle	0.259	0.394
Solid triangle	0.214	0.326

Table 5.2: Compliance reduction for $\mathcal{C}$ beams with $\xi = 0, 1$ and $n = 2$.

5.2.2 Discussion and numerical example

The analysis carried out is interesting if the solution permits to obtain a high compliance reduction with respect to the uniform (cylindrical) counterpart of the same material volume. Generally, the compliance of this latter is given by

$$\Phi_{cyl} = \frac{4\pi l^2}{EV^2} \int_0^l M(x)^2 \, dx \,, \tag{5.25}$$

while the compliance Φ^* of optimal solutions can be obtained substituting in (5.8) the optimal value of $A(x)$. A reasonable performance index could then be the compliance reduction given by the ratio Φ^*/Φ_{cyl}. Hereinafter, for the sake of simplicity, we refer only to triangularly ($\xi = 0$) and uniformly ($\xi = 1$) distributed loads.

Firstly, the performance of optimal solutions for $\mathcal{C}$ beams is addressed for solid cross sections with $n = 2$. Table 5.2 lists some numerical ratios Φ^*/Φ_{cyl}. As one may note, the reduction of the compliance is of the order of $3 \div 5$ with respect to uniform counterparts of the same mass and of the same cross-sectional shape. The stiffest response, in terms of compliance reduction, is provided by the triangular cross section both for $\xi = 0$ and for $\xi = 1$.

Now, attention is drawn to assess the performance of optimal solutions for hollow cross sections ($n = 1$) within a numerical example for $\mathcal{C}$, $\mathcal{SS}$ and $\mathcal{GS}$ beams. Consider a hollow cross section beam with $l = 0.5$ m, $E = 2.1 \times 10^5$ MPa and $\widetilde{V} = 2.5 \times 10^5$ mm^3. Numerical values of the gain in compliance relative to optimal solutions for $\alpha = 0$ and $\xi = 0, 1$ are listed in tabular format. It is important to note that the reference length ω should be taken into account (see Figure 5.3). Values of compliance reduction

Φ^*/Φ_{cyl} in the $\mathcal{C}$ configuration for hollow shapes						
ω/l	0.05		0.1		0.2	
ξ	0	1	0	1	0	1
Triangle	0.343	0.435	0.086	0.109	0.021	0.027
Square	0.171	0.218	0.043	0.054	0.011	0.014
Circle	0.228	0.290	0.057	0.072	0.014	0.018

Table 5.3: Compliance reduction for the hollow sections in the $\mathcal{C}$ configuration for $\alpha = 0$ and for different values of ω/l and ξ.

for the $\mathcal{C}$ configuration ($\alpha = 0$) and for different values of ω/l and ξ are reported in Table 5.3. Among optimal solutions, beams of hollow square sections present the stiffest geometric configuration, once fixed the material mass, even when compared with the shapes reported in Table 5.2. As ω/l increases, Φ^*/Φ_{cyl} decreases significantly and the more the optimal thickness is decreased. This theoretical result arises since the optimization problem does not provide lower and upper bound constraints on the thickness. In practical engineering, these bounds are superimposed in order to avoid structural instability phenomena, such as buckling.

In $\mathcal{SS}$ or $\mathcal{GS}$ beams, unlike $\mathcal{C}$ ones, α can be chosen different from zero. For these two configurations, numerical values for Φ^*/Φ_{cyl} for different values of α and for $\omega/l = 0.1$ are reported in Table 5.4. Again, for a fixed value of the mass, hollow square cross sections still present the stiffest behavior. Moreover, when α increases the performance of optimal solutions change marginally. This is in accordance with Figures 5.7a, 5.7b, 5.8a and 5.8b, where the optimization problem leads to practically identical optimal design shapes as α tends to 1. Eventually, note that for all the hollow shapes the compliance of optimal solutions is of the order of 10 times that of uniform beams, giving rise to a stiffer behavior employing the same amount of material volume.

	$\mathcal{SS}$ configuration (hollow shapes)						$\mathcal{GS}$ configuration (hollow shapes)					
α	0	0	0.5	0.5	0.75	0.75	0	0	0.5	0.5	0.75	0.75
ξ	0	1	0	1	0	1	0	1	0	1	0	1
Triangle	0.161	0.163	0.153	0.154	0.150	0.150	0.171	0.163	0.183	0.178	0.190	0.187
Square	0.080	0.082	0.077	0.077	0.075	0.075	0.086	0.082	0.091	0.089	0.094	0.093
Circle	0.107	0.109	0.102	0.102	0.100	0.100	0.114	0.109	0.122	0.118	0.126	0.124

Table 5.4: Compliance reduction Φ^*/Φ_{cyl} for the hollow sections in the $\mathcal{SS}$ and $\mathcal{GS}$ configurations for $\omega/l = 0.1$ and for different values of ξ and α.

5.3 Shape optimization of beams against buckling

In this section, an attention is dedicated to problems where closed-form solutions cannot be easily obtained, thus requiring a numerical approach. In particular, the shape optimization of elastic beams, namely the minimization of their material volume when to avoid elastic instability, is presented within the plane deformation hypothesis. The historical example concerning beams subject to a concentrated compressive force (Lagrange's beam)is addressed. In particular, the numerical approach by means of the LGR pseudospectral method given in Chapter 3 is considered, by which cross sectional area distributions are forecast within a unified fashion and without resorting to accurate guesses of optimal solutions beforehand, as typically occurs for numerical techniques employed in the literature (e.g., the shooting method).

5.3.1 Governing static equations

Consider a slender beam of a given length L represented by a plane curve $\mathcal{C}$ in a rectangular Cartesian coordinate system whose horizontal and vertical axes are denoted by $\bar{z}$ and $\bar{y}$, respectively. Let $\mathbf{i}$ and $\mathbf{j}$ be the unit vectors along $\bar{z}$ and $\mathbf{y}$, respectively, and $\mathbf{k} = \mathbf{i} \times \mathbf{j}$. The curve $\mathcal{C}$ represents the beam axis which coincides with the centroidal line of the beam cross section. Suppose that the bending rigidity of the beam and the angle between the tangent to the beam axis and the $\bar{z}$ axis are denoted by EI and θ, both functions of the arc length of $\mathcal{C}$ measured from one end point, namely $EI(S)$ and $\theta(S)$ where $S \in [0, L]$. Denoting by $A(S)$ the area of the cross section, the material volume of the beam is given by

$$W = \int_0^L A(S)\, dS\,. \tag{5.26}$$

Moreover, let $q_z(S)$ and $q_y(S)$ denote the intensities of the distributed forces along $\bar{z}$ and $\bar{y}$, respectively, both per unit of the beam axis (see Figure 5.9a). Besides, let $H(S)$ and $V(S)$ denote the components of the contact force $\mathbf{R}(S)$ in an arbitrary section of the beam and $\mathbf{M}(S)$ denote the contact couple, which represent the influence of the cut-off part $[0, S)$ of the beam on the element of length dS. Hence, $\mathbf{R}(S) = H(S)\,\mathbf{i} + V(S)\,\mathbf{j}$, and $\mathbf{M}(S) = M(S)\,\mathbf{k}$.

Assume the beam is made of material exhibiting a linear stress–strain relation. Based on the framework reported in [112], if Euler-Bernoulli assumptions hold, namely plane sections in the natural state remain plane in the deformed state and extensional and shear rigidity are infinite, the

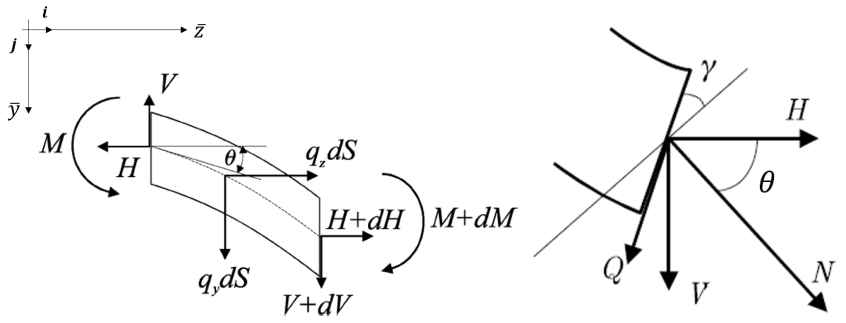

(a) (b)

Figure 5.9: Coordinate system, load configuration and definition of the employed variables for plane (a) and generalized plane (b) deformation.

nonlinear governing equations for the static behavior of an elastic beam are

$$\begin{cases} \frac{dH(S)}{dS} = -q_z(S)\,, \\ \frac{dV(S)}{dS} = -q_y(S)\,, \\ \frac{dM(S)}{dS} = -V(S)\cos\theta(S) + H(S)\sin\theta(S)\,, \\ \frac{dz(S)}{dS} = \cos\theta(S)\,, \\ \frac{dy(S)}{dS} = \sin\theta(S)\,, \\ \frac{d\theta(S)}{dS} = M(S)/(E\kappa A(S)^k)\,, \end{cases} \tag{5.27}$$

where E is Young's modulus and κ and k are two constants depending on the shape of the cross section (for a circular shape, $\kappa = 1/4\pi$ and $k = 2$). In case the extensibility of the beam axis ε and the rotation of the cross section with shear angle γ are taken into account, the variation of coordinates along S take the form [112]

$$\begin{cases} \frac{dz(S)}{dS} = (1+\varepsilon(S))\cos\theta(S)\,, \\ \frac{dy(S)}{dS} = (1+\varepsilon(S))\sin\theta(S)\,, \end{cases} \tag{5.28}$$

and the contact couple is given by

$$M(S) = EI\left(\frac{d\theta(S)}{dS} - \frac{d\gamma(S)}{dS}\right)\,. \tag{5.29}$$

Besides, referring to the constitutive equations of the beam in the form that follows from [113], the shear angle and the beam axis extensibility take the form (see Figure 5.9b)

$$\begin{cases} \sin\gamma(S) = \frac{cQ(S)}{GA(S)}\,, \\ \varepsilon(S) = \frac{N(S)}{EA(S)}\,, \end{cases} \tag{5.30}$$

respectively, where c is the shear correction factor, $EA(S)$ and $GA(S)$ are the extensional and shear rigidity, respectively, while $Q(S)$ and $N(S)$ are the components of the contact force in the direction of the sheared plane and tangent to the beam axis, respectively, which according to Engesser's model, are given by

$$\begin{cases} N(S) = H(S)\frac{\cos(\theta(S)-\gamma(S))}{\cos\gamma(S)} + V(S)\frac{\sin(\theta(S)-\gamma(S))}{\cos\gamma(S)}\,, \\ Q(S) = V(S)\frac{\cos\theta(S)}{\cos\gamma(S)} - H(S)\frac{\sin\theta(S)}{\cos\gamma(S)}\,. \end{cases} \tag{5.31}$$

On a hand, with prescribed loads $\{q_z(S), q_y(S)\}$, cross sectional distribution $A(S)$ and boundary conditions at endpoints, the system (5.27) determines the horizontal and vertical contact forces, the contact couple, coordinates and and the angle $\theta(S)$ and therefore the static behavior of the beam is completely determined. Therefore, $H(S)$, $V(S)$, $M(S)$, $z(S)$, $y(S)$ and $\theta(S)$ may be considered to be the state variables. On the other hand, one may be interested in finding out the cross sectional area distribution so that a prescribed functional is minimized while static equations are satisfied. More precisely, denoting by $\mathbf{x}$ the state variables and recasting static equations into the form

$$\frac{d\mathbf{x}(S)}{dS} = \mathbf{f}(\mathbf{x}(S), A(S))\,, \tag{5.32}$$

the shape optimization problem associated with a goal functional $J(\mathbf{x}, A)$ and characterized by states at endpoints $\mathbf{x}_0$ and $\mathbf{x}_L$, an admissible state space $\mathcal{X}$ and an admissible shape space $\mathcal{A}$ consists in finding the cross sectional area distribution $A : [0, L] \to \mathcal{A}$ which minimizes J and such that, if $\mathbf{x}(0) = \mathbf{x}_0$, then $\mathbf{x}(S) \in \mathcal{X}$ for all $S \in [0, L]$ and $\mathbf{x}(L) = \mathbf{x}_L$.

5.3.2 Lagrange's beam

In the following, Pearson's formulation of the Lagrange's beam problem is recalled [114], namely to find the curve which by its revolution about an axis in its plane determines the beam of great efficiency, i.e., the simply supported beam of circular cross section ($\kappa = \frac{1}{4\pi}$ and $k = 2$) and maximum resistance to buckling under axial compression (see Figure 5.10).

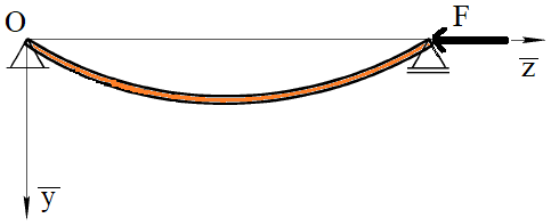

Figure 5.10: A simply supported beam under buckling load.

The case of plane deformation

Here it is implicitly assumed that extensional and shear rigidity are infinite. The nonlinear static equation for this case is [112]

$$\frac{d}{dS}\left(A(S)^2\frac{d\theta(S)}{dS}\right)+\frac{4\pi}{E}F\sin\theta(S)=0\,. \tag{5.33}$$

Introducing the dimensionless quantities $s=\frac{S}{L},\ a=\frac{A}{L^2},\ w=\frac{W}{L^3},\ \lambda=\frac{4\pi F}{EL^2}$, Equation (5.33) reads

$$(a^2\theta')'+\lambda\sin\theta=0\,, \tag{5.34}$$

where a prime denotes the first derivative with respect to s, subject to the boundary conditions

$$\theta(1/2)=0\,,\quad \theta'(0)=0\,. \tag{5.35}$$

Due to symmetry considerations, the problem can be studied for $S\in[0,L/2]$. The normalized half volume of the beam is therefore

$$w=\int_0^{1/2}a(s)\,ds\,. \tag{5.36}$$

Introducing $x_1=\theta$, $x_2=a^2\theta'$, $x_3=w$ and $x_4=\lambda$ as state variables, the beam's resistance to buckling under axial compression as a shape optimization problem can be expressed in the following two different ways:

Problem 5.2. *Find the distribution of material along the length of the beam so that the beam is of minimum volume and supports a given load $\tilde{\lambda}$ without*

buckling, i.e.,

$$\begin{aligned} \min_{a(s)} \quad & \int_0^{1/2} a(s)\, ds \\ s.t. \quad & x_1'(s) = x_2(s)/a(s)^2\,, \\ & x_2'(s) = -\tilde{\lambda} x_1(s)\,, \\ & x_1(1/2) = 0\,, \\ & x_2(0) = 0\,. \end{aligned} \tag{5.37}$$

Problem 5.3. *Find the distribution of material along the length of the beam of a given half volume $\tilde{w}$ which gives the largest possible buckling load, i.e.,*

$$\begin{aligned} \min_{a(s)} \quad & -x_4(1/2) \\ s.t. \quad & x_1'(s) = x_2(s)/a(s)^2\,, \\ & x_2'(s) = -x_1(s)\, x_4(s)\,, \\ & x_3'(s) = a(s)\,, \\ & x_4'(s) = 0\,, \\ & x_1(1/2) = 0\,, \\ & x_2(0) = 0\,, \\ & x_3(0) = 0\,, \\ & x_3(1/2) = \tilde{w}\,. \end{aligned} \tag{5.38}$$

Note that in the above mentioned two problems static equations have been linearized since the optimal beam is supposed to still remain straight, i.e., no post-buckling analysis is considered. Moreover, goal functionals are of Lagrange and Mayer types in the first and second problem, respectively. In [106], a slightly different form of the two problems above has been considered, where the optimal beam having the same volume of a uniform one has been numerically obtained by means of the shooting method, while here, as mentioned above, the cross sectional area is normalized with respect to the square of the beam length instead.

Hamiltoninans and necessary conditions for optimal solutions have been firstly derived. Following the formulation of Chapter 2 and omitting the functional dependence on s for brevity, one obtains

$$\mathcal{H} = a + \frac{p_1\, x_2}{a^2} - \tilde{\lambda}\, p_2\, x_1\,,$$

$$a = \sqrt[3]{2 p_1\, x_2},$$

$$p_1' = \tilde{\lambda}\, p_2\,, \quad p_2' = -p_1/a^2\,,$$
$$p_1(0) = p_2(1/2) = 0\,,$$

for the first problem, and

$$\mathcal{H} = \frac{p_1\, x_2}{a^2} - p_2\, x_1\, x_4 + p_3\, a\,,$$

$$a = \sqrt[3]{\frac{2p_1\, x_2}{p_3}}\,,$$
$$p_1' = p_2\, x_4\,, \quad p_2' = -\frac{p_1}{a^2}\,, \quad p_3' = 0\,, \quad p_4' = p_2\, x_1\,,$$
$$p_1(0) = p_2(1/2) = p_4(0) = 0\,, \quad p_4(1/2) = -1\,,$$

for the second problem, where p_k are the costates associated with states x_k, with $k = 1, 2, 3, 4$. In [106], it has been found that the goal functional associated with the optimal cross sectional area distribution in the first problem associated with $\tilde{\lambda} = \pi^2$ is $w^* = 0.433$. Once this latter result is introduced into the second problem as $\tilde{w}$, one obtains $x_4^*(1/2) = 9.869 \approx \pi^2$, which leads to the conclusion that the two problems are equivalent. Furthermore, it is obvious that the condition $p_1(0) = 0$ always implies that the cross section vanishes at the end of the beam, i.e., $a(0) = 0$ (Clausen's solution).

It is worth noting that by employing the approach presented here, there is no need to obtain necessary conditions for optimality and therefore, unlike the shooting method, the burden of accurately guessing optimal states and costates is bypassed. In particular, referring to Equation (5.32) and taking

$$\mathbf{f}(\mathbf{x}, a) = [x_2/a^2 \quad -\tilde{\lambda} x_1]$$

and

$$\mathbf{f}(\mathbf{x}, a) = [x_2/a^2 \quad -x_1 x_4 \quad a \quad 0]$$

for the first and second problem, respectively, optimal states and optimal objective functions can be directly obtained solving the corresponding NLP problems.

As far as the first problem is concerned, Figures 5.11a and 5.11b show the optimal states and optimal cross sectional area distributions obtained by the orthogonal collocation method taking as $\tilde{\lambda} = \pi^2, 1.2\pi^2$ and $1.5\pi^2$. As expected, the high $\tilde{\lambda}$, the high the volume required to withstand the load without buckling. Optimal values of the goal functional associated with the first problem are $w^* = 0.4330$, 0.4743 and 0.5303, respectively.

Numerical solution associated with $\tilde{\lambda} = \pi^2$ has been compared to that obtained in [106]. It is easy to notice that both solutions are in good agreement and the cross section vanishes at the end (Clausen's solution). In parallel, one may be interested in imposing a minimal value of the cross sectional area distribution a_{min}. Unlike the shooting method, the present approach allows to consider this requirement as an inequality constraint. For instance, besides the Clausen's solution, optimal states as well as optimal area distributions have been numerically forecast so that $a \geq 0.3$ and $a \geq 0.5$ (Figures 5.12a-5.12d and 5.13). Optimal values for the goal functional associated with the second problem read $x_4^*(1/2) = 9.869,\ 9.7578,\ 7.4376$, for the Clausen's solution, with $a \geq 0.3$ and with $a \geq 0.5$, respectively, namely the maximum buckling resistance diminishes as the a_{min} increases for a given half volume $\tilde{w} = 0.4330$.

The case of generalized plane deformation

Here, the same load configuration as well as the symmetric buckling mode are considered, but now with finite values for the extensional and shear rigidity. To this purpose, Equations (5.28)-(5.31) are employed. When the beam is subject to a compressive force F, then $H = -F$ and $V = 0$ and therefore the axis extensibility and the shear angle are given by [113]

$$\varepsilon(S) = -\frac{F}{EA(S)}\frac{\cos(\theta(S) - \gamma(S))}{\cos\gamma(S)} \tag{5.39}$$

and

$$\gamma(S) = \frac{1}{2}\arcsin\left(\frac{2cF}{GA(S)}\sin\theta(S)\right), \tag{5.40}$$

respectively. Now, defining the angle $\alpha(S) = \theta(S) - \gamma(S)$ and taking into consideration the linearized version of the static equations, one obtains

$$\begin{cases} M'(S) = F\dfrac{1 - \frac{F}{EA(S)}}{1 - \frac{cF}{GA(S)}}\alpha(S)\,, \\ \alpha'(S) = \dfrac{M(S)}{EI(S)} \end{cases} \tag{5.41}$$

and subject to the boundary conditions

$$M(0) = 0\,, \quad \alpha(1/2) = 0\,. \tag{5.42}$$

Introducing the additional dimensionless quantities $m = \frac{4\pi M}{EL^3}$, $\tilde{\mu} = \frac{F}{EL^2}$ and $\tilde{\beta} = \frac{cF}{GL^2}$ and denoting by x_1 and x_2 the variables α and m, respectively, the minimum mass shape optimization problem reads

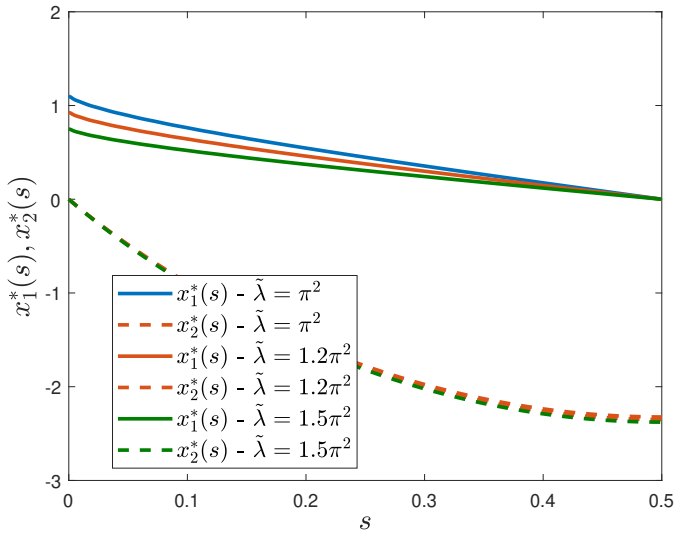

(a)

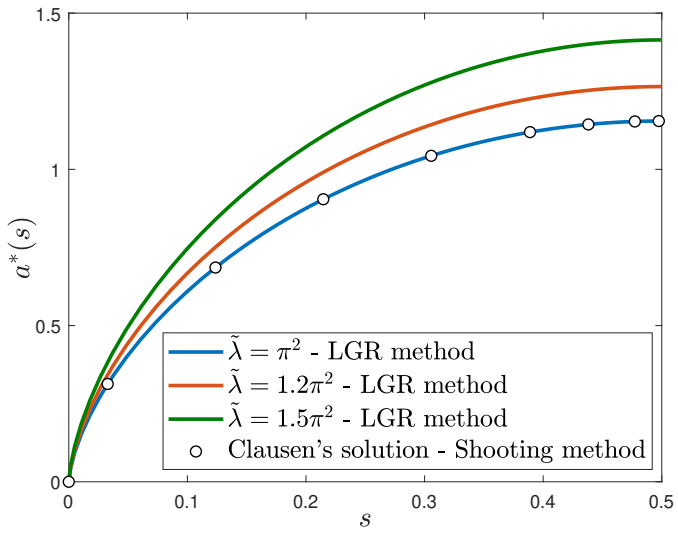

(b)

Figure 5.11: Numerical optimal states (a) and cross sectional area distributions (b) for the first version of Lagrange's beam problem.

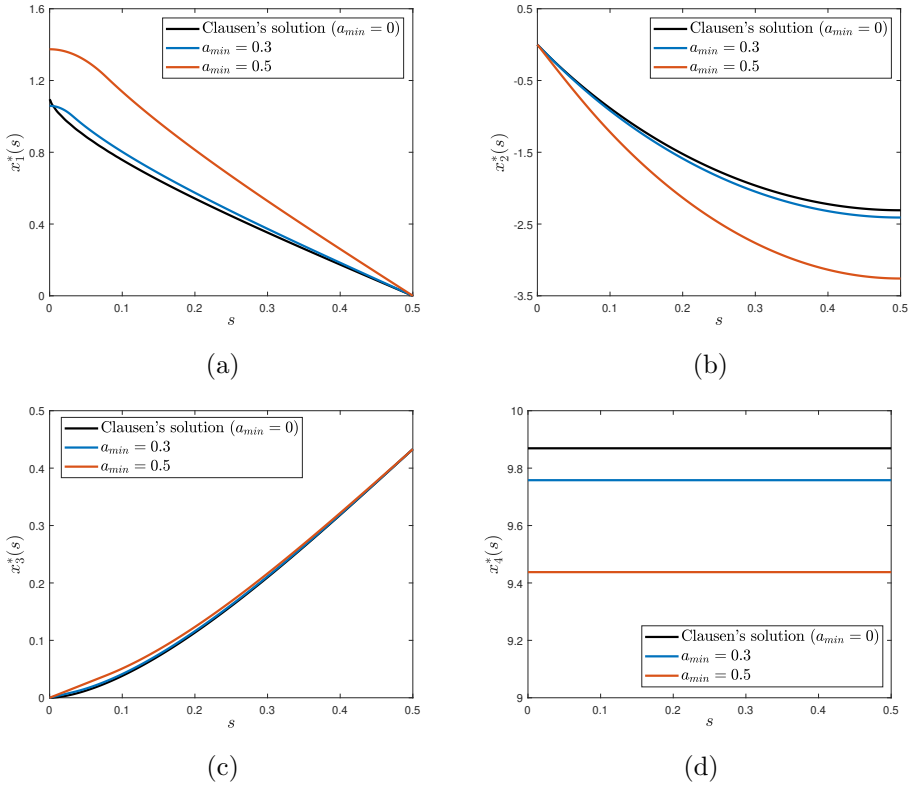

Figure 5.12: Numerical optimal states for the second version of Lagrange's beam problem.

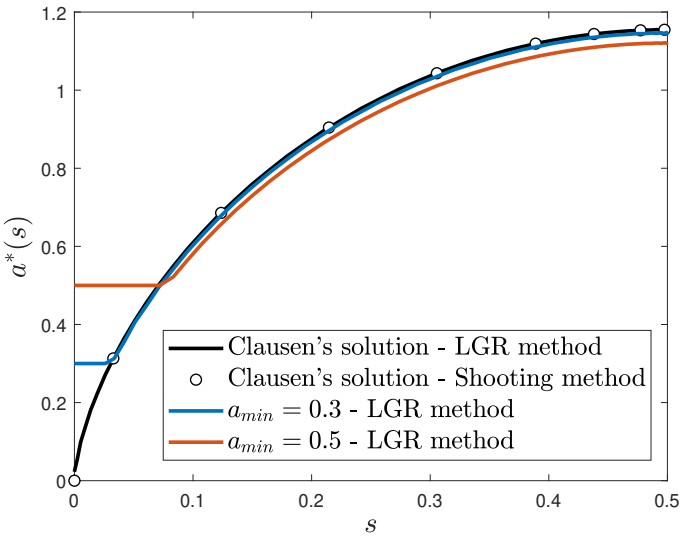

Figure 5.13: Numerical optimal cross sectional area distribution for the second version of Lagrange's beam problem.

Problem 5.4.

$$\begin{aligned} \min_{a(s)} \quad & \int_0^{1/2} a(s)\, ds \\ s.t. \quad & x_1'(s) = \frac{x_2(s)}{a(s)^2}\,, \\ & x_2'(s) = -\tilde{\lambda}\left(\frac{a(s)-\tilde{\mu}}{a(s)-\tilde{\beta}}\right) x_1(s)\,, \\ & x_1(1/2) = 0\,, \\ & x_2(0) = 0\,, \end{aligned} \tag{5.43}$$

where $\tilde{\lambda}$, $\tilde{\mu}$ *and* $\tilde{\beta}$ *are linked through the relation*

$$\tilde{\lambda} = \pi^2 \frac{1-\tilde{\beta}}{1-\tilde{\mu}}. \tag{5.44}$$

It is worth noting that shear and compressibility have opposite influence on Euler buckling load and for $\tilde{\beta} = \tilde{\mu} = 0$, one obtains the classical dimensionless critical load. Besides, according to [115], it is assumed that $\tilde{\mu} < 1$ and $\tilde{\beta} > \tilde{\mu}$.

Omitting the functional dependence on s, necessary conditions for optimal solutions are given by

$$\mathcal{H} = a + \frac{p_1\, x_2}{a^2} - \tilde{\lambda}\left(\frac{a-\tilde{\mu}}{a-\tilde{\beta}}\right) p_2\, x_1\,,$$

$$\frac{\partial \mathcal{H}}{\partial a} = 0 = 1 - \frac{2p_1\, x_2}{a^3} - p_2\, x_1 \frac{\tilde{\lambda}(\tilde{\mu}-\tilde{\beta})}{(a-\tilde{\beta})^2}\,,$$

$$p_1' = \tilde{\lambda}\left(\frac{a-\tilde{\mu}}{a-\tilde{\beta}}\right) p_2\,, \quad p_2' = -p_1/a^2\,,$$

$$p_1(0) = p_2(1/2) = 0\,.$$

Table 5.5 lists optimal values of the goal functional and minimal and maximal values of the optimal normalized cross sectional area distribution for different values of $\tilde{\beta}$ and $\tilde{\mu}$. Besides, optimal cross area distributions for two instances of $\tilde{\beta}$ and $\tilde{\mu}$ are shown in Figure 5.14 and compared to Clausen's solution. Unlike before, here the cross section does not vanish at the beam end, as a consequence of the application of the strong form of Pontryagin's Principle (2.19), namely

$$a(0) = \tilde{\beta} + \sqrt{\tilde{\lambda}(\tilde{\mu}-\tilde{\beta}) x_1(0) p_2(0)}\,,$$

confirming that the shape of the optimal beam and its end depends on the load and material.

5.4 Paradoxical weight minimization in curved beams

It is a well known fact that in some mechanical components the stresses can be relieved by wisely removing material. This interesting result is achieved by machining grooves in specific zones [116]. However, as far as elastic beams are concerned, this technique may not work properly, except for rare cases encountered in literature, specifically for straight beams subjected to bending [117]. For a straight beam, in particular, the zones from which a material removal, from a generic initial cross section, produces a bending stress reduction, are farthest from the neutral axis [23]. In the realm of curved beams modeled in terms of Winkler theory, it has been shown recently [109] that an analogous paradoxical behavior occurs by removing material from section zones close to the neutral axis. In a subsequent work [110],

$\tilde{\beta}$	$\tilde{\mu}$	$\tilde{\lambda}$	$\int_0^{1/2} a^*(s)\,ds$	$a^*(0)$	$a^*(1/2)$
0	0	π^2	0.4330	0	1.1545
1.5×10^{-2}	1×10^{-3}	9.7313	0.4376	0.1569	1.1580
	1×10^{-2}	9.8118	0.4350	0.1028	1.1560
1.5×10^{-1}	1×10^{-3}	8.3976	0.4637	0.5100	1.1597
	1×10^{-2}	8.4739	0.4628	0.5021	1.1599
	1×10^{-1}	9.3213	0.4504	0.3864	1.1603

Table 5.5: Optimal values of the goal functional, the minimal and maximal values of the normalized cross sectional area distributions for different instances of $\tilde{\beta}$ and $\tilde{\mu}$.

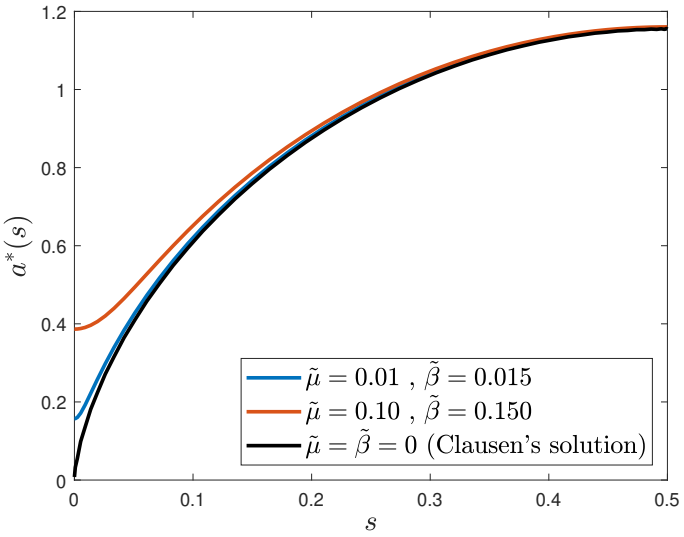

Figure 5.14: Numerical optimal cross sectional area distribution for two instances of $\tilde{\beta}$ and $\tilde{\mu}$ compared to Clausen's solution.

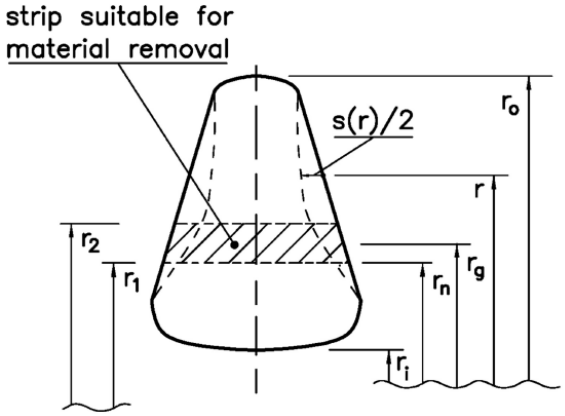

Figure 5.15: Initial cross section and its modifications by laterally removing material according to the cumulative removal depth function $s(r)$.

the demanding achievement of a concurrent stress and mass reduction is relaxed in favor of two weaker requests. One request consists in removing material from all sections without essentially altering the stress level in a generic section. The second request consists in removing material without increasing the stress in a most loaded section, and in removing material from the adjacent sections until the stress for a generic section equals the maximum stress. The second request may be interpreted as an application of the idea of uniform strength body.

Unlike [110], the delimiting radii defining the lateral lightening pocket are here assumed to be equidistant from the neutral radius. This assumption simplifies remarkably the functional expression for the intrados stress and leads to closed form solutions for the pocket width. Admittedly, solutions obtained with this simplification do not provide both mass and stress reduction at the same time. However, as shown below, significant mass reduction can be obtained at the cost of a small intrados stress increase.

5.4.1 Recall on the paradox

The theoretical framework of the paradoxical behavior is briefly recalled next. Consider a curved beam subjected to a bending moment and an axial force. Let A denote the cross section area, r_g the radius of the center of mass, r_n the neutral radius and r the radius of a generic line. See Figure 5.15, where a generic cross section is depicted. Let r_i and r_o be the inner and outer radii, respectively, and let r_1 and r_2 define the extrema of the groove

obtained as the consequence of a possible removal of material. Finally the cumulative lateral removal depth at the radius r is denoted by $s(r)$.

According to Winkler theory for curved beams, the bending and normal stresses for a generic radius r are given by

$$\sigma_M = \frac{M(r_n - r)}{A(r_g - r_n)r}\,, \quad \sigma_N = \frac{N}{A}\,, \tag{5.45}$$

where M and N denote the bending moment and the normal force, respectively. Herein, the simplifying assumption of a uniform normal force is adopted. In the following, as suggested by [109], a distinction is made between the symbols addressing the initial and modified cross sections. In particular, a subscript 0 is added to denote the variables belonging to the former.

The expression of the intrados stress functional in terms of the cumulative removal depth function $s(r)$ is given by [109, 118]

$$\sigma_i = \frac{M}{A_0 - \int_{r_i}^{r_o} s(r)\,dr} \frac{\left[\dfrac{A_0 - \int_{r_i}^{r_o} s(r)\,dr}{\frac{A_0}{r_{n,0}} - \int_{r_i}^{r_o} \frac{s(r)}{r}\,dr} - r_i\right]}{\left[\dfrac{A_0 r_{g,0} - \int_{r_i}^{r_o} s(r) r\,dr}{A_0 - \int_{r_i}^{r_o} s(r)\,dr} - \dfrac{A_0 - \int_{r_i}^{r_o} s(r)\,dr}{\frac{A_0}{r_{n,0}} - \int_{r_i}^{r_o} \frac{s(r)}{r}\,dr}\right] r_i}\,, \tag{5.46}$$

where A_0, $r_{g,0}$ and $r_{n,0}$ are the initial cross section area, center of mass and neutral radii, respectively, and a positive value of $s(r)$ describes a lateral removal of material. In [109], Equation (5.46) has been simplified by linearizing the effect of the removal depth $s(r)$ through a first order Taylor expansion based upon Gateaux differentiation, namely

$$\begin{aligned}\sigma_i \approx & \frac{M(r_{n,0} - r_i)}{A_0(r_{g,0} - r_{n,0})r_i} \\ & - \frac{M}{A_0^2(r_{g,0} - r_{n,0})^2 r_i} \int_{r_i}^{r_o} \frac{s(r)}{r}(r_{n,0} - r)[r(r_{n,0} - r_i) - r_{n,0}(r_{g,0} - r_i)]\,dr\,,\end{aligned} \tag{5.47}$$

where the first term expresses the initial intrados bending stress $\sigma_i|_{s=0}$. The factor multiplying $\frac{s(r)}{r}$ in the integrand of Equation (5.47) is a second-degree polynomial in r, whose roots are

$$r_1 = r_{n,0}\,, \quad r_2 = r_1 \frac{(r_{g,0} - r_i)}{(r_{n,0} - r_i)}\,. \tag{5.48}$$

The above polynomial remains positive for $r_1 < r < r_2$ and negative elsewhere. Consequently, if material is removed between the two roots r_1

and r_2, the paradoxical result is achieved according to which the intrados bending stress diminishes upon mass reduction.

In [110], the normal force has been taken into account, adding in (5.46) the term $\frac{N}{A_0 - \int_{r_i}^{r_o} s(r)\,dr}$ and a lightening pocket of rectangular profile described by linear $s(r)$ has been assumed, i.e.,

$$s(r) = \frac{2Sr}{r_1 + r_2}\,, \tag{5.49}$$

where $S > 0$ is a constant quantifying the mean cumulative groove depth; $s(r)$ is assumed to be non null only within the interval delimited by r_1 and r_2 and to be null elsewhere. This pocket shape is technically an approximation of a more realistic pocket with constantly deep bottom. Hence, two modifications of the strictly paradoxical approach have been proposed [110]. In particular, two conditions have been addressed:

- Unaltered intrados stress (UIS): The intrados stress of a particular groove-free cross section is assumed to be the reference stress and the maximum mass reduction of that particular cross section, achieved by laterally removing material, is sought under the condition that the intrados stress equals such reference stress;
- Imposed intrados stress (IIS): It requires that the radial extent of the lightening pocket produces a constant intrados stress with respect to a reference value when considering various sections along the beam axis. With this approach an optimized uniform-strength shape may be achieved.

While the achievement of closed form expressions for r_1 and r_2 after linearization and through implicit differentiation has been made possible only for UIS, on the other hand, for IIS, it was not possible to derive a closed form solution and it was necessary to compute r_1 and r_2 numerically. Here, an assumption on the shape of the lightening pocket is made. In particular, r_1 and r_2 are taken in such a way that the lightening pocket symmetrically straddles $r_{n,0}$. Consequently, the intrados stress expression becomes remarkably simplified and the proposed theory is more amenable to practically significant optimization applications.

5.4.2 Problem setup

For the sake of a simpler notation we introduce the following functionals:

$$x_1(r_1, r_2, s(r)) = \int_{r_1}^{r_2} s(r)\,dr\,,$$

$$x_2(r_1, r_2, s(r)) = \frac{1}{r_{g,0}} \int_{r_1}^{r_2} s(r) r \, dr \,,$$

and

$$x_3(r_1, r_2, s(r)) = r_{n,0} \int_{r_1}^{r_2} \frac{s(r)}{r} \, dr \,.$$

The dependence of these quantities on r_1, r_2 and $s(r)$ is omitted hereinafter. The integrals are defined from r_1 to r_2 since s is assumed to be null elsewhere. Taking into account the normal stress term, Equation (5.46) can be written as

$$\sigma_i = \frac{M\left[\frac{r_{n,0}(A_0 - x_1)}{A_0 - x_3} - r_i\right]}{(A_0 - x_1)\left[\frac{r_{g,0}(A_0 - x_2)}{A_0 - x_1} - \frac{r_{n,0}(A_0 - x_1)}{A_0 - x_3}\right] r_i} + \frac{N}{A_0 - x_1}. \tag{5.50}$$

Considering linear lightening pockets (obeying Equation (5.49)) around the neutral axis, i.e., such that

$$r_1 = 2r_{n,0} - r_2 \,, \tag{5.51}$$

one obtains $x_1 = S(r_2 - r_1)$, $x_2 = \frac{2S}{3r_{g,0}} \frac{r_2^3 - r_1^3}{r_1 + r_2}$ and $x_3 = x_1$. Accordingly, the intrados stress may be written as

$$\sigma_i = \frac{M(r_{n,0} - r_i)}{[r_{g,0}(A_0 - x_2) - r_{n,0}(A_0 - x_1)] r_i} + \frac{N}{A_0 - x_1}, \tag{5.52}$$

showing a remarkable complexity reduction with respect to (5.50). Equation (5.52) can be further simplified by linearizing the effect of the removal depth s through a first order Taylor expansion and omitting the nonlinear terms, namely

$$\Sigma = \frac{\Gamma}{A_0^2 (r_{g,0} - r_{n,0})^2 r_i} \,, \tag{5.53}$$

where $\Sigma = \sigma_i|_{s=0} - \sigma_i$ and

$$\Gamma = \int_{r_1}^{r_2} [M(r_{n,0} - r_i)(r_{n,0} - r) + N(r_{g,0} - r_{n,0})^2 r_i] s(r) \, dr \,.$$

Substituting (5.49) in (5.53) and rearranging, one obtains

$$\begin{aligned} \frac{A_0^2 \Sigma (r_{g,0} - r_{n,0})^2 r_i}{S} = {} & (r_2 - r_1) \left[M(r_{n,0} - r_i) r_{n,0} + N(r_{g,0} - r_{n,0})^2 r_i \right] \\ & - \frac{2M(r_{n,0} - r_i)}{3(r_1 + r_2)} (r_1^2 + r_1 r_2 + r_2^2)(r_2 - r_1) \,, \end{aligned} \tag{5.54}$$

which, together with (5.51), permits the groove delimiting radii r_1 and r_2 to be found. This problem setup presents a unified formulation for both conditions: Solutions of (5.54) and (5.51) with $\Sigma = 0$ and $\Sigma \neq 0$ give the lateral groove delimiting radii for the UIS and IIS conditions, respectively. Closed form solutions for delimiting groove radii are reported next.

5.4.3 Solution for purely flexural loads

The special case of purely flexural loading, i.e. $N = 0$, is emphasized first. While the UIS condition leads to the trivial solutions ($r_1 = r_2 = r_{n,0}$), the IIS condition for a grooved section yields

$$(r_2 - r_{n,0})^3 = \frac{-3A_0^2\Sigma(r_{g,0} - r_{n,0})^2 r_{n,0} r_i}{2M(r_{n,0} - r_i)S} \tag{5.55}$$

and the groove delimiting radii read

$$\begin{cases} r_1 = r_{n,0} + \sqrt[3]{\dfrac{3A_0^2\Sigma(r_{g,0} - r_{n,0})^2 r_{n,0} r_i}{2M(r_{n,0} - r_i)S}}, \\ r_2 = r_{n,0} - \sqrt[3]{\dfrac{3A_0^2\Sigma(r_{g,0} - r_{n,0})^2 r_{n,0} r_i}{2M(r_{n,0} - r_i)S}}. \end{cases} \tag{5.56}$$

It is appreciated that the above simplification of the expressions of r_1 and r_2 delimiting the groove produces approximations in the stress analysis of a curved beam. However, the two r_1 and r_2 values determined in [109, 110] with Gateaux linearization are themselves inevitably approximate.

As an example, Figure 5.16 shows the normalized radii r_1/b and r_2/b for a curved beam of square cross section of edge b for three imposed intrados stresses, 1%, 5% and 10% higher than $\sigma_i|_{s=0}$. The plotted values correspond to $r_i = 1$, $r_o = 2$ and $b = 1$. The corresponding neutral radius is $r_{n,0} = 1.442$. For small values of S/b, the radii r_1 and r_2 tend to the inner and outer borders r_i and r_o, respectively. This behavior is remarked as $\sigma_i/\sigma_i|_{s=0}$ increases. Since the neutral radius is lower than the radius of center of mass, the former is closer to r_1 than r_2 and solutions are thought valid and physically acceptable when $r_i < r_1 < r_2 < r_o$. These design limitations are represented by dashed lines in Figures 5.16, 5.17 and 5.18. For instance, a designer can not claim to impose an intrados stress 1.1 times than that of the groove-free section with $S/b = 0.1$ (see dashed lines in Figure 5.16).

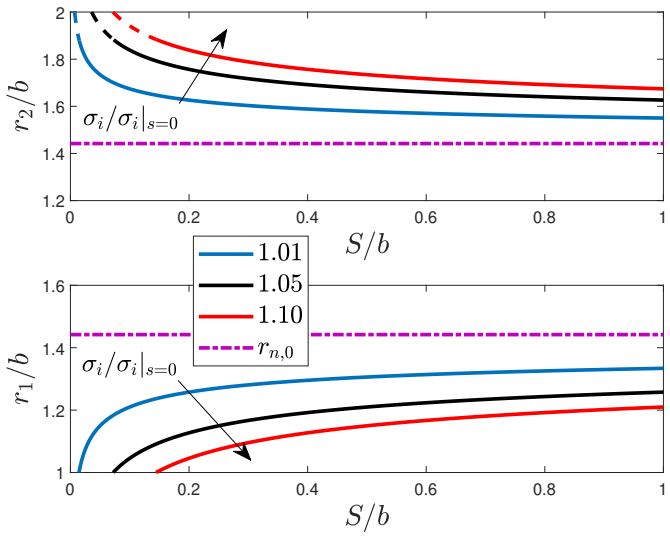

Figure 5.16: Normalized delimiting radii r_1/b (bottom) and r_2/b (top) b in terms of S/b for different values of $\sigma_i/\sigma_i|_{s=0}$ in a square section curved beam. Solid lines refer to acceptable solutions.

Mass reduction

Another effect of the machining of a groove symmetric with respect to $r_{n,0}$ is that solutions for imposed intrados stresses lower than $\sigma_i|_{s=0}$ are in $\mathbb{C}$, i.e. have an imaginary part, implying that they are not feasible. This fact entails that the relaxation of the strictly paradoxical approach in [109], namely linear groove around the neutral radius, cannot lead to the simultaneous reduction of mass and bending stress. However, significant mass reduction can still be achieved (see Figure 5.17, where the percentage mass reduction $\%m_R$ in terms of S/b for different values of $\sigma_i/\sigma_i|_{s=0}$ has been reported). In fact, by imposing $S/b = 0.5$ (an excessively thin hub thickness shall be avoided for stability-related issues [118, 119]), the reduction of the cross section is $(1.578 - 1.306) \times 0.5 \approx 0.136 = 13.6\%$, $(1.674 - 1.210) \times 0.5 \approx 0.232 = 23.2\%$ and $(1.734 - 1.150) \times 0.5 \approx 0.292 = 29.2\%$, for $\sigma_i|_{s=0}/\sigma_i = 1.01$, 1.05 and 1.10, respectively. For an intrados stress 1.2 times larger than that computed in the absence of groove, the delimiting radii are $r_1 = 1.074$ and $r_2 = 1.810$ and the corresponding section diminution is about 37%, while. In [110], the mass reduction for the same geometric parameters (b, r_i, r_o and S) turns out to be 40%, yet solutions were obtained numerically.

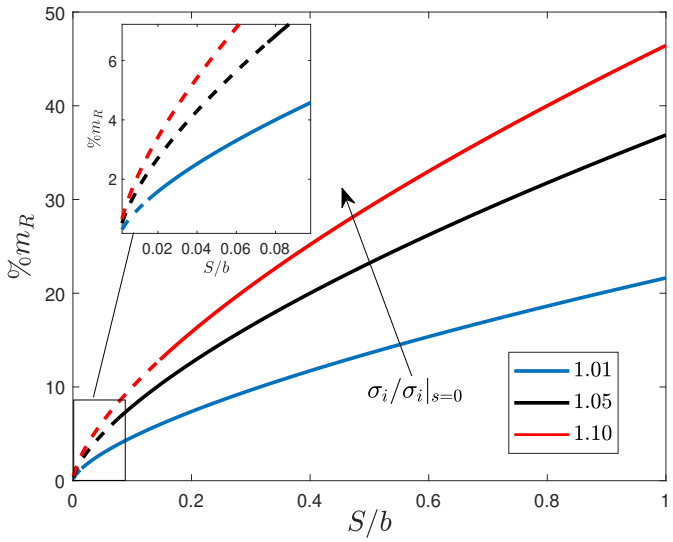

Figure 5.17: Percentage mass reduction $\%m_R$ in terms of S/b for different values of $\sigma_i/\sigma_i|_{s=0}$ in a square section curved beam. Solid lines refer to acceptable solutions.

Further comments

Figure 5.18 shows r_1/b and r_2/b for different values of S/b, as $\sigma_i/\sigma_i|_{s=0}$ increases. It is not hard to see that low values of S/b restrict the domain of desirable imposed intrados stresses with respect to those obtained in free-groove sections. Analogous to Figure 5.16, solutions are considered valid and physically acceptable when $r_i < r_1 < r_2 < r_o$: A designer can not claim to impose, for example, an intrados stress 1.25 times larger than that of the groove-free section with $S/b = 0.1$ or 0.3 (see dashed lines in Figure 5.18).

Eventually, Figure 5.19 reports on the $x-$axis the normalized imposed stress $\sigma_i/\sigma_i|_{s=0}$ and on the $y-$axis the normalized exact intrados stress $\sigma_{i,exact}/\sigma_i|_{s=0}$ computed using Equation (5.46). The cumulative groove depth is expressed by S and its value is kept fixed ($S/b = 0.5$). If the linearization provided exact results, the curve would mirror the x values over the y values. However, the nonlinear behavior is fiddling, showing that the nonlinear terms in the Taylor expansion series are limited, reaching a value of about 12% for $\sigma_i/\sigma_i|_{s=0} = 1.2$, which is technically acceptable. Moreover, for small x values, the linearization seems to fit very well.

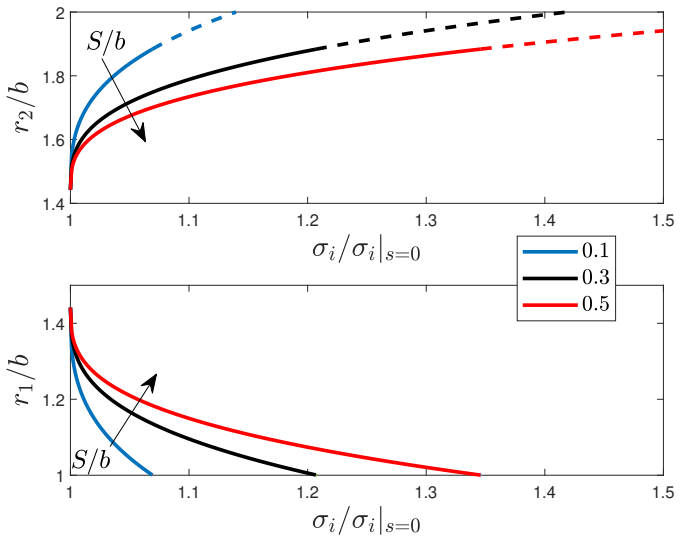

Figure 5.18: Normalized delimiting radii r_1/b (bottom) and r_2/b (top) in terms of $\sigma_i/\sigma_i|_{s=0}$ for different values of S/b in a square section curved beam. Solid lines refer to acceptable solutions.

5.4.4 Solution for flexural and normal loads

In the following, both flexural and normal stresses are considered. Starting from Equation (5.54) and calling $\bar{\Sigma} = \frac{A_0^2 \Sigma (r_{g,0}-r_{n,0})^2 r_i}{S}$ one obtains

$$\frac{\bar{\Sigma}}{M(r_{n,0}-r_i)} = 2(r_2 - r_{n,0}) \left[r_{n,0} - \frac{1}{3r_{n,0}}(r_2^2 + 4r_{n,0}^2 - 2r_{n,0}r_2) + \frac{N(r_{g,0}-r_{n,0})^2 r_i}{M(r_{n,0}-r_i)} \right]. \tag{5.57}$$

Recalling that $\sigma_i|_{s=0} = \frac{M(r_{n,0}-r_i)}{A_0(r_{g,0}-r_{n,0})r_i} + \frac{N}{A_0}$, Equation (5.57) may be recast as

$$(r_2 - r_{n,0})^3 - \left[\frac{3N(r_{g,0}-r_{n,0})r_{n,0}}{A_0(\sigma_i|_{s=0} - \frac{N}{A_0})} \right] (r_2 - r_{n,0}) + \frac{3\bar{\Sigma} r_{n,0}}{2M(r_{n,0}-r_i)} = 0. \tag{5.58}$$

Defining the parameters

$$p = \frac{-3N(r_{g,0}-r_{n,0})r_{n,0}}{A_0(\sigma_i|_{s=0} - \frac{N}{A_0})}, \quad q = \frac{3\bar{\Sigma} r_{n,0}}{2M(r_{n,0}-r_i)},$$

one obtains the following cubic equation

$$\rho^3 + p\rho + q = 0, \tag{5.59}$$

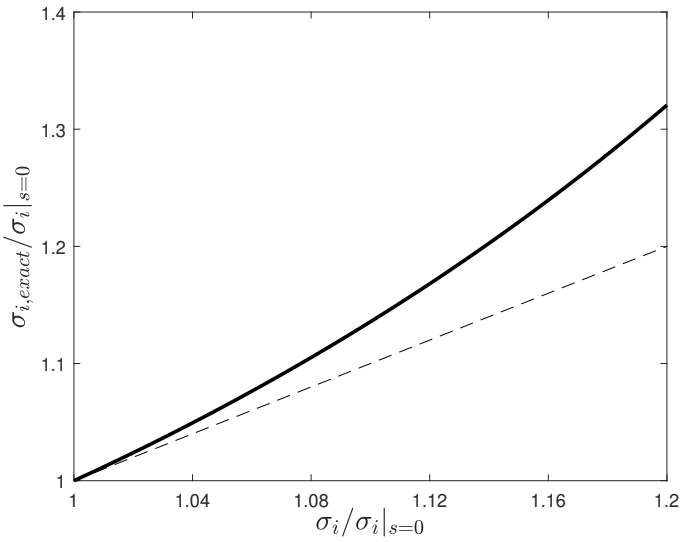

Figure 5.19: Normalized exact stress versus the normalized linearized stress and the effect of nonlinear terms for $S/b = 0.5$ in a square section curved beam.

where $\rho = r_2 - r_{n,0}$. Obviously, assuming $N = 0$, Equation (5.59) turns to be (5.55). Solutions of (5.59) for the UIS and IIS conditions are

$$r_2 = r_{n,0} + \sqrt{\frac{3N(r_{g,0} - r_{n,0})r_{n,0}}{A_0(\sigma_i|_{s=0} - \frac{N}{A_0})}} \tag{5.60}$$

and

$$r_2 = r_{n,0} + \sqrt[3]{-\frac{q}{2} + \sqrt{\frac{q^2}{4} + \frac{p^3}{27}}} + \sqrt[3]{-\frac{q}{2} - \sqrt{\frac{q^2}{4} + \frac{p^3}{27}}}\,, \tag{5.61}$$

respectively. The discussion of Equations (5.60) and (5.61) is provided within the numerical example given below.

A numerical example: crane hook optimization

Following [120], a crane hook of square section is considered. The length of the sides of the square section is 12 mm. The applied load P is 5600 N. The inner radius $r_i = 24$ mm, the outer radius $r_o = 36$mm and the cross section $A_0 = 144$ mm^2. Consequently, $r_{n,0} = 29.5956$ mm and $r_{g,0} = 30$ mm. The

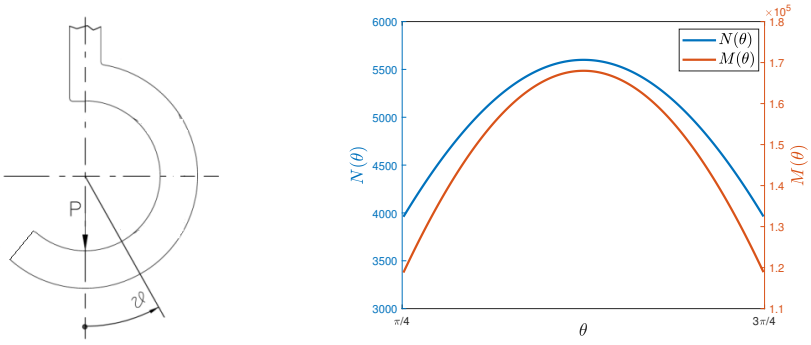

(a) (b)

Figure 5.20: Initial geometry of the crane hook and definition of the angle θ (a). Normal force and bending moment in function of θ (b).

cumulative groove depth S has been imposed to be 4.8 mm. Denoting by θ the angle measured counterclockwise from the vertical line passing through the hook center (see Figure 5.20a) the maximum bending moment M is $Pr_{g,0}\sin\theta$, while the corresponding normal force N is $P\sin\theta$. Consequently, the maximum values for M and N are achieved at $\theta = \pi/2$ (see Figure 5.20b, where $M(\theta)$ and $N(\theta)$ are plotted for $\theta \in [\pi/4, 3\pi/4]$). The analytical maximum intrados bending stress is 672.70 MPa, the maximum normal stress is 38.89 MPa, so that the total maximum intrados stress is $\bar{\sigma} = 711.59$ MPa.

To derive a graphical representation of the stress distribution along the crane hook, a three-dimensional FE model has been developed. To assess the validity of numerical solutions, a convergence analysis has been done and a mesh of tetrahedral elements has been employed (with about 153000 elements and 30000 nodes). The upper surface has been clamped and the concentrated force has been modeled as a uniformly distributed pressure acting along three adjacent rows of intrados nodes defined by $\theta = 0$.

The determination of the values of r_1 and r_2 so that, for a general section, the intrados stress equals its ungrooved analogue (UIS condition) is firstly addressed. Since for the hook loading the bending moment M is proportional to the normal force N for any value of θ, the radii delimiting the groove width remain constant. Their values $r_2 = 31$ mm and $r_1 = 28.19$ mm are computed with (5.60) and (5.51), respectively. The area diminution with respect to the ungrooved geometry is 9.36%, about two percent higher than that obtained in [109]. Figure 5.21a shows the von Mises stress field, whose

	UIS	IIS
σ_i [MPa]	741	808
$\frac{\sigma_i - \bar{\sigma}}{\sigma_i}$ [%]	3.96	11.93
m_R [%]	9.36	18.00
$r_1/b\|_{\theta=\pi/2}$ [-]	2.349	2.349
$r_2/b\|_{\theta=\pi/2}$ [-]	2.583	2.583

Table 5.6: FE maximum intrados stress σ_i, deviation from analytical solution, mass reduction and normalized pocket delimiting radii at $\theta = \pi/2$ for UIS and IIS conditions.

maximum value is about 741 MPa occurring at $\theta = \pi/2$, agreeing well with analytical result.

When considering the IIS condition, the reference intrados stress is the bending plus the normal stress for $\theta = \pi/2$. A lateral groove is therefore manufactured so that intrados stress in the understressed regions increases. The values adopted for the radii delimiting the groove width have been computed using (5.61) and (5.51) for an angular interval around $\theta = \pi/2$. The profile is clearly shown in Figure 5.21b. However, in order to avoid unfeasible solutions, the inner and outer borders have been superimposed to be at least 2 mm thick. This value has been chosen, after several FE simulations, as the minimum value guaranteeing an acceptable stress concentration factor in this region. FE simulations (Figure 5.21b) evidence that around $\theta = \pi/2$ the hook exhibits a constant intrados stress of about 808 MPa, corresponding to a volume reduction of 18% and highlighting that the relaxation made in this paper does not lead to simultaneous reduction of bending stress and mass. However, the variation with respect to the analytical counterpart is $\frac{\sigma_i - \bar{\sigma}}{\sigma_i} \approx 0.1193 = 11.93\%$, which is technically acceptable taking into account the inevitable discrepancy between the 1D nature of Winkler model and the 3D nature of the FE model. For comparison, in [110] the numerical evaluation of the delimiting radii produced a weight reduction of 23.88%. Finally, Table 5.6 summarizes the achieved results by the two conditions in terms of maximum stress, deviation from analytical result and mass reduction.

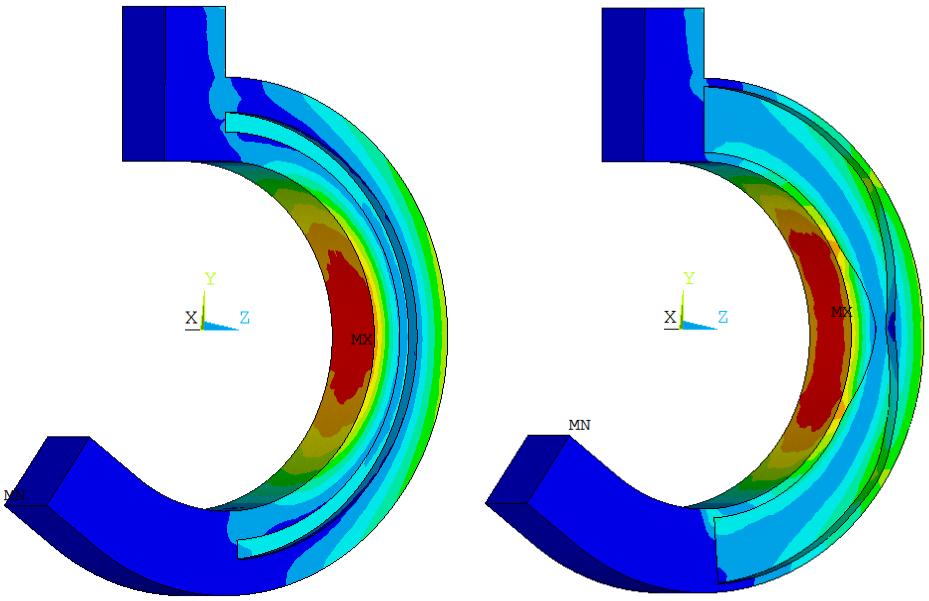

(a) (b)

Figure 5.21: FE model and von Mises stress distribution in the crane hook for the UIS (a) and IIS (b) conditions.

5.5 Summary

This chapter dealt with several optimization problems in the realm of one-dimensional structural elements. In particular, beams with an initially straight axis have been considered. Potential cost functionals and constraints were the material mass, the compliance and the buckling load. Also, a problem including a recently stated paradox have been formulated, whose optimal solutions have been derived in both analytical and numerical fashions, depending on the resulting necessary conditions.

Chapter 6

Functionally graded pressurized cylinders

6.1 Introduction

In recent years, composite materials have been used in many applications in civil and mechanical engineering. They consist of an assembly of layers of fibrous metallic, ceramic or polymeric materials distributed in a matrix, allowing excellent combinations between different materials. However, since they are realized by means of discrete change of properties, interlaminar shear stresses may arise, which may cause failure by delamination. A smoother change of properties can be achieved by using novel heterogeneous composite materials called "Functionally Graded Materials" (FGMs), whose constituents (e.g., a metal and a ceramic) spatially grade according to specific requirements which may range from a response to deformation, to corrosion and wear. Due to their excellent mechanical performance, they are gradually being more and more used in mechanical and aeronautical applications.

The general idea of structural gradients was first advanced for composites in the Seventies [121]. However, there was no genuine investigation about how to design, fabricate and evaluate graded structures until the Eighties [24]. More recently, FGMs are present in many engineering applications such as space shuttles, nuclear fusion reactors and energy conversion systems [122]. Since FGMs are not homogeneous materials, it is clear that in order to create them, comprehensive studies need to be performed in design methodology and theoretical modeling as well as in processing and properties evaluation. On the other hand, unlike conventional homogeneous materials,

the spatial variation of mechanical and physical properties in FGMs can be exploited to obtain better performances by microstructural control.

Generally, the variation in material properties of FGMs is exclusively examined within two categories of analyses. While in the first one the mechanical and physical properties are assumed to vary according to specific functions with respect to spatial coordinates by means of the so called *heterogeneity factors*, the second category is based on the description of the material heterogeneity by means of volume fractions of the constituents. Volume fractions are in turn linked to the material properties through the so called *micromechanical models*, which may range from explicit traditional rule of mixtures, such as Voigt, Reuss, Mori-Tanaka and Wakashima-Tsukamoto models, to implicit ones (such as Hill-Budianski model) to variational ones (e.g., Hashin-Shtrikman model) [24]. Works pertaining to both categories can be found in the literature concerning, for instance, the torsion in bars [123], the stress concentration factors and the static, buckling, and free- and forced-vibration in plates [124, 125] as well as the out of plane displacement field in inclined cracks [126].

As far as axisymmetric bodies are concerned, several papers are devoted to the stress analysis in hollow cylinders subject to internal pressure [127], thermal [128] and axial [129] loads, pressure vessels [130] and rotating disks [131]. The optimum response of the material to an actual environment is one of the most important aspects in the design of FGMs [132], leading to interesting results for several different functionally graded structures. However, the overwhelming majority of works belongs to the first category, namely dealing with optimization problems in FGMs which consist in finding the values of some tuning parameters of the heterogeneity factors for prefixed types of property variations (e.g., power-law, exponential, trigonometric models, etc.) such that an objective function is minimized or maximized. Gradient-based methods as well as meta-heuristic algorithms led researchers towards these objectives. For instance, a finite element based optimization of a pressure vessel consisting in a finite length hollow cylinder and two spherical closed ends has been performed in [133]. In [134], a combination of a co-evolutionary particle swarm optimization approach coupled with a differential quadrature method is applied to obtain minimized stress and displacement fields through the geometry of a disk under thermoelastic loads. Not by chance, the aforementioned works consider power-law property distributions, as they are simple and allow closed-form solutions amenable for numerical optimization, yet imposing considerable limitations to the generalization of the optimization procedures. Another strong limitation not mentioned in the aforementioned works is that once fixed

the class of property variation and once the optimized heterogeneity factors have been found, optimal solutions for material properties do not necessarily give rise to realistic structures, i.e., with unfeasible associated metallic and ceramic volume fractions, being considered a micromechanical model.

The above mentioned facts entail that a more intrinsic optimization procedure should a priori consist in the search for the best volume fractions and not merely in the tuning of the parameters of prefixed property behaviors. In this case, the formulation of the resulting problem is also useful from the technological viewpoint. In fact, although it must be based on a micromechanical model to relate elastic properties to volume fractions, it does not hinder one to deal with a specified class of functions describing property variations. Only a few studies concerning with a material tailoring approach have been addressed. For instance, the simultaneous optimization of material properties and structural layout for an elastic continuum with maximum structural stiffness is formulated and analyzed in [135]. The optimization of a two-phase isotropic composite under time-dependent thermomechanical loadings with no a priori assumptions are made regarding the spatial distribution of each phase is addressed in [136]. In [137], an algorithm is proposed to minimize the time-averaged stress energy of a two-phase composite under dynamic loading. A three-layer cylinder consisting of a functionally graded interlayer sandwiched between a metallic layer and a ceramic layer is considered in [138], where the problem of finding the interlayer composition profile minimizing the stresses resulting from material property mismatch and induced in the cylinder by temperature and pressure loading is addressed. In [139], thermoelastic bodies composed of two-constituent FGMs under steady-state conditions are considered and the problem of the optimal choice of composition profile is addressed. Moreover, in [140, 141], the inverse problem of finding the variation with the radius of the shear modulus is considered, yet it is desired that the difference between the radial and the hoop stress satisfies a particular relation along the radius. Moreover, in [142], the shear modulus such that stresses radially evolve in rubber-like cylinders and spheres within a more general functional constraint is sought. These three latter works give nontrivial peculiarities, however they have been written in a context different from that of optimal design, which is the framework that the present chapter belongs to.

The present chapter addresses the problem of finding the optimal composition profile of the constituents for cylinders subject to mechanical loadings and for which plane elasticity holds. The material is assumed to be functionally graded in the radial direction. In light of these considerations, equilibrium, compatibility and constitutive relations are firstly recalled. The

problem of minimizing the equivalent stresses is formulated in two different ways. The first one is exclusively based on the radial stresses and can lead to an analytical solution under some mild hypotheses if Pontryagin's Principle is properly employed, however some critical remarks are observed so that it is found to be not exhaustive. Another formulation is therefore given in terms of both radial stress and radial displacement, yet hinders one to resort to numerical tools presented in Chapter 3. Nevertheless, in both cases optimal solutions perform better than classic variations distributions commonly employed in the literature and lead to promising results in terms of stress reduction.

6.2 Governing equations

Consider a radially graded axisymmetric cylindrical body and let R_i and R_o denote the inner and outer radii, respectively. Define a cylindrical coordinate system and let the radial, circumferential and axial coordinates be denoted by r, θ and z, respectively. If the body is subject to an axially-uniform and axisymmetric load, then deformations are also axisymmetric, i.e., they vary only in the radial direction. In particular, the strains and the internal stresses, denoted by ε_i and σ_i (with $i = r, \theta, z$), respectively, are supposed to be continuous functions of r only. According to the theory of elasticity, a problem may be simplified if either one of the stresses or the strains is zero along a particular direction. Such behaviors are referred to as plane stress (in which a generic infinitesimal element is subject to a biaxial stress condition accompanied by a triaxial strain state) and plane strain (in which a generic infinitesimal element is subject to a triaxial stress condition accompanied by a biaxial strain state), respectively. The resulting elastic problem may be formulated following either Navier or Beltrami-Michell approaches, so far as boundary conditions are expressed in terms of radial displacements or stresses, respectively [143]. With reference to the latter approach, the equilibrium equation written for the infinitesimal element in the radial direction and the consideration of Hooke's constitutive laws for linear, elastic, isotropic and non-homogeneous materials entail that both the hoop σ_θ and axial σ_z stresses may be written in terms of the radial stress σ_r. Consequently, the stress analysis may be described in terms of σ_r only.

6.2.1 Equilibrium, kinematic and constitutive laws

According to the infinitesimal linear elasticity theory (in absence of body forces), the stress equilibrium equation in the radial direction may be written

in the form [144]

$$(r\sigma_r(r))' - \sigma_\theta(r) = 0\,, \tag{6.1}$$

where the prime symbol denotes a first derivative with respect to r. The strain-displacement (or kinematic) equations for an axisymmetric body loaded by axisymmetric forces are

$$\varepsilon_r(r) = u'(r)\,, \quad \varepsilon_\theta(r) = u(r)/r\,, \tag{6.2}$$

where u is the radial displacement, while the plane stress state Hookean constitutive relations in terms of Young's modulus E and Poisson's coefficient ν are

$$\begin{cases} \varepsilon_r(r) = \dfrac{\sigma_r(r) - \nu(r)\sigma_\theta(r) - \nu(r)\sigma_z(r)}{E(r)}\,, \\ \varepsilon_\theta(r) = \dfrac{\sigma_\theta(r) - \nu(r)\sigma_r(r) - \nu(r)\sigma_z(r)}{E(r)}\,, \\ \varepsilon_z(r) = \dfrac{\sigma_z(r) - \nu(r)\sigma_\theta(r) - \nu(r)\sigma_r(r)}{E(r)}\,. \end{cases} \tag{6.3}$$

Situation where the axial stress or the axial strain identically vanishes throughout the domain are referred to as plane stress and plane strain conditions, respectively. It is emphasized that the Hookean constitutive relations for the plane strain condition can be obtained from the plane stress condition by substituting E with $\frac{E}{1-\nu^2}$ and ν with $\frac{\nu}{1-\nu}$ [144].

6.2.2 Micromechanical models

Realistic predictions of the stress and strain behavior of FGMs require appropriate constitutive relations. This aspect represents the most significant difficulty in FGM modeling when subjected to thermal or mechanical loading conditions. Efforts to analytically determine the effective properties of heterogeneous structures were initiated more than a century ago by such famous scientists as Maxwell, Lord Rayleigh, and Einstein [24]. Recently, due to the increased interest in composite structures for industrial applications, the subject of composite materials properties has been thoroughly developed, and a large literature nowadays exists. In several extensive review articles and textbooks, both good overviews of the subject and insight into the significant involved complexities are provided (see, e.g., [145, 146]). For simple geometries and reasonably simple material properties (e.g., elastic behavior) analytical solutions are often available in terms of volume fractions. It is worthwhile to note that in case the micromechanical

models are expressed in terms of effective bulk K and shear G moduli, these latter, due to the isotropy assumption, are linked to the Young's modulus E and Poisson's ratio ν by the relations

$$E = \frac{9KG}{3K + G} \tag{6.4}$$

and

$$\nu = \frac{3K - 2G}{2(3K + G)}\,, \tag{6.5}$$

respectively.

Voigt (V) and Reuss (R) models

The simplest micromechanical model to achieve the equivalent macroscopic material properties is the rule of mixture which was first formulated by Voigt. Voigt's idea is to determine material properties by averaging stresses over all phases with the strain uniformity assumption within the material [24]. The resulting model, that is frequently used in most FGM analyses, estimates effective properties P as a volume based arithmetic average, i.e., [147]

$$P(r) = P_m V_m(r) + P_c V_c(r), \tag{6.6}$$

where P_m and P_c are bulk properties of the metal and ceramic constituents and $V_m(r)$ and $V_c(r)$ are their volume fractions at the generic radius r, respectively, and related to each other by the relation

$$V_c(r) + V_m(r) = 1. \tag{6.7}$$

It is convenient to rewrite (6.6) in terms of one volume fraction function only (usually V_c) exploiting (6.7), namely

$$P(r) = P_m[1 - V_c(r)] + P_c V_c(r) = P_m + (P_c - P_m)V_c(r). \tag{6.8}$$

Another well-known mixture rule is that based on the harmonic mean estimate (Reuss model), namely [24]

$$P(r) = \frac{P_c P_m}{P_m V_c(r) + [1 - V_c(r)]P_c}. \tag{6.9}$$

In their most basic form, the above rules of mixtures are employed using bulk constituent properties, assuming no interactions between phases. They are often used for FGMs, since a single relationship can be used for all volume fractions and microstructures. However, due to their simplicity, their validity is limited.

Mori-Tanaka (MT) model

The Mori-Tanaka model provides estimates for effective mechanical properties of a graded microstructure with ceramic and metal phases. The steps for obtaining the overall material properties depend on the bulk and shear moduli of the metal and the ceramic. More precisely, if K_m and K_c, G_m and G_c denote bulk and shear moduli of the metal and ceramic, respectively, the effective bulk K and shear G moduli are given by [148]

$$K(r) = \frac{(K_c - K_m)V_c(r)}{1 + \frac{3(K_c - K_m)}{3K_m + 4G_m}(1 - V_c(r))} + K_m \tag{6.10}$$

and

$$G(r) = \frac{(G_c - G_m)V_c(r)}{1 + \frac{(G_c - G_m)}{G_m + \frac{G_m(9K_m + 8G_m)}{6(K_m + 2G_m)}}[1 - V_c(r)]} + G_m, \tag{6.11}$$

and E and ν are given by (6.4) and (6.5), respectively.

Other models

It is worth to note that several other models are covered in the literature, such as the models proposed by Kerner [149], Hashin and Shtrikman [150], Tamura [151], Wakashima and Tsukamoto [152], etc. A comparison of various analytical methods with experimental data is graphically made to find out the best suitable micromechanical model in [153]. Notwithstanding the above mentioned models generally yield dissimilar estimates (discrepancies of more than 50% may be observed in the case of some volume fractions [125]), they are explicit in terms of phases' volume fractions, offering a possibility to estimate the FGM properties for the whole composition range with a single model.

6.3 Formulations of the optimization problem

Consider a cylinder subject to an intrernal pressure and made of FGM, whose microstructure compositionally grades from a ceramic to metallic materials, whose bulk mechanical properties are generically denoted by P_c and P_m, respectively. In order to formulate the optimization problem in the context of dynamic optimization theory, a state-space representation, boundary conditions and a goal functional are needed. Reference is made to two different formulations. The first one is based on the Beltrami-Michell approach, namely states are given by stresses and their derivatives. The

other formulation includes both the radial displacement and the radial stress, and therefore referred to as Beltrami-Michell-Navier based formulation.

6.3.1 A Beltrami-Michell based formulation

For the sake of simplicity, let the Poisson's ratio be constant throughout the radial domain and only the Young's modulus be the only mechanical property that vary. The radial strain in Equation (6.2) can be written as

$$\varepsilon_r(r) = (\varepsilon_\theta(r) r)' = \left(\frac{\sigma_\theta(r)}{E(r)} r - \nu \frac{\sigma_r(r)}{E(r)} r \right)', \tag{6.12}$$

which, together with Equation (6.3), yields

$$(1+\nu)[\sigma_\theta(r) - \sigma_r(r)]E(r) - [\sigma_\theta(r) - \nu\sigma_r(r)]E'(r)r + E(r)[r\sigma'_\theta(r) - \nu r\sigma'_r(r)] = 0. \tag{6.13}$$

From Equation (6.1) the hoop stress and its first derivative with respect to r are

$$\sigma_\theta(r) = \sigma_r(r) + r\sigma'_r(r) \tag{6.14}$$

and

$$\sigma'_\theta(r) = 2\sigma'_r(r) + r\sigma''_r(r), \tag{6.15}$$

respectively. Substituting Equations (6.14) and (6.15) in (6.13) and rearranging the terms one obtains

$$\mathcal{O}\sigma_r(r) = 0 \tag{6.16}$$

where $\mathcal{O}$ is a differential operator given by

$$\mathcal{O}(*) = r^2(*)'' + r[3 - r\mathcal{E}'(r)](*)' - \tilde{\nu}\mathcal{E}'(r)r(*) \tag{6.17}$$

with $\mathcal{E} = \ln(E)$ and $\tilde{\nu} = 1 - \nu$. If the plane strain condition holds, the differential operator reads

$$\mathcal{O}(*) = r^2(*)'' + r[3 - r\mathcal{E}'(r)](*)' - \breve{\nu}\mathcal{E}'(r)r(*), \tag{6.18}$$

where $\breve{\nu} = 1 - \frac{\nu}{\tilde{\nu}}$.

Hereinafter, the Young's modulus is expressed as a function of the ceramic volume fraction, namely $E = E(V_c)$. Therefore, the term $\mathcal{E}'$ can be written as

$$\mathcal{E}' = (\ln(E(V_c)))' = g(V_c)v_c\,, \tag{6.19}$$

where $v_c = \frac{dV_c}{dr}$ is the rate of change of the ceramic volume fraction through the domain and is chosen to be the input function, while

$$g(V_c) = \frac{1}{E(V_c)} \frac{dE(V_c)}{dV_c} \,,$$

whose explicit expression is derived from the involved micromechanical model. Just by way of an example,

$$g(V_c) = \frac{1}{\frac{E_m}{E_c - E_m} + V_c}$$

and

$$g(V_c)) = \frac{E_c - E_m}{E_m V_c + (1 - V_c) E_c}$$

for Voigt and Reuss models, respectively. Introducing the state variables $x_1 = \sigma_r$, $x_2 = d\sigma_r/dr$ and $x_3 = V_c$, the differential equation (6.16) may be written as the first-order nonlinear system

$$\begin{cases} x_1'(r) = x_2(r) \,, \\ x_2'(r) = g(x_3(r)) \left(x_2(r) + \tilde{\nu} \dfrac{x_1(r)}{r} \right) v_c(r) - \dfrac{3 x_2(r)}{r} \,, \\ x_3'(r) = v_c(r) \,, \end{cases} \tag{6.20}$$

or, defining $\mathbf{x} = (x_1 \; x_2 \; x_3)$, in more compact form as

$$\mathbf{x}'(r) = \mathbf{f}(r, \mathbf{x}(r), v_c(r)) \,. \tag{6.21}$$

Note that not all the boundary states are specified. In particular, $x_1(R_i)$ and $x_1(R_o)$ can be deduced from the mechanical loads, yielding

$$x_1(R_i) = -p_i \,, \quad x_1(R_o) = 0 \,, \tag{6.22}$$

where p_i is the internal pressure, while $x_2(R_i)$ and $x_2(R_o)$ are unknown. As far as concerns x_3, if the cylinder is compositionally graded from ceramic to metal, then

$$x_3(R_i) = 1 \,, \quad x_3(R_o) = 0 \,. \tag{6.23}$$

Firstly, a goal functional of the Mayer form is considered, consisting in a function $\mathcal{K}$ depending on the initial and final state conditions, namely

$$J(v_c) = \mathcal{K}(\mathbf{x}(R_i), R_i, \mathbf{x}(R_o), R_o) \,. \tag{6.24}$$

Taking into account the plane stress condition and using the above introduced state variables and Equation (6.14), the equivalent Tresca stress may be written as

$$\sigma_{eq}^{T}(r) = |\sigma_\theta(r) - \sigma_r(r)| = |x_1(r) + rx_2(r) - x_1(r)| = |rx_2(r)|\,.$$

Now if the body is pressurized only internally, x_1 strictly increases along the radius, and therefore $x_2 > 0$. Consequently, the absolute value can be omitted and

$$\mathcal{K} = x_2(R_i)$$

leads to the minimization of the internal Tresca stress, being fixed R_i. The same problem can be stated within the plane strain condition, taking into account that

$$\sigma_z(r) = \nu[\sigma_r(r) + \sigma_\theta(r)] = \nu[2x_1(r) + rx_2(r)]\,.$$

According to [132], there are a few optimization studies in which the manufacturability cost is taken into consideration. Adding technological constraints to the optimization studies is highly recommended since it leads to more practical designs with prospects of being produced in large scales. To this purpose, one may model the cost in such a way that steep variations of the volume fractions along the radius are, reasonably, more costly and more difficult to obtain than moderate variations. As a consequence, in the present optimization framework, it is reasonable to assume that v_c be constrained in an admissible range of values. More precisely, we assume, for all values of r, $v_c \in [v_-, v_+]$. However, the following analysis remains unchanged if, instead of $[v_-, v_+]$, one considers the union of a set of disjoint closed and bounded intervals $[v_-, v_1] \cup [v_2, v_3] \cup \ldots \cup [v_n, v_+]$, with $v_- < v_1 < \ldots < v_n < v_+$, thus including in the model also situations for which, for some technological reasons, some values of v_c between v_- and v_+ are not admissible. Suitable values for v_- and v_+ can be deduced from fixed radial property variations or from technological process data.

The optimization problems can now be stated formally. In the formulation of the problem, as well as in the computation of the solution, reference is made to the goal functional (6.24) in its general form. Hence, solutions to the inner Tresca stress minimization problem within the plane stress and plane strain conditions can be found in a common fashion.

Problem 6.1. *Find the distribution of the derivative of the ceramic volume fraction $v_c^*(r)$ so that the inner Tresca stress due to internal pressure is as*

minimum as possible, i.e.,

$$
\begin{aligned}
\min_{v_c(r)} \quad & \mathcal{K} = x_2(R_i) \\
s.t. \quad & x_1'(r) = x_2(r)\,, \\
& x_2'(r) = g(x_3(r)) \left(x_2(r) + \tilde{\nu} \frac{x_1(r)}{r} \right) v_c(r) - \frac{3x_2(r)}{r}\,, \\
& x_3'(r) = v_c(r)\,, \\
& x_1(R_i) = -p_i\,, \\
& x_1(R_o) = 0\,, \\
& x_3(R_i) = 1\,, \\
& x_3(R_o) = 0\,, \\
& v_- \leq v_c(r) \leq v_+\,, \\
& 0 \leq x_3(r) \leq 1\,,
\end{aligned}
\tag{6.25}
$$

where R_i, R_o, v_-, v_+, p_i and $\tilde{\nu}$ are given constants and g is a specified function.

Pontryagin's principle applied to Problem 6.1 states that the optimal control function v_c, i.e., the one which minimizes the cost functional $J(v_c)$ is, among all admissible functions, the one which, at any value of r, minimizes the Hamiltonian function $\mathcal{H}(r, \mathbf{x}, \mathbf{p}, v_c)$ which, recalling Equation (2.13), it is given by

$$
\mathcal{H}(r, \mathbf{x}, \mathbf{p}, v_c) = s(r, \mathbf{x}, \mathbf{p}) + q(r, \mathbf{x}, \mathbf{p})\, v_c\,, \tag{6.26}
$$

where $\mathbf{p} = (p_1 \;\; p_2 \;\; p_3)$ is the vector of the costate variables associated with the states $\mathbf{x}$, all functions of r, whereas s and q are functions of the states and costates, whose explicit expressions for the plane stress condition are given by

$$
s = p_1 x_2 - \frac{3 p_2 x_2}{r}\,, \quad q = g(x_3) p_2 \left(x_2 + \tilde{\nu} \frac{x_1}{r} \right) + p_3\,. \tag{6.27}
$$

It is worth noting that the problem is characterized by a Hamiltonian function linear with respect to v_c and since the set of admissible values for v_c is compact, Pontryagin's Principle yields extremal solution for the minimization of (6.26). More precisely, the optimal control function v_c^* is defined, when $q \neq 0$, by

$$
v_c^*(r) = \arg\min_{v_c} \mathcal{H}(r, \mathbf{x}, \mathbf{p}, v_c) = \begin{cases} v_-\,, & \text{if } q(r, \mathbf{x}, \mathbf{p}) > 0\,, \\ v_+\,, & \text{if } q(r, \mathbf{x}, \mathbf{p}) < 0\,, \end{cases} \tag{6.28}
$$

that is, the optimal control function may undergo two scenarios. In the first one, the v_c^* assumes its minimum or maximum value, possibly switching among them when $q = 0$. In the parlance of control theory, the design admits a "bang-bang" control, jumping in value at certain points r_j (with $j = 1, 2, 3, \dots$). The roots of q are called *switching points* since the control function switches from a bound to the other. In the second scenario, q vanishes in a finite length interval and the solution in this subinterval shall be found from other considerations. For the sake of analytical tractability, the investigation of the second scenario is omitted. Hence, recalling the definition of v_c, optimal ceramic volume fraction V_c^* turns out to be piece-wise linear with respect to r. This conclusion is particularly interesting since the piece-wise linearity is supposed to be the simplest volume fraction profile among all possible forms of variation.

Equation (6.28) does not yet provide the explicit expression of the optimal solution; in fact, it is clear that in order to know the explicit value of v_c for any value of r one should know the value of q. In turn, the computation of q requires the knowledge of the solution of the dynamical system (6.20) and of the differential equations (2.18), which for the plane stress condition are given by

$$\begin{cases} p_1'(r) = -\dfrac{\tilde{\nu}\, p_2(r)\, g(x_3(r))\, v_c(r)}{r}, \\ p_2'(r) = -p_1(r) - p_2(r)\, g(x_3(r))\, v_c(r) + \dfrac{3p_2(r)}{r}, \\ p_3'(r) = -p_2(r)\, \dfrac{dg(x_3)}{dx_3}\, v_c(r) \left(x_2(r) + \tilde{\nu} \dfrac{x_1(r)}{r} \right). \end{cases} \tag{6.29}$$

Moreover, boundary conditions for costates are determined by Equations (2.22) and (2.23) which, once again, for the plane stress condition, yield

$$p_2(R_i) = -1\,, \quad p_2(R_o) = 0\,. \tag{6.30}$$

The state-space representation, boundary states, costate equations and boundary costates for the plane strain condition are the same as (6.20)-(6.23), (6.29) and (6.30), provided that $\tilde{\nu}$ is replaced by $\breve{\nu}$.

A special attention is drawn to the case in which q has only one root, i.e., when the optimal solution admits a single switching point. Beside its simplicity, this choice is justified since the resulting volume fraction profile is amenable for physical realization from the technological viewpoint. Denoting by $\bar{v}$ the rate of the linear variation between $x_3(R_i) = 1$ and $x_3(R_o) = 0$, namely

$$\bar{v} = -\frac{1}{R_o - R_i}\,,$$

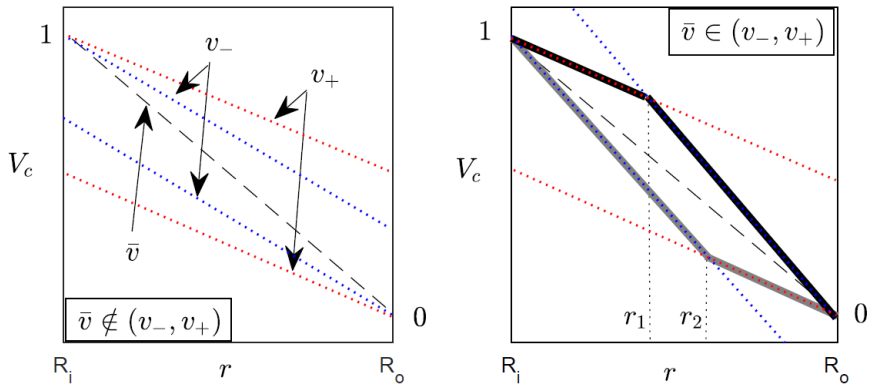

Figure 6.1: Optimal control function V_c^* and definition of $\bar{v}$, v_-, v_+, r_1 and r_2. Case $\bar{v} \notin [v_-, v_+]$ (left) where no solutions are feasible and $\bar{v} \in [v_-, v_+]$ (right) where two solutions may exist (black and grey solid lines).

two situations may occur. Firstly, if $\bar{v} \notin [v_-, v_+]$, there is no feasible solution, since no variation $v_c : [R_i, R_o] \to [v_-, v_+]$ is consistent with the boundary conditions (see Figure 6.1, left). As a consequence, no optimal solution exists either. On the other hand, if $\bar{v} \in [v_-, v_+]$, two optimal solutions are possible. More precisely, one characterized by a subinterval in which $v_c = v_+$ followed by a subinterval in which $v_c = v_-$ (black bold line in Figure 6.1, right) and the other one with the opposite situation (first $v_c = v_-$ and then $v_c = v_+$, as in the grey bold line in Figure 6.1, right). With reference to Figure 6.1, right, the switching points r_1 and r_2 can be geometrically determined as

$$r_1 = \frac{-1 - v_- R_o - v_+ R_i}{v_+ - v_-}, \quad r_2 = \frac{1 - v_- R_i + v_+ R_o}{v_+ - v_-}. \tag{6.31}$$

A motivating example

To this purpose, a numerical example concerning the design of a family of internally pressurized thick-walled FG cylinders is shown, where the material variation has to be chosen to minimize the inner equivalent Tresca stress. We first show the results obtained with three "classic" material variations widely used in the literature. These results are then compared with the ones associated with the optimal solution previously described where, for simplicity, a single switching point is supposed to exist. The inner radius is selected to be 20 mm, while the outer radius is chosen to vary from

$R_{o,min} = 30$ mm to $R_{o,max} = 50$ mm. The hollow cylinder is subject to an internal pressure $p_i = -10$ MPa. Alumina and steel are taken as the ceramic and metallic constituents at the inner and outer radii, respectively, whose Young's moduli are taken to be 3.9×10^5 MPa and 2.1×10^5 MPa. For simplicity, Poisson's ratio is chosen to be $\nu = 0.3$.

Results of classic variations

In a first analysis, linear, sinusoidal and sigmoidal volume fraction profiles have been taken into account. They are widely used in the literature and exhibit different stress behaviors throughout the thickness. Employing the micromechanical models introduced in Section 6.2.2, effective bulk and shear moduli are obtained while the effective Young's modulus is derived using (6.4). Figure 6.2 shows the above mentioned volume fractions and the associated Young's moduli for a fixed R_o/R_i ratio. A dedicated FE model has been developed to numerically forecast the stress behavior within the plane stress and plane strain conditions. Numerical values for the inner Tresca stress have been computed for selected R_o/R_i ratios. The effect of micromechanical models on the stress responses can be readily seen in Table 6.1, where the values of the ratio $\sigma_{eq}^T(R_i)/p_i$ are reported. Voigt and Reuss estimates yield the lowest and highest normalized inner equivalent stress values, respectively, for all the aforementioned volume fraction profiles, while results for Mori-Tanaka model present an intermediate stress behavior. Moreover, the employment of a sigmoidal volume fraction leads to lower $\sigma_{eq}^T(R_i)/p_i$ values with respect to the linear and sinusoidal ones, regardless of the involved micromechanical model.

Results of the Pontryagin's solution

Solutions associated with the Pontryagin's Principle have been, then, investigated and compared to the three above-mentioned volume fractions. In light of the single switching point assumption, two possible extremal solutions may occur (see Equation (6.31)). One of the two solutions corresponds to the minimum value of $\sigma_{eq}^T(R_i)/p_i$, while the other one can be discarded. Upper and lower limits for v_- and v_+, respectively, are firstly determined. In particular, from simple geometric considerations, an optimal solution exists for all R_o/R_i ratios when

$$v_- < \frac{1}{R_i - R_{o,min}} = -1/10\,, \quad v_+ > \frac{1}{R_i - R_{o,max}} = -1/30\,. \tag{6.32}$$

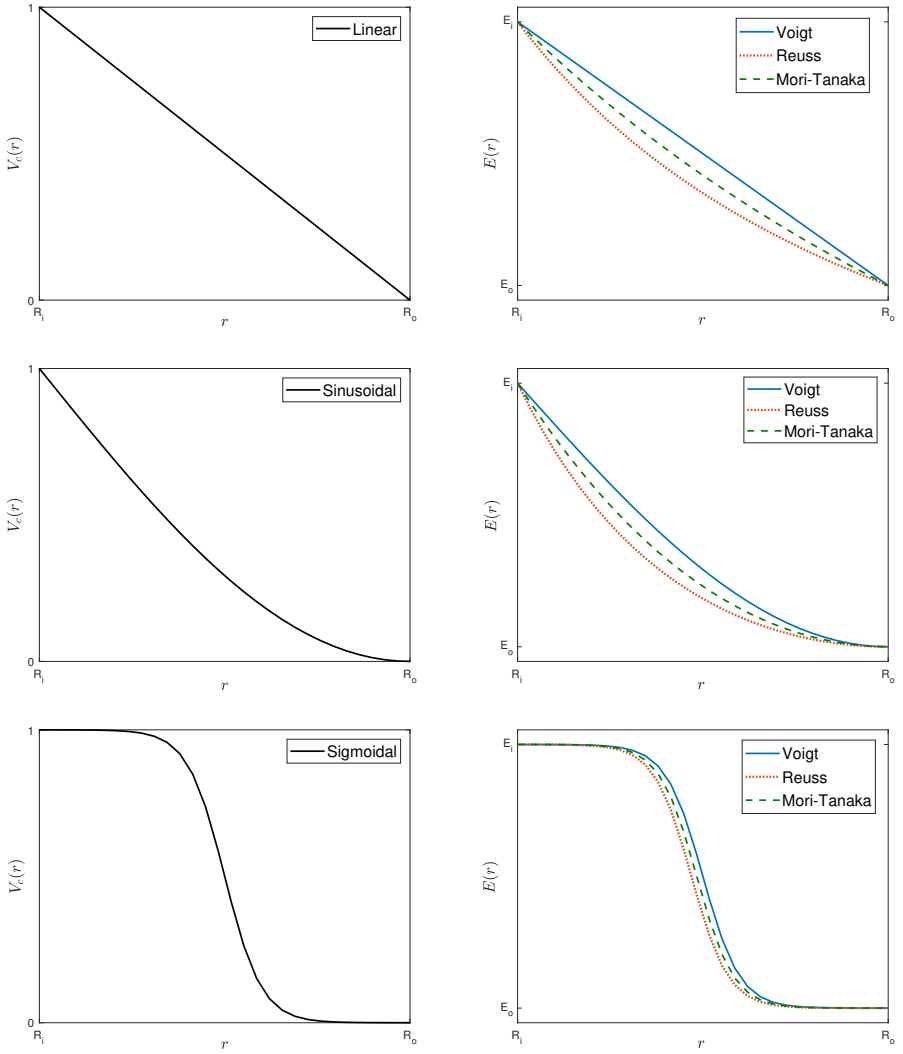

Figure 6.2: Linear, sinusoidal and sigmoidal volume fractions (left) and the associated Young's moduli (right) by Voigt (solid line), Reuss (dotted line) and Mori-Tanaka (dashed line) micromechanical models.

		Plane stress			Plane strain		
	R_o/R_i	V	R	MT	V	R	MT
Linear	1.50	4.309	4.526	4.422	4.327	4.552	4.444
	1.75	3.469	3.630	3.552	3.486	3.654	3.573
	2.00	3.057	3.189	3.125	3.073	3.212	3.144
	2.25	2.815	2.929	2.874	2.830	2.950	2.892
	2.50	2.657	2.758	2.709	2.670	2.778	2.726
Sinusoidal	1.50	4.591	4.807	4.706	4.618	4.843	4.737
	1.75	3.674	3.839	3.761	3.698	3.872	3.790
	2.00	3.222	3.361	3.294	3.245	3.392	3.322
	2.25	2.954	3.077	3.018	2.976	3.106	3.044
	2.50	2.778	2.889	2.836	2.798	2.917	2.860
Sigmoidal	1.50	4.253	4.312	4.284	4.263	4.324	4.295
	1.75	3.410	3.452	3.432	3.419	3.462	3.442
	2.00	2.996	3.029	3.014	3.004	3.039	3.022
	2.25	2.753	2.781	2.768	2.760	2.789	2.775
	2.50	2.595	2.618	2.607	2.601	2.625	2.614

Table 6.1: Numerical values of $\sigma_{eq}^{T}(R_i)/p_i$ for linear, sinusoidal and sigmoidal volume fraction profiles and for Voigt (V), Reuss (R) and Mori-Tanaka (MT) micromechanical models.

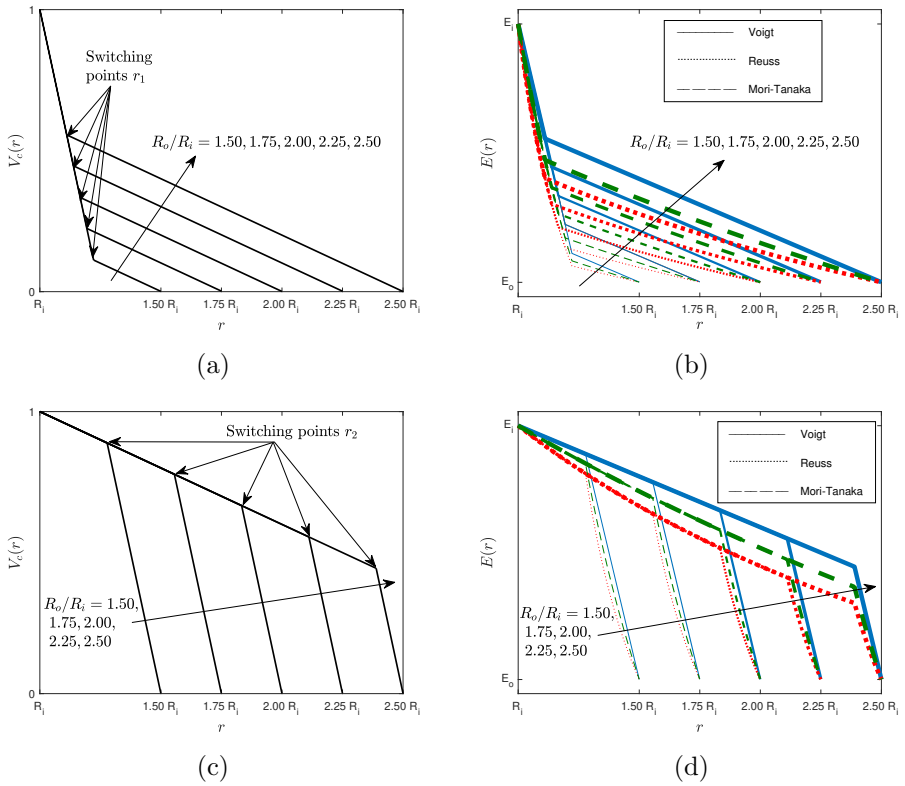

Figure 6.3: Extremal solutions for ceramic volume fractions and the locus of switching points as R_o/R_i increases (a,c) and the associated effective Young's moduli (b,d) by Voigt (solid lines), Reuss (dotted lines) and Mori-Tanaka (dashed lines) micromechanical models with $v_-/v_+ = 10$.

Two suitable values for v_- and v_+ are therefore preliminary chosen to be -0.2 and -0.02, respectively ($v_-/v_+ = 10$). The associated extremal solutions for ceramic volume fractions and the effective Young's moduli obtained by Voigt, Reuss and Mori-Tanaka models are represented in Figures 6.3a-6.3d as R_o/R_i increases. The equations for the locus of switching points can be derived easily from (6.31), showing a linear dependence with respect to R_o/R_i, being fixed v_-/v_+. In particular, the switching points r_1 and r_2 get close to the inner and outer radii, respectively, as R_o/R_i increases. Numerical values of $\sigma_{eq}^T(R_i)/p_i$ for both extremal solutions are reported in Table 6.2, showing worse and best stress scenarios when the switching point occurs at r_1 and r_2, respectively. These considerations allow one to conclude

that the optimal solution is the one associated with r_2 (grey bold line in Figure 6.1, right) while the one associated with r_1 (black bold line in Figure 6.1, right) has to be discarded.

Comparison

From the results described above, it is clear that the optimal solution, despite its simplicity, outperform the classical linear, sinusoidal and sigmoidal variations. Taking for instance R_o/R_i as 1.50 and considering Voigt and Mori-Tanaka models, optimal volume fraction profile shows, for the Pontryagin's solution, a significant normalized inner equivalent stress reduction of about 10%, 15% and 9% with respect to the linear, sinusoidal and sigmoidal ones, respectively, for both plane stress and plane strain conditions. The reduction percentages read slightly higher considering Reuss model for the same R_o/R_i ratio. The normalized inner equivalent stress reduction percentage decreases as R_o/R_i increases, reaching averagely 3% for $R_o/R_i = 2.50$.

To further analyze the performance of the Pontryagin's solution the effect of the v_-/v_+ has also been investigated. It has been pointed out above that volume fraction profiles switching at r_1 can be discarded. As a consequence, numerical analyses have been performed considering only the switching in r_2 (grey bold line in Figure 6.1, right). In particular, results have been obtained by keeping v_+ constant and acting on v_- only. The resulting volume fraction profile is characterized by a switching point r_2 getting linearly closer to R_o as v_-/v_+ increases. Figure 6.4 shows the optimal volume fraction profiles and the corresponding switching points for $v_-/v_+ = 10, 20, 30$ and for $R_o/R_i = 1.50, 2.00$. The corresponding numerical values of $\sigma_{eq}^T(R_i)/p_i$ are listed in Table 6.3 considering only Voigt and Reuss models for the assessment of lower and higher stress behaviors, respectively, showing further inner stress reduction as v_-/v_+ increases (see Table 6.2, where results are reported for $v_-/v_+ = 10$). Finally, analyses show marginal stress percentage reduction for higher R_o/R_i ratios for higher v_-/v_+ ratios.

		Plane stress			Plane strain		
	R_o/R_i	V	R	MT	V	R	MT
Switching point r_1	1.50	4.797	4.994	4.903	4.832	5.038	4.942
	1.75	3.945	4.117	4.038	3.985	4.167	4.084
	2.00	3.473	3.645	3.567	3.515	3.697	3.614
	2.25	3.161	3.333	3.254	3.200	3.383	3.299
	2.50	2.931	3.100	3.021	2.965	3.147	3.062
Switching point r_2	1.50	3.920	4.026	3.977	3.929	4.036	3.983
	1.75	3.162	3.251	3.206	3.162	3.251	3.206
	2.00	2.833	2.919	2.876	2.837	2.927	2.881
	2.25	2.653	2.739	2.696	2.657	2.745	2.700
	2.50	2.543	2.628	2.586	2.551	2.643	2.595

Table 6.2: Numerical values of $\sigma_{eq}^{T}(R_i)/p_i$ for both extremal scenarios with $v_-/v_+ = 10$ and for Voigt (V), Reuss (R) and Mori-Tanaka (MT) micromechanical models.

		Plane stress		Plane strain	
	R_o/R_i	V	R	V	R
$v_-/v_+ = 20$	1.50	3.814	3.905	3.818	3.912
	2.00	2.819	2.904	2.825	2.916
$v_-/v_+ = 30$	1.50	3.777	3.866	3.780	3.872
	2.00	2.814	2.902	2.821	2.912

Table 6.3: The effect of variation of v_-/v_+ on the normalized inner Tresca stress $\sigma_{eq}^T(R_i)/p_i$ for two instances of R_o/R_i.

Critical remarks

Although optimal solutions perform better than classic property variations employed in the literature, the aforementioned formulation of the problem could suffer from some critical aspects. The first one concerns the absence of a criterion for the selection of v_- and v_+. Bounds for these latter can be derived from Equation (6.32) but most importantly, after imposing the number of switching points beforehand. By doing so, it is implicitly assumed that the function $q(r, \mathbf{x}, \mathbf{p})$ in (6.26) is either strictly positive or strictly negative along r. This assumption has been made to favor the analytical tractability of the problem. In fact, it is emphasized that the Beltrami-Michell based formulation has not been of much help to determine whether the function q identically vanishes in a finite interval or in more finite intervals throughout the radial direction. Secondly, it is observed that the expression for optimal solutions (6.28) thus derived is paradoxically insensitive neither to whether the pressurized cylinder is exhibiting a plane stress or a plane strain load condition nor to the employed micromechanical model.

These considerations hint one to reconsider the optimization problem by means of a different formulation, possibly bypassing the exploitation of Pontryagin's Principle so that it overcomes the aforementioned shortcomings. To this purpose, a mixed formulation based on both Navier and Beltrami-Michell approaches is illustrated next.

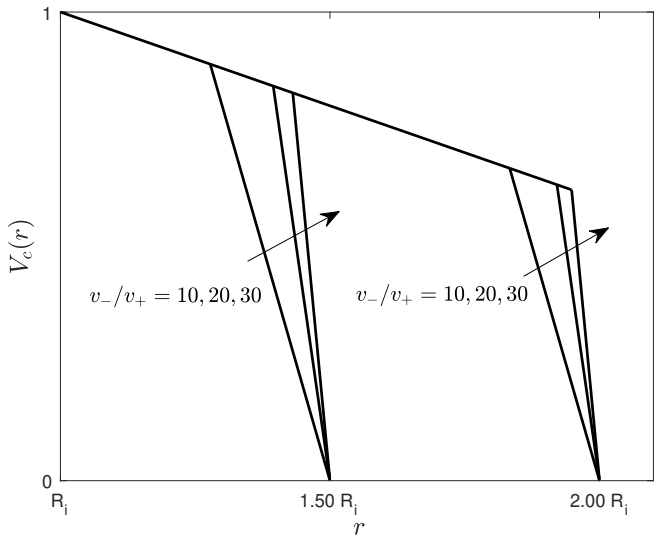

Figure 6.4: The effect of the variation of v_-/v_+ on the optimal volume fraction profile for two instances of R_o/R_i.

6.3.2 A Beltrami-Michell-Navier based formulation

Unlike the Beltrami-Michell based formulation, states are taken to be the radial displacement and the radial stress. Hereinafter, the variation of Poisson's ratio along the radial coordinate is included.

Firstly, the assumption of plane stress load condition is made. On a hand, from Equations (6.2), (6.3) and (6.14), the radial strain can be expressed as

$$u'(r) = \frac{\sigma_r(r) - \nu(r)\sigma_\theta(r)}{E(r)} = \frac{\sigma_r(r) - \nu(r)[\sigma_r(r) + r\sigma_r'(r)]}{E(r)}\,. \tag{6.33}$$

On the other hand, the hoop strain can be expressed as

$$\frac{u(r)}{r} = \frac{\sigma_\theta(r) - \nu(r)\sigma_r(r)}{E(r)}\,,$$

and consequently, the hoop stress can be expressed in terms of the states as follows

$$\sigma_\theta(r) = E(r)\frac{u(r)}{r} + \nu(r)\sigma_r(r)\,.$$

Consequently, the variation of the radial displacement and the radial displacement with respect to the radial coordinate, in terms of the two

states, are given by

$$u'(r) = -\frac{\nu(r)}{r}u(r) + \frac{1-\nu(r)^2}{E(r)}\sigma_r(r) \tag{6.34}$$

and

$$\sigma_r'(r) = \frac{E(r)}{r^2}u(r) + \frac{\nu(r)-1}{E(r)}\sigma_r(r)\,, \tag{6.35}$$

respectively, where Equation (6.15) has been used to derive (6.35).

Now, the assumption of a plane strain load condition is assumed. Here, the axial stress should be taken into account, whereas the axial strain is identically zero. This latter yields a relation between the three stresses, namely

$$\sigma_z(r) = \nu(r)[\sigma_r(r) + \sigma_\theta(r)]\,. \tag{6.36}$$

From constitutive equations (6.3) and Equation (6.14), the variation of the radial displacement and radial stress with respect to the radial coordinate, in terms of the two states, are given by

$$u'(r) = \frac{\nu(r)}{[\nu(r)-1]r}u(r) + \frac{[1+\nu(r)][1-2\nu(r)]}{E(r)[1-\nu(r)]}\sigma_r(r) \tag{6.37}$$

and

$$\sigma_r'(r) = \frac{E(r)}{[1-\nu(r)^2]r^2}u(r) + \frac{2\nu(r)-1}{[1-\nu(r)]}\sigma_r(r)\,, \tag{6.38}$$

respectively.

Unlike Problem 6.1, the maximum value for the Tresca equivalent stress is taken as the objective functional to be minimized and not that occurring at the inner radius. Nevertheless, a sound comparison can be still made since in all previous FE forecasts the inner Tresca stress was found to be the maximum throughout the radial coordinate. However, This is particularly true only for the plane stress condition. In fact, the equivalent Tresca stress is given by

$$\sigma_{eq}^T(r) = \max\{|\sigma_\theta(r)-\sigma_r(r)|, |\sigma_\theta(r)-\sigma_z(r)|, |\sigma_r(r)-\sigma_z(r)|\}\,, \tag{6.39}$$

which, in the case of plane stress condition, is just reduced to the first argument at the right hand-side and can be written in terms of the two states as follows

$$\sigma_{eq}^T(r) = |\sigma_\theta(r)-\sigma_r(r)| = \left|E(r)\frac{u(r)}{r} + [\nu(r)-1]\sigma_r(r)\right| \tag{6.40}$$

and its maximum value can be approximated by the p-norm (p even) and is given by:

$$\sigma_{eq,max}^{T} \approx \left\{ \int_{R_i}^{R_o} \left[E(r)\frac{u(r)}{r} + [\nu(r)-1]\sigma_r(r) \right]^p \, dr \right\}^{1/p}. \tag{6.41}$$

As far as the plane strain condition is concerned, it is not trivial to decide which argument in Equation (6.39) is prevalent. Consequently, a potential candidate for the objective functional can be the maximum value for the hoop stress, which can be approximated as

$$\sigma_{\theta,max} \approx \left\{ \int_{R_i}^{R_o} \left[\frac{1}{1-\nu(r)^2} \left(E(r)\frac{u(r)}{r} + \nu(r)[1+\nu(r)]\sigma_r(r) \right) \right]^p \, dr \right\}^{1/p}. \tag{6.42}$$

Consequently, two formulations are stated depending on the load condition. Hereinafter, states y_1 and y_2 denote the radial displacement and the radial stress, respectively. Besides, to broad the spectrum of analysis, the Poisson's ratio is allowed to vary along the radial coordinate.

Problem 6.2. *Find the distribution of the ceramic volume fraction along the radial direction of the cylinder so that the maximum Tresca stress attains its minimum value, i.e.,*

$$\begin{aligned}
\min_{V_c(r)} \quad & \sigma_{eq,max}^{T} = \left\{ \int_{R_i}^{R_o} \left[E(r)\frac{y_1(r)}{r} + [\nu(r)-1]y_2(r) \right]^p \, dr \right\}^{1/p} \\
s.t. \quad & y_1'(r) = -\frac{\nu(r)}{r}y_1(r) + \frac{1-\nu(r)^2}{E(r)}y_2(r)\,, \\
& y_2'(r) = \frac{E(r)}{r^2}y_1(r) + \frac{\nu(r)-1}{E(r)}y_2(r)\,, \\
& y_2(R_i) = -p_i\,, \\
& y_2(R_o) = 0\,, \\
& 0 \le V_c(r) \le 1\,,
\end{aligned} \tag{6.43}$$

where R_i, R_o, p_i and p are given constants and $E(r)$ and $\nu(r)$ are linked to $V_c(r)$ through a micromechanical model.

Problem 6.3. *Find the distribution of the ceramic volume fraction along the radial direction of the cylinder so that the maximum hoop stress attains*

its minimum value, i.e.,

$$
\begin{aligned}
\min_{V_c(r)} \quad & \sigma_{\theta,max} = \left\{ \int_{R_i}^{R_o} \left[\frac{1}{1-\nu(r)^2} \left(E(r) \frac{y_1(r)}{r} + \nu(r)[1+\nu(r)] y_2(r) \right) \right]^p \, dr \right\}^{1/p} \\
s.t. \quad & y_1'(r) = \frac{\nu(r)}{[\nu(r)-1]r} y_1(r) + \frac{[1+\nu(r)][1-2\nu(r)]}{E(r)[1-\nu(r)]} y_2(r) \,, \\
& y_2'(r) = \frac{E(r)}{[1-\nu(r)^2]r^2} y_1(r) + \frac{2\nu(r)-1}{[1-\nu(r)]r} y_2(r) \,, \\
& y_2(R_i) = -p_i \,, \\
& y_2(R_o) = 0 \,, \\
& 0 \leq V_c(r) \leq 1 \,,
\end{aligned}
\tag{6.44}
$$

where R_i, R_o, p_i and p are given constants and $E(r)$ and $\nu(r)$ are linked to $V_c(r)$ through a micromechanical model.

Problems 6.2 and 6.3 have been solved by means of the numerical method described in Chapter 3. In all the simulations presented here, the exponent p was taken to be equal to 60. The two bulk materials are Steel and Alumina, whose Poisson's ratios are taken to be 0.33 and 0.25, respectively, but firstly a comparison with results in Tables 6.2 and 6.3 is made, namely when the Poisson's ratio is uniform ($\nu = 0.3$) and for $p_i = -10$ MPa. The corresponding optimal ceramic volume fractions are shown in Figures 6.5a-6.5d for both Voigt and Reuss models and for both load conditions. Optimal solution associated with $R_o/R_i = 1.50$ in both load conditions apart, it can be seen that optimal solutions behave similarly, namely there is a finite interval between R_i and R_o where the material grades, while it is homogeneous elsewhere. In particular, there is an initial and final radial strips where the optimal distribution of the material yields ceramic ($V_c = 1$) and metal ($V_c = 0$) phases, respectively. Therefore, unlike the Beltrami-Michell formulation, this new formulation goes beyond the limits on the maximum and minimum derivatives of V_c and can yield a solution where the material partly grades throughout the radial coordinate. The position of these radial strips depends on the geometric aspect of the cylinder. Moreover, numerical solutions for the maximum equivalent Tresca stress have been forecast for $R_o/R_i = 1.50 \div 2.50$ and are identical for both models. The associated normalized maximum equivalent stress (which still occurs at the inner boundary) are given in Table 6.4, where it is shown that arising maximum stresses are much lower than those employed in the literature ($\approx 40\%$), and even the optimal solution associated

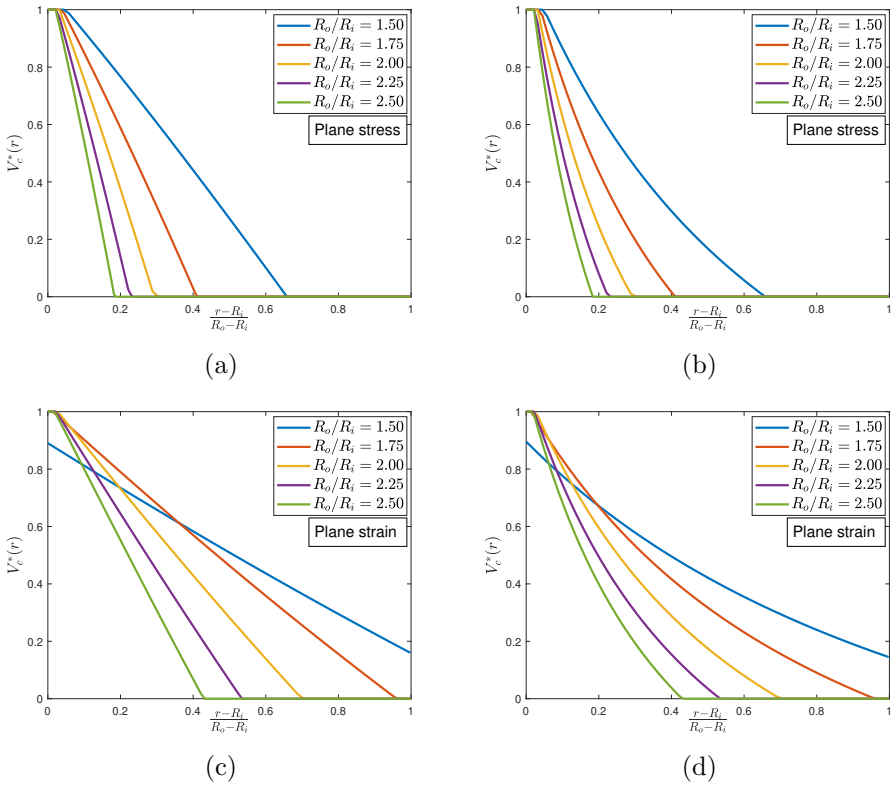

Figure 6.5: Numerical optimal solutions for ceramic volume fractions for Voigt (a,c) and Reuss (b,d) models for a plane stress (a,b) and plane strain (c,d) load conditions and for different values of R_o/R_i.

	R_o/R_i	σ^T_{max}/p_i
Plane stress	1.50	2.647
	1.75	2.132
	2.00	1.908
	2.25	1.785
	2.50	1.708
Plane strain	1.50	3.000
	1.75	2.358
	2.00	2.081
	2.25	1.922
	2.50	1.824

Table 6.4: Normalized maximum equivalent stress associated with the optimal numerical solutions for both plane stress and plane strain load conditions (uniform ν).

with the Pontryagin's best extremal obtained from the Beltrami-Michell formulation ($\approx 30\%$).

Finally, the variation of the Poisson's ratio is taken into account and optimal solutions are computed for the aspect ratio $R_o/R_i = 2.00$. Figures 6.6a and 6.6b show the optimal ceramic volume fractions for uniform and variable Poisson's ratios, where it is emphasized that numerical solutions for the ceramic volume fractions do not remarkably differ from those associated with uniform ν, which in turn it leads to marginal differences between corresponding maximum Tresca stresses (see Tables 6.4 and 6.5).

6.4 Summary

The optimization of functionally graded internally pressurized cylinders has been the central objective of this chapter. The description of the stress and strain states has been addressed by borrowing notions from

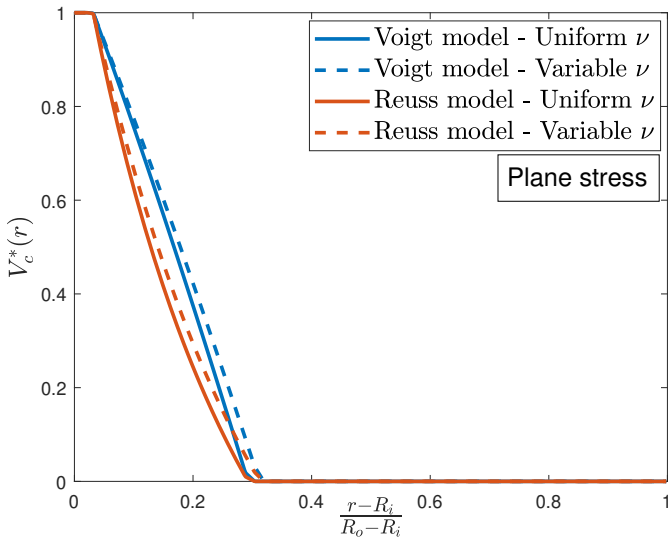

(a)

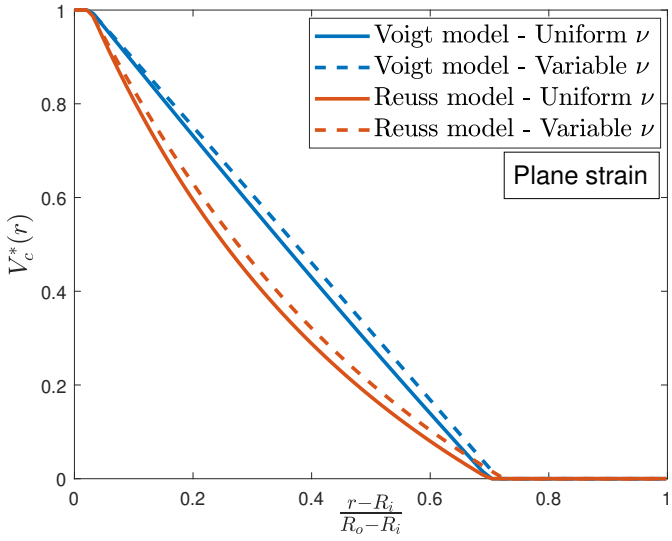

(b)

Figure 6.6: Effect of the variation of Poisson's ratio on the numerical optimal solutions for ceramic volume fractions for Voigt and Reuss models, for a plane stress (a) and plane strain (b) load conditions and for $R_o/R_i = 2.00$.

	R_o/R_i	σ^T_{max}/p_i	
		V	R
Plane stress	1.50	2.635	2.633
	1.75	2.108	2.107
	2.00	1.878	1.877
	2.25	1.752	1.752
	2.50	1.674	1.674
Plane strain	1.50	3.000	3.000
	1.75	2.358	2.355
	2.00	2.075	2.073
	2.25	1.909	1.908
	2.50	1.807	1.806

Table 6.5: Normalized maximum equivalent stress associated with the optimal numerical solutions with variable ν.

the theory of linear elasticity. Unlike the overwhelming studies in the literature, the distribution of elastic properties along the radial direction is not fixed a priori, thus offering an intrinsic setting for their derivation based on optimality principles. To this purpose, two formulations have been proposed depending in the nature of the involved states. The first formulation showed a relatively higher analytical tractability under some mild hypotheses, while challenges associated with the second one have been tackled numerically. Nevertheless, optimal solutions over-performed with respect to several gradation strategies commonly employed in the literature.

Chapter 7

Conclusions

This chapter recapitulates the principal findings of this dissertation and suggests advancements for future research work.

In the first part, variational principles have been employed to derive necessary conditions for optimality in continuous dynamic optimization problems subject to algebraic and differential constraints (Chapter 2). In particular, strong and weak forms of Pontryagin's Principle have been presented and discussed. It has been shown that optimality conditions, unless in a few cases, are hardly tractable from the analytical point of view, and therefore required the development of dedicated numerical tools. This shortcoming has been addressed by means of the direct orthogonal collocation (or pseudospectral) method (Chapter 3). More precisely, the transcription process of (infinite-dimensional) dynamic optimization problems into (finite-dimensional) static ones is shown in both global and local forms. Moreover, explicit expressions for the first derivatives of the resulting nonlinear programming problem this discretization have been reported and used for the sake of an efficient computation efficiency.

In the second part, optimization problems formulated in the realm of membrane shells of revolutions (Chapter 4), one-dimensional structural elements (Chapter 5) and functionally graded cylinders (Chapter 6) have been formulated, solved, thoroughly discussed and compared to the literature. Potential goal functionals and structural constrains ranged from lightweightness, to maximum storage capacity, stiffness, resistance to buckling and load bearing capacity. In some cases, optimal solutions have been derived analytically or even in closed-form, otherwise computational tools have been exploited. Among these applications, an optimized axisymmetric pressure vessel has been considered, a detailed discussion

on its manufacturability by means of metal additive techniques has been reported and highlighting several aspects of reverse engineering such as its scanning measurement, finite element based validation and rugosity evaluation, showing satisfactory results.

Results summarized in this dissertation formed a considerable part of the research activities carried out during my doctoral studies and led to the publications of a few journal articles [154, 155, 156, 157, 158, 159, 160]. Moreover, further efforts and relatively close analyses have been performed in other works [161, 162, 163, 164, 165]. Nevertheless, three potential challenges hinting future investigations are listed next:

1. It is known that cracks can form as a consequence of manufacturing processes or during operation. For membrane shells of revolution subject to a cyclic internal pressure, it is required to formulate longevity constraints in terms of critical stress intensity factors by means of the well-known Paris-Erdogan law [166]. As mentioned in Chapter 4, efforts employing the so-called minimax (or guaranteed) approach have been done in [59, 60] for membrane shells. However, solutions are provided for a particular class of materials, for which the longevity constraints are simplified. A similar effort has been proposed for cantilever beams in [167] by using a probabilistic approach. Also here, solutions are analytically provided for a basic load case. To overcome these shortcomings, the numerical approach in Chapter 3 can be employed to find optimal shapes beyond these analytical tractability issues.

2. The analysis of micro/nano beams has been gaining a considerable attention by researchers. Nano beams are modeled within the framework of second grade elasticity and within integral-based nonlocal theories. Recently, there has been a number of studies of buckling of nonlocal nano beams, e.g., [107, 108, 168]. It was shown in these works that the Pontryagin's principle may be used successfully to determine the shape of the rod that has minimal mass and is stable under the action of a prescribed force, yet the development of nontrivial variational principles is needed. The idea is to study to what extent pseudospectral methods can be helpful in the determination of optimal solutions, bypassing this nontrivial stage.

3. Increased interest in recent years can be attributed to many interesting studies on functionally graded materials when multiple loads are acting, e.g., centrifugal forces, forces due to the presence of

electromagnetic fields and under hydrogenated environment [24, 169, 170]. In Chapter 6, only cylinders subject to an internal pressure have been taken into account. Apart from extensions to other axisymmetric bodies (e.g., spheres, annular rings and disks), it is believed that the developed numerical method can address problems not only when the loads are simultaneously applied, but also when mechanical and thermal properties vary with temperature.

Appendices

Appendix A

Calculus of variations

Correspondences which assign a definite (real) number to each function (or curve) belonging to some class are commonly referred to as functionals. In other words, functionals are a kind of functions, whose independent variables are themselves functions (or curves). They play an important role in many problems arising in analysis, mechanics, geometry, etc. Typical examples are the following:

- Consider the set of all rectifiable plane curves. A definite number is associated with each curve, namely, its length. Thus, the length of a curve is a functional defined on the set of rectifiable curves.

- Suppose that each rectifiable plane curve is regarded as being made out of a homogeneous material. Then a functional can be defined if each curve is associated with the ordinate of its center of mass.

- Consider all possible paths joining two given points A and B in the plane. Suppose that a particle can move along any of these paths and let the particle have a definite velocity. Then, a functional can be defined by associating with each curve the time the particle takes to move from A to B.

Particular instances of problems involving the concept of a functional have been considered more than three hundred years ago. The first important results in this area are due to Euler. Nevertheless, up to now, the calculus of functionals still does not have methods of generality comparable to classical analysis, i.e., ordinary calculus of functions. The most developed branch of the calculus of functionals is concerned with finding the maxima and minima of functionals. This particular branch is referred to as calculus

of variations. An important factor in the development of the calculus of variations was the investigation of a number of mechanical and physical problems. In turn, the methods of the calculus of variations are widely applied in various physical and engineering problems. Besides, it should be emphasized that the application of the calculus of variations to mechanics and physics does not consist merely in the solution of individual, albeit very important problems. In fact, the so-called variational principles are essentially a manifestation of very general physical laws, which are valid in diverse branches of physics and engineering.

The present Appendix gives a concise introduction to this classic field through basic definitions and theorems and aims to derive necessary conditions for the existence of extremal solutions for different basic variational problems. Necessary conditions turn out to be second-order ordinary differential equations which, together to boundary conditions, constitute boundary value problems. Eventually, a few generalizations have been eventually formulated, discussed and linked to the simplest variational problem.

A.1 Preliminary concepts

To understand the basic meaning of the problems and methods of the calculus of variations, it is very important to see how they are related to problems of classical analysis, i.e., to the study if functions of multiple variables. Euler works made considerable effort to establish this link. For the sake of an example, consider the minimization of the functional of the form

$$J[y] = \int_a^b \mathcal{F}(x, y, y')\, dx, \quad y(a) = A, \quad y(b) = B, \tag{A.1}$$

where a prime denotes the first derivative with respect to x and $\mathcal{F} : [a, b] \times \mathbb{R} \times \mathbb{R} \to \mathbb{R}$, namely, to find the curve $y = y(x)$ with $y : [a, b] \to \mathbb{R}$ joining the fixed points A and B such that the cost (or goal) functional J is as minimum as possible. By replacing smooth curves by polygonal lines, Euler reduced the problem of finding extrema of a functional to the problem of finding extrema of a function of multiple variables. In particular, to find a related function of the sort considered in classical analysis, one may use the points

$$x_0 = a, \quad x_1, \quad x_2, \quad \ldots, \quad x_n, \quad x_{n+1} = b$$

and divide the interval $[a, b]$ into $n + 1$ equal parts. Then the curve y is replaced by the polygonal line with vertices

$$(x_0, A), \quad (x_1, y(x_1)), \quad (x_2, y(x_2)), \quad \ldots, \quad (x_n, y(x_n)), \quad (x_{n+1}, B)$$

and the functional J is approximated by the sum

$$J(y_1, ..., y_n) = \sum_{i=1}^{n+1} \mathcal{F}\left(x_i, y_i, \frac{y_i - y_{i-1}}{h}\right) h, \tag{A.2}$$

where $y_i = y(x_i)$ and $h = x_i - x_{i-1}$. Each polygonal line is uniquely determined by the ordinates $y_1, y_2, \ldots, y_n$ of its vertices and the sum (A.2) is therefore a function of n variables. Hence, one can regard the variational problem as the problem of finding the extrema of the function $J(y_1, y_2, ..., y_n)$. It is clear that exact solutions can be obtained by passing to the limit as $n \to \infty$. In this sense, functionals can be regarded as functions of infinitely many variables and the calculus of variations can be considered as the corresponding analog of differential calculus.

In the study of functions of n variables, it is convenient to use geometric language by regarding a set of n numbers $(y_1, y_2, \ldots, y_n)$ as point in an n-dimensional space. Similarly, geometric language is useful when studying functionals. Thus, we shall regard each function $y(x)$ belonging to some class as a point in some space and spaces whose elements are functions will be called function spaces. In fact, there is no universal space, it is the nature of the problem under consideration that determines the choice of the function space. For example, if a functional of the form (A.1) is considered, it is natural that this functional should be defined on the set of all functions with a continuous first derivative.

Next, preliminary concepts regarding involved functional spaces, a few useful definitions and theorems are given to fix the basic concepts and terminology without worrying about technical details. Concise proofs of these theorems are addressed, whereas more rigorous analyses can be found in several textbooks, e.g. [171, 172, 173].

A.1.1 Linear normed spaces

The concept of continuity plays an important role for functionals and should be properly defined. To this purpose, it is necessary to introduce the concept of closeness for elements in a function space. This is most conveniently done by introducing the concept of the norm of a function in a general and abstract form, namely by introducing the concept of a normed linear space.

A set $\mathcal{R}$ of elements $x, y, z, \ldots$ is referred to as linear space if for which the operations of addition and multiplication by (real) numbers $\alpha, \beta, \ldots$ are defined and obey the following properties:

- $x + y = y + x$;
- $(x + y) + z = x + (y + z)$;
- There exists an element 0 (the zero element) such that $x + 0 = x$ for any $x \in \mathcal{R}$;
- For each $x \in \mathcal{R}$, there exists an element $-x$ such that $x + (-x) = 0$;
- $\alpha(\beta x) = (\alpha\beta)x$;
- $(\alpha + \beta)x = \alpha x + \beta x$;
- $\alpha(x + y) = \alpha x + \alpha y$.

A linear space $\mathcal{R}$ is said to be normed if each element $x \in \mathcal{R}$ is assigned a non-negative number $||x||$, called norm of x, such that

- $||x|| = 0$ iff $x = 0$;
- $||\alpha x|| = |\alpha| \; ||x||$;
- $||x + y|| \leq ||x|| + ||y||$.

Examples of normed linear spaces that are useful for subsequent considerations are $\mathcal{D}_0$, $\mathcal{D}_1$ and $\mathcal{D}_n$, consisting of all continuous functions, all continuous functions having continuous first derivative and all continuous functions having continuous derivatives up to order $n \in \mathbb{N}$ inclusive, respectively. More precisely, if functions are defined on $\mathcal{I} = [a, b]$, they are denoted by $\mathcal{D}_0(\mathcal{I})$, $\mathcal{D}_1(\mathcal{I})$ and $\mathcal{D}_n(\mathcal{I})$, respectively. Letting $||y||_0$, $||y||_1$ and $||y||_n$ denote the associated norms of a function $y = y(x)$ with $y : \mathcal{I} \to \mathbb{R}$, respectively, defined as

$$||y||_n = \sum_{i=0}^{n} \max_{a \leq x \leq b} |y^{(i)}(x)|,$$

where $y^{(i)} = \frac{d^i y(x)}{dx^i}$ and $y^{(0)}$ denotes the function $y(x)$ itself, it is easily verified that all the properties of a normed linear space are satisfied. After a norm has been introduced in the linear space $\mathcal{R}$, it is natural to give the following definition:

Definition A.1. *The functional $J[y]$ is said to be continuous at the point $\hat{y} \in \mathcal{R}$ if for any $\varepsilon > 0$ there is a $\delta > 0$ such that*

$$|J[y] - J[\hat{y}]| < \varepsilon,$$

provided that $||y - \hat{y}|| < \delta$.

A.1.2 Variation of a functional

In this section, the variation of a functional is introduced. It is analogous to the concept of differential of a function of multiple variables.

Definition A.2. *Given a normed linear space $\mathcal{R}$, let each element $h \in \mathcal{R}$ be assigned a number $\varphi[h]$. Then $\varphi[h]$ is said to be a linear functional if*

1. *$\varphi[\alpha h] = \alpha\varphi[h]$ for any $h \in \mathcal{R}$ and any real number α;*
2. *$\varphi[h_1 + h_2] = \varphi[h_1] + \varphi[h_2]$;*
3. *$\varphi[h]$ is continuous for all $h \in \mathcal{R}$.*

Based on Definition A.2, the following examples hold:

Example A.1. *If each function $h(x) \in \mathcal{D}_0(\mathcal{I})$ is associated with its value at a fixed point $x_0 \in \mathcal{I}$, i.e. if*

$$J[h] = h(x_0),$$

then $J[h]$ is a linear functional on $\mathcal{D}_0(\mathcal{I})$.

Example A.2. *The integrals*

$$J[h] = \int_a^b h(x)\,dx$$

and

$$J[h] = \int_a^b g(x)h(x)\,dx$$

define linear functionals on $\mathcal{D}_0(\mathcal{I})$, where $g(x)$ is a fixed function in $\mathcal{D}_0(\mathcal{I})$.

Example A.3. *More generally, the integral*

$$J[h] = \int_a^b [g_0(x)h(x) + g_1(x)h'(x) + \cdots + g_n(x)h^{(n)}(x)]\,dx$$

defines a linear functional on $\mathcal{D}_n(\mathcal{I})$, where $g_i(x)$ are fixed functions in $\mathcal{D}_0(\mathcal{I})$.

Definition A.3. *Let $J[h]$ be a functional defined on some normed linear space. The increment of the functional is defined as*

$$\Delta J[y,h] = J[y+h] - J[y],$$

namely corresponding to the increment $h = h(x)$ of the variable $y = y(x)$.

Definition A.4. *The functional is said to be differentiable at $y = \hat{y}$ if*

$$\Delta J[h] = J[\hat{y}+h] - J[\hat{y}]$$

can be written as

$$\Delta J[h] = \varphi[h] + \varepsilon||h||,$$

where $\varphi[h]$ is a linear functional and $\varepsilon \to 0$ as $||h|| \to 0$.

Letting the variation of the functional be the principal linear part of ΔJ, i.e., φ, and denoting it by $\delta J[h]$, therefore, from Definition A.4, the functional is differentiable at $y = \hat{y}$ if

$$\Delta J[h] = \delta J[h] + \varepsilon||h||. \tag{A.3}$$

A.1.3 Necessary condition for extremal solutions

Proposition A.1. *If φ is a linear functional and $\frac{\varphi[h]}{||h||} \to 0$ as $||h|| \to 0$, then $\varphi[h] = 0$ for all admissible h.*

Proof. Suppose that the above statement is not true. It means that there exists h_0 such that $\varphi[h_0] \neq 0$. Now let $h_n = \frac{h_0}{n}$, with $n > 0$, and $\lambda = \frac{\varphi[h_0]}{||h_0||}$. From the construction of h_n, it is clear that $\lim_{n\to\infty} h_n = 0$, but

$$\lim_{n\to\infty} \frac{\varphi[h_n]}{||h_n||} = \lim_{n\to\infty} \frac{\varphi[\frac{h_0}{n}]}{||\frac{h_0}{n}||} = \lim_{n\to\infty} \frac{\varphi[h_0]}{||h_0||} = \lambda \neq 0. \tag{A.4}$$

On the other hand, from the properties of limits

$$\lim_{n\to\infty} \frac{\varphi[h_n]}{||h_n||} = \frac{\varphi[\lim_{n\to\infty} h_n]}{||\lim_{n\to\infty} h_n||} = 0,$$

which is in contradiction with (A.4) and therefore proves the statement. □

Theorem A.1. *The variation of a differentiable functional is unique.*

Proof. Suppose the variation of the functional $J[y]$ is not uniquely defined, so that

$$\Delta J[h] = \varphi_1[h] + \varepsilon_1||h||$$

and

$$\Delta J[h] = \varphi_2[h] + \varepsilon_2||h||,$$

where $\varphi_1[h]$ and $\varphi_2[h]$ are linear functionals and ε_1, $\varepsilon_2 \to 0$ as $||h|| \to 0$. This implies

$$\varphi_1[h] - \varphi_2[h] = (\varepsilon_2 - \varepsilon_1)||h||.$$

Defining $\varepsilon = \varepsilon_2 - \varepsilon_1$ and from linearity of φ_1 and φ_2 one obtains

$$(\varphi_1 - \varphi_2)[h] = \varepsilon||h||,$$

where $\varepsilon \to 0$ as $||h|| \to 0$. Manipulating terms, the equivalent expression

$$\frac{(\varphi_1 - \varphi_2)[h]}{||h||} \to 0$$

holds as $\|||h|| \to 0$. Since $\varphi_1 - \varphi_2$ is a linear functional, from Proposition A.1 one obtains $\varphi_1 = \varphi_2$ for all admissible h. This is in contradiction with the above assumption and therefore proves the theorem. □

Theorem A.2. *A necessary condition for the differentiable functional $J[y]$ to have an extremum for $y = \hat{y}$ is that its variation vanishes for $y = \hat{y}$, i.e.,*

$$\delta J[h] = 0$$

for $y = \hat{y}$ and all admissible h.

Proof. Without loss of generality, assume that $J[y]$ assumes minimum value at $y = \hat{y}$. Therefore,

$$\Delta J[h] = J[\hat{y} + h] - J[\hat{y}] \geq 0 \tag{A.5}$$

for all h in a neighborhood N of $\hat{y}$. The differentiability of the functional implies that

$$\Delta J[h] = \delta J[h] + \varepsilon||h||,$$

where $\varepsilon \to 0$ as $||h|| \to 0$. Thus, for sufficiently small $||h||$, which in turn defines the neighborhood of $\hat{y}$, the sign of $\Delta J[h]$ will be the same as $\delta J[h]$. Now suppose that $\delta J[h_0] \neq 0$, for an admissible h_0, in contradiction to the

statement. Then for any $\alpha > 0$, no matter how small, $\hat{y} + \alpha h_0$ and $\hat{y} - \alpha h_0$ live in N and the corresponding variations read

$$\delta J[\hat{y} + \alpha h_0] - J[\hat{y}] = \delta J[\alpha h_0]$$

and

$$\delta J[\hat{y} - \alpha h_0] - J[\hat{y}] = \delta J[-\alpha h_0],$$

respectively. Besides, since δJ is linear, both variations have opposite signs, namely

$$\delta J[-\alpha h_0] = -\delta J[\alpha h_0],$$

which is impossible because of relation (A.5). This contradiction proves the theorem. □

In the next section, the fundamental theorem to determine extrema of functionals depending on a single function is used. In particular, it will be assumed initially that end points are fixed and then will be allowed to be free. Necessary conditions are derived and comments on extrema are addressed for problems summarized in Figure A.1.

A.2 The simplest variational problem

Necessary conditions for extremum solutions for the simplest variational problem is considered next. It consists of finding a smooth curve $y = y(x)$ joining two fixed points, which extremizes a given functional, whose integrand depend on y itself and its derivative (see Figure A.1a). The problem is formulated as follows:

Problem A.1. *Among all continuous differentiable functions* $y : [x_0, x_f] \to \mathbb{R}$ *satisfying given boundary conditions*

$$y(x_0) = y_0, \quad y(x_f) = y_f, \tag{A.6}$$

find the extremum of the cost functional

$$J[y] = \int_{x_0}^{x_f} \mathcal{F}(x, y(x), y'(x))\, dx. \tag{A.7}$$

Problem A.1 was originally proposed by Lagrange in his monograph Mécanique Analytique in 1788. The assumption $y \in \mathcal{D}_1$ is made to ensure that J is well defined (of course one does not need it if y' does not appear in

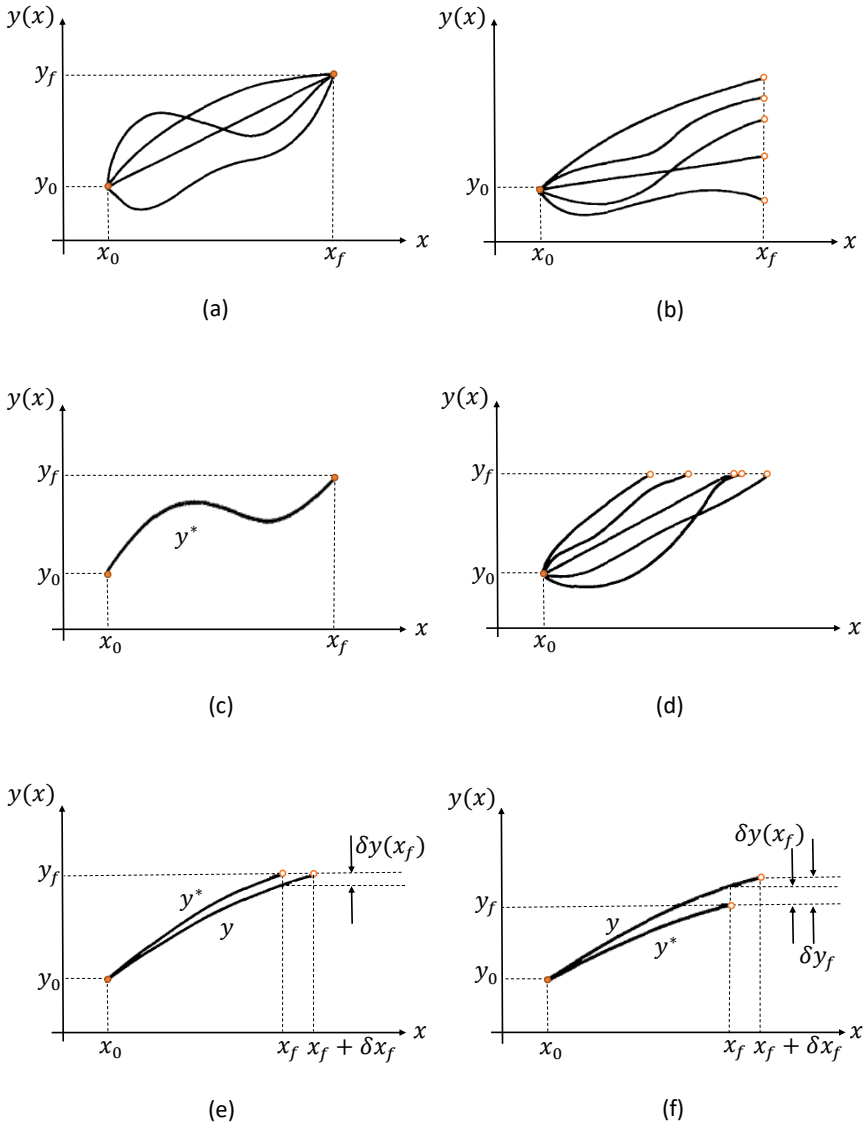

Figure A.1: Schematizing admissible curves for fixed and free end points problems.

$\mathcal{F}$). As previously asserted in Theorem A.2, the necessary condition for an extremum is to set the first variation of the functional equal to zero, namely

$$\delta J = 0 = \delta \int_{x_0}^{x_f} \mathcal{F}(x, y(x), y'(x))\, dx = \int_{x_0}^{x_f} \delta\mathcal{F}(x, y(x), y'(x))\, dx, \quad \text{(A.8)}$$

where it can be seen that the variation sign moved under the integral sign since x_0 and x_f are fixed, due to Leibniz integral rule for differentiation under the integral sign. Thus, neglecting higher order terms, the variation of the integrand function is given by

$$\delta\mathcal{F}(x, y(x), y'(x)) = \frac{\partial\mathcal{F}}{\partial y}\delta y + \frac{\partial\mathcal{F}}{\partial y'}\delta y'$$

and therefore, from Equation (A.8), necessary conditions can be recast as

$$\int_{x_0}^{x_f} \frac{\partial\mathcal{F}}{\partial y}\delta y\, dx + \int_{x_0}^{x_f} \frac{\partial\mathcal{F}}{\partial y'}\delta y'\, dx = 0. \quad \text{(A.9)}$$

Now, consider the second term at the left-hand side of (A.9). By employing integration by parts, one obtains

$$\int_{x_0}^{x_f} \frac{\partial\mathcal{F}}{\partial y'}\delta y'\, dx = \left[\frac{\partial\mathcal{F}}{\partial y'}\delta y\right]_{x_0}^{x_f} - \int_{x_0}^{x_f} \frac{d}{dx}\frac{\partial\mathcal{F}}{\partial y'}\delta y\, dx. \quad \text{(A.10)}$$

Since boundary conditions (A.6) are fixed, admissible variations δy require

$$\delta y(x_0) = \delta y(x_f) = 0 \quad \text{(A.11)}$$

and therefore relation (A.9) may be recast as

$$\int_{x_0}^{x_f} \left(\frac{\partial\mathcal{F}}{\partial y} - \frac{d}{dx}\frac{\partial\mathcal{F}}{\partial y'}\right)\delta y\, dx = 0. \quad \text{(A.12)}$$

The only way that the integral appearing in (A.12) equals zero for all admissible variations δy satisfying (A.11) is that

$$\frac{\partial\mathcal{F}}{\partial y} - \frac{d}{dx}\frac{\partial\mathcal{F}}{\partial y'} = 0. \quad \text{(A.13)}$$

Relation (A.13) is commonly referred to as Euler-Lagrange equation and yields the necessary condition for the existence of an extremum solution for Problem A.1. It gives a necessary condition for an extremum, but in general, one which is not sufficient. The question of sufficient conditions for

an extremum is out of the scope of this dissertation. In many cases, however, Euler-Lagrange equation by itself is enough to give a complete solution of the problem. In fact, the existence of an extremum is often clear from the physical or geometric meaning of the problem, e.g., in the brachistochrone problem, the problem concerning the shortest distance between two points, etc. If in such a case there exists only one extremal satisfying the boundary conditions of the problem, this extremal must perforce be the curve for which the extremum is achieved.

A.2.1 Particular cases

Euler-Lagrange equation plays a fundamental role in the calculus of variations, and is in general a second-order differential equation. However, there are some special cases where it can be reduced to a first-order differential equation or its solution can be obtained entirely in terms of quadratures or by solving an algebraic equation. For the sake of light notation, let subscripts y and y' denote the first partial derivative with respect to y and y' respectively, namely $(.)_y = \frac{\partial(.)}{\partial y}$ and $(.)_{y'} = \frac{\partial(.)}{\partial y'}$.

Case 1: $\mathcal{F} = \mathcal{F}(x, y')$

Suppose the integrand does not depend on y, i.e., let the functional under consideration have the form

$$\int_{x_0}^{x_f} \mathcal{F}(x, y'(x))\, dx,$$

where $\mathcal{F}$ does not contain y explicitly. In this case, from relation (A.13), Euler-Lagrange equation becomes

$$\frac{d}{dx}\mathcal{F}_{y'} = 0$$

which has the first integral

$$\mathcal{F}_{y'} = C, \tag{A.14}$$

where C is a constant. This is a first-order differential equation which does not contain y. Solving Equation (A.14) for y', one obtains an equation of the form

$$y' = f(x, C),$$

from which y can be found by a quadrature.

Case 2: $\mathcal{F} = \mathcal{F}(y, y')$

If the integrand does not depend on the independent variable x, i.e., if

$$J = \int_{x_0}^{x_f} \mathcal{F}(y(x), y'(x))\, dx,$$

then

$$\mathcal{F}_y - \frac{d}{dx}\mathcal{F}_{y'} = \mathcal{F}_y - \mathcal{F}_{y'y}y' - \mathcal{F}_{y'y'}y'' = 0. \tag{A.15}$$

Multiplying Equation (A.15) by y', one obtains

$$\mathcal{F}_y y' - \mathcal{F}_{y'y}y'^2 - \mathcal{F}_{y'y'}y'y'' = \frac{d}{dx}\left(\mathcal{F} - \mathcal{F}_{y'}y'\right)$$

and therefore, Euler-Lagrange equation has the first integral

$$\mathcal{F} - \mathcal{F}_{y'}y' = C, \tag{A.16}$$

where C is a constant. Equation (A.16) is commonly referred to as Beltrami's identity.

Case 3: $\mathcal{F} = \mathcal{F}(x, y)$

If $\mathcal{F}$ does not depend on y', Euler-Lagrange equation takes the form

$$\mathcal{F}_y(x, y) = 0\,, \tag{A.17}$$

and hence is not a differential equation, but an algebraic one, whose solution consists of one or more curves $y = y(x)$.

Case 4

In a variety of problems, one encounters functionals of the form

$$\int_{x_o}^{x_f} \Gamma(x, y)\sqrt{1 + y'^2}\, dx$$

representing the integral of a function $\Gamma(x, y)$ with respect to the so-called arc length s ($ds = \sqrt{1 + y'^2}\, dx$). In this case, Euler-Lagarnge equation can be transformed into

$$\begin{aligned}
\mathcal{F}_y - \frac{d}{dx}\mathcal{F}_{y'} &= \Gamma_y\sqrt{1 + y'^2} - \frac{d}{dx}\left[\Gamma\frac{y'}{\sqrt{1 + y'^2}}\right] \\
&= \Gamma_y\sqrt{1 + y'^2} - \Gamma_x\frac{y'}{\sqrt{1 + y'^2}} - \Gamma_y\frac{y'^2}{\sqrt{1 + y'^2}} - \Gamma\frac{y''}{(1 + y'^2)^{3/2}} \\
&= \frac{1}{\sqrt{1 + y'^2}}\left[\Gamma_y - \Gamma_x y' - \Gamma\frac{y''}{1 + y'^2}\right] = 0,
\end{aligned}$$

i.e.,

$$\Gamma_y - \Gamma_x y' - \Gamma \frac{y''}{1+y'^2} = 0.$$

A.2.2 Free end points problems

Unlike the simplest variational problem, problems having end points that are not fixed are now considered. Suppose now to be given the same functional (A.7), but either x_f or $y(x_f)$ (or both) are not fixed, i.e., free. Three possible cases may therefore arise and are investigated below, yet it is convenient to highly remark a few important quantities. In particular, δx_f, $\delta y(x_f)$ and δy_f denote the variation in x_f, the variation in the value of $y(x)$ at x_f and the variation in the final value of $y(x)$, respectively. In Problem A.1, it is easy to show that $\delta y(x_f)$ is identically δy_f, since both end points are specified, yet they can be related one another with the aid of the former quantity via other relations, depending on the problem under consideration.

Specified x_f and free $y(x_f)$

Problem A.2. *Find a necessary condition for a function to be an extremal for the functional*

$$J[y] = \int_{x_0}^{x_f} \mathcal{F}(x, y(x), y'(x))\, dx,$$

where x_0, $y(x_0)$ and x_f are specified and $y(x_f)$ is free.

Admissible curves all start from the same point and terminate on a vertical line, as shown in Figure A.1b. Before setting the first variation to be zero, suppose y^* is an extremal for Problem A.2, as shown in Figure A.1c. Therefore $\delta J(y^*)$ must be zero. Moreover, suppose that $y^*(x_f) = y_f$. Now consider a fixed end point problem with the same functional, the same x_0 and x_f and with specified end points $y(x_0) = y_0$ and $y(x_f) = y_f$ that are the same as for the extremal y^* in the free end point problem. Therefore, the curve y^* must be a solution of the Euler-Lagrange equation (A.13). In other words, an extremal for a free end point problem is also an extremal for the fixed end point problem with the same end points and the same functional. Thus, regardless of the boundary conditions, Euler-Lagrange equation must be satisfied. However, an additional boundary condition (at x_f) is still needed. To this purpose, the following considerations are made. Firstly, mathematical manipulations from Equation (A.8) to Equation (A.10) are

still valid. In particular, one obtains

$$\begin{aligned}\delta J &= \int_{x_0}^{x_f} \mathcal{F}_y \delta y \, dx + \left[\mathcal{F}_{y'} \delta y\right]_{x_0}^{x_f} - \int_{x_0}^{x_f} \frac{d}{dx}\mathcal{F}_{y'} \delta y \, dx \\ &= \int_{x_0}^{x_f} \left(\mathcal{F}_y - \frac{d}{dx}\mathcal{F}_{y'}\right) \delta y \, dx + \left[\mathcal{F}_{y'} \delta y\right]_{x_f} - \left[\mathcal{F}_{y'} \delta y\right]_{x_0} = 0.\end{aligned} \tag{A.18}$$

Now, since admissible variations δy require $\delta y(x_0) = 0$, it follows

$$\int_{x_0}^{x_f} \left(\mathcal{F}_y - \frac{d}{dx}\mathcal{F}_{y'}\right) \delta y \, dx + \mathcal{F}_{y'}(x_f)\delta y(x_f) = 0. \tag{A.19}$$

On the other hand, admissible variations are characterized with $\delta y(x_f) \neq 0$, consequently the first variation can be identically zero when both

$$\mathcal{F}_y - \frac{d}{dx}\mathcal{F}_{y'} = 0 \tag{A.20}$$

and

$$\mathcal{F}_{y'}(x_f) = 0 \tag{A.21}$$

are satisfied. It is worth noting that Equation (A.21) provides the second required boundary condition for Euler-Lagrange equation and it is commonly referred to as the natural boundary condition of the problem.

Free x_f and specified $y(x_f)$

Problem A.3. *Find a necessary condition for a function to be an extremal for the functional*

$$J[y] = \int_{x_0}^{x_f} \mathcal{F}(x, y(x), y'(x)) \, dx,$$

where x_0, $y(x_0)$ and $y(x_f)$ are specified and x_f is free.

Admissible curves all start from the same point and terminate on a horizontal line with ordinate y_f, as shown in Figure A.1d. Because of the free final value x_f, necessary conditions for Problem A.3 are different when compared with those for Problem A.2. In Figure A.1e an extremal curve y^*, terminating at the point (x_f, y_f) and a neighboring curve y terminating at the point $(x_f + \delta x_f, y_f)$ are shown. Limiting ourselves to first order terms, it is easy to show by inspection of Figure A.1e that

$$\delta y(x_f) + y'(x_f)\delta x_f = 0$$

or

$$\delta y(x_f) = -y'(x_f)\delta x_f. \tag{A.22}$$

Setting the first variation of the functional equal to zero, namely

$$\delta J = 0 = \delta \int_{x_0}^{x_f} \mathcal{F}(x, y(x), y'(x))\, dx, \tag{A.23}$$

and making use of Leibniz integral rule for differentiation, one obtains

$$\int_{x_0}^{x_f} \delta\mathcal{F}(x, y(x), y'(x))\, dx + \delta_{x_f} \int_{x_0}^{x_f} \mathcal{F}(x, y(x), y'(x))\, dx = 0,$$

where the symbol $\delta_{x_f}(.)$ at the second term at the left hand-side denotes the variation of (.) due to the variation in x_f. Integrating the first term by parts and using the fundamental theorem of calculus for the second term, one obtains

$$\int_{x_0}^{x_f} \left(\mathcal{F}_y - \frac{d}{dx}\mathcal{F}_{y'}\right) \delta y\, dx + \left[\mathcal{F}_{y'}\delta y\right]_{x_f} - \left[\mathcal{F}_{y'}\delta y\right]_{x_0} + [\mathcal{F}]_{x_f}\delta x_f = 0 \tag{A.24}$$

Now, since admissible variations δy require $\delta y(x_0) = 0$, it follows

$$\int_{x_0}^{x_f} \left(\mathcal{F}_y - \frac{d}{dx}\mathcal{F}_{y'}\right) \delta y\, dx + \left[\mathcal{F}_{y'}\right]_{x_f} \delta y(x_f) + [\mathcal{F}]_{x_f}\delta x_f = 0$$

and using Equation (A.22), one obtains

$$\int_{x_0}^{x_f} \left(\mathcal{F}_y - \frac{d}{dx}\mathcal{F}_{y'}\right) \delta y\, dx - \left[\mathcal{F}_{y'}(x_f)y'(x_f) - \mathcal{F}(x_f)\right] \delta x_f = 0.$$

Besides, admissible variations are characterized with $\delta x_f \neq 0$, consequently the first variation can be identically zero when Euler-Lagrange equation

$$\mathcal{F}_y - \frac{d}{dx}\mathcal{F}_{y'} = 0$$

holds and the following relation

$$\mathcal{F}_{y'}(x_f)y'(x_f) - \mathcal{F}(x_f) = 0 \tag{A.25}$$

is satisfied.

Free x_f and $y(x_f)$

In this section, problems having both x_f and $y(x_f)$ free are considered. Not surprisingly, necessary conditions for Problems A.2 and A.3 are included as special cases. The problem is stated as follows:

Problem A.4. *Find a necessary condition for a function to be an extremal for the functional*

$$J[y] = \int_{x_0}^{x_f} \mathcal{F}(x, y(x), y'(x))\, dx,$$

where x_0 and $y(x_0)$ are specified, while x_f and $y(x_f)$ are free.

Figure A.1f shows an extremal y^* and an admissible neighboring curve y. Neglecting higher order terms, a relation for $\delta y(x_f)$ and δy_f may be easily found, namely

$$\delta y_f = y'(x_f)\delta x_f + \delta y(x_f) \tag{A.26}$$

or

$$\delta y(x_f) = \delta y_f - y'(x_f)\delta x_f. \tag{A.27}$$

It is easy to note that mathematical manipulations for Problem A.4 are identical to those for Problem A.3 up to Equation (A.24), which taking into account Equation (A.27) and highlighting that admissible variations δy require $\delta y(x_0) = 0$, one obtains

$$\int_{x_0}^{x_f} \left(\mathcal{F}_y - \frac{d}{dx}\mathcal{F}_{y'}\right) \delta y\, dx - \left[\mathcal{F}_{y'}(x_f)y'(x_f) - \mathcal{F}(x_f)\right] \delta x_f + \mathcal{F}_{y'}(x_f)\delta y_f = 0. \tag{A.28}$$

Consequently, the first variation is identically zero when

$$\mathcal{F}_y - \frac{d}{dx}\mathcal{F}_{y'} = 0$$

holds and the following relations

$$\begin{cases} \mathcal{F}_{y'}(x_f)y'(x_f) - \mathcal{F}(x_f) = 0, \\ \mathcal{F}_{y'}(x_f) = 0 \end{cases} \tag{A.29}$$

are satisfied.

A.3 Further generalizations

A.3.1 Functionals depending on higher-order derivatives

So far, the aforementioned variational problems considered functionals whose integrands depend on the independent x, the function $y(x)$ and its derivative $y'(x)$. However, many problems involve functionals whose integrands contain not only $y(x)$ and $y'(x)$, but also higher-order derivatives, e.g., $y''(x)$, namely

$$J[y] = \int_{x_0}^{x_f} \mathcal{F}(x, y(x), y'(x), y''(x))\, dx, \tag{A.30}$$

where $\mathcal{F} : [a, b] \times \mathbb{R} \times \mathbb{R} \times \mathbb{R} \to \mathbb{R}$. Considering fixed boundary conditions expressed by $y(x_0) = y_0$, $y(x_f) = y_f$, $y'(x_0) = \hat{y}_0$ and $y'(x_f) = \hat{y}_f$, the first variation becomes

$$\delta J = \int_{x_0}^{x_f} (\mathcal{F}_y \delta y + \mathcal{F}_{y'} \delta y' + \mathcal{F}_{y''} \delta y'')\, dx. \tag{A.31}$$

In fact, necessary conditions for an extremal ($\delta J = 0$) can be carried out by using the method illustrated above without essential changes, yet integration by parts applies twice, leading to the following Euler-Lagrange equation

$$\mathcal{F}_y - \frac{d}{dx}\mathcal{F}_{y'} + \frac{d^2}{dx^2}\mathcal{F}_{y''} = 0. \tag{A.32}$$

More generally, if derivatives of y appear in the integrand of the functional up to the order n, i.e.,

$$J[y] = \int_{x_0}^{x_f} \mathcal{F}(x, y(x), y'(x), \ldots, y^{(n)}(x))\, dx, \tag{A.33}$$

where $\mathcal{F} : [a, b] \times \mathbb{R} \times \mathbb{R} \times \cdots \times \mathbb{R} \to \mathbb{R}$, and an extremal is seeked satisfying the (fixed) boundary conditions $y(x_0) = A_0$, $y'(x_0) = A_1$, $y''(x_0) = A_2$, $\ldots$, $y(x_0)^{(n-1)} = A_{n-1}$ and $y(x_f) = B_0$, $y'(x_f) = B_1$, $y''(x_f) = B_2$, $\ldots$, $y(x_f)^{(n-1)} = B_{n-1}$, the necessary condition for the existence of extremals assumes the form

$$\mathcal{F}_y - \frac{d}{dx}\mathcal{F}_{y'} + \frac{d^2}{dx^2}\mathcal{F}_{y''} - \cdots + (-1)^n \frac{d^n}{dx^n}\mathcal{F}_{y^{(n)}} = 0, \tag{A.34}$$

which is commonly denoted as Euler-Poisson equation.

A.3.2 Variational problems with subsidiary conditions

In the simplest variational problem, the class of admissible curves was specified (apart from certain smoothness requirements) by conditions imposed on the end points of the curves. However, many application of the calculus of variations lead to problems in which not only boundary conditions, but also conditions of quite a different type known as subsidiary (or side) conditions are imposed on the admissible curves. As an example, consider the following isoperimetric problem, which can be stated as follows:

Problem A.5. *Find the curve $y = y(x)$ for which the functional*

$$J[y] = \int_{x_0}^{x_f} \mathcal{F}(x, y(x), y'(x))\, dx$$

has an extremum, where admissible curves satisfy the (specified) boundary conditions $y(x_0) = y_0$ and $y(x_f) = x_f$ and are such that another functional

$$K[y] = \int_{x_0}^{x_f} \mathcal{G}(x, y(x), y'(x))\, dx$$

has a fixed value, being $\mathcal{F}$, $\mathcal{G} : [a, b] \times \mathbb{R} \times \mathbb{R} \to \mathbb{R}$.

To solve this problem, we assume that functions $\mathcal{F}$ and $\mathcal{G}$ defining the functionals J and K have continuous first and second derivatives for arbitrary values of y and y'. For this kind of variational problems, one defines the so-called augmented cost functional J^a defined as

$$J^a[y] = J[y] - \lambda K[y], \tag{A.35}$$

where λ is a constant, commonly referred to as the Lagrangian multiplier. By doing so, the constraint has been included within the (new) cost functional and therefore the constrained problem becomes an unconstrained one, allowing the use of Theorem A.2, namely

$$\begin{aligned} \delta J^a &= \delta J[y] - \lambda \delta K[y] \\ &= \int_{x_0}^{x_f} \left[\left(\mathcal{F}_y \delta y + \mathcal{F}_{y'} \delta y' \right) - \lambda \left(\mathcal{G}_y \delta y + \mathcal{G}_{y'} \delta y' \right) \right] dx = 0. \end{aligned} \tag{A.36}$$

Hence, after integration by parts of integrals including $\delta y'$ and taking into account the fixed boundary conditions, the corresponding Euler-Lagrange equation may be recast as

$$\mathcal{F}_y - \frac{d}{dx}\mathcal{F}_{y'} - \lambda \left(\mathcal{G}_y - \frac{d}{dx}\mathcal{G}_{y'} \right) = 0. \tag{A.37}$$

where the constant λ is derived using the isoperimetric constraint.

Bibliography

[1] Cohn MZ, Dinovitzer AS, Application of structural optimization, *J Struct Eng* **120(2)**, pp. 617-650, 1994.

[2] Lee KS, Geem ZW, A new meta-heuristic algorithm for continuous engineering optimization: Harmony search theory and practice, *Comput Methods Appl Mech Eng* **194(36-38)**, pp. 3902-3933, 2005.

[3] Yang XS, Gandomi AH, Bat algorithm: A novel approach for global engineering optimization, *Eng Comput* **29(5)**, pp. 464-483, 2012.

[4] Panagant N, Pholdee N, Bureerat S, Kaen K, Yildiz AR, Sait SM, Seagull optimization algorithm for solving real-world design optimization problems, *Mater Test* **62(6)**, pp. 640–644, 2020.

[5] Thanedar PB, Vanderplaats GN, Survey of discrete variable optimization for structural design, *J Struct Eng* **121(2)**, pp. 301-306, 1995.

[6] Błachut J, Magnucki K, Strength, Stability and optimization of pressure vessels: Review of selected problems, *Appl Mech Rev* **61(6)**, 2008.

[7] Zingoni A, Parametric stress distribution in shell-of-revolution sludge digesters of parabolic ogival form, *Thin-Walled Struct* **40(7-8)**, pp. 691-702, 2002.

[8] Zingoni A, Shell forms for egg-shaped concrete sludge digesters: a comparative study on structural efficiency, *Struct Eng Mech* **19(3)**, pp. 321-336, 2005.

[9] Zhu L, Boyle JT, Optimal shapes for axisymmetric pressure vessels: A Brief overview, *J Pressure Vessel Technol* **122(4)**, pp. 443-449 , 2000.

[10] Prager W, Rozvany GIN, Optimal spherical cupola of uniform strength, *Ingenieur-Archiv* **49**, pp. 287–293, 1980.

[11] Nakamura H, Dow M, Rozvany GIN, Optimal spherical cupola of uniform strength: Allowance for Selfweigth, *Ingenieur-Archiv* **51**, pp. 159-181, 1981.

[12] Dow M, Namakmura H, Rozvany GIN, Optimal cupolas of uniform strength: Spherical M-shells and axisymmetric T-shells, *Ingenieur-Archiv* **52**, pp. 335-353, 1982.

[13] Serra M, Design of membrane shells of revolution with optimal stiffness, *Mech Base Des Struct Mach* **38**, pp. 403-416, 2010.

[14] Banichuk NV, Shape optimization for membrane shells of revolutions, *Dokl Phys* **50(11)**, pp. 338-342, 2005.

[15] Banichuk NV, Optimization of axisymmetric membrane shells, *J Appl Math Mech* **71**, pp. 527-535, 2007.

[16] Kozikowska A, Geometry and topology optimization of statically determinate beams under fixed and most unfavorably distributed load, *Lat Am J solids Struct* **13(4)**, pp. 775-795, 2016.

[17] Eschenauer HA, Olhoff N, Topology optimization of continuum structures: A review, *Appl Math Rev* **54**, pp. 331-390, 2001.

[18] Rozvany GIN, A critical review of established methods of structural topology optimization, *Struct Multidisc Optim* **37**, pp. 217–237, 2009.

[19] Kim YY, Kim TS, Topology optimization of beam cross sections, *Int J Solids Struct* **37(3)**, pp. 477-493, 2000.

[20] Mota Soares C, Rodrigues HC, Oliveira Faria LM, Haug EJ, Optimization of the geometry of shafts using boundary elements, *J Mech Transms Automa Des* **106**, pp. 199-202, 1984.

[21] Schramm U, Pilkey WD, Structural shape optimization for the torsional problem using direct integration and B-splines, *Comp Meth Appl Mech Eng* **107**, pp. 251-268, 1993.

[22] Leary M, Merli L, Torti F, Mazur M, Brandt M, Optimal topology for additive manufacture: A method for enabling additive manufacture of support-free optimal structures, *Mater Des* **63**, pp. 678-690, 2014.

[23] Timoshenko SS, *Strength of materials*, John Wiley and Sons, New York, 1930.

[24] Miyamoto Y, Kaysser WA, Rabin BH, Kawasaki A, Ford RG, *Functionally graded materials. Design, processing and applications*, Kluwer Academic Publishers, London, 1999.

[25] Birman V, Byrd LW, Modeling and analysis of functionally graded materials and structures, *Appl Mech Rev* **60**, pp. 195-216, 2007.

[26] Kirk DE, *Optimal control theory. An introduction*, Dover Publications, New York, 2004.

[27] Bertsakes DP, *Dynamic programming and optimal control, volume 1*, Athena Scientific Publishers, Belmont, 2012.

[28] Bertsakes DP, *Dynamic programming and optimal control, volume 2: Approximate dynamic programming*, Athena Scientific Publishers, Belmont, 2012.

[29] Bertsakes DP, *Nonlinear programming*, Athena Scientific Publishers, Belmont, 2004.

[30] Nocedal J, Wright S, *Numerical optimization*, Springer-Verlag, New York, 2006.

[31] Polak E, An historical survey of computational methods in optimal control, *SIAM Rev* **15**, pp. 553-584, 1973.

[32] Miele A, Recent advances in gradient algorithms for optimal control problems, *J Optim Theory App* **17**, pp. 361-430, 1975.

[33] Stryk OV, Bulirsch R, Direct and indirect methods for trajectory optimization, *Ann Oper Res* **37**, pp. 357-373, 1992.

[34] Betts JT, Survey of numerical methods for trajectory optimization, *J Guid Control Dyn* **21**, pp. 193-207, 1998.

[35] Rao AV, A Survey of Numerical Methods for Optimal Control, *Proceedings of the Astrodynamics Specialist Conference AAS/AIAA*, Pittsburgh, USA, AAS Paper 09-334, August, 2009.

[36] Stoer J, Bulirsch R, *Introduction to Numerical Analysis*, Springer-Verlag, New York, 1980.

[37] Grimm W, Markl A, Adjoint estimation from a multiple shooting method, *J Optim Theory App* **26**, pp. 185-189, 2003.

[38] Sagliano M, Theil S, Bergsma M, D'Onofrio V, Whittle L, Viavattene G, On the Radau pseudospectral method: Theoretical and implementation advances, *CEAS Space J* **9**, pp. 313-331, 2017.

[39] Vlassebroeck J, Dooren RV, A Chebyshev technique for solving nonlinear optimal control problems, *IEEE Trans Automat Contr* **33(4)**, pp. 333-340, 1988.

[40] Elnagar G, Kazemi M, Razzaghi M, The pseudospectral Legendre method for discretizing optimal control problems, *IEEE Trans Automat Contr* **40(10)**, pp. 1793-1796, 1995.

[41] Rao AV, Benson DA, Darby C, Patterson MA, Francolin C, Sanders I, Huntington GT, Algorithm 902: GPOPS, a MATLAB software for solving multiphase optimal control problems using the Gauss pseudospectral method, *ACM T Math Software* **37(2)**, pp. 22:1-22:39, 2010.

[42] Garg D, Patterson MA, Darby C, Francolin C, Huntington GT, Hager WW, Rao AV, Direct trajectory optimization and costate estimation of finite-horizon and infinite-horizon optimal control problems using a Radau pseudospectral method, *Comput Optim Appl* **49**, pp. 335–358, 2011.

[43] Garg D, *Advances in global pseudospectral methods for optimal control*, PhD dissertation, University of Florida, Gainesville, USA, 2011.

[44] Vlassenbroeck J, A Chebyshev polynomial method for optimal control with state constraints, *Automatica* **24(4)**, pp. 499-506, 1988.

[45] Cichella V, Kaminer I, Walton C, Hovakimyan N, Pascoal AM, Consistent approximation of optimal control problems using Bernstein polynomials, *Proceedings of the IEEE 58th Conference on Decision and Control* Nice, France, pp. 4292-4297, 11-13 December, 2019.

[46] Cizniar M, Salhi D, Fikar M, Latifi MA, A Matlab package for orthogonal collocations on finite elements in dynamic optimisation, *Proceedings of the 15th International Conference Process Control* Strbske Pleso, Slovakia, 7-10 June, 2005.

[47] Biegler LT, An overview of simultaneous strategies for dynamic optimization, *Chem Eng Process* **46(11)**, pp. 1043-1053, 2007.

[48] Wang Y, Zhu Y, Jiang X, Li S, Comparison of LPM, GPM and RPM for optimization of low-thrust Earth-Mars rendezvous trajectories, *Proceedings of 2014 IEEE Chinese Guidance, Navigation and Control Conference* Yantai, China, 8-10 August, 2014

[49] Patterson MA, Rao AV, Exploiting sparsity in direct collocation pseudospectral methods for solving optimal control problems, *J Spacecr Rockets* **49(2)**, pp. 364-377, 2012.

[50] Hildebrand FB, *Introduction to Numerical Analysis*, Dover Publications, New York, 1987.

[51] Abramowitz M, Stegun I, *Handbook of mathematical functions with formulas, graphs and mathematical tables*, Dover Publications, New York, 1965.

[52] Fahroo F, Ross IM, Pseudospectral methods for infinite-horizon nonlinear optimal control problems, *J Guid Control Dyn* **31(4)**, pp. 927–936, 2008.

[53] Ross IM, Fahroo F, Convergence of the costates does not imply convergence of the controls, *J Guid Control Dyn* **31(5)**, pp. 1492–1496, 2008.

[54] Carbonari RC, Munoz-Rojas PA, Andrade EQ, Paulinjo GH, Nishimoto K, Silva ECN, Design of pressure vessels using shape optimization: An integrated approach, *Int J Pres Ves Pip* **88(5)**, pp. 198-212, 2011.

[55] Vu VT, Minimum weight design for toroidal shells with strengthening component, *J Pressure Vessel Technol* **138**, 021202, 2016.

[56] Kruzelecki J, Proszowski R, Shape optimization of thin-walled pressure vessel end closures, *Struct Multidisc Optim* **46**, pp. 739-754, 2012.

[57] Santhosh R, Shaik Ismail, Jain PC, Anjaneyulu PSR, Shape optimization of shallow domes subjected to external pressure, *Struct Multidisc Optim* **57**, pp. 903-908, 2018.

[58] Sowinski K, Magnucki K, Shaping of dished heads of the cylindrical pressure vessel for diminishing of the edge effect, *Thin-Walled Struct* **131**, pp. 746-754, 2018.

[59] Banichuk NV, Yu Ivanova S, Makeev EV, Sinistin AV, Optimal shape design of axisymmetric shells for crack initiation and propagation under cyclic loading, *Mech Base Des Struct Mach* **33(2)**, pp. 253-269, 2005.

[60] Banichuk NV, Ragnedda F, Serra M, Axisymmetric shell optimization under fracture mechanics and geometric constraint, *Struct Multidisc Optim* **31**, pp. 223-228, 2006.

[61] Kobelev V, The anisotropic pressure vessel of minimal mass, *Struct Multidisc Optim* **55**, pp. 375-380, 2017.

[62] Timoshenko SS, *Theory of plates and shells*, Mc Graw Hill, New York, 1959.

[63] Flugge W, *Stresses in shells*, Springer, Berlin, 1973.

[64] Plocher J, Panesar A, Review on design and structural optimisation in additive manufacturing: towards next-generation lightweight structures, *Mater Des* **182**, 108164, 2019.

[65] McNelly BP, Hooks RL, Additive manufacturing of pressure vessels (with plating), *Proceedings of the ASME 2017 Pressure Vessels and Piping Conference PVP2017*, Waikoloa, Hawaii, USA 9V92017-65888, July 16-20, 2017.

[66] Kroll E, Buchris E, Weight reduction of 3D-printed cylindrical and toroidal pressure vessels through shape modification, *Procedia Manuf* **21**, pp. 133-140, 2018.

[67] Hassani V, An investigation of additive manufacturing technologies for development of end-use components: a case study, *Int J Pres Ves Pip* **187**, 104171, 2020.

[68] Ni XQ, Kong DC, Wen Y, Zhang L, Wu WH, He BB, Lu L, Zhu DX, Anisotropy in mechanical properties and corrosion resistance of 316L stainless steel fabricated by selective laser melting, *Int J Mineral Metall* **26(3)**, pp. 319-328, 2019.

[69] Liu JS, Parks GT, Clarkson PJ, Shape optimisation of axisymmetric cylindrical nozzles in spherical pressure vessels subject to stress constraints, *Int J Pres Ves Pip* **78**, pp. 1-9, 2001.

[70] Solberg K, Guan S, Razavi SMJ, Welo T, Chan KC, Berto F, Fatigue of additively manufactured 316L stainless steel: the influence of porosity and surface roughness, *Fatig Fract Eng Mater Struct* **42(9)**, pp. 2043-2052, 2019.

[71] Maleki E, Bagherifard S, Bandini M, Guagliano M, Surface post-treatments for metal additive manufacturing: Progress, challenges, and opportunities, *Addit Manuf* **37**, 101619, 2021.

[72] Wang CY, Longest reach of a cantilever with a tip load, *Eur J Phys* **37**, 012001, 2016.

[73] Plaut RH, Virgin LN, Furthest reach of a uniform cantilevered elastica, *Mech Res Commun* **83**, pp. 18–21, 2017.

[74] Bigoni D, Kirillov ON, Misseroni D, Noselli G, Tommasini M, Flutter and divergence instability in the Pflüger column: Experimental evidence of the Ziegler destabilization paradox, *J Mech Phys Solids* **116**, pp. 99-116, 2018.

[75] Magnucki K, Lewinski J, Cichy R, Bending of beams with bisymmetrical cross sections under non-uniformly distributed load: Analytical and numerical-FEM studies, *Arch Appl Mech* **89(10)**, pp. 2103-2114, 2019.

[76] Yan Y, Carrera E, Pagani A, Kaleel I, Garcia A, Isogeometric analysis of 3d straight beam-type structures by Carrera unified formulation, *Appl Math Model* **79**, pp. 768-792, 2020.

[77] Croccolo D, De Agostinis M, Fini S, Olmi G, Robusto F, Cylindrical cross section optimization, *Proc Inst Mech Eng, Part C* **235(13)**, pp. 2426–2436, 2021.

[78] Cox HL, *The design of structures of least weight*, Pergamon, Oxford, 1965.

[79] Hemp W, *Optimum structures*, Clarendon Press, Oxford, 1973.

[80] Lewinski J, Sokol T, Graczykowski C, *Michell structures*, Springer, Cham, 2019.

[81] Bendsoe MP, Optimal shape design as a material distribution problem, *Struct Multidisc Optim* **1(4)**, pp. 193-202, 1989.

[82] Pedersen P, Pedersen NL, Analytical optimal designs for long and short statically determinate beam structures, *Struct Multidisc Optim* **39(4)**, pp. 343-357, 2009.

[83] Xie YM, Zuo ZH, Huang XD, Rong JH, Convergence of topological patterns of optimal periodic structures under multiple scales, *Struct Multidisc Optim* **46(1)**, pp. 41-54, 2012.

[84] Lee E, James KA, Martins JR, Stress-constrained topology optimization with design-dependent loading, *Struct Multidisc Optim* **46(5)**, pp. 647-661, 2012.

[85] Gerzen N, Barthold FJ, Enhanced analysis of design sensitivities in topology optimization, *Struct Multidisc Optim* **46(6)**, pp. 585-595, 2012.

[86] Qiao H, Liu S, Topology optimization by minimizing the geometric average displacement, *Eng Optim* **45(1)**, pp. 1-18, 2013.

[87] Qiao H, Li H, The discussion on optimization models of pure bending beam, *Int J Adv Struct Eng* **5(11)**, 2013.

[88] Sigmund O, Maute M, Topology optimization approaches, *Struct Multidisc Optim* **48(6)**, pp. 1031-1055, 2013.

[89] Nadir W, Kim IY, de Weck OL, Structural Shape Optimization Considering Both Performance and Manufacturing Cost, *Proceedings of the 10th Multidisciplinary Analysis and Optimization Conference AIAA/ISSMO*, New York, USA, AIAA 2004-4593, August 31 - September 1, 2004.

[90] Banichuk NV, Ragnedda F, Serra M, Optimum shapes of bar cross-sections, *Struct Multidisc Optim* **23**, pp. 222-232, 2002.

[91] Ragnedda F, Serra M, On optimum thin-walled closed cross section, *Struct Multidisc Optim* **30**, pp. 233-235, 2005.

[92] Gobbi M, Levi F, Mastinu G, previati G, On the analytical derivation of the pareto-optimal set with applications to structural design, *Struct Multidisc Optim* **51(3)**, pp. 645-657, 2015.

[93] Gobbi M, Levi F, Mastinu G, previati G, Bending of beams of arbitrary cross sections-optimal design by analytical formulae, *Struct Multidisc Optim* **55**, pp. 827-838, 2017.

[94] Clausen T, Uber die Form architektonischer Saulen, *Bull Cl Physico Math Acad St Petersbourg* **IX**, pp. 371–380, 1851.

[95] Nikolai EL, Lagrange's problem of optimal shape of a column, *Izvestia St Petersbourg Politechn Inst* **8(1)**, pp. 255–288, 1955.

[96] Keller JB, The shape of the strongest column, *Arch Rational Mech Anal* **5**, pp. 275–285, 1960.

[97] Tadjbakhsh I, Keller JB, Strongest columns and isoperimetric inequalities, *ASME J Appl Mech* **29**, pp. 159-164, 1962.

[98] Olhoff N, Rasmussen S, On single and bimodal optimum buckling loads of clamped columns, *Int J Solids Struct* **13**, pp. 605-614, 1977.

[99] Antman SS, Kenney CS, Large buckled states of nonlinearly elastic rods under torsion, thrust and gravity, *Arch Rational Mech Anal* **76**, pp. 289-338, 1981.

[100] Seyranian AP, Privalova OG, The Lagrange problem on an optimal column: Old and new results, *Struct Multidisc Optim* **25**, pp. 393–410, 2003.

[101] Atanackovic TM, On the optimal shape of a compressed rotating rod, *Meccanica* **39**, pp. 147–157, 2004.

[102] Atanackovic TM, Braun DJ, The strongest rotating rod, *Int J Non Linear Mech* **40**, pp. 747-754, 2005.

[103] Atanackovic TM, Novakovic BN, Optimal shape of an elastic column on elastic foundation, *Eur J Mech A/Solids* **25**, pp. 154-165, 2006.

[104] Atanackovic TM, Jakovljevic BB, Petkovic MR, On the optimal shape of a column with partial elastic foundation, *Eur J Mech A/Solids* **29**, pp. 283-289, 2010.

[105] Novakovic BN, Optimal shape of a column with clamped-elastically supported ends positioned on elastic foundation, *J Theor Appl Mech* **42**, pp. 191-200, 2015.

[106] Spasic DT, *Optimal design of elastic columns for maximum buckling load*, Book chapter in Volume 3 of Stability, Vibration and Control of Systems, Birkhauser, Boston, 1997.

[107] Glavardanov VB, Spasic DT, Atanackovic TM, Stability and optimal shape of Pflüger micro/nano beam, *Int J Solids Struct* **49**, pp. 2559-2567, 2012.

[108] Janev M, Vrcelj Z, Atanackovic TM, Optimal shape of the rotating nano rod, *Int J Non Linear Mech* **132**, 103688, 2021.

[109] Strozzi A, Bertocchi E, Mantovani S, A paradox in curved beams, *Proc Inst Mech Eng, Part C* **233(8)**, pp. 2830-2833, 2019.

[110] Leopardi L, Strozzi A, Two extensions towards practical applications of a paradox in curved beams, *Proc CIRP* **84**, pp. 761-768, 2019.

[111] Young C, Budyans G, *Roark's formulas for stress and strain*, McGraw-Hill, New York, 2011.

[112] Atanackovic TM, *Stability theory of elastic rods*, World Scientific, Singapore, 1997.

[113] Atanackovic TM, Spasic DT, A model for plane elastica with simple shear deformation pattern, *Acta Mech* **104**, pp. 241-253, 1994.

[114] Cox SJ, Overton ML, On the optimal design of columns against buckling, *SIAM J Math Anal* **23**, pp. 87–325, 1992.

[115] Renton JD, Generalized beam theory applied to shear stiffness, *Int J Solids Struct* **27**, pp. 1955-1967, 1991.

[116] Peterson RE, *Stress concentration factors*, John Wiley and Sons, New York, 1974.

[117] Navier CLMH, *De la resistance des corps solides. 3 ed. avec des notes et des appendices par M. Barre de Saint-Venant*, Dunod, Paris, 1864.

[118] Barber JR, *Intermediate mechanics of materials*, Springer, Dordrecht, 2010.

[119] Boresi AP, Schmidt RJ, Sidebottom RM, *Advances mechanics of materials*, Wiley, New York, 1993.

[120] Ratnakumar GEV, Kumar BJ, Prasad K, Design and stress analysis of various cross section of hook, *Int J Innovation in Eng and Tech* **4(4)**, pp. 90-97, 2013.

[121] Shen M, Bever MB, Gradients in composite materials, *J Mater Sci* **7**, pp. 741-746, 1972.

[122] El-Galy IM, Saleh BI, Ahmed MH, Functionally graded materials classifications and development trends from industrial point of view, *SN Appl Sci* **1**, 1378, 2019.

[123] Horgan CO, Chan AM, Torsion of functionally graded isotropic linearly elastic bars, *J Elast* **52**, pp. 181-199, 1998.

[124] Kubair DV, Stress concentration factor in functionally graded plates with circular holes subjected to anti-plane shear loading, *J Elast* **114**, pp. 179–196, 2014.

[125] Akbarzadeh AH, Abedini A, Chen ZT, Effect of micromechanical models on structural responses of functionally graded plates, *Compos Struct* **119**, pp. 598-609, 2015.

[126] Chalivendra VB, Shukla A, Parameswaran V, Dynamic out of plane displacement fields for an inclined crack in graded materials, *J Elast* **69**, pp. 99–119, 2002.

[127] Li X, Peng X, A pressurized functionally graded hollow cylinder with arbitrarily varying material properties, *J Elast* **96**, pp. 81–95, 2009.

[128] Moosaie A, A nonlinear analysis of thermal stresses in an incompressible functionally graded hollow cylinder with temperature-dependent material properties, *Eur J Mech A/Solids* **55**, pp. 212-220, 2016.

[129] Birman V, Mechanics and energy absorption of a functionally graded cylinder subjected to axial loading, *Int J Eng Sci* **78**, pp. 18-26, 2014.

[130] Wang ZW, Zhang Q, Xia LZ, Wu JT, Liu PQ, Thermomechanical analysis of pressure vessels with functionally graded material coating, *J Pressure Vessel Technol* **138(1)**, 011205, 2016.

[131] Horgan CO, Chan AM, The stress response of functionally graded isotropic linearly elastic rotating disks, *J Elast* **55**, pp. 219-230, 1999.

[132] Nikbakht S, Kamarian S, Shakeri M, A review on optimization of composite structures Part II: Functionally graded materials, *Compos Struct* **214**, pp. 83-102, 2019.

[133] Wang ZW, Zhang Q, Xia LZ, Wu JT, Liu PQ, Stress analysis and parameter optimization of an FGM pressure vessel subjected to thermo-mechanical loadings, *Procedia Eng* **130**, pp. 374-389, 2015.

[134] Khorsand M, Tang Y, Design functionally graded rotating disks under thermoelastic loads: Weight optimization, *Int J Pres Ves Pip* **161**, pp. 33-40, 2018.

[135] Turteltaub S, Washabaugh P, Optimal distribution of material properties for an elastic continuum with structure-dependent body force, *Int J Solids Struct* **36(30)**, pp. 4587-4608, 1999.

[136] Turteltaub S, Optimal control and optimization of functionally graded materials for thermomechanical processes, *Int J Solids Struct* **39(12)**, pp. 3175-3197, 2002.

[137] Turteltaub S, Optimal non-homogeneous composites for dynamic loading, *Struct Multidisc Optim* **30**, pp. 101–112, 2005.

[138] Boussaa D, Optimizing the composition profile of a functionally graded interlayer using a direct transcription method, *Comput Mech* **39**, pp. 59–71, 2006.

[139] Boussaa D, Optimization of temperature-dependent functionally graded material bodies, *Comput Methods Appl Mech Eng* **198**, pp. 2827–2838, 2009.

[140] Nie J, Batra RC, Material tailoring and analysis of functionally graded isotropic and incompressible linear elastic hollow cylinders, *Compos Struct* **92**, pp. 265-274, 2010.

[141] Nie J, Zhong Z, Batra RC, Material tailoring for functionally graded hollow cylinders and spheres, *Compos Sci Technol* **71**, pp. 666-673, 2011.

[142] Batra RC, Material tailoring and universal relations for axisymmetric deformations of functionally graded rubberlike cylinders and spheres, *Math Mech Solids* **16(7)**, pp. 729-738, 2011.

[143] Kurrer KE, *The history of the theory of structures. From arch analysis to computational mechanics*, Ernst & Sohn, Berlin, 2008.

[144] Vullo V, Vivio F, *Rotors: Stress analysis and design*, Springer Science & Business Media, New York, 2013.

[145] Gross D,Seelig T, *Fracture mechanics with an introduction to micromechanics*, Springer, Berlin, 2006.

[146] Mishnaevsky JL, *Computational mesomechanics of composites*, John Wiley & Sons, Chichester, 2007.

[147] Voigt W, Über die beziehung zwischen den beiden elastizitätskonstanten isotroper körper, *Wied Ann Phys* **38**, pp. 573–587, 1889.

[148] Mori T, Tanaka K, Average stress in matrix and average elastic energy of materials with misfitting inclusions, *Acta Metall* **21**, pp. 571–574, 1973.

[149] Kerner EH, The elastic and thermo-elastic properties of composite media, *Proc Phys Soc B* **69**, pp. 808-813, 1956.

[150] Hashin Z, Shtrikman S, A variational approach to the theory of the elastic behaviour of multiphase materials, *J Mech Phys Solids* **11(2)**, pp. 127–140, 1963.

[151] Tamura I, Tomota Y, Ozawa M, Strength and ductility of Fe–Ni–C alloys composed of austenite and martensite with various strength, *Proceedings Third International Conference on Strength of Metals and Alloys*, Cambridge, volume 1, pp. 611–615, 1973.

[152] Wakashima K, Tsukamoto H, A unified micromechanical approach toward thermomechanical tailoring of metal matrix composites, *ISIJ Int* **32**, pp. 883–892, 1992.

[153] Madan R, Shubhankar B, Modeling of functionally graded materials to estimate effective thermomechanical properties, **to appear in** *World J Eng*, 2021.

[154] Abdalla HMA, Casagrande D, De Bona F, Thin-walled pressure vessels of minimum mass or maximum volume, *Struct Multidisc Optim* **61(1)**, pp. 111-121, 2020.

[155] Abdalla HMA, Casagrande D, Analytical thickness distribution for minimum compliance axisymmetric vessels, *Thin-Walled Struct* **149**, 106641, 2020.

[156] Abdalla HMA, Casagrande D, De Bona F, A dynamic optimization setting for functionally graded thick-walled cylinders, *Materials*, **13**, 3988, 2020.

[157] Abdalla HMA, Casagrande D, Strozzi A, A unified relaxed approach easing the practical application of a paradox in curved beams, *Proc IMechC: J Mechanical Engineering Science* **234(22)**, pp. 4535-4542, 2020.

[158] Abdalla HMA, Casagrande D, Optimal area variation for maximum stiffness isostatic beams under parametric linear distributed loads, *Mech Res Commun* **111**, 103659, 2021.

[159] Abdalla HMA, Casagrande D, De Bona F, De Monte T, Sortino M, Totis G, An optimized pressure vessel obtained by metal additive manufacturing: Preliminary results, *Int J Pres Ves Pip* **192**, 104434, 2021.

[160] Abdalla HMA, Casagrande D, An intrinsic material tailoring approach for functionally graded axisymmetric hollow bodies under plane elasticity, *J Elast*, **144**, pp. 15-32, 2021.

[161] Abdalla HMA, Casagrande D, On the longest reach problem in large deflection elastic rods, *Int J Non Linear Mech* **119**, 103310, 2020.

[162] Abdalla HMA, Casagrande D, Moro L, Thermo-mechanical analysis and optimization of functionally graded rotating disks, *J Strain Anal Eng Des*, **55(5-6)**, pp. 159–171, 2020.

[163] D'Agostino S, Abdalla HMA, Strozzi A, Practical repercussions of a paradox in curved beams, *AIP Conf Proc* **2309**, 020035, 2020.

[164] Abdalla HMA, Srnec JN, Casagrande D, Lower bound estimate for buckling in axially graded cantilever rods, *Eng Res Express* **2**, 035033, 2020.

[165] Marcu GG, Abdalla HMA, Casagrande D, Less is better: Coated spherical vessels over-perform their entirely graded counterparts, *Compos Struct*, **276**, 114529, 2021.

[166] Broek D, *Elementary engineering fracture mechanics*, M. Nijhoff Publishers, Dordrecht, 1986.

[167] Serra M, Optimum beam design based on fatigue crack propagation, *Struct Multidisc Optim* **19**, pp. 159-163, 2000.

[168] Atanackovic TM, Novakovic B, Vrcelj Z, Application of Pontryagin's principle to bimodal optimization of nano rods, *Int J Struct Stab Dyn* **12**, 1250012, 2012.

[169] Zenkour AM, On the magneto-thermo-elastic responses of FG annular sandwich disks, *Int J Eng Sci* **75**, pp. 54–66, 2014.

[170] Yildirim S, Hydrogen elasticity solution of functionally-graded spheres, cylinders and disks, *Int J Hydrog Energy* **45(41)**, pp. 22094-22101, 2020.

[171] Gelfand IM, Fomin SV, *Calculus of variations*, Prentice-Hall, London, 1963.

[172] Young LC, *Lecture on the calculus of variations and optimal control theory*, American Mathematical Society, New York, 2000.

[173] Liberzon D, *Calculus of variations and optimal control theory: A concise introduction*, Princeton University Press, Oxford, 2012.